Integrated Light Stellar Population Synthesis of Globular Clusters Using Non-Local Thermodynamic Equilibrium Modelling

by

Mitchell E. Young

A Thesis Submitted to Saint Mary's University, Halifax, Nova Scotia in Partial Fulfillment of the Requirements for the Degree of

DOCTOR OF PHILOSOPHY

in

Astronomy

(Department of Physics and Astronomy)

November 22, 2018,Halifax, Nova Scotia

Approved: Dr. C. Ian Short
Supervisor

Approved: Dr. Viktor Khalack
External Examiner

Approved: Dr. Marcin Sawicki
Examiner

Approved: Dr. Phillip Bennett
Examiner

Date: November 22, 2018

Contents

[1] This chapter originally appeared in Young, M. and Short, C. I. 2017, Astrophysical Journal, 832, 292

[2]This chapter has been accepted for publication in the Astrophysical Journal

[3]This chapter is ready for submission to the Astrophysical Journal, pending publication of Chapter 3

List of Figures

List of Tables

Acknowledgements

First and foremost, I would like to thank my supervisor, Dr. C. Ian Short, without whom, this project would have never been possible. He has provided direction and encouragement above and beyond expectations. I would also like to thank my wife, Hannah Horne-Robinson, for emotional support and for driving me on when I lost sight of the finish line. Further thanks go to Dr. Kirsten Bonson, Dr. Michael Casey, and Christopher Cooke for discussions about atmospheric modelling and debugging techniques. I appreciate the rest of the graduate students with whom I have spent the last few years for helping to create a good graduate student community. I would like to thank the ACEnet support staff, specifically Dr. Chris Geroux who enthusiastically helped with debugging some environment specific problems with my code. Thanks also to Department and ICA Administrative Assistant Florence Woolaver who has handled expenses and organizing appointments. Finally I would like to thank my parents for their support and encouragement with my schooling through the many years.

A large part of this work was performed by the ACEnet computational resources. ACEnet, a part of Compute Canada, provides academic high-performance computing to Atlantic Canada. I am grateful for financial support from an NSERC Discovery Grant to C. I. Short.

Abstract

Integrated Light Stellar Population Synthesis of Globular Clusters Using Non-Local Thermodynamic Equilibrium Modelling

by Mitchell E. Young

We present an investigation of McWilliam & Bernstein's 2008 globular cluster (GC) stellar population synthesis method, focusing on the impact of non-local thermodynamic equilibrium (NLTE) modeling effects. For this purpose, we have generated comprehensive, fully NLTE libraries of individual stellar spectra and GC integrated light (IL) spectra. The stellar library spans large ranges in $T_{\rm eff}$, log g, and $[M/H]$, reproduced for 0.5 and 1 $M_{\odot}$ and two degrees of α-enhancement. The IL library spans 9 to 15 Gyr in age, and -1.790 to -0.253 in $[M/H]$. The IL spectral library is used to investigate Johnson-Cousins-Bessel $UBVIJK$ IL colours, sensitivity of IL spectral features to cluster age or metallicity, and deriving the ages and metallicities of 11 GCs for which IL spectra are acquired from Colucci, Bernstein & McWilliam (2017). The IL colours confirm previously reported trends of GC reddening with increasing age or metallicity, and demonstrate that NLTE colours are bluer than LTE by up to a few tens of millimagnitudes, as are α-enhanced colours. We find a dependence of a few millimagnitudes on the discretization resolution of population CMDs when using the 25-30 boxes suggested in the literature. This dependence is minimized when the number of boxes increased to 40-50. We find 240 spectral features sensitive to either cluster age or metallicity, of which 209 are newly identified as potential GC diagnostic features. These features represent 19 different species, including Fe I, Fe II, Ca I, and Ti I. Chi-squared minimization is used to determine the best fit to the observed GC IL spectra, deriving ages for six of the 11 clusters, and metallicities for all of them. The uncertainties of both the ages and metallicities are reduced by a factor of two to three times when fit with NLTE IL spectra when compared with those from fitting LTE spectra.

November 22, 2018

1 Introduction

Globular clusters (GCs) have long played an important role in astronomy. The discovery of the first GC is credited to Abraham Ihle in 1662 (Monaco *et al.*, 2004), for discovering what would become M22. However, GCs were not resolved into clusters of individual stars until 1764, when Charles Messier observed M4. Today, we now know of 157 GCs within our own Galaxy (Harris 1996, 2010 ed), and over 400 within our nearest neighbour, M31 (Peacock *et al.*, 2010). Globular cluster stellar populations, that is, their constituent stars, can be studied directly if they can be spatially resolved, or indirectly via the integrated light (IL) of all the stars in the cluster. The focus of this work is investigating the effects of non-local thermodynamic equilibrium (NLTE) modelling of stellar atmospheres and spectra on the parameters of GCs derived from their integrated light (IL) spectra.

Globular clusters can be used to place constraints on galaxy chemical, dynamical, and merger evolution histories as a consequence of being among the oldest and brightest objects in any galaxy, with the exception of AGN. They can provide independent distance estimates to other galaxies (di Criscienzo *et al.*, 2006), complementing standard candles such as Cepheid variables and supernovae type Ia, and are also used to trace the mass distribution and estimate the total mass of galaxies and their dark matter halos (Eadie, Springford & Harris, 2017). Combining the location of the main sequence (MS) turnoff in the Hertzprung-Russell (HR) diagrams of GCs with evolu-

tionary models provides estimates of GC ages and puts constraints on cosmological models.

Thus, understanding GCs is important for many aspects of astronomy. Our understanding has come a long way since the 17^{th} century. The term "globular cluster" itself didn't arise until 1789 when William Herschel published his *Catalogue of a Second Thousand New Nebulae and Clusters of Stars*, more than a century after they were first observed (Herschel, 1789). Starting in 1914, Harlow Shapley began a series of studies on variable stars in GCs, measuring their distances using the period-luminosity relationship of the variable stars within the clusters, which he assumed were Cepheid variables (Shapley, 2014, 1916). In reality, they turned out to be RR Lyrae variables, which are dimmer than Cepheids, and his distance estimates were consequently too large. In 1939, Pieter Oosterhoff observed two distinct populations of GCs based on the periodicities of their RR Lyrae variables, which would come to be known as the Oosterhoff groups (Oosterhoff, 1939). Type I group members have shorter period variables than type II, typically ~ 0.55 and 0.65 days, respectively. We now know that the Oosterhoff groups also represent a Galactic bimodal metallicity distribution, with type I and II groups peaking at $[M/H] \approx -0.6$ and -1.5, respectively (van Albada & Baker, 1973), and that they are spatially distributed with the metal-rich clusters generally concentrated near the bulge, and metal-poor clusters diffused in the halo (Yoon & Lee, 2002). Additionally, recent works have demonstrated that the vast majority of GCs are likely to contain multiple stellar populations, indicative of mul-

tiple distinct episodes of, or continuous, star formation within the clusters (Bastian & Lardo, 2018; Milone *et al.*, 2018; Niederhofer *et al.*, 2016). But there is still much that needs to be understood. For example, what is the fraction of GCs that form *in situ* in their host galaxies versus those that are captured from dwarf galaxies, what, if any, are the differences between Milky Way GCs and extragalactic GCs, and what is the origin of multiple stellar populations within GCs.

Globular cluster IL is complex enough that we rely on computational modelling to make progress on the above questions. Much work, nearly all using local thermodynamic equilibrium (LTE) models, has already been done and considerable progress has been made. In section 1.1 we outline the recent observational history of GC IL studies, and in section 1.2 we describe the current state and mention some of the successes of modelling GC IL high spectral resolution spectra ($R \sim 30000$). One important limitation of the modelling to date is the LTE approximation. This modelling treatment of stellar atmospheres and spectra employs an unrealistic simplifying assumption regarding the coupled equilibrium of the gas and radiation field in a way that neglects global boundary conditions at the top of the atmosphere. One consequence of this in some cases is a significant error in computed atomic energy level and ionization stage populations, which contributes to the prediction of unrealistic spectral line strengths. Local thermodynamic equilibrium will also lead to estimates of effective temperature, $T_{\rm eff}$, based on spectral energy distribution, SED, fitting that are too great by up to $\sim$100 K (Short & Hauschildt, 2003; Short *et al.*, 2012). These

failures, and others of the current methodology, will be discussed in more detail in section 1.3. The current work aims to explore a more physically realistic alternative to LTE modelling of GC IL by quantifying the differences in derived parameters of GCs when fit with NLTE spectra and colours instead of LTE.

1.1 Studies of Observed GC Integrated Light

The IL of GCs can be used to place constraints on their stellar populations, ie. what stars make up the stellar membership of the cluster, and on their overall parameters. Early attempts at deriving ages and metallicities of GCs with stellar population synthesis, SPS, models of IL generally fell into one of two camps: broad-band photometric colours or low- to medium-resolution spectroscopy. Integrated light metallicities have been estimated for systems ranging from M31 to the Virgo cluster of galaxies, using broadband photometric colours (Forte, Strom, & Strom, 1981; Geisler, Lee, & Kim, 1996). The results, while promising, are not as robust as could be hoped because of limitations of the early models and uncertainties associated with the age-metallicity degeneracy (Worthey, 1994). This degeneracy is a manifestation of the similar $T_{\rm eff}$ dependence of main sequence and giant stars on cluster age and metallicity, which causes the integrated colours of stellar populations to respond in similar ways to variations in these two parameters. It was only after the systematic modelling of Balmer lines as age indicators by Worthey (1994) that reliable quantitative estimates of GC ages became available.

Early on, the low-resolution spectra typically employed the Lick index system (Faber, 1973), which is based on correlations between strong absorption features at low resolution and detailed abundances obtained for individual stars at high spectral resolution. All of these indices contain numerous lines from several elements, although many are dominated by particular species that can be empirically calibrated to give approximate composition information (Peng, Ford & Freeman, 2004). While useful for obtaining information on the general chemical properties of GC systems, even state of the art line index techniques for lower resolution will always be limited to measurements of, at most, several elements (Graves & Schiavon, 2008). In fact, line index systems were originally designed to target unresolved galaxies in which spectral lines of individual elements are not possible to resolve due to the high internal velocity dispersions ($100 - 300\frac{\mathrm{km}}{\mathrm{s}}$) of the galaxies themselves (Faber & Jackson, 1976). Globular clusters are, in general, not limited in this way, with internal velocity dispersions that are one to two orders of magnitude smaller.

Low- to medium-resolution ($R \lesssim 5000$) IL spectroscopic analysis methods have been tested and calibrated on Galactic GCs within the last few decades (Schiavon *et al.*, 2002; Lee & Worthey, 2005) and have proven capable of determining ages, metallicities and abundances of some elements with strong spectral features like C, N, and Mg (Caldwell *et al.*, 2011; Schiavon *et al.*, 2013). For extragalactic GCs, integrated light metallicities have been estimated for systems ranging from M31 to the Virgo cluster of galaxies (Racine, Oke, & Searle, 1978; Brodie & Huchra, 1990).

IL spectral observations have identified, among other things, a possible metallicity bimodality (Perrett *et al.*, 2002) and metallicity gradient (Caldwell *et al.*, 2011) in M31s GC population and α-deficiencies in distant GCs that are associated with dwarf galaxies (Puzia & Sharina, 2008).

1.2 IL SPS Modelling

Although detailed high-resolution chemical abundance analysis of individual stars in Galactic GCs was already a well developed field in 2008, McWilliam & Bernstein (2008) were the first to perform such an analysis on a high-resolution ($R \sim 35000$) IL spectrum of Galactic GC 47 Tuc. Using a new IL spectrum synthesis procedure they had developed, they computed abundances of 20 different elements with uncertainties of 0.10 dex or less, comparable to, and in good agreement with, high-resolution studies of individual stars within 47 Tuc. The procedure they employed involved two independent methods of analyzing the IL. 1) They characterized the stellar population by discretizing the colour-magnitude diagram (CMD) of the cluster into ~ 30 regions ("boxes") and synthesized theoretical equivalent widths (EWs) of visible wavelength diagnostic lines for a star representative of the sub-population within each box. These EWs were averaged, weighted by the continuum flux at each line, and the total flux in each box, to obtain theoretical IL EWs, which were fit to the observed IL spectrum. This method has the advantage of prior knowledge of the stellar population in a cluster, but is limited to GCs where the individual stars can be resolved into a CMD. 2)

The second method employed theoretical isochrones in place of the resolved cluster photometry. This method has the advantage of being able to analyze an IL spectrum without *a priori* knowledge of the underlying stellar population, but is limited by the accuracy of the stellar evolution models used to compute the isochrones, and how well the isochrones match the luminosity functions and effective temperatures of the cluster stars. While McWilliam & Bernstein (2008) worked with a spectral resolution of $R \sim 35000$ initially, it has since been demonstrated that the procedure will work for resolutions in the range $22500 \leq R \leq 40000$.

Similar to diagnostic techniques used on single stars (Drake & Smith, 1991), the stability of the derived iron abundance with respect to individual line parameters (equivalent width, excitation potential, and wavelength) can provide a check on the accuracy of the parameters of an assumed isochrone. The abundance versus excitation potential (EP) diagnostic is sensitive to the $T_{\rm eff}$ of the stars, while the abundance versus EW diagnostic is sensitive to the microturbulent velocities of stars. The abundance versus wavelength diagnostic is indirectly sensitive to the age of the CMD, because stars of different temperatures dominate the IL flux at different wavelengths (McWilliam & Bernstein, 2008; Young & Short, 2017), and the temperature distribution will change as the population ages. In an IL spectrum, correlations with EP and wavelength can be caused by an inaccurate temperature distributions in the CMD, which, for example, could be the result inaccurate modelling of HB morphology or an incorrect selection of isochrone age. Likewise, correlations with EW can be the

result of inaccurate proportions of stars of different gravities as well as a symptom of an inaccurate microturbulent velocity law.

A year later, Colucci *et al.* (2009) began applying this technique to unresolved GCs in M31. A study of five extragalactic GCs, they find that the clusters are similar to Milky Way GC systems in several respects, including ages > 10 Gyr, a range of $-2.2 < [Fe/H] < -0.9$, and similar levels of α-enhancement for Ca, Si, and Ti. In Colucci *et al.* (2011) the technique is adapted to fitting line profiles as well as EWs in young unresolved M31 clusters. They demonstrate that ages can be fit to clusters younger than 1 Gyr, and that $[Fe/H]$ can be measured for any cluster younger than 12 Gyr with only a slight increase in the uncertainty over older Milky Way GCs (0.10-0.25 dex and $\sim$0.10 dex, respectively). In Colucci *et al.* (2012), they present an IL χ^2-minimization technique to fit weak lines (EW$\sim$ 15mÅ) in low signal-to-noise spectra (S/N$\sim$ 30), allowing detailed abundances to be derived for the young M31 clusters.

Sakari *et al.* (2013) demonstrate that assuming an incorrect horizontal branch, HB, morphology has minimal impact on the derived abundances of Mg, Na, and Eu in five Galactic GCs. Fitting IL EWs generated from isochrones which only differ in HB morphology, the abundances of the three elements only vary by $\lesssim 0.06$ dex, demonstrating that IL spectrum syntheses can therefore be applied to unresolved GCs not only over a wide range of metallicities, but also horizontal branch morphologies. In Sakari *et al.* (2016), they extend high-resolution IL spectrum synthesis to the $H-$band

of 25 M31 GCs, deriving abundances for 11 elements, including C, N, and O (derived from molecular features), and for the first time in IL spectrum synthesis, K. The CNO abundances are shown to be consistent with typical RGB stellar abundances, but are offset from optical Lick index abundances. The other elements agree with optical abundances within 1σ uncertainties. The combination of independent IR and optical abundances allows for better determinations of GC properties, and may enable probing for multiple populations in unresolved extragalactic GCs.

Alternatively to fitting EWs and line profiles, individual abundances can be determined from full spectrum fitting. Larsen, Pugliese & Brodie (2018) adapt McWilliam & Bernstein's method to this purpose by calculating the representative model atmospheres and spectra in real time during the fit, iteratively solving individual elemental abundances in their models to minimize χ^2 over their whole spectral range of optical wavelengths. This approach requires significant modelling approximations to make it computationally feasible (LTE, 1D, static, and plane-parallel, discussed further in Section 1.3), and is performed on three Fornax GCs with resolved CMDs, only using isochrones to extrapolate the main sequence below the detection limit. The results are comparable with EW measurements and fitting individual lines, with uncertainties in $[Fe/H]$ of 0.1 dex. The authors comment that the modelling assumptions being made are common in the analysis of GC stars, but will become invalid in the analysis of younger clusters, where hot young stars or stars with low surface gravities contribute significant fractions of the total light.

1.3 Atmospheric Modelling

In this section, we will give a brief overview of stellar atmospheric modelling. For a more in-depth review of atmospheric modelling theory, see Hubeny (2017).

A stellar atmosphere is the outer region of a star, surrounding the interior, and acts as a transition region from the stellar interior to the interstellar medium. This region represents somewhere between a fraction of a percent to a few percent of the total stellar radius , inversely proportional to the surface gravity of the star. For observational purposes, the atmosphere is the most important region of a star, because the atmosphere is where the radiation of the stellar spectrum originates. Since, in the vast majority of cases, radiation is the only information about a distant astronomical object we have (exceptions being solar wind particles, neutrinos, and gravitational waves), all the information we gather about stars is derived from observing their radiation.

It is therefore of considerable importance to be able to decode the information about a star contained in its spectrum with confidence. Understanding the physics of the problem and being able to carry out detailed numerical simulations enables us to construct theoretical models of a stellar atmosphere and predict stellar spectra, SEDs, and photometric colours. While these quantities are all fundamentally connected, and many of the refinements in modelling techniques apply to all of them, these quantities may be independently used for comparison with observations. Much of what is now known about all types of stars comes from fitting the predicted stellar

quantities of atmospheric models to observations. Estimates of the solar chemical abundances come from fitting synthetic spectral line profiles and equivalent widths to those observed in the Sun (Ross & Aller, 1976; Asplund *et al.*, 2009; Caffau *et al.*, 2011). Calibrations of stellar parameters, such as surface gravity (g), absolute visual magnitude (M_V), effective temperature ($T_{\rm eff}$), luminosity (L), and stellar radius (R_0), for different spectral types are found from fitting models to, variously, spectral line EWs or profiles, SEDs, and colours (Martins, Schaerer & Hillier, 2005). Stellar atmospheric modelling has important applications in other branches of astrophysics, such as: 1) derived stellar parameters can be used to verify predictions of the stellar evolution theory; 2) models provide ionizing fluxes for the interstellar medium and nebular models; 3) predicted stellar spectra are basic blocks for population syntheses of stellar clusters, starburst regions, and whole galaxies. The age-metallicity and colour-metallicity relations of GCs, for example, can be determined from the abundances of individual red giants within the clusters (Pilachowski, Olszewski & Odell, 1983; Carretta & Gratton, 1997; Carretta *et al.*, 2010).

One of the most important equations for modelling a stellar atmosphere and spectrum is the radiative transport equation for a ray. In its most general form, it makes no assumptions on the geometry of the medium, special relativistic effects, or time dependence. While this general form of the equation is always applicable, a number of simplifying assumptions exist that may be applicable under certain conditions. First, assuming that an atmosphere is static, i.e. that there are no macroscopic ma-

terial motions in the atmosphere, it will be in hydrostatic and radiative equilibrium, and any time dependence is removed. Hydrostatic equilibrium assumes that there is no net radial force acting on any point within the atmosphere, and that the outward pressure gradient is balanced by the gravitational force. Assuming time-independence for the atmosphere prevents the number densities of ionization stages and atomic and molecular energy levels, defined by statistical equilibrium (SE), at every point in the atmosphere from changing. In cases where the geometric extent of the atmosphere is much smaller than the radius of the star (e.g. dwarf stars), plane-parallel geometry is assumed, otherwise a spherical geometry is necessary (e.g. red giants). Horizontal homogeneity assumes that all position-dependent modelling variables, such as temperature or density, vary only along the depth axis and are constant over a surface of given depth. Such models are one-dimensional (1D) stellar atmospheres. These assumptions reduce the radiative transport equation to its more commonly employed forms: the monochromatic radiative transfer equation of 1D plane parallel stellar atmospheres,

$$\mu \frac{\mathrm{d}I_\nu(\mu, z)}{\mathrm{d}z} = \eta_\nu(\mu, z) - I_\nu(\mu, z)\chi(\mu, z), \tag{1.1}$$

where I_ν is the specific monochromatic intensity, χ_ν and η_ν are the monochromatic absorption and emission coefficients, z is the geometric depth, and we introduce a directional cosine, $\mu \equiv cos\theta$, where θ is measured between the direction of propagation of the ray and the normal to the surface of the atmosphere; and the monochromatic

radiative transfer equation of 1D spherically symmetric stellar atmospheres,

$$\mu \frac{\partial I_\nu(\mu, r)}{\partial r} + \frac{1-\mu^2}{r} \frac{\partial I_\nu(\mu, r)}{\partial \mu} = \eta_\nu(\mu, r) - I_\nu(\mu, r)\chi_\nu(\mu, r), \tag{1.2}$$

where r is the radial depth. The atmospheric models we compute in this work are static, 1D, spherical models.

1.3.1 LTE vs NLTE

It is well known from statistical physics that a description of gas properties is greatly simplified if strict thermodynamic equilibrium (TE) holds. From the very nature of a stellar atmosphere it is clear that it cannot be in strict thermodynamic equilibrium - we can see stars, therefore we know that photons must be escaping. However, even if the assumption of strict TE cannot be applied for a stellar atmosphere, we may still assume the concept of LTE. This assumption asserts that we may employ the standard thermodynamic relations not globally over the whole atmosphere, but locally, at local temperature values. In LTE, all gas populations are dominated by collisional transition rates, so the temperature is taken to be the kinetic gas temperature ($T_{\rm Kin}(\mathbf{r})$). This simplifies the problem enormously, for it allows all particle distributions to be approximated as if in TE locally.

Specifically, LTE is characterized by the following three distributions:

Maxwellian velocity distribution of particles

$$f(\mathbf{v})d\mathbf{v} = (m/2\pi kT)^{3/2} e^{(mv^2/2kT)} d\mathbf{v}, \tag{1.3}$$

where $\mathbf{v}$ is the velocity, m is the particle mass, and k is the Boltzmann constant.

Boltzmann excitation equation

$$\left(\frac{n_j}{n_i}\right) = \left(\frac{g_j}{g_i}\right) e^{[-(E_j - E_i)/kT]}, \tag{1.4}$$

where n_i is the number density of level i, g_i is the statistical weight, and E_i is the level energy, measured from the ground state.

Saha ionization equation

$$\frac{N_I}{N_{I+1}} = n_e \frac{U_I}{U_{I+1}} C T^{3/2} e^{(\chi_I/kT)}, \tag{1.5}$$

where N_I is the total number density of ionization stage I, U is the partition function $U = \sum_{i=1}^{\infty} g_i e^{(-E_i/kT)}$, χ_I is the ionization potential of ion I, and $C = (h^2/2\pi mk)^{3/2}$ is a constant. Note that the equilibrium values of distribution functions are assigned only to gas particles; the radiation field is allowed to depart from its equilibrium.

In LTE, all gas particle level populations, including atomic, ionic, and molecular populations, are given by the combined Saha-Boltzmann statistics defined at the local value of $T_{\rm Kin}$, and the radiative source function ($S_\lambda \equiv \frac{\eta_\nu}{\chi_\nu}$) **is assumed to be**

thermal, and given by $S_\lambda = B_\lambda(T = T_{\rm Kin})$, where B_λ is the Planck function,

$$B_\lambda(\lambda, T) = \frac{2hc^2}{\lambda^5} \frac{1}{e^{\frac{hc}{\lambda kT}} - 1}, \tag{1.6}$$

λ is the wavelength, c is the speed of light, and h is Planck's constant. However, the radiation field intensity (I_λ), computed from the radiative transfer equation, is not set to the Planck function, $I_\lambda \neq B_\lambda$. Otherwise strict TE would hold, there would be no radial temperature gradient, and no outward transfer of radiant energy.

In the NLTE treatment, populations of ionization stages and energy levels generally are allowed to depart from their LTE value by relaxing the condition that transitions be collisionally dominated and accounting for radiative transitions, while velocity distributions of all particles are assumed to be Maxwellian so that $T_{\rm Kin}$ is still defined locally. One of the big issues of modern stellar atmospheres theory is to what extent should departures from LTE be accounted for in numerical modelling. Generally, to understand why and where we may expect departures from LTE, we distinguish between two types of transitions: collisionally driven transitions (interactions between two or more massive particles), and radiative transitions (interactions involving particles and photons). Under conditions deeper in a stellar atmosphere where gas densities are higher, collisions between massive particles tend to maintain the local equilibrium since velocities are given by equation 1.3. Therefore, the validity of LTE hinges on whether the radiative transitions play a significant role in determining particle populations.

That the radiation escapes from a star implies that LTE should eventually become a poor approximation above a certain optical depth in the atmosphere. Essentially, this is because detailed balance in radiative transitions generally breaks down at a certain point near the surface. Consequently, the number of photoexcitations is less than the number of the inverse process, spontaneous emissions. This explains that we may expect departures from LTE if the following two conditions are met: 1) radiative rates are significant in some important atomic transition; and 2) radiation is not in equilibrium.

In any NLTE study, the first step is to select which chemical elements are to be considered out of LTE, ie. those for which the equations of statistical equilibrium (SE) will be used. Every ion, for each chemical element, has its own set of SE equations, with different ionization stages of a given element coupled by ionizations and recombinations in the SE equations. Coupled multi-species NLTE iteratively accounts for coupling among all species via the radiation field. In PHOENIX, the rate equations for a species treated in NLTE are given by

$$\sum_{j<i} n_j(R_{ji}+C_{ji}) - n_i\left(\sum_{j<i}(R_{ij}+C_{ij}) + \sum_{j>i}\left(\frac{n_j^*}{n_i^*}\right)(R_{ij}+C_{ij})\right) + \sum_{j>i} n_j\left(\frac{n_j^*}{n_i^*}\right)(R_{ji}+C_{ji}) = 0 \tag{1.7}$$

where n_i is the level population of i, n_i^* is the LTE level population, and R_ij and C_ij are the radiative and collisional rates of the transition from i to j. The set of rate equations for a given atom would form a linearly dependent system, and therefore

one equation out of each set is replaced by the abundance definition equation:

$$\sum_{i=1}^{NL_I} n_i(1+S_i) = N_I = (N - n_e)\alpha_I \tag{1.8}$$

where where NL_I is the total number of energy levels of ionization stage I, S_j is the upper sum, N is the total number of atoms I in all ionization stages, n_e is the number of free electrons, and α_I is the fractional abundance of element I.

For each species selected to be treated in NLTE, the next step is to identify a set of ionization stages that are to be treated explicitly, creating a set of explicit ions. Then, for each explicit ion, a set of explicit excitation levels must be selected. And finally, for each explicit excitation level, a set of explicit transitions needs to be selected. With the appropriate data in hand, the final step is to simultaneously iterate solutions to the linearized forms of the transfer equation, the hydrostatic equilibrium equation, the radiative equilibrium equation, charge conservation equations, and the SE equations. For each iteration, the equations are formally solved with the current values of all other state parameters. Specifically, corrections may be applied to arrive at new values of temperature, electron density, and mean intensities, but not the new populations. They are obtained by using the new temperature, electron density, and mean intensities to solve the collision rates and SE equations. Finally, the process is repeated until a desired number of iterations have been completed, or predetermined convergence criteria are met.

2 Constructing the IL Spectra

2.1 INTRODUCTION

Because of their old ages, relative homogeneity of their populations, and high luminosities, globular clusters (GCs) can be used to study the chemical evolution history of galaxies. The most luminous GCs presumably only trace the major star forming events, including mergers. Even basic metallicity provides interesting information for comparison with the Galaxy. However, the detailed chemical composition of GCs could potentially provide much more information on galaxy evolution, because the chemical elements are produced by a variety of stars, with varying sensitivity to stellar mass and metallicity. High resolution spectroscopic chemical abundance analysis of individual stars in Galactic GCs has long been pursued (Cohen, 1978; Pilachowski, Canterna, & Wallerstein, 1980). Such abundance studies are a useful tool for probing the chemical evolution of the Galaxy (Sneden *et al.*, 1991; Briley, Smith, & Lambert, 1994). Unfortunately, similar studies have not been possible outside of the Milky Way, as individual stars cannot be resolved in distant galaxies.

For extragalactic GCs, cluster metallicities have been estimated using broadband photometric colours (Forte, Strom, & Strom, 1981; Geisler, Lee, & Kim, 1996) and low-resolution integrated light (IL) spectra (Racine, Oke, & Searle, 1978; Brodie & Huchra, 1990). Results from such studies include the discovery of bimodal GC

metallicity and colour distributions in extragalactic systems (Elson & Santiago, 1996; Whitmore *et al.*, 1995) reminiscent of the bimodal GCs in the Milky Way (Zinn , 1985).

In recent years, stellar population synthesis (SPS) of GC populations has provided a new avenue of investigating the chemical composition of either spatially resolved or unresolved GCs, provided high spectral-resolution IL spectra can be obtained (McWilliam & Bernstein, 2008; Colucci *et al.*, 2009, 2011). Using both broadband photometric colours and equivalent widths (EWs) of spectroscopic absorption lines as diagnostics, detailed information on the chemical composition of a cluster as a whole can be derived.

Non-local thermodynamic equilibrium effects have been demonstrated to be present in the spectra of asymptotic-giant branch (AGB) stars in the Galactic GCs 47 Tuc (Lapenna *et al.*, 2014), affecting the analysis of Fe I and II abundances. While the same effects have yet to be demonstrated in red-giant branch (RGB) GC stars, there is a possibility that the effects will be reflected in the IL spectra of a cluster if it is present in its brightest members.

2.1.1 Present Work

Our primary goal is to investigate NLTE modelling effects on the IL spectra of synthetic GCs, as well as ages and metallicities subsequently derived from them, using the population synthesis methodology presented by McWilliam & Bernstein (2008).

We test two degrees of NLTE treatment, one where we model only the component of the population more evolved than the sub-giant branch in NLTE, and the other where we model the entire population in NLTE. WE also investigate the uncertainty associated with the colour-magnitude diagram (CMD) discretization used in this method. We compare ages for synthetic clusters derived from photometric colours of both LTE and NLTE spectra, and we assess the significance of deviations caused by NLTE effects by comparing them to those caused by photometric uncertainty.

2.2 LIBRARY OF SYNTHETIC SPECTRA

We used PHOENIX v.15 to compute spherically symmetric model atmospheres and high resolution synthetic spectra ($R \approx 300000$) over the wavelenght range $\lambda =$ 2000 to 27000 $\mathring{A}$, for stars that cover the CMD parameter spaces of GCs at various ages and metallicities spanning Galactic values. **Our atmospheric structure models are considered converged if after 10 iterations, the atmospheres depart from radiative equilibrium throughout non-convective regions by** $\leq 0.5\%$ **for LTE models, or by** $\leq 2.0\%$ **after 15 iterations for NLTE models.** We produced a library of stellar atmospheres covering the ranges of $T_{\rm eff}$ = 3000 to 15000 K (in steps of 200 K below $T_{\rm eff}$ = 4000 K, 1000 K above $T_{\rm eff}$ = 10000 K, and 250 K otherwise) and -0.5 to 5.0 dex in log g (in steps of 0.5 dex) (Coelho, 2014). Figure 2.1 shows the extent of the coverage in $T_{\rm eff}$ vs log g space. This coverage was reproduced for three values of metallicity, [M/H] = -1.49, -1.00, and -0.66, and

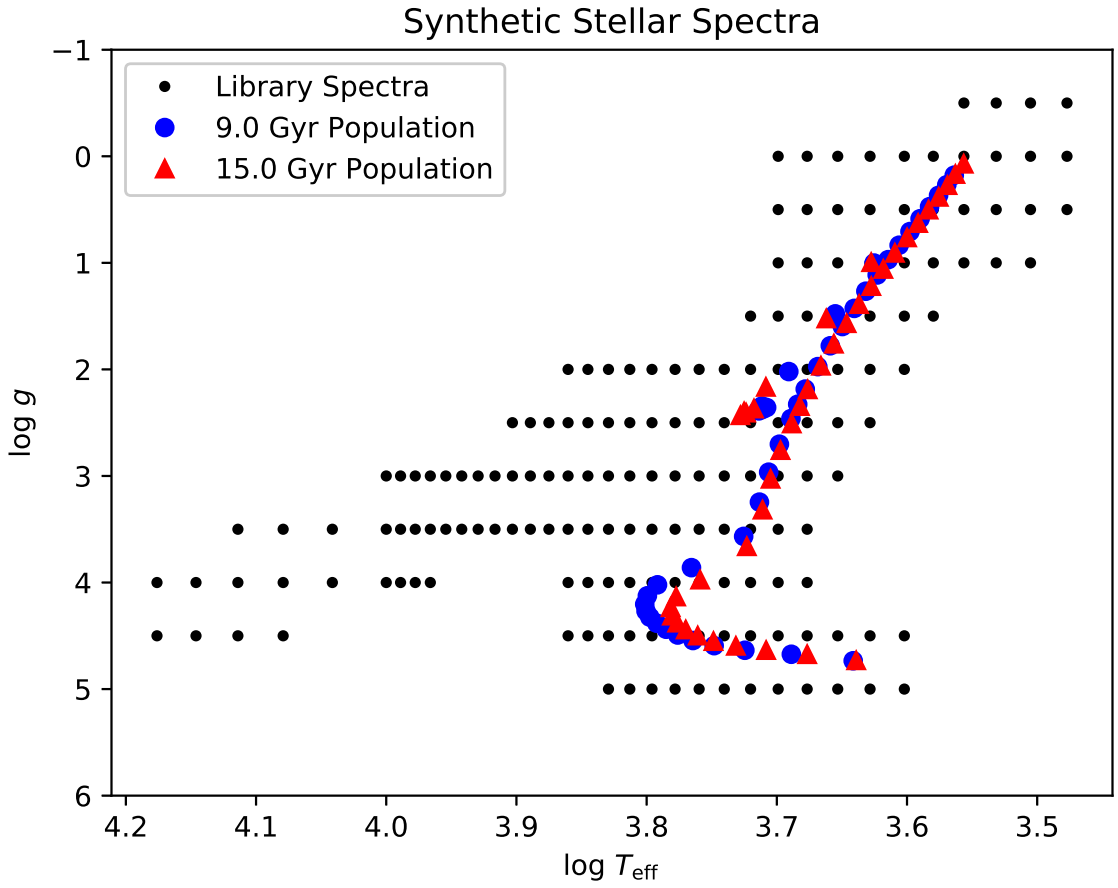

Figure 2.1 Coverage of our library of stellar atmospheres and spectra in $T_{\rm eff}$ vs log g space. This selection is reproduced at both 0.5 and 1 $M_{\odot}$ and at each of [M/H] = −0.66, −1.0, and −1.49. Two sample representative populations produced from the 9.0 and 15.0 Gyr isochrones have been plotted to indicate where library interpolation occurs.

two values of stellar mass, M = 0.5 and 1.0 $M_{\odot}$.

Our library was built in two halves, "warm" stars and "cool" stars, using a separate pipeline for each. For cool star models, we consider 47 different molecules, with a combined total of 119 isotopologues and isotopomers, in both the equation of state (E.O.S.) and opacity calculations. The molecules taken into consideration are listed in Table 2.1. The atmospheres are also left to naturally form convection zones. For

warm star models, we do not consider molecules in the E.O.S. or opacity calculations. Molecules are fully dissociated in stars earlier than F0, which Cox (2000) lists as $T_{\rm eff} \gtrsim 7300$ K; we choose to err on the side of including molecules unnecessarily and include them in models with $T_{\rm eff} \leq 7500$ K, to ensure they are present in all models where they are significant. We also take this as the $T_{\rm eff}$ value above which the possibility of convection is no longer considered in our models, treating the whole extent of the atmosphere as if it were in radiative equilibrium. The one exception to this division of warm and cool stars is modelling the linear Stark broadening of H I lines. We include the broadening in the spectra of atmospheres with $T_{\rm eff} \geq 5000$ K; spectra cooler than this do not have significant Stark wings on H I features (Cox, 2000).

All of our atmospheric models have alpha enhanced abundances, with $\alpha = +0.4$ dex. For our initial solar composition, we take our abundances up to O from Grevesse, Noels, & Sauval (1996), and take the revised abundances of Scott *et al.* (2015a) (F to Ca), Scott *et al.* (2015b) (Sc to Ni), and Grevesse *et al.* (2015) (Cu to Cs). We assume values for microturbulent velocities of $\xi = 4\ \mathrm{km\,s^{-1}}$ for stars of $\log g = 3.0$ and lower, and $\xi = 1\ \mathrm{km\,s^{-1}}$ for stars of $\log g = 3.5$ and higher. Two distinct values are used here instead of a more realistic continuous variation to artificially enhance the distinction between spectral lines dominated by evolved and unevolved populations in the IL spectrum.

The synthetic spectral output of PHOENIX is the monochromatic flux spectral

Table 2.1 List of molecules used by PHOENIX in E.O.S. and opacity calculations. Number of isotopologues and isotopomers considered for each species included.

Molecule	Number of Isotopologues & Isotopomers	Molecule	Number of Isotopologues & Isotopomers	Molecule	Number of Isotopologues & Isotopomers
C_2	3	H_2O	4	NO	3
C_2H_2	2	H_2O_2	1	NO_2	1
C_2H_6	1	H_2S	3	O_2	3
CH	2	H_3^+	1	O_3	3
CH_3Cl	2	HBr	2	OCS	4
CH_4	5	HCN	3	OH	4
CN	4	HCl	2	PH_3	1
CO	7	HF	1	SF_6	1
CO_2	8	HI	1	SO_2	2
COF_2	1	HNO_3	1	SiH	3
CaH	2	HOCl	2	SiO	4
ClO	2	MgH	3	TiO	5
CrH	1	N_2	1	VO	1
FeH	1	N_2O	5	YO	1
H_2	1	NH	2	ZrO	7
H_2CO	3	NH_3	2		

energy distribution (SED) of a model atmosphere, measured at an optical depth surface of $\tau_{12000} = 0$. Each synthetic spectrum in our library needs to be scaled by a factor of $(R_{\tau=0}/R_{\tau=1})^2$, where the radii are obtained from the corresponding structural models, to convert to the flux spectrum at the $\tau_{12000} = 1$ surface. This provides consistency between models of equivalent $T_{\rm eff}$ that have varying values of log g. We sample our spectra over the wavelength range $\lambda = 2000$ to 27000 Å at a spectral resolution of R = 300000, allowing us to compare values of cluster parameters derived from UV (Bellini *et al.*, 2015; Piotto *et al.*, 2015) and IR (Cohen *et al.*, 2015; Valcheva *et al.*, 2015) photometry, to those derived from more traditional optical

photometry and spectroscopy.

2.2.1 NLTE Atmospheres

In this work, we explore the effects of NLTE atmospheric modelling on synthetic IL spectra and cluster ages and metallicities derived from them. The atmospheric structures and synthetic spectra are self-consistently modelled in NLTE by synthesizing NLTE spectra only from NLTE atmospheric structures. We focus on NLTE modelling because Fe I line strengths and EWs in an IL spectrum are the main diagnostic features for deriving cluster parameters (McWilliam & Bernstein, 2008), and Fe I is one of the atomic species most heavily affected by NLTE in synthetic spectra.

NLTE Model Atoms

Because we study NLTE effects on GC parameters derived from IL spectra, the accuracy and completeness of our NLTE treatment is an important concern. It was shown by Mashonkina *et al.* (2011) that using a more complete Fe I atomic model will reduce NLTE overionization effects by providing more high energy excited states to facilitate recombination from Fe II. They found that the greater the number of energy levels within $\Delta E = kT_{\rm eff}$ of the ground state ionization energy ($\chi_{\rm Ion}$), the greater the accuracy of the NLTE ionization equilibrium solution.

To this end, we have adopted a set of new and updated NLTE model atoms, that are improved with respect to Young & Short (2014). These new atoms generally add to the numbers and refine the exact atomic data values of the energy levels and

transitions over the old model atoms. Table 2.2 shows a comparison of the numbers of levels and lines between the old and new model atoms. In addition to the species listed in the table, H I, He I, and Ne I are also treated in NLTE, but are handled internally by PHOENIX and have not been updated. However, in the cases of He I and Ne I, these species do not dominate massive line blanketing, while the old H I treatment is sufficiently complete to model the asymptotic convergence of the Balmer series lines for rounding out the Balmer jump. For details on the NLTE treatment of these species, see Young & Short (2014).

These new model atoms provide a significant improvement for some species, such as Fe I and II. Specifically, for Fe I, the new model atom has nearly double the number of energy levels, and more than triple the number of b-b transitions than the old. Additionally, the difference between the highest energy level and $\chi_{\rm ion}$ in the old Fe I model atom was $\Delta E = 0.322eV$, which meant that stars cooler than $T_{\rm eff} \sim 3750\,K$ would not have any energy levels within $kT_{\rm eff}$ of $\chi_{\rm ion}$. With the new model atom, there are now 45 energy levels closer to $\chi_{\rm ion}$, and for the coolest stars in our library at $T_{\rm eff} = 3000\,K$, 17 energy levels are within $kT_{\rm eff}$ of $\chi_{\rm ion}$.

Table 2.2 Comparison of old and new model atoms for atomic species treated in NLTE energy level calculations. Numbers of energy levels and b-b transitions given for each ionization stage treated in NLTE. The ground state ionization energy for each species as well as the highest energy levels in the old and new model atoms are also listed.

Species	Old ELs / B-B Trans	New ELs / B-B Trans	$\chi_{\rm I}$ (eV)	$\chi_{\rm High,Old}$ (eV)	$\chi_{\rm High,New}$ (eV)
Li I	57/333	60/394	5.392	5.296	5.296
Li II	55/124	55/135	75.640	74.128	74.128
C I	228/1387	230/3262	11.260	11.155	11.155
N I	252/2313	254/3704	14.534	14.460	14.460
O I	36/66	146/855	13.618	12.728	13.482
Na I	53/142	58/334	5.139	5.044	5.044
Na II	35/171	35/171	47.287	45.260	45.257
Mg I	273/835	179/1584	7.646	7.644	7.634
Mg II	72/340	74/513	15.035	14.585	14.585
Al I	111/250	115/482	5.986	5.977	5.977
Al II	188/1674	191/2608	18.828	18.665	18.665
P I	229/903	230/945	10.487	10.266	10.266
P II	89/760	90/882	19.726	17.542	17.542
S I	146/349	152/1995	10.360	10.146	10.284
S II	84/444	84/501	23.334	20.375	20.375
K I	73/210	80/576	4.341	4.300	4.300
K II	22/66	22/66	31.625	27.177	27.177
Ca I	194/1029	196/2893	6.113	6.054	6.054
Ca II	87/455	89/760	11.872	11.641	11.641
Ti I	395/5279	555/13304	6.820	6.653	6.653
Ti II	204/2399	204/2586	13.577	10.504	10.504
Mn I	316/3096	297/3067	7.435	7.418	7.418
Mn II	546/7767	512/8299	15.640	14.968	14.968
Fe I	494/6903	902/24395	7.871	7.539	7.815
Fe II	617/13675	894/22453	16.183	14.665	14.814
Co I	316/4428	364/6447	7.864	7.363	7.472
Co II	255/2725	255/2853	17.057	15.618	15.618
Ni I	153/1690	180/2671	7.635	7.422	7.422
Ni II	429/7445	670/17935	18.169	17.359	17.359
Total	6134/70492	8632/130728	...	...	...

2.3 SYNTHETIC colour MAGNITUDE DIAGRAMS

2.3.1 Isochrones

For this work, we have employed the Teramo theoretical isochrones, from the BaSTI group (Pietrinferni *et al.*, 2006). The Teramo isochrones are offered with a variety of theoretical assumptions made in calculating the stellar evolutionary tracks, including alpha-enhanced or scaled solar compositions, with or without convective core overshooting, two different mass-loss rates following the Reimers' Law, and normal or extended AGBs. The isochrones cover ranges of -3.27 to 0.51 dex in metallicity and 30 Myr to 19 Gyr in age. Each one is sampled at 2000 mass points with a variable sampling frequency to ensure that each area of the CMD is critically sampled. The 30 Myr isochrones cover a range of initial masses from 0.5 to 8.5 $M_{\odot}$, with the upper mass limit being reduced for isochrones with greater ages as stars evolve beyond the modelled tip of the AGB. The mass sampling frequency is increased for these isochrones to maintain the 2000 sampling points.

We select a subset of isochrones to investigate, with alpha enhancement of $\alpha = +0.4$, mass loss parameter $\eta = 0.2$, normal AGBs, and without core overshoot, similar to the selection of Colucci *et al.* (2009). We focus our investigation on those isochrones with ages and metallicities covering the range of observed Galactic GC values, spanning 9 to 15 Gyr and [M/H] = -1.49 to -0.66 dex. These values were

chosen as the isochrone metallicities closest to the peak values of the metal-rich and metal-poor Galactic GC populations (Zinn , 1985). We extend our ages beyond the range of average Galactic values (10-13 Gyr), to investigate the possible size of the effect NLTE modelling can have on derived ages.

The isochrones include stars mapping out the transition from the tip of the RGB to the red end of the HB. We remove these stars before populating our CMD for two reasons: 1) This transition is not well understood theoretically; and 2) Including these stars would interfere with our CMD discretization procedure, outlined below in Section 2.4.1. When included in a population, these stars contribute $< 1\,\%$ of the total cluster luminosity, and have a negligible impact on the IL SED.

2.3.2 Initial Mass Function

To expand the isochrones into full populations, we use Kroupa's initial mass function (IMF) (Kroupa, 2001), normalized as a probability density function of the form

$$p_{\mathrm{Kroupa}}(m) = \begin{cases} Ak_0 m^{-0.3} & 0.01\,\mathrm{M}_\odot < m < m_1 \\ Ak_1 m^{-1.3} & m_1 < m < m_2 \\ Ak_2 m^{-2.3} & m_2 < m < m_3 \\ Ak_3 m^{-2.3} & m_3 < m \end{cases} \tag{2.1}$$

with $k_0 = 1$, $k_1 = k_0 m_1^{-0.3+1.3}$, $k_2 = k_1 m_2^{-1.3+2.3}$, and $k_3 = k_2 m_3^{-2.3+2.3}$ ensuring a continuous function, where $m_1 = 0.08\,\mathrm{M}_\odot$, $m_2 = 0.50\,\mathrm{M}_\odot$, and $m_3 = 1.00\,\mathrm{M}_\odot$ (Maschberger, 2012). A is a global normalization constant. This form gives information about the relative frequencies of stars of various masses as opposed to the number of stars of different masses in a unit spatial volume.

The normalization constant, A, is determined for each isochrone individually, relative to their respective mass sampling ranges. To get the relative frequencies of the stars in each isochrone independently, we take a continuous mass range and divide it into bins centered on the isochrone points, with bin divisions halfway between adjacent points. The IMF is then numerically integrated over these bins using the extended trapezoid rule to get the relative frequency for each.

2.3.3 Populating the CMDs

To build our synthetic populations, we take a given target luminosity for the population, L_{tot}, representative of the luminosity of a real cluster, and analytically allocate fractions of L_{tot} to the isochrone points according to the relative frequencies. This determines the total luminosity of each point and, when divided by a point's individual luminosity, the number of stars representing that point in the population. This can result in non-whole numbers of stars for each isochrone point.

There is no intrinsic spread of CMD features or observational scatter from any source inherent in the synthetic population of our CMDs; they are built as simple

stellar populations out of single isochrones. We choose not to introduce any spread or scatter in the population artificially. This is unnecessary, as any random variations introduced will be averaged away in the creation of the IL spectrum, outlined in Section 2.4.2.

2.4 SYNTHETIC INTEGRATED LIGHT SPECTRA

The integrated light spectrum of a globular cluster is the combined light of every individual star within the cluster. Since it is not feasible to model hundreds of thousands of stars for each cluster that is to be studied, even when interpolating within a library of stellar models, a method by which an IL spectrum can be approximated is necessary.

2.4.1 Discretizing the CMD

We choose to represent groups of parametrically similar stars in a GC CMD by a single stellar spectrum per group and weight their contributions to the IL spectrum, following the method of McWilliam & Bernstein (2008). The method involves discretizing a CMD by binning parametrically similar stars areas bounded by lines of constant $T_{\rm eff}$ and $L_{\rm Bol}$. These areas, or boxes, are established such that an approximately equal fraction of the total cluster luminosity is emitted by the stars contained

in each. McWilliam & Bernstein (2008) limit the luminosity contained in any box to $\sim$ 3 to 4 % of the total luminosity for a given cluster ($\sim$ 25 to 30 boxes total); we choose to increase the total number of boxes to 50 ($\sim$ 2 % of $L_{\rm tot}$ each), effectively doubling the discretization resolution in our CMDs. This prevents the boxes from covering too large a range of values of the stellar parameters, which ensures that a single representative stellar spectrum will be an accurate approximation of the integrated spectrum for a box.

Starting at the low-mass end of the main sequence, stars of increasing mass are added to a box until the sum of their luminosities matches the allotted percentage of the total cluster luminosity for a box. The box is then considered full and subsequent stars are added to a new box. The process is repeated for increasing stellar mass until everything up to the tip of the RGB is enclosed in a box. We repeat the process starting at the low-mass end of the HB and proceed up the AGB, until the entire population has been placed into boxes. The process is explicitly broken and restarted here to avoid too large of a box from encompassing both the RGB tip and HB by blindly adding stars of increasing masses to boxes. This effectively splits our CMD into two components by ignoring short lived and poorly understood stars in the transition from the RGB to the HB. The first component is comprised of the main sequence, sub-giant branch, and red giant branch (the MR component), while the second encompasses the asymptotic giant and horizontal branches (the HA component). Figure 2.2 shows an example of a theoretical population similar in age

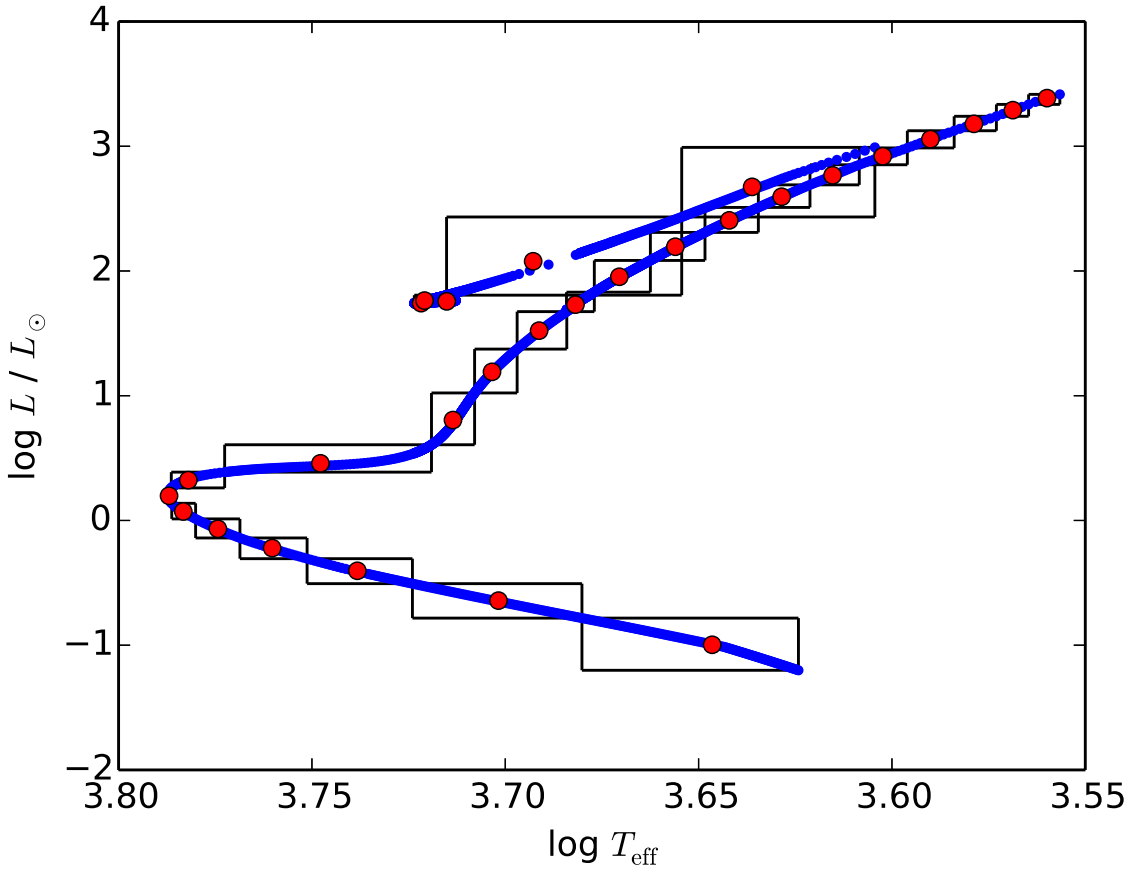

Figure 2.2 CMD of a sample population similar to 47 Tuc (age = 13.0 Gyr, [M/H] = -0.66). The black outlines are our CMD discretization "boxes", the blue points are isochrone sampling points, and the red circles are box representative average stars.

and metallicity to 47 Tuc (age = 13.06 Gyr, [M/H] = -0.78) (Forbes, 2010), including the discretization boxes.

To determine the number of boxes necessary to properly sample the CMD, while maintaining approximately equal luminosity for each box, we calculate the ratio of the luminosity of the MR component ($L_{\rm MR}$) to that of the HA component ($L_{\rm HA}$). We then iterate through a total number of boxes, as well as the numbers of boxes allotted to each component, finding the optimal combination to be the one where the ratio of

MR boxes ($N_{\rm MR}$) to HA boxes ($N_{\rm HA}$) most closely matches the ratio of luminosities. By limiting the total number of boxes to between 25 and 50, this combination gives the closest agreement between

$$\frac{L_{\rm MR}}{N_{\rm MR}} \sim \frac{L_{\rm HA}}{N_{\rm HA}} \tag{2.2}$$

maintaining approximately equal luminosity in each box, while still limiting each box to 2 to 4 % of the total cluster luminosity.

2.4.2 Creating the Representative Stars

Once the CMD discretization is completed, we proceed to calculate the atmospheric modelling parameters for a representative star in each box. To produce a synthetic spectrum for this box star, we require $T_{\rm eff}$, log g, [M/H], and either M or R. Metallicity is constant along each isochrone, and prescribes the value for a box star directly. As we are interested in representing the combined light of every star in a box with a single stellar spectrum, we take the average of the parameters over a whole box, weighted by

$$w_* \; = \; N_* \; / \; N_{\rm box} \tag{2.3}$$

the fractional number of stars of each isochrone mass sampling bin per box.

The $T_{\rm eff}$ of our box star is found from

$$< T_{\rm eff} > = < w_* \; * \; T_{{\rm eff},*}^{\;4} >^{1/4} \tag{2.4}$$

where the values for individual stars, $T_{\rm eff,*}$, are taken directly from the isochrones. We take the average of the fourth power, rather than a linear average, to include the relative contribution each star makes to the total luminosity of a box. Similarly, the average mass and luminosity can be found from

$$< M > = < w_* \ * \ M_* > \tag{2.5}$$

$$< L_{\rm bol} > = < w_* \ * \ L_{\rm bol,*} > \tag{2.6}$$

where once again, the individual quantities are taken directly from the isochrones.

There is some ambiguity in calculating the average log g for a box. Because log g is not a stellar interior modelling parameter, it is not included directly in the isochrones used in this work, so a direct average is unavailable in this case. We note that as of Hidalgo *et al.* (2018), the isochrones now include log g values. We choose to take the averages of the relevant isochrone quantities and calculate a single g from those average values,

$$< g > = \ \frac{G \ < M > \ 4\pi \ \sigma \ < T_{\rm eff}^{\ 4} >}{< L >} \tag{2.7}$$

without calculating individual g values for the isochrone sampling points. This method has the benefit of being consistent with the reverse process of observers inferring parameters from the IL spectrum of a group of spatially unresolved stars.

2.4.3 Synthesizing IL Spectra

Now that the full CMD distribution has been reduced to the representative stars, we generate stellar spectra for each box by interpolating among synthetic spectra in our library. We linearly interpolate our library spectra weighted by three or four atmospheric modelling parameters; $T_{\rm eff}$, $\log g$, M, and, in cases where the isochrone value is not a direct match to one of the values in our library, [M/H]. This interpolation scheme results in each box spectrum being formed by interpolating among either 8 (matching library [M/H]) or 16 (interpolating [M/H]) individual spectra from our library. We chose to interpolate using a linear method because our library is already pushing the lower boundaries of atmospheric structure convergence in $T_{\rm eff}$ and $\log g$, and higher order methods would require additional synthetic spectra with even lower values for these parameters. We test the accuracy of this interpolation by comparing two IL spectra generated using this procedure (one interpolating linear flux spectra and one interpolating log flux spectra) to one generated from synthetic spectra with the exact parameters of the representative stars. Figure 2.3 shows that there is relatively little difference between our interpolated and exact IL spectra, except for the shortest wavelengths that we model, and that there is little appreciable difference between interpolating linear or log fluxes. Representative populations for the youngest and oldest isochrones in this study are plotted in Figure 2.1 as a visual indication of where the interpolation between library spectra will occur for $T_{\rm eff}$ and $\log g$.

In nature, IL spectra are combinations of the luminosity spectra of individual

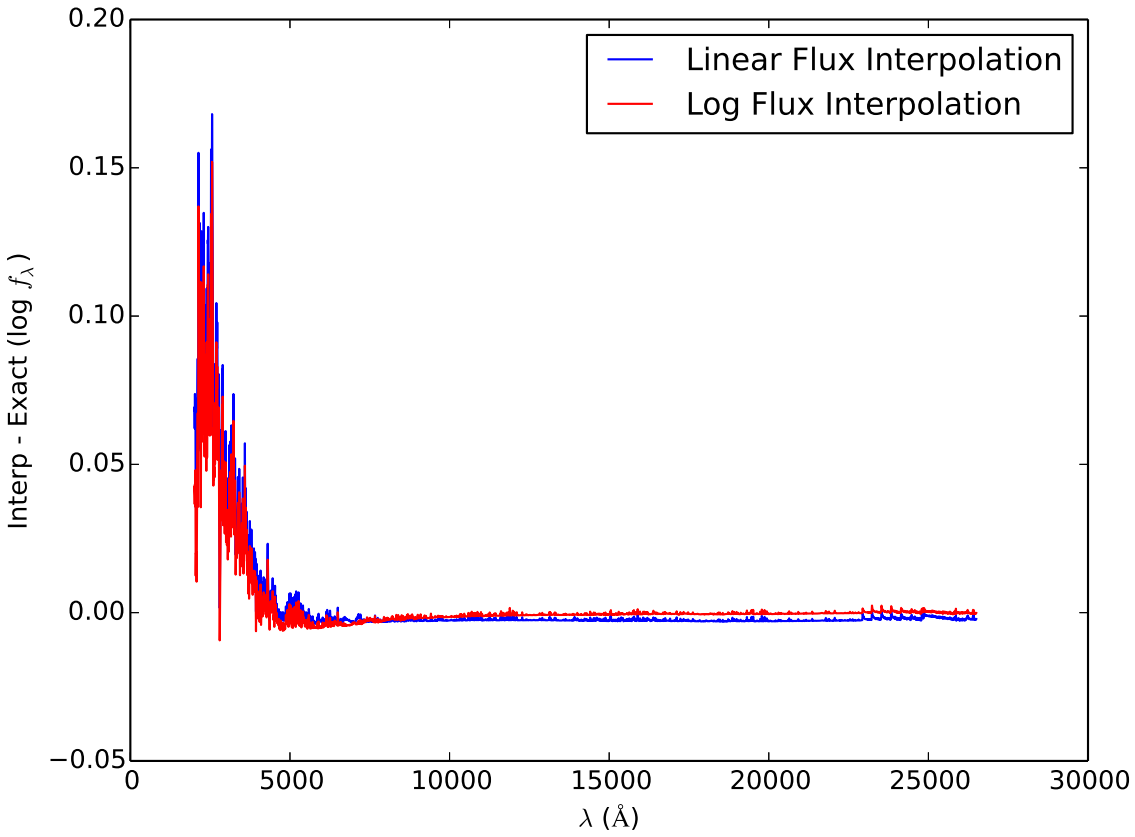

Figure 2.3 The differences between IL spectra generated by interpolating library spectra and an IL spectrum generated from spectra with the exact parameters of the representative stars. *Blue* - Linear interpolation of linear fluxes. *Red* - Linear interpolation of log fluxes.

stars, not the flux spectra. Because of this, we must convert our box representative spectra from PHOENIX surface fluxes to luminosities. The most direct method of doing so takes advantage of

$$\frac{L_\lambda}{F_\lambda} = \frac{L_{\rm bol}}{F_{\rm bol}} \tag{2.8}$$

where $L_{\rm bol}$ for a box is the average value as calculated above, and we calculate the $F_{\rm bol}$ by numerically integrating low resolution PHOENIX spectra from 10 to 10,000,000 Å using the extended trapezoid rule, ensuring sufficient coverage of both the Wien side and Rayleigh-Jeans tail of the spectra.

We now combine the box spectra into a synthetic IL spectrum. Each spectrum is scaled by

$$L_{\lambda,box} = N_{\rm box} * L_\lambda \tag{2.9}$$

to account for the total luminosity of the box, and then added together. Three IL spectra per CMD are created this way; one composed of LTE stellar spectra, one of NLTE stellar spectra, and one composed of both LTE and NLTE stellar spectra where only the evolved population were NLTE. For our purposes, we consider any star more evolved than the sub-giant branch to be "evolved". These hybrid IL spectra allow us to isolate and study the impact NLTE modelling of the evolved population has on cluster parameters inferred from IL spectra. The LTE and NLTE spectra for our 47 Tuc population are overplotted for comparison in Figure 2.4, with the absolute and relative NLTE-LTE differences, to highlight the most disparate spectral features.

Identifying the atomic and molecular species responsible for the large differences

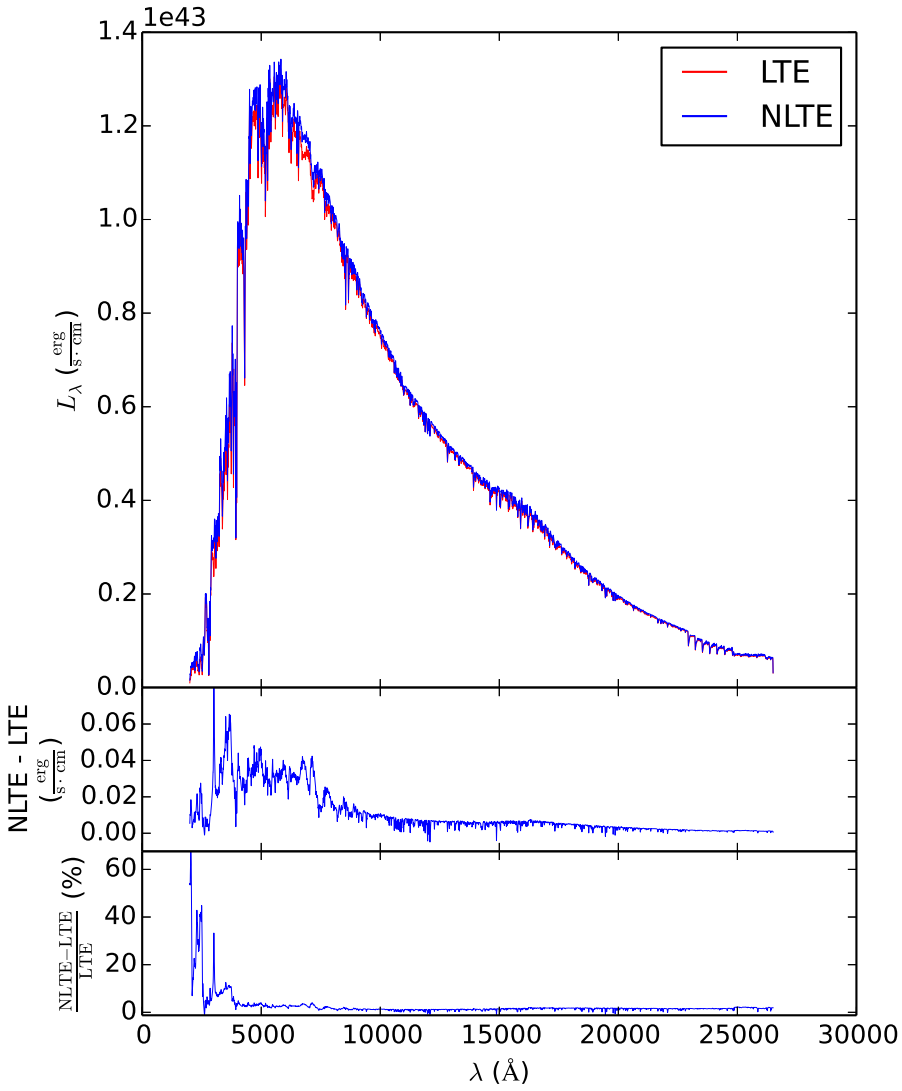

Figure 2.4 Comparison of NLTE and LTE IL spectra for the population of Figure 2.2. The species responsible for the majority of discrepancies between the spectra are light metals, primarily Fe I, with a few exceptions. The large deviation observed in the range from $\lambda \approx = 4000$ to 8500 Å is caused by TiO molecular bands. The clusters of lines seen in the range $\lambda \approx = 10000$ to 12000 Å are those of Ti I, and the strong lines near $\lambda \approx = 19000$ to 20000 Å are those of Ca I. All three panels have been convolved from our high resolution spectra to a spectral resolution of R $\sim$ 5000 for ease of viewing. *Top* - Synthetic IL spectra for the population of Figure 2.2. *Middle* - Absolute difference between NLTE and LTE synthetic IL spectra. The NLTE spectrum is more luminous in the UV than LTE, while showing stronger absorption features in the IR. *Bottom* - Relative difference between NLTE and LTE synthetic IL spectra.

between the LTE and NLTE spectra is not a straightforward task when dealing with IL spectra. Because an IL spectrum is the co-added light of multiple spectra of different spectral types, what appears to be a single feature in the IL spectrum may be caused by multiple sources of opacity. Additionally, at the modest spectral resolution of Figure 2.4, blending of features in crowded regions can confuse the issue even further. To proceed with IL feature identification, we take five sample stars from our library models ($T_{\rm eff}$ = 6500 K and $\log g$ = 4.5, $T_{\rm eff}$ = 5750 K and $\log g$ = 3.5, $T_{\rm eff}$ = 5000 K and $\log g$ = 3.0, $T_{\rm eff}$ = 4250 K and $\log g$ = 2.0, $T_{\rm eff}$ = 3600 K and $\log g$ = 0.5), and identify the sources of any large discrepancies between the sample NLTE and LTE spectra. We weight a NLTE-LTE difference in the spectrum of a sample star by that star's relative contribution to the IL luminosity in the photometric band corresponding to the wavelength of that difference. Figure 2.5 displays an example of these relative contributions for the 15.0 Gyr population. If the discrepancies in the sample stars are also found to be present in the IL spectrum, the sources in the individual spectra are considered to be responsible. The species responsible for the majority of large differences were found to be primarily light metals in their ground states, Fe I being the most prominent among these, with a few exceptions. The large deviation observed in the range from $\lambda \approx$ = 4000 to 8500 Å was identified as TiO molecular bands from our cool giant stars. The clusters of lines seen in the range $\lambda \approx$ = 10000 to 12000 Å were Ti I, and the strong lines near $\lambda \approx$ = 19000 to 20000 Å were found to be Ca I. A full set of high resolution diagnostics will be included

in a forthcoming paper in this series.

2.5 PHOTOMETRIC ANALYSIS & RESULTS

To take an initial estimate of the magnitude of the effect NLTE modelling has on parameters derived from IL spectra, we examine four photometric colour indices (U − B, B − V, V − I, and J − K) produced using Bessel's updated Johnson-Cousins UBVRI photometric system (Bessel, 1990) as well as Bessel and Brett's JHK photometric system (Bessel, 1988). We analyze a collection of IL spectra for synthetic CMDs approximating 47 Tuc, with [M/H] = -0.66 and substituting M_v = -8.64 for$L_{\rm tot}$, except ranging in age from 9 to 15 Gyr. Two sets of these spectra are generated, each using the LTE, NLTE, and hybrid prescriptions, limiting the number of boxes to 25 to 35 (set 1) and 40 to 50 (set 2). Synthetic photometric colours for these IL spectra are single-point calibrated to both a NLTE synthetic spectrum approximating Vega ($T_{\rm eff}$ = 9600 K, $\log g$ = 4.1, [M/H] = -0.5), and the library spectrum that most closely approximates Arcturus ($T_{\rm eff}$ = 4250 K, $\log g$ = 2.0, [M/H] = -0.66). Arcturus was chosen for this second calibration to compare the IL colours to that of a standard star that is representative of the populations. We denote colour values calibrated to each star as $X - Y_{\rm Vega}$ and $X - Y_{\rm Arc}$ respectively.

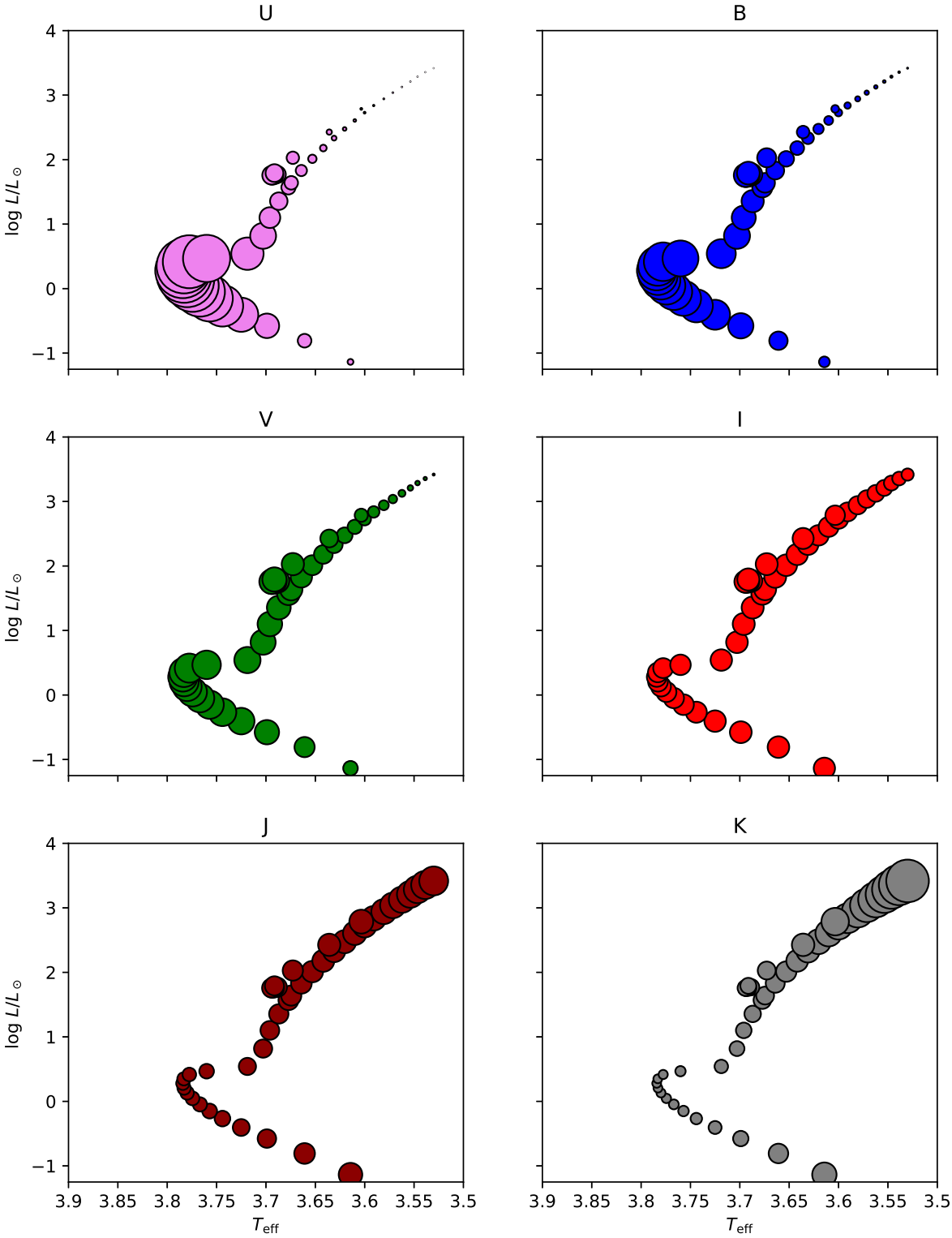

Figure 2.5 CMDs of the 15.0 Gyr population representative stars, displaying each star's relative contribution to the IL spectrum in select photometric bandpasses. For each filter, the radius of each circle is scaled to the percentage of the total IL flux in that band contributed by the star. Circle sizes are not correlated across different filters.

2.5.1 colours and Ages

Figures 2.6 and 2.7 present the values of the colour indices as a function of population age for sets 1 and 2 respectively, highlighting the NLTE - LTE differences. Qualitatively, there is little difference between the two sets. All four colour indices display a reddening of IL colour as the population ages, as more of the population evolves into older, cool stars. The NLTE colours for the first three colour indices are bluer than LTE at all ages, because NLTE overionization of Fe I weakens the myriad weak Fe I lines that have the character of a pseudo-continuous opacity in the blue and near UV bands. Conversely, the $J - K$ NLTE colours are redder than LTE, where the surplus of free electrons produced by the overionization increases H^- opacity in the J band (< 1.6 μm). The NLTE-LTE colour differences for the indices in both sets are consistent with a constant value as a function of age, with the exception of $U - B$, where the difference is seen to increase as a function of age.

The hybrid colour values fall midway between the LTE and NLTE colours for the UV and optical indices, and converge with the NLTE values at IR wavelengths. There are two possible explanations for this convergence: 1) Evolved stars dominate the IL spectra in these filters' wavebands; and 2) NLTE effects in main sequence stars negligible in these wavebands. To determine which of the two effects is responsible for the convergence, we refer back to the representative stars' relative luminosity contributions in Figure 2.5. As can be seen for $V - I$, evolved stars do not dominate the IL spectrum, with all representative stars making approximately equal contributions

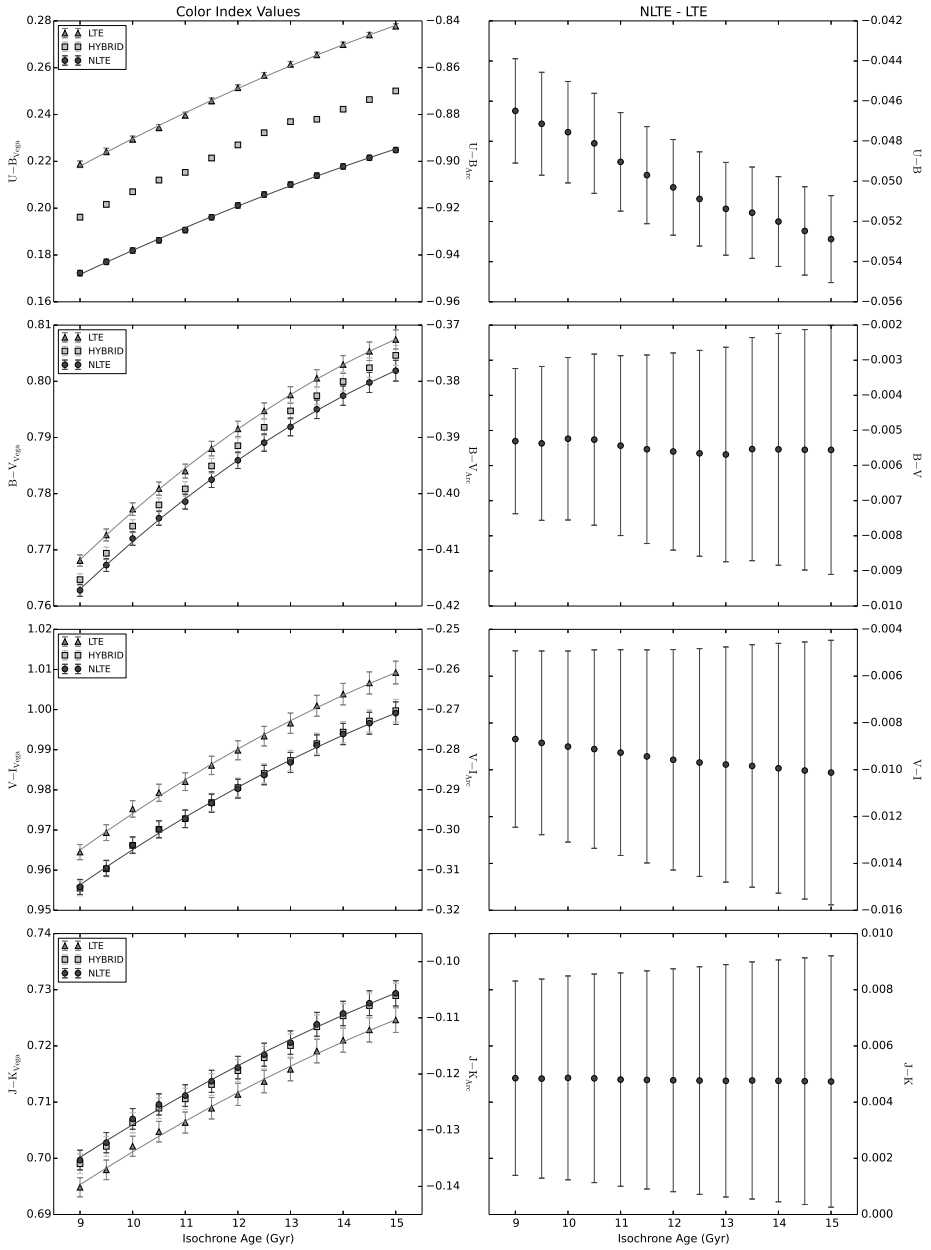

Figure 2.6 *Left Column* - Photometric colours for synthetic IL spectra of populations with constant bolometric luminosity, and [M/H] = -0.66. All populations are discretized with 25 to 35 boxes. The error bars are the CMD discretization uncertainty, outlined in Section 2.5.2. Solid lines are second order polynomials used for parameterizing the data. *Right Column* - Difference between NLTE and LTE photometric colours.

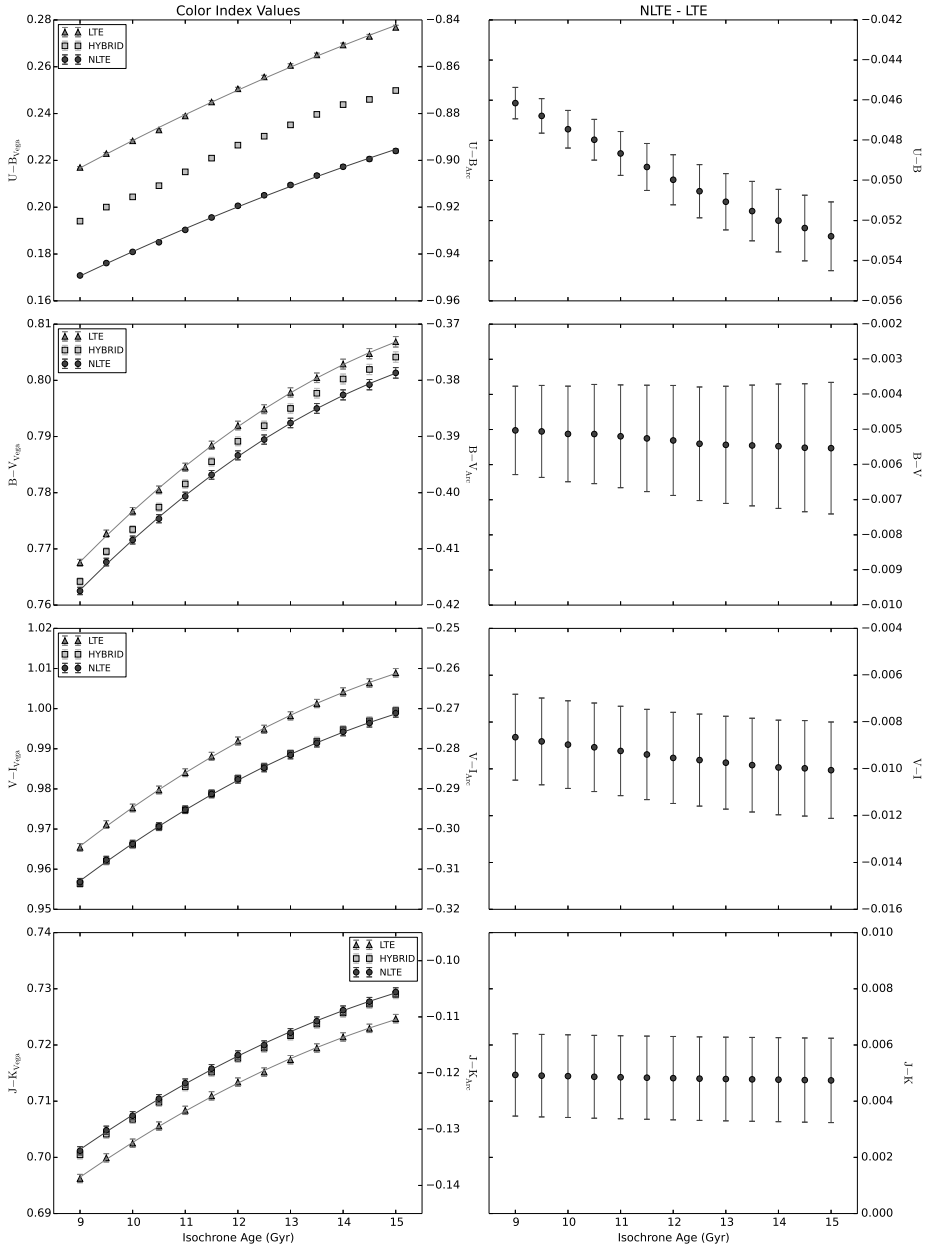

Figure 2.7 Similar to Figure 2.6, but for populations discretized with 40 to 50 boxes.

to the IL spectrum in the I band, and the main sequence stars near the turnoff are the strongest contributors in the V band. In this case, it would suggest that negligible NLTE effects in main sequence stars at these wavelengths are responsible for the observed convergence of hybrid to NLTE colours. For J − K, the same explanation is likely responsible, but a combination of the two effects is also possible. For both the J and K bands, evolved stars on the red giant branch are the strongest contributors to the IL spectrum (although they do not dominate it).

To give a quantitative estimate for how much of an impact NLTE effects in IL spectra have on derived ages, we first define the quantity $\Delta_{\rm Age}$, the uncertainty in derived age from the uncertainty in measured colour index value, such that

$$\Delta_{\rm Age} \;=\; \Delta_{\rm colour}\frac{{\rm d}A({\rm colour})}{{\rm d}({\rm colour})} \tag{2.10}$$

where $\Delta_{\rm colour}$ is the numerical uncertainty of a given colour value, and A(colour) describes the derived cluster age as a function of "observed" colour value, found by parameterizing the IL colour vs age relation with a low order polynomial. We find that a linear function does not provide a good match to the relation, but a parabola provides an excellent match for all colour indices, with coefficients of determinations of at least $R^2 \geq 0.997$. We contrast these $\Delta_{\rm Age}$ values with the difference between the NLTE and LTE derived ages for a given colour, $A_{\rm colour,NLTE} - A_{\rm colour,LTE}$. The full list of $\Delta_{\rm Age}$ values and the differences in NLTE and LTE derived ages for all colour indices are presented in Table 2.3. For comparison, we also present the uncertainty

in derived ages found from setting $\Delta_{\rm colour}$ equal to 0.01 mag, the limiting precision of the Harris catalog (Harris 1996, 2010 ed).

Table 2.3 Error estimates in derived LTE ages caused by NLTE effects in IL spectra, and uncertainties in derived ages from our numerical uncertainty and the limiting observational precision of the Harris Catalog (0.01 dex) (Harris 1996, 2010 ed) for all four colour indices. Age differences are presented for the bluest and reddest colour value for the LTE IL spectra for each index. Subscripts on colour indices denote which set estimates are associated with.

colour Index	NLTE Effect		Numerical Uncertainty		Observational Uncertainty	
	Blue	Red	Blue	Red	Blue	Red
$U-B_1$	5.07	11.50	0.24	0.27	0.83	1.26
$U-B_2$	4.97	10.29	0.06	0.21	0.83	1.20
$B-V_1$	0.61	1.58	0.22	0.82	1.12	2.41
$B-V_2$	0.55	2.53	0.13	0.53	1.05	2.84
$V-I_1$	0.98	2.28	0.40	1.06	1.06	1.88
$V-I_2$	0.92	2.54	0.19	0.50	0.99	2.39
$J-K_1$	0.79	1.19	0.56	1.18	1.65	2.66
$J-K_2$	0.74	1.46	0.23	0.53	1.54	3.52

The $U-B$ colour index returned the largest differences, but these results were considered to be unrealistic for a number of reasons, including keeping the metallicity fixed throughout this experiment and the difficulty associated with modelling the near-UV region of stellar spectra. The other three indices, $B-V$, $V-I$, and $J-K$, produced comparable age differences, with those derived from $V-I$ generally being the largest by $\lesssim 40$ %. Age differences for our $B-V$ index ranged from 0.61 to 1.58 Gyr for set 1, and 0.55 to 2.53 Gyr for set 2. The smaller age difference for each set corresponds to the bluest colour measured for the LTE IL spectra, and the larger difference corresponds to the reddest measured LTE colour. For comparison,

the range of $\Delta_{\rm Age}$ values for B − V are 0.22 to 0.82 Gyr and 0.13 to 0.53 Gyr, for sets 1 and 2 respectively. Assuming an observational limiting precision of 0.01 mag for B − V, the limiting precision of the Harris catalog, results in $\Delta_{\rm Age}$ values of 1.12 to 2.41 Gyr and 1.05 to 2.84 Gyr.

We note that all of our IL spectra were produced from isochrones of fixed metallicity, and that age estimates derived in this fashion may vary greatly with changing metallicity. It should also be noted that both LTE and NLTE model atmospheres have been shown to overpredict near-UV flux in the spectra of cool giant stars (Short & Hauschildt, 2009), and this will likely be reflected in the IL spectra. Any results found from fitting synthetic IL spectra to observed spectra at UV wavelengths would be impacted by this overprediction. Either or both of these effects may help explain the large differences in ages derived from our U − B colours. Additionally, this work is only concerned with a differential analysis between LTE and NLTE IL spectra, and in turn is only affected by any difference in the overpredictions. NLTE models are worse in the overprediction than their LTE counterparts as a result of NLTE Fe I overionization, but the updated Fe I NLTE model atom we have implemented should minimize this for the range of stellar parameters with which we are concerned. We also expect that, to first order, the NLTE-LTE difference in the overprediction of UV flux to be constant as a function of isochrone age.

2.5.2 Numerical Uncertainty

Figure 2.8 shows the B − V colours for two isochrones, ages 9 and 15 Gyr, as a function of the number of boxes used to discretize the CMD. The value of a colour index for a given population varies at the millimagnitude level as a function of the CMD discretization resolution. As might be expected, the variations are larger for lower discretization resolution, and are reduced for higher resolution. This trend is qualitatively repeated for the other colour indices.

To isolate which regions of the CMD are being over- or under-sampled, we plot in Figure 2.9 the $T_{\rm eff}$ of the representative stars in three histograms, comparing the CMDs on either side of the largest change in colour (ie. that between 30 and 32 boxes), and two control cases to either side of the largest change where there is relatively little change (29 to 30 boxes, and 32 to 33 boxes). The bin size for each histogram was set to 250 K, the temperature resolution of our library of spectra, and the bar heights for the four sets of representative stars (29, 30, 32, and 33 boxes) were each weighted by a factor of f_B/f_V, the flux in the B band emitted by stars in that bin divided by the flux in the V band, the influence a given bin has on the IL B − V value, and independently normalized to sum to 1. We use a reduced χ^2_ν statistic, listed with each panel in Figure 2.9, to confirm that there is a greater difference between the populations in the 30 to 32 boxes histogram than in either the 29 to 30 boxes or the 32 to 33 boxes histograms. Inspection of this histogram reveals the most significant differences between the two populations occur for $T_{\rm eff}$ values $\geq$ 4750

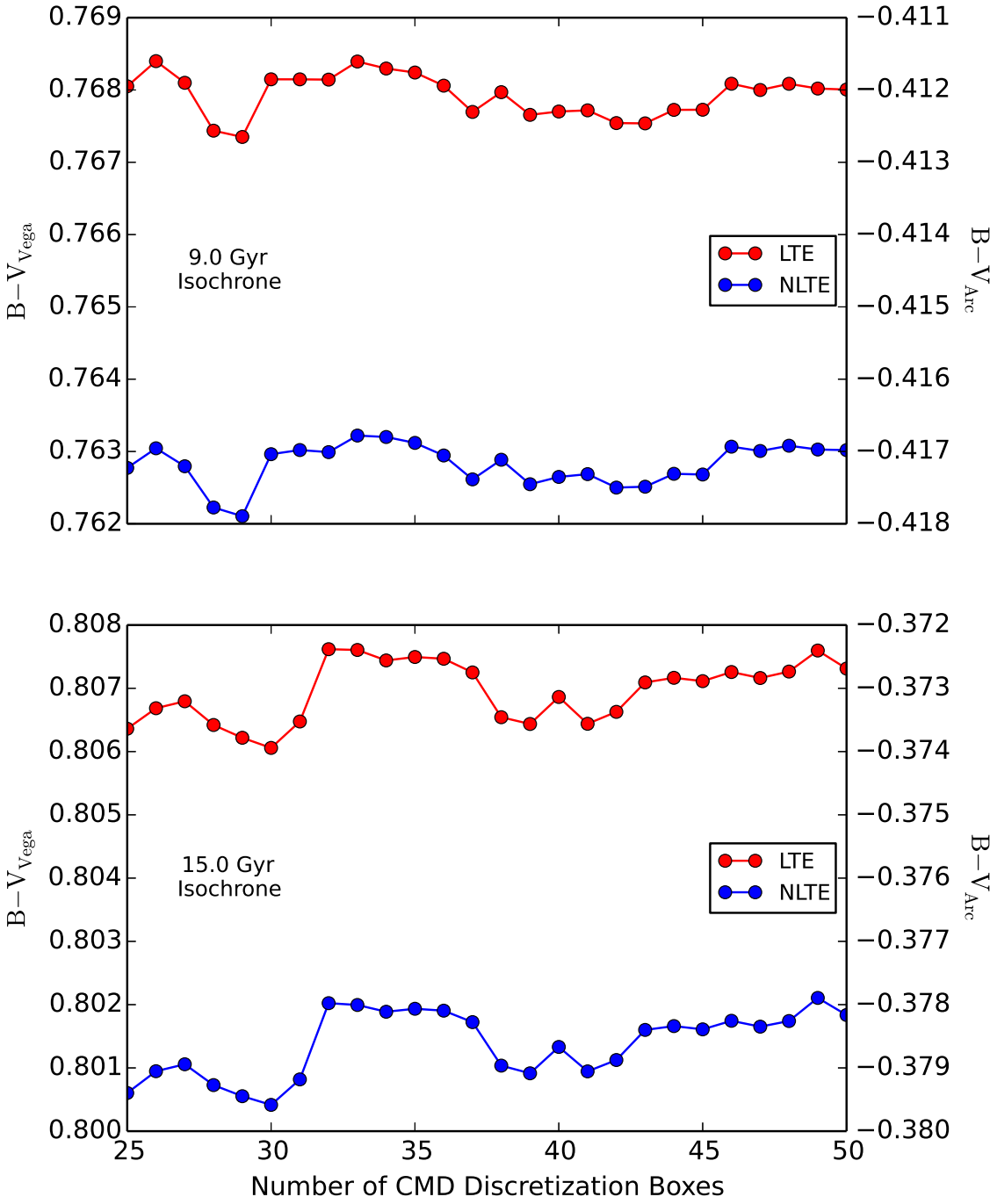

Figure 2.8 Variation of B − V colour with CMD discretization resolution. *Top* - 9.0 Gyr population. *Bottom* - 15.0 Gyr population.

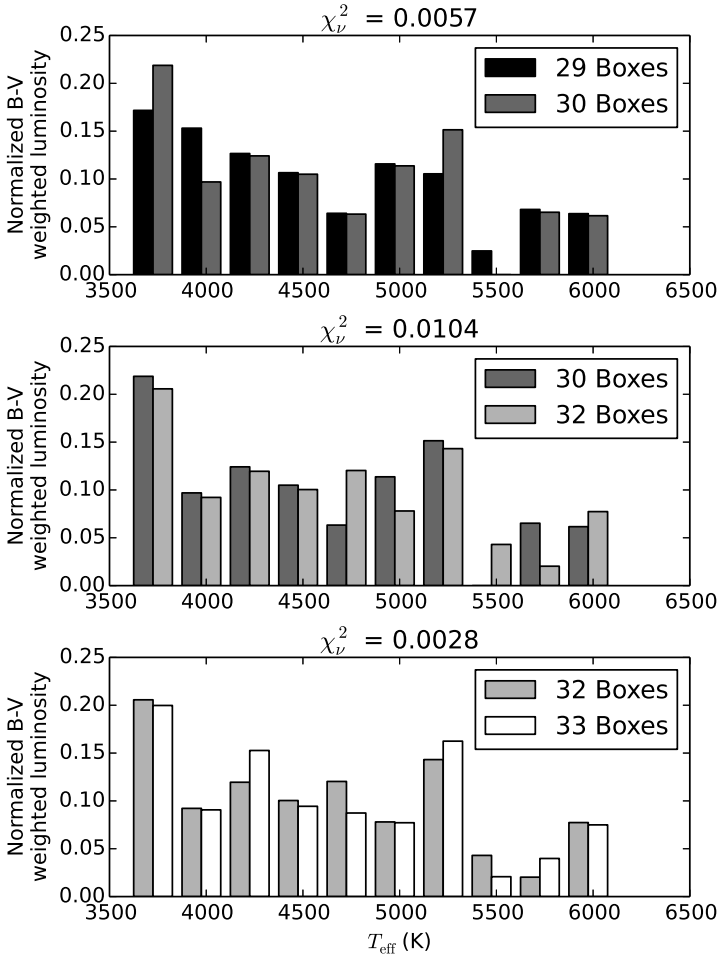

Figure 2.9 Binned representative populations for the 15.0 Gyr isochrone, with different levels of CMD discretization. The bin size is set to 250 K, the $T_{\rm eff}$ resolution of our library. Each bin is weighted by a factor of f_B/f_V, the flux the bin contributes to the IL spectrum in the B band divided by the flux in the V band, representing the influence each bin has on the IL B − V value. The χ^2 statistics, calculated in each case as $\Sigma\frac{(N-n)^2}{n^2}$, where N and n are the bin values for the sets with the greater and fewer number of boxes respectively, are used as a confirmation that the histograms in the middle panel exhibit greater differences than those in either the top or bottom panels. The middle panel, which compares discretization resolutions on either side of the large jump observed in Figure 2.8, shows noticeable differences in bins with $T_{\rm eff}$ values $\geq$ 4750 K.

K. For our populations, this corresponds to the upper main sequence (including the turnoff), the base of the red giant branch, and the horizontal branch. Special care must be paid to these regions when discretizing the CMD to ensure they are not under-sampled.

As a measure of the numerical uncertainty in the IL spectrum resulting from CMD discretization, we evaluate the 3σ deviations in the computed integrated B-V index as a function of the number of boxes used to discretize isochrones at several ages spanning the age range. Uncertainties for the other colour indices are obtained in a similar fashion. These uncertainties are represented as the error bars in Figures 2.6 and 2.7.

2.6 SUMMARY

We have investigated a number of aspects of the method presented by Colucci *et al.* (2011), refined from that of McWilliam & Bernstein (2008), for synthesizing GC populations and IL from a library of stellar atmospheric models and spectra. Following this method, a collection of 98 IL spectra for clusters approximating 47 Tuc were generated with different CMD discretization resolutions and different degrees of NLTE treatment.

For these clusters, age estimates that may be derived by fitting observed photometric colours with synthetic LTE colours were shown to differ from those similarly obtained from NLTE modelling by up to 2.54 Gyr. These age differences, while larger

than the numerical uncertainties inherent in our methodology, are comparable with the limiting observational precision of current catalogs.

Our investigation of CMD discretization resolution has shown that the IL spectrum is resolution-dependent, and that the effects on the spectrum are stronger at lower resolution. These effects are more prominent at shorter wavelengths. We also find that the 25 to 35 boxes recommended in the literature do not provide enough resolution to critically sample the upper main sequence and horizontal branch. At least 40-50 boxes are necessary to minimize the resolution dependency.

Initial analysis suggests that NLTE effects in MS stars have approximately equivalent influence on IL spectra as do those in evolved stars for UV and optical wavelengths, but negligible influence for IR wavelengths. This effect appears to be independent of CMD discretization resolution for those resolutions investigated here.

3 Photometry and Sensitivity of n-IR Lines to Age and Metallicity

3.1 INTRODUCTION

Globular clusters (GC) can provide valuable clues about the chemical evolution history of galaxies, past starforming episodes, and merger events, even when individual cluster stars cannot be spatially resolved. In such cases, the cluster must be studied as a single body by investigating the integrated light (IL) spectrum of the cluster, the co-added spectra of the entire stellar population. Globular clusters and their IL spectra are studied using multiple techniques, including spectrophotometry and low spectral resolution spectroscopy (R $\leq$ 5000) for general population age and metallicity determination, and high resolution spectroscopy (R $\geq$ 20000) for individual chemical abundances.

While IL photometry may not provide the detailed abundance analysis that high resolution spectroscopy can, there is still plenty of information to be had. Goudfrooij *et al.* (2006) have used VRI photometry to calibrate the ages of stellar population synthesis models for Magellanic clouds GCs whose bolometric luminosity is dominated by asymptotic giant branch (AGB) stars. In Young & Short (2017) (hereafter Paper I), we show a general reddening of $UBVIJK$ colour indices with cluster age for a

given metallicity. Bowman *et al.* (2017) have even demonstrated that it is possible to detect the presence of multiple stellar populations in GCs with g' and CN-λ3883 photometry.

Though previous IL spectroscopy studies have typically focused on optical wavelengths ($\sim$ 4000 to 9000 Å) (Colucci, Bernstein & McWilliam, 2017), recent work has been done to expand the field to near-infrared (nIR) wavelengths ($\sim$ 15000 to 17000 Å) (Sakari *et al.*, 2016). Integrated light spectroscopy at these wavelengths offers several advantages over optical wavelengths. 1) IL spectra are insensitive to hot stars in the IR. Blue horizontal branch (HB) stars and main sequence turnoff stars can complicate analyses of optical wavelengths (Schiavon *et al.*, 2004; Sakari *et al.*, 2014), but red giant branch and asymptotic giant branch stars dominate the spectrum at IR wavelengths (Paper I). 2) IR wavelengths offer different spectral lines than optical wavelengths, including strong molecular features of CN, CO, and OH, which facilitate determinations of C, N, and O abundances (Smith *et al.*, 2013). And 3) IR wavelengths offer opportunities to probe the existence of multiple populations in extragalactic GCs. The H-band in particular offers detectable lines from elements that should vary within GCs, including C, N, O, Mg, and Al. The ability to detect [O/Fe] and directly probe the Mg/Al anticorrelation makes the IR particularly valuable for extragalactic GC studies.

Infrared integrated light (IR IL) spectroscopy is not without its drawbacks compared with optical wavelengths (Sakari *et al.*, 2016). Molecular features are present

in many regions of the nIR, and dominate the spectrum in metal rich clusters. This can be especially significant in clusters with a high velocity dispersion, which will further blend molecular bands together. Conversely, metal poor clusters will see features weaken significantly, and may see some disappear entirely. As previously stated, IR IL is sensitive primarily to RGB and AGB stars. Cluster parameters are therefore sensitive to how the AGB stars are modelled in terms of both the isochrones and model atmospheres. And, while there are numerous lists of diagnostic lines for optical wavelengths that contain more than 1000 unique spectral lines in total, the literature has a distinct lack of resources regarding IR spectral lines that serve as good diagnostics for cluster age and metallicity.

Regardless of the waveband of interest, nearly all IL analyses to date has been performed assuming local thermodynamic equilibrium (LTE) when modelling stellar atmospheres. For individual stars, abundances inferred from non-local thermodynamic equilibrium (NLTE) modelling can differ significantly (up to 0.3 dex) from those of LTE modelling (Short & Hauschildt, 2009). Differences in derived abundances from LTE and NLTE models and spectra have been shown to increase for decreasing metallicity, peaking at $[Fe/H] \approx -2.0$. Hence, it seems reasonable that abundances derived from IL spectra would also experience NLTE effects. Indeed, Lapenna *et al.* (2014) and Mucciarelli *et al.* (2015) have demonstrated the presence of NLTE effects in AGB stars in the GC 47 Tuc, and we have shown in Paper I that assuming LTE can introduce an error in the inferred age of a GC of more than 2.0

Gyr for a given metallicity.

3.1.1 Current Work

Our primary goal is to investigate the effects of modelling the opacity sources of stellar atmospheres and spectra in NLTE on the IL spectra of synthetic GCs, as well as ages and metallicities subsequently derived from them, using the population synthesis methodology presented by McWilliam & Bernstein (2008). We compare ages for synthetic clusters derived from photometric colours of both LTE and NLTE spectra, and degeneracies in the derived ages caused by varying the cluster metallicities. We assess the significance of deviations caused by NLTE effects by comparing them to those caused by photometric uncertainty, and those caused by assuming convective core overshoot when modelling the evolutionary tracks for the isochrones. We also identify infrared spectral features that may potentially serve as diagnostics of cluster age, metallicity, and degree of α-enhancement for both LTE and NLTE spectra.

3.2 EXPANDED LIBRARIES OF SYNTHETIC STELLAR AND IL SPECTRA

The library of α-enhanced NLTE and LTE high spectral resolution (R $\approx$ 300000) synthetic spectra, sampled over the wavelength range λ = 2000 to 27000 Å computed with PHOENIX v15, as presented in Paper I, has been updated for greater

self consistency between the stellar models and isochrones, and has been expanded to a total of five metallicities, $[Fe/H]$ = 0.0, -0.5, -1.0, -1.5, and -2.0. Corresponding synthetic continuum spectra, in which only continuous opacity sources are included, have also been computed. For α-enhanced models and spectra, we have enhanced the even numbered elements from O to Ti inclusive by a factor of $\alpha = +0.4$. For our initial solar composition, we take our abundances up to O from Grevesse, Noels, & Sauval (1996), and take the revised abundances of Scott *et al.* (2015a) (F to Ca), Scott *et al.* (2015b) (Sc to Ni), and Grevesse *et al.* (2015) (Cu to Cs). The library has also been reproduced at this scaled solar distribution with no α-enhancement, creating ten unique abundance distributions; five metallicities each for scaled solar and α-enhanced, for a total of 6600 synthetic spectra and corresponding continua.

As a quality check on our library of stellar spectra, we compare our models to three spectra retrieved from the MILES spectral library for stellar population synthesis (Sánchez-Blázquez *et al.*, 2006), HD116316, HD010380, and HD023439B. These three stars are representative of different spectral types within our synthetic populations, an F2V dwarf (main sequence turnoff), a K3III giant (red giant branch), and a K2V dwarf (lower main sequence). A list of the stellar parameters for the three stars may be found in Table 3.1. The MILES spectra cover a subset of our full wavelength range, λ = 3525 to 7500 Å, but for wavelenghts shorter than 4000 Å, the signal-to-noise is too low for meaningful comparisons to be made. As such, comparison is limited to λ = 4000 to 7500 Å . We convolve our spectra to the spectral resolution of the

MILES spectra ($R \sim 2200$), and convert our library spectra from vacuum wavelengths to air wavelengths to match the MILES library. For the vacuum-to-air wavelength conversion, we calculate the index of refraction at each wavelength according to the formula presented by Morton (2000).

Table 3.1 Properties of select MILES spectra. Stellar parameters are retrieved from Cenarro *et al.* (2007).

ID	MILES No.	Spectral Type	$T_{\rm eff}$	log g	$[Fe/H]$
HD010380	0065	K3III	4057	1.43	-0.25
HD023439B	0128	K2V	4755	4.37	-1.02
HD116316	0471	F5V	6428	4.18	-0.64

Figures 3.1 to 3.3 display the relative differences between our library spectra and the MILES spectra. We display the closest library model and bracketing models in $T_{\rm eff}$, log g, and $[M/H]$, for all four combinations of modelling treatment and abundance distribution. All three spectral types are fit well, with the increased noise in the K3III fits primarily caused by lower signal-to-noise in the MILES spectrum.

The expanded library has facilitated the production of additional IL spectra, incorporating the Teramo isochrones (Pietrinferni *et al.*, 2006) and Kroupa's IMF (Kroupa, 2001), following the procedure in Paper I. We have selected isochrones computed with a mass loss rate of $\eta = 0.2$, normal AGB morphologies, and for the α-enhanced isochrones, the ones computed with the updated low temperature opacities of Ferguson *et al.* (2005). The alpha element distribution used in computing the isochrones is listed in Pietrinferni *et al.* (2006), and scales the alpha elements by variable amounts,

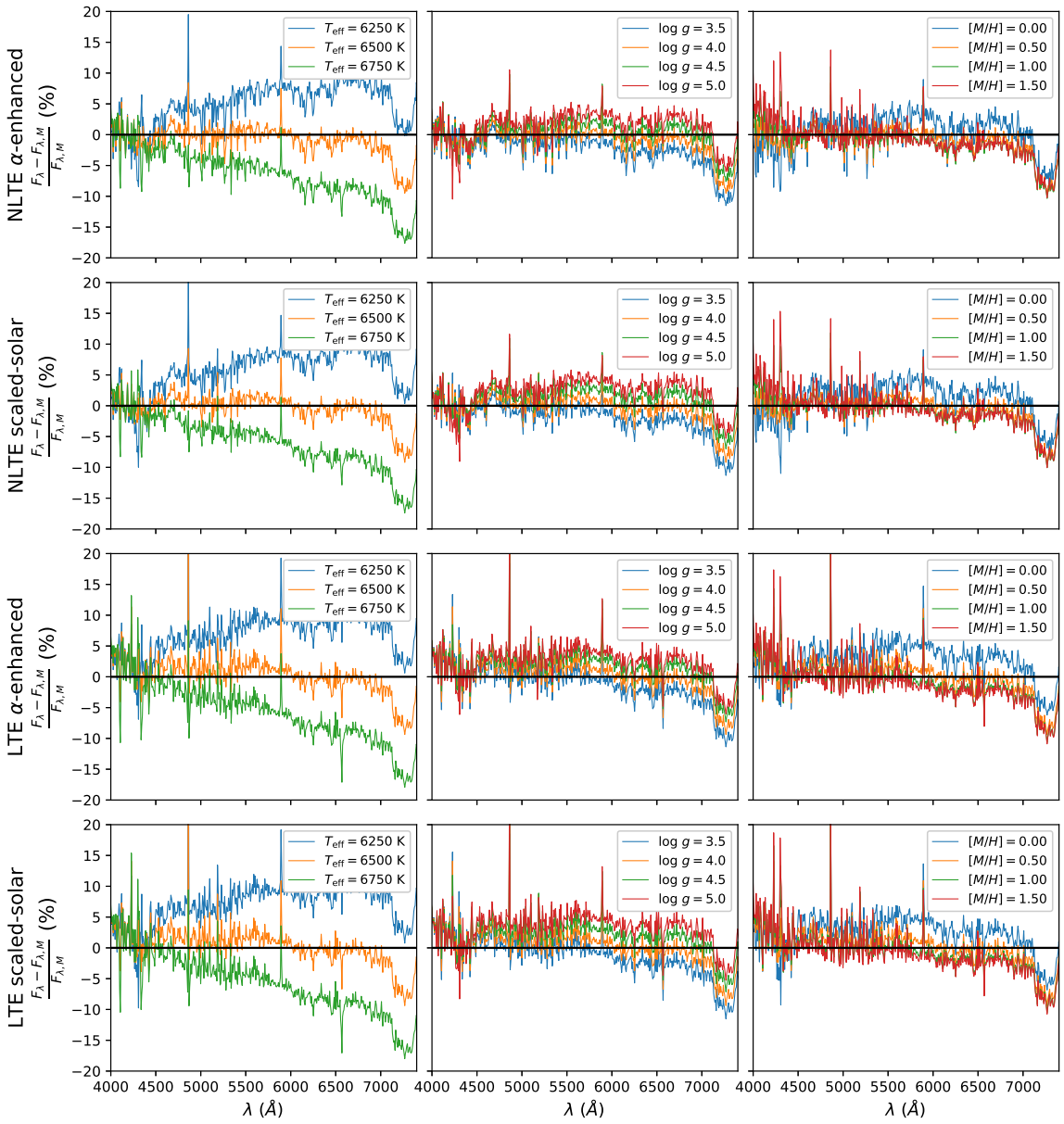

Figure 3.1 Comparison of our library spectra with HD116316, an F5V star, for four different modelling assumptions (rows). All plots are presented as the percentage difference between our spectra (F_λ), and the MILES spectra ($F_{\lambda,M}$). For each column, we vary one stellar parameter from our closest grid model of $T_{\rm eff} = 6500$ K, log $g = 4.0$, $[M/H] = -0.50$. In the left column, we vary $T_{\rm eff}$, in the middle, log g, and in the right, $[M/H]$.

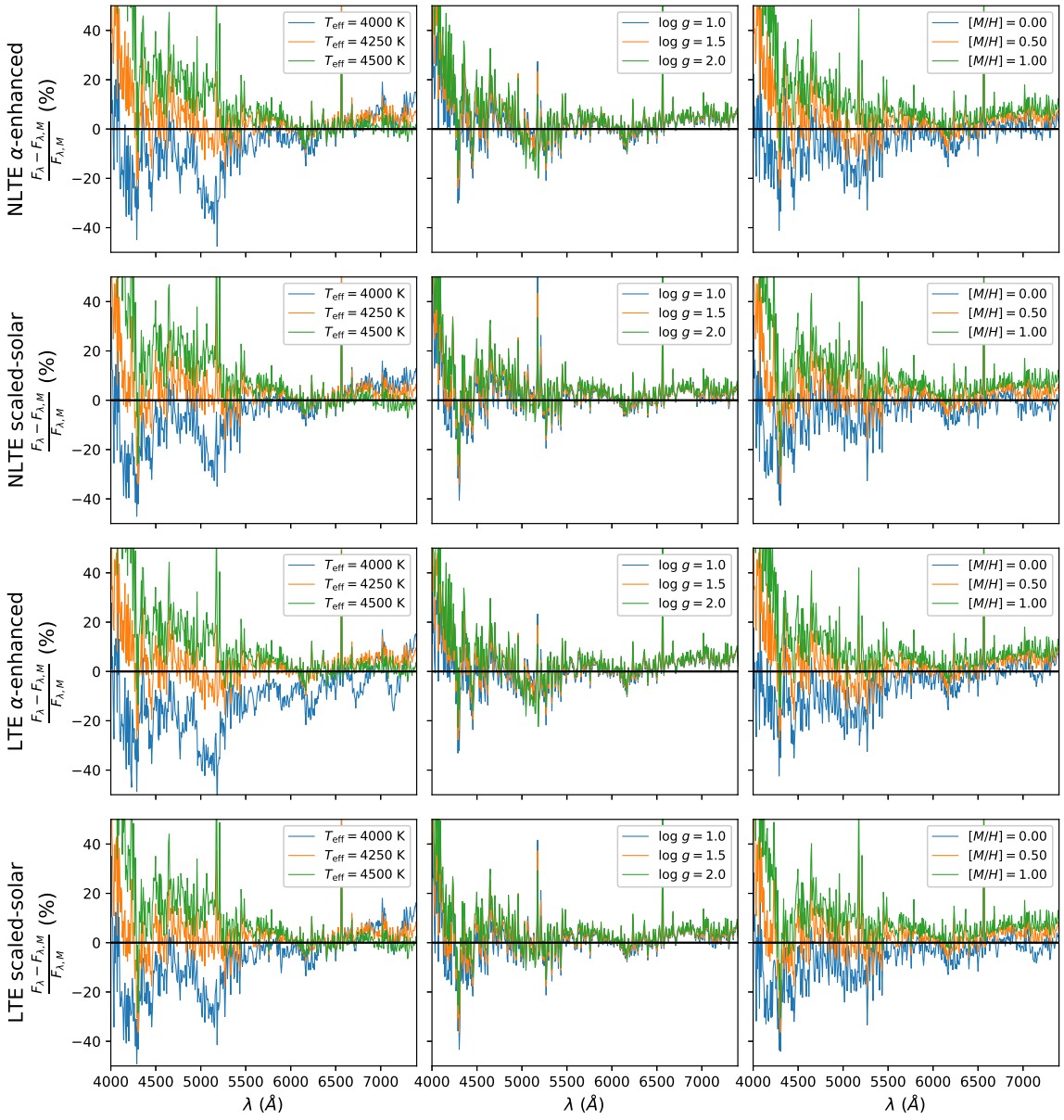

Figure 3.2 Similar to Figure 3.1, but for HD010380, a K3III star, with closest grid parameters $T_{\rm eff} = 4000$ K, log $g = 1.5$, $[M/H] = -0.50$.

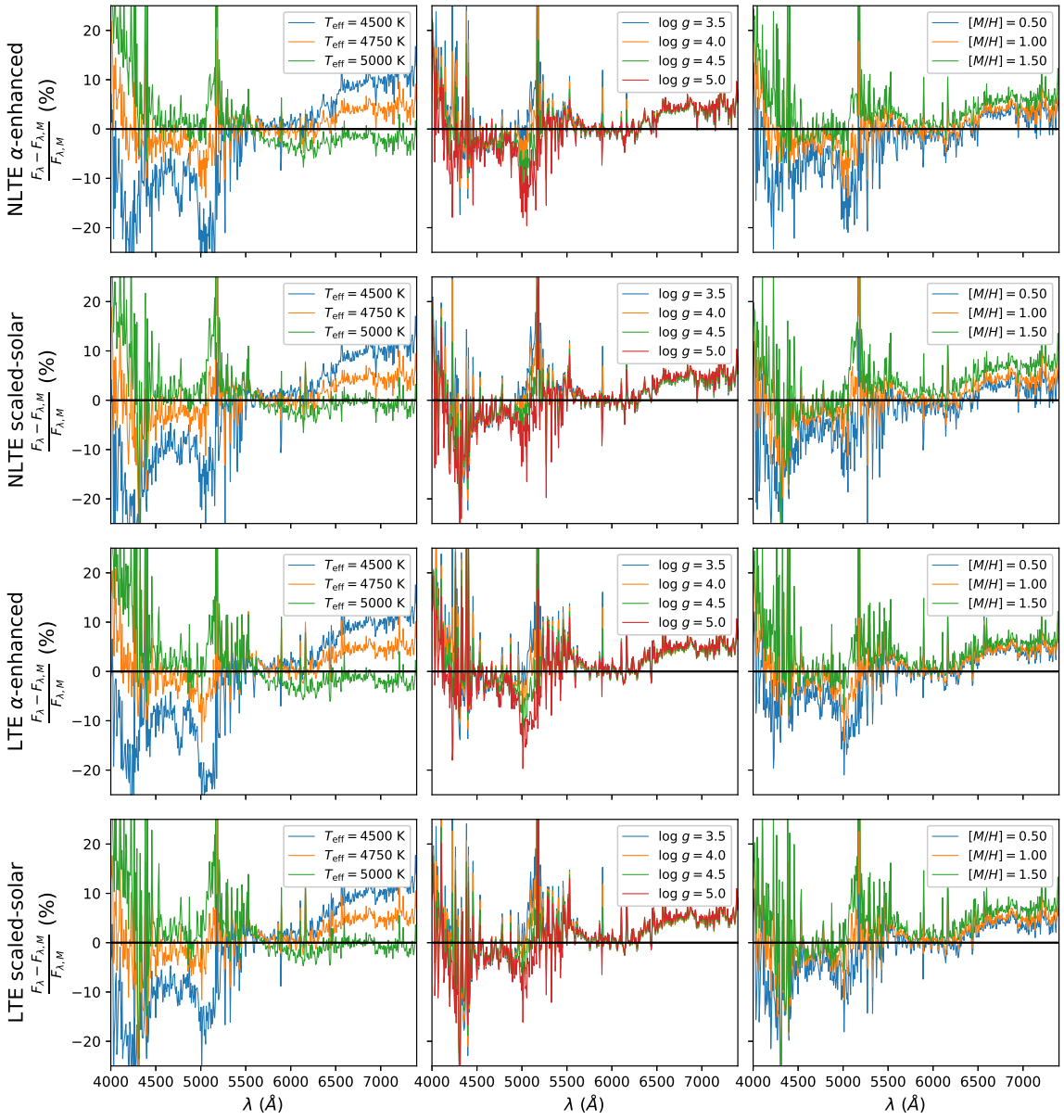

Figure 3.3 Similar to Figure 3.1, but for HD023439B, a K2V star, with closest grid parameters $T_{\rm eff} = 4750$ K, $\log g = 4.5$, $[M/H] = -1.00$.

with an average global alpha enhancement of $\alpha = +0.4$ over the solar composition of (Grevesse & Noels, 1993). Scaled-solar and $\alpha = +0.4$ IL spectra have been generated for isochrone metallicity values of $[M/H]$ = -0.253, -0.353, -0.659, -0.963, -1.266, -1.488, and -1.790, and ages of 9.0 to 15.0 Gyr, sampled every 0.5 Gyr, for 169 IL spectra in both LTE and NLTE. Additional IL spectra have been linearly interpolated between metallicities, and to an α-enhancement of $\alpha = +0.2$, for a total of 910 IL spectra. We choose to interpolate using a linear method because higher order methods would require additional IL spectra of extreme metallicities and ages beyond what our current library of stellar spectra can produce. We test the accuracy of this interpolation by comparing two NLTE α-enhanced IL spectra interpolated to a metallicity of $[M/H] = -0.659$ (one interpolating flux spectra and one interpolating log flux spectra) with an IL spectrum generated from an isochrone at this metallicity. Age is held constant at 13.0 Gyr for this test. Figure 3.4 shows that there is relatively little difference between our interpolated and exact IL spectra, except for the shortest wavelengths that we model, and that there is little appreciable difference between interpolating linear or log fluxes over most of our range, with interpolated log fluxes performing slightly better at the shortest wavelengths. We therefore choose to interpolate log fluxes in this work. The same procedure was followed with the synthetic stellar continuum spectra to produce IL continuum spectra for use in rectifying line blanketed IL spectra.

Because of a difference in how the Teramo group and PHOENIX define metallicity

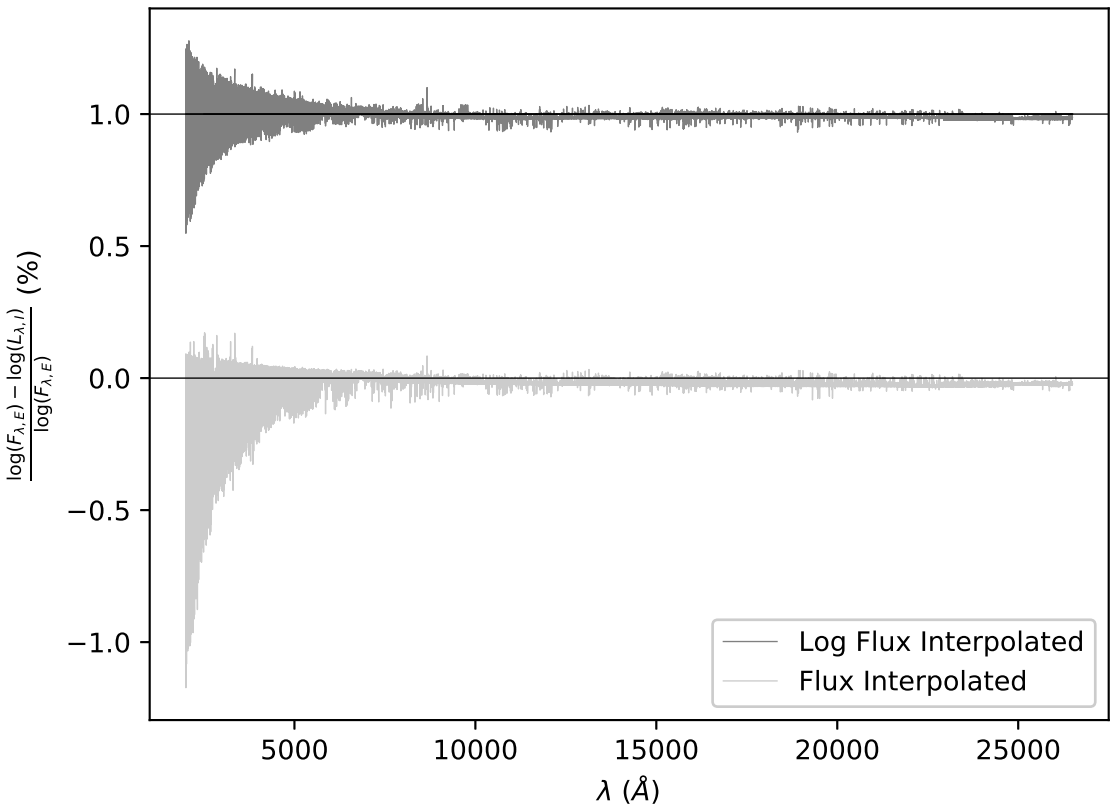

Figure 3.4 The differences between NLTE α-enhanced IL spectra interpolated to a metallicity of $[M/H] = -0.659$ vs one generated at this metallicity. The difference spectrum for interpolating in log flux has been vertically offset by +1.0. $F_{\lambda,E}$ and $F_{\lambda,I}$ indicate the exact and interpolated IL spectra, respectively.

for α-enhanced models, the $[M/H]$ = -1.790 isochrones are only used for scaled-solar IL spectra. The Teramo group takes the global metallicity, $[M/H]$, as a constant between scaled solar and α-enhanced isochrones. To then achieve an α-enhancement of $\alpha = +0.4$, the α-elemental abundances are increased by $\sim$ 0.35 dex, while the abundances of non-alpha elements are decreased by ~ -0.05 dex, relative to the corresponding scaled solar isochrones, maintaining a constant $[M/H]$. PHOENIX models and spectra keep $[Fe/H]$ constant when enhancing α-abundances, such that the α elemental abundances are increased by 0.40 dex, and $[M/H]$ is increased for α-enhanced models and spectra, relative to scaled solar composition. Consequently, we interpolate our α-enhanced stellar synthetic spectra to a $[Fe/H]$ value -0.35 dex less than the isochrone $[M/H]$ value when generating α-enhanced IL spectra. For an isochrone metallicity of $[M/H]$ = -1.790, we would require being able to interpolate metallicity within our grid to $[Fe/H]$ = -2.140, more metal poor than our lower limit. We consequently leave the $[M/H]$ = -1.790 scaled-solar IL spectra our of our comparative analysis herein.

A subset of additional LTE IL spectra have been generated from isochrones computed from stellar evolution models that allow for convective core overshoot. These core overshoot IL spectra, identified as IL_{co} spectra, have been generated with the purpose of contrasting differences in derived parameters from NLTE and LTE IL spectra with those derived from spectra with another common modelling assumption. The core overshoot Teramo isochrones are limited to a maximum age of 10.0 Gyr for both

the scaled solar and α-enhanced compositions, allowing for a total of three ages (9.0, 9.5, and 10.0 Gyr) for each of our metallicity and composition combinations.

3.3 PHOTOMETRIC ANALYSIS & RESULTS

As a measure of the magnitude of the effect NLTE modelling has on parameters derived from IL photometry, six photometric colour indices are examined ($U-B$, $B-V$, $V-I$, $V-J$, $V-K$, and $J-K$), produced using Bessel's updated Johnson-Cousins $UBVRI$ photometric system (Bessel, 1990) as well as Bessel and Brett's JHK photometric system (Bessel, 1988). Synthetic photometric colours for these IL spectra are single-point calibrated to a PHOENIX NLTE synthetic spectrum approximating Vega ($T_{\rm eff}$ = 9600 K, $\log g$ = 4.0, [M/H] = -0.5) (Kinman & Castelli, 2002). We parameterize the IL colour *vs* age and metallicity relations independently with low order polynomials, and find that a linear function does not provide a good match to the relations for any colour index, but a parabola provides an excellent match for all cases, with coefficients of determination of at least $R^2 \geq 0.98$. We introduce the notations $\Delta_{\rm NLTE}(X)$ and $\Delta_{\rm CO}(X)$ to mean the NLTE $-$ LTE and LTE$_{\rm CO}$ $-$ LTE differences, respectively, in a modelled quantity, X, where the subscript CO indicates a quantity relating to core overshoot IL spectra.

We take the uncertainty in our photometric colours to be the numerical uncertainty of the IL spectrum resulting from CMD discretization. For a differential comparison of models, this is the only source of uncertainty we are aware of that can be

assessed. We evaluate the 3σ deviations in the computed integrated colour indices as a function of the number of boxes used to discretize isochrones at several ages and metallicities spanning the parameter space. Typical values are on the order of a few milli-magnitudes. For a more detailed discussion of these numerical uncertainties, we refer the reader to Paper I.

3.3.1 COLOURS VS CLUSTER AGE

We present the IL values of the six indices as a function of cluster age, for all cluster metallicities and compositions, and the $\Delta_{\rm NLTE}(colour)$ and $\Delta_{\rm CO}(colour)$ values, in Figures 3.5 to 3.10. Error bars representing the numerical uncertainty are small to be displayed at the scales used. The six indices display the following general properties:

1. Scaled-solar colours are universally redder than α-enhanced colours for a given age and metallicity, by 0.003 to 0.150 mag, dependent on index

2. For both scaled-solar and α-enhanced clusters, $-0.06 \leq \Delta_{\rm NLTE}(colour) \leq 0$, with the exception of $0 \leq \Delta_{\rm NLTE}(J-K, \alpha) \leq 0.006$

3. For all scaled solar and most α-enhanced clusters, $\Delta_{\rm CO}(colour) = 0$ within uncertainty

4. The exceptions to the above ($[M/H]_{\alpha-enh.}$ = -0.506, -0.659, and -0.811), exhibit $\Delta_{\rm CO}(U-B) \leq 0.05$ and $0 < \Delta_{\rm CO}(colour) \leq 0.015$ otherwise

The colours also display the following properties as functions of cluster age:

1. All indices are seen to redden with increasing cluster age, up to 13.0 Gyr

2. Older than 13.0 Gyr, metal rich clusters continue to redden, while old metal poor clusters with $[M/H] < -1$ show a reversal towards bluer colours in $B-V$, $V-I$, $V-J$, and $V-K$

3. For all indices except $U-B$, $\Delta_{\rm NLTE}(colour)$ values are constant within uncertainty as a function of cluster age, while $\Delta_{\rm NLTE}(U-B)$ increases with age

α-Enhanced $J-K$

While $J-K$ values for scaled-solar clusters follow the trend of other indices with bluer colours in NLTE, $J-K$ values for NLTE α-enhanced clusters are redder than LTE. The $\Delta_{\rm NLTE}(L_\lambda)$ for 12.0 Gyr, $[M/H]$ = -0.253 clusters are displayed in Figure 3.11, normalized to their integrated K-band luminosities, and are qualitatively similar to the other ages and metallicities. Scaled-solar IL spectra display $\Delta_{\rm NLTE}(L_J) > 0$, and hence a bluer colour in NLTE, while the α-enhanced IL spectra show $\Delta_{\rm NLTE}(L_J) < 0$, giving the redder NLTE colour. The clear discrepancy in continuum luminosity levels between scaled-solar and α-enhanced clusters attributes these redder NLTE colours to a difference in continuous opacities.

Individual giant and dwarf stars which contribute strongly to the J and K-band luminosities of their α-enhanced IL spectra have $\Delta_{\rm NLTE}(\kappa_{\lambda,\rm cont}) > 0$ when normalized to their K-bands. Conversely, for scaled-solar spectra, $\Delta_{\rm NLTE}(\kappa_{\lambda,\rm cont}) > 0$ is only seen in giants; $\Delta_{\rm NLTE}(\kappa_{\lambda,\rm cont}) < 0$ is seen in dwarfs. Figure 3.12 displays the $\Delta_{\rm NLTE}(\kappa_{\lambda,\rm cont})$

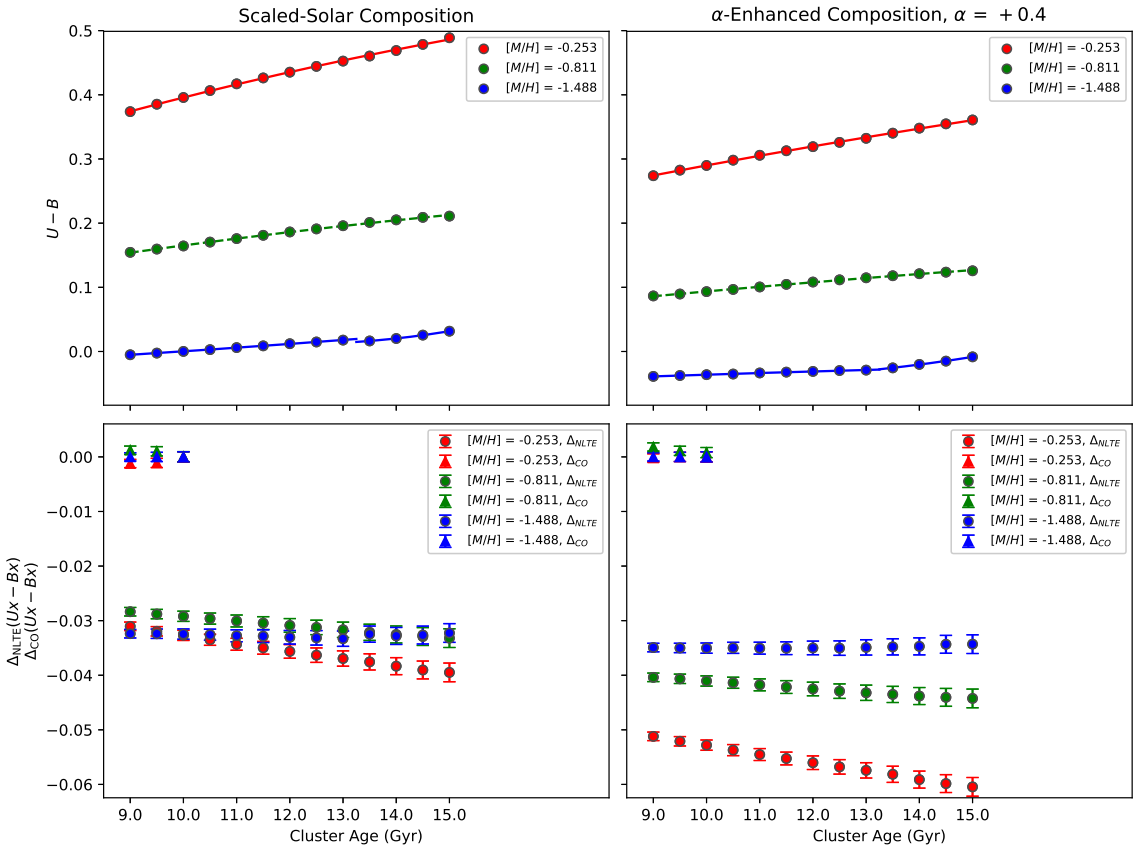

Figure 3.5 *Top* - Photometric LTE $U - B$ colour values *vs* cluster age. *Bottom* - $\Delta_{\rm NLTE}$ (circles) and $\Delta_{\rm CO}$ (triangles) *vs* cluster age. Only a sample of the metallicities are shown for ease of viewing. Error bars for isochrone discretizeation uncertainty are too small to be seen at this scale. Best fitting second order polynomials are plotted as solid lines for isochrone IL spectra, and dashed lines for interpolated IL spectra. Clusters with $[M/H]$ = -1.115 or poorer are fit with two second order polynomials, one for ages up to and including 13.0 Gyr, and for 13.5 Gyr and older.

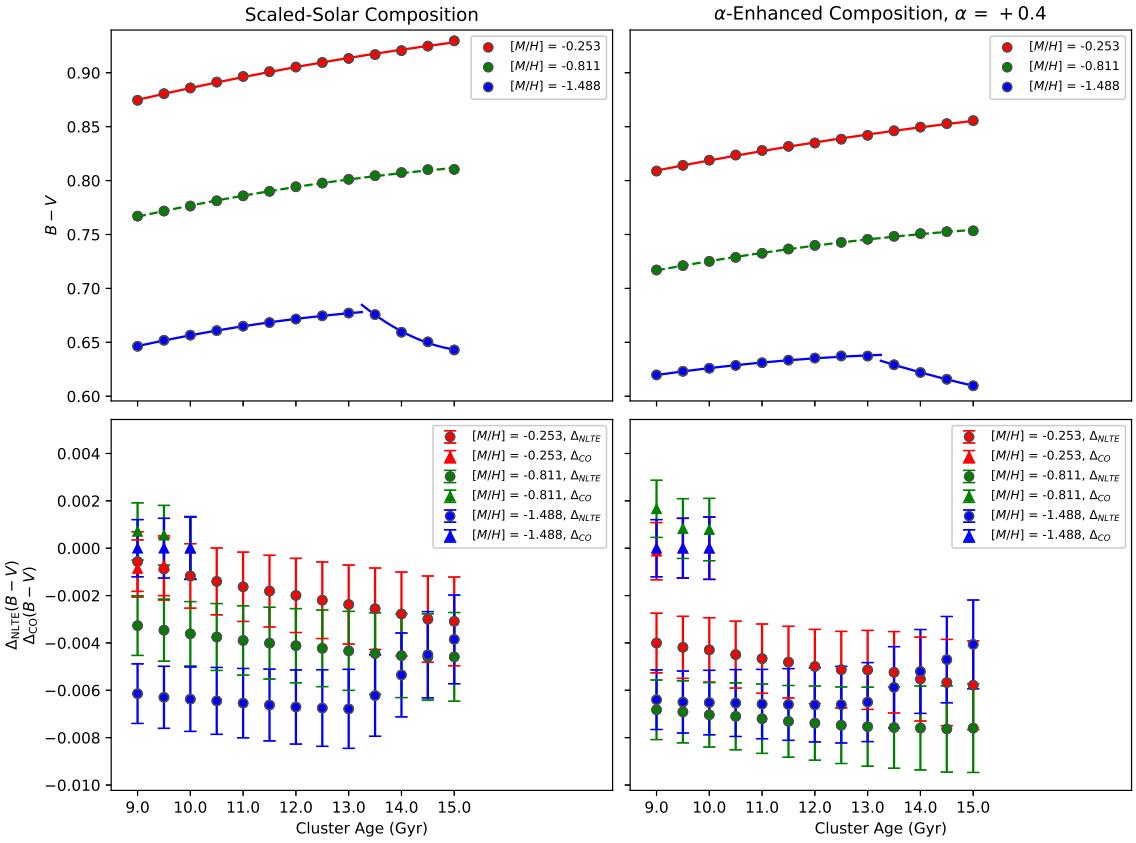

Figure 3.6 Same as Figure 3.5, but for $B - V$.

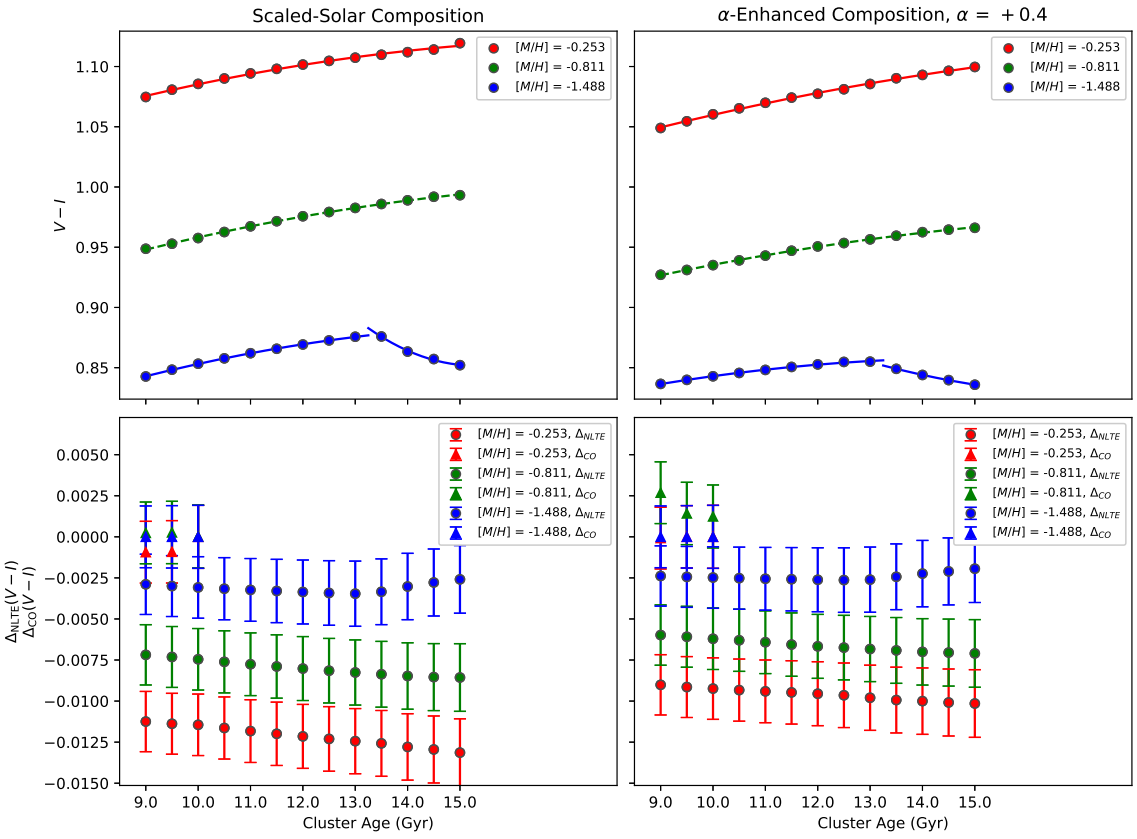

Figure 3.7 Same as Figure 3.5, but for $V - I$.

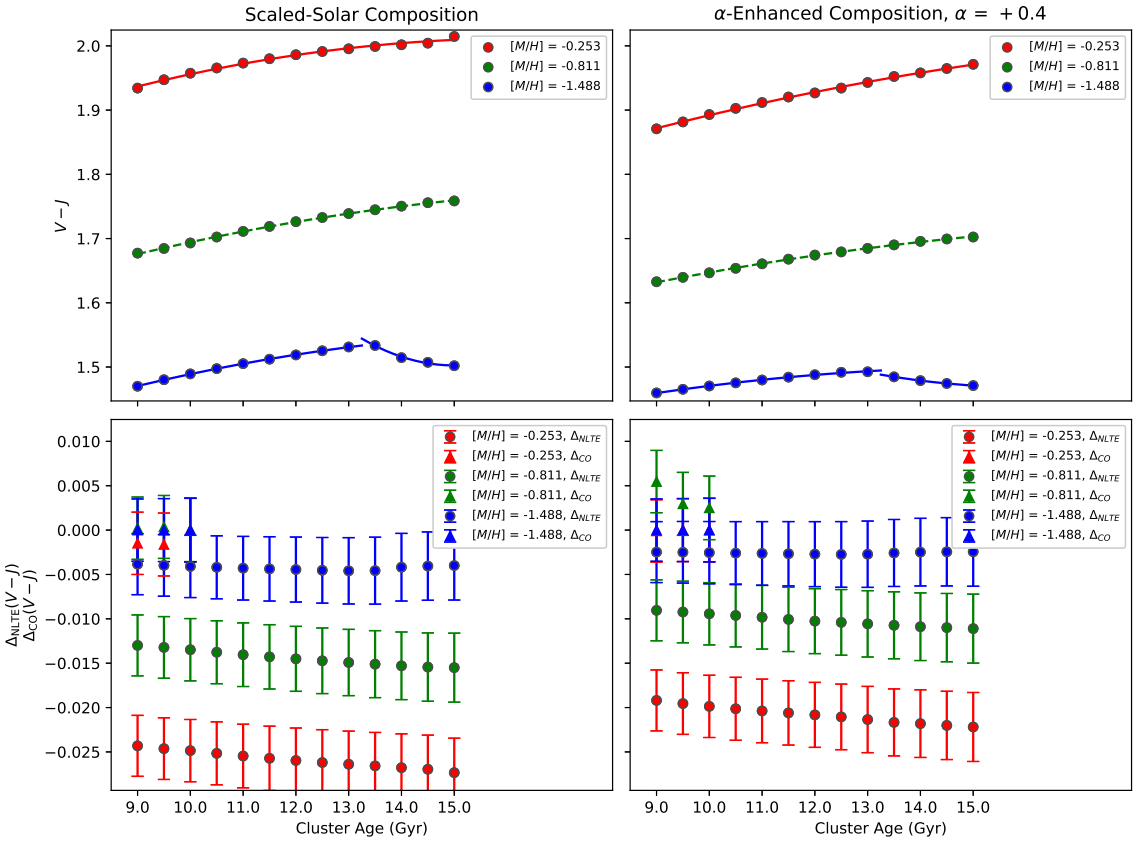

Figure 3.8 Same as Figure 3.5, but for $V - J$.

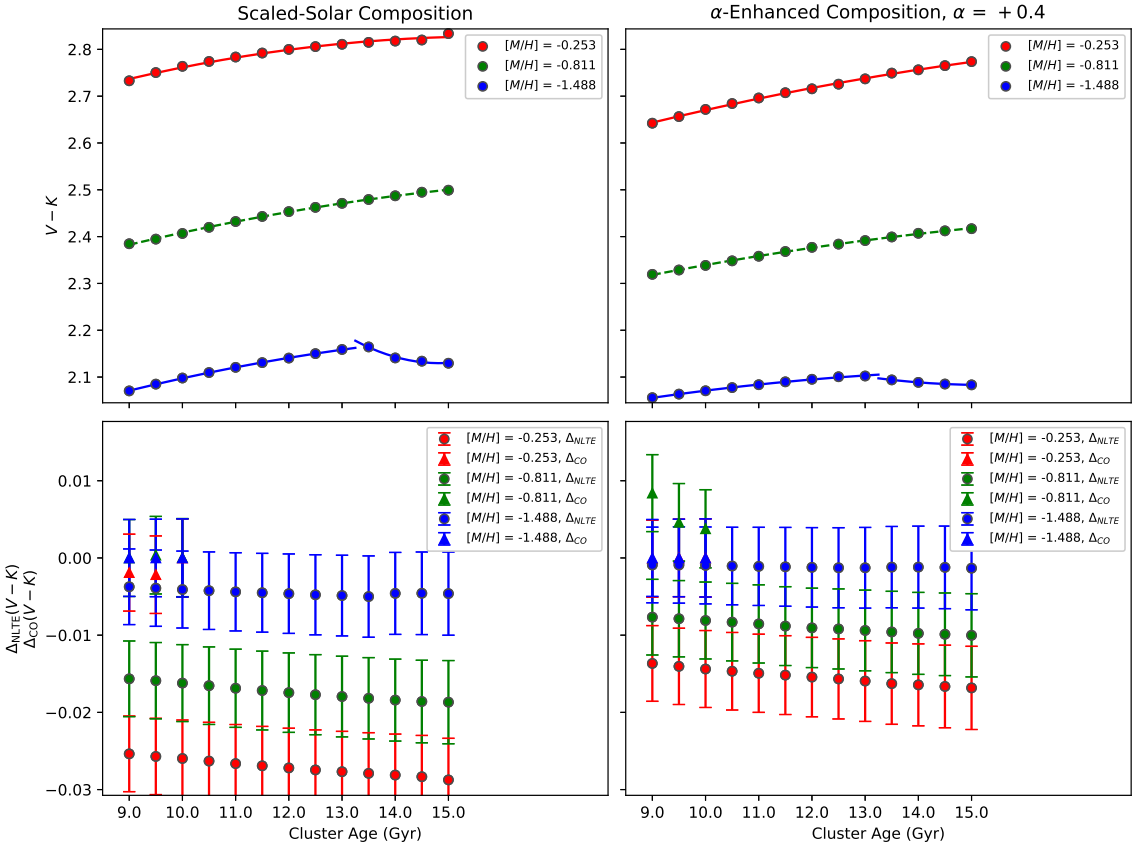

Figure 3.9 Same as Figure 3.5, but for $V - K$.

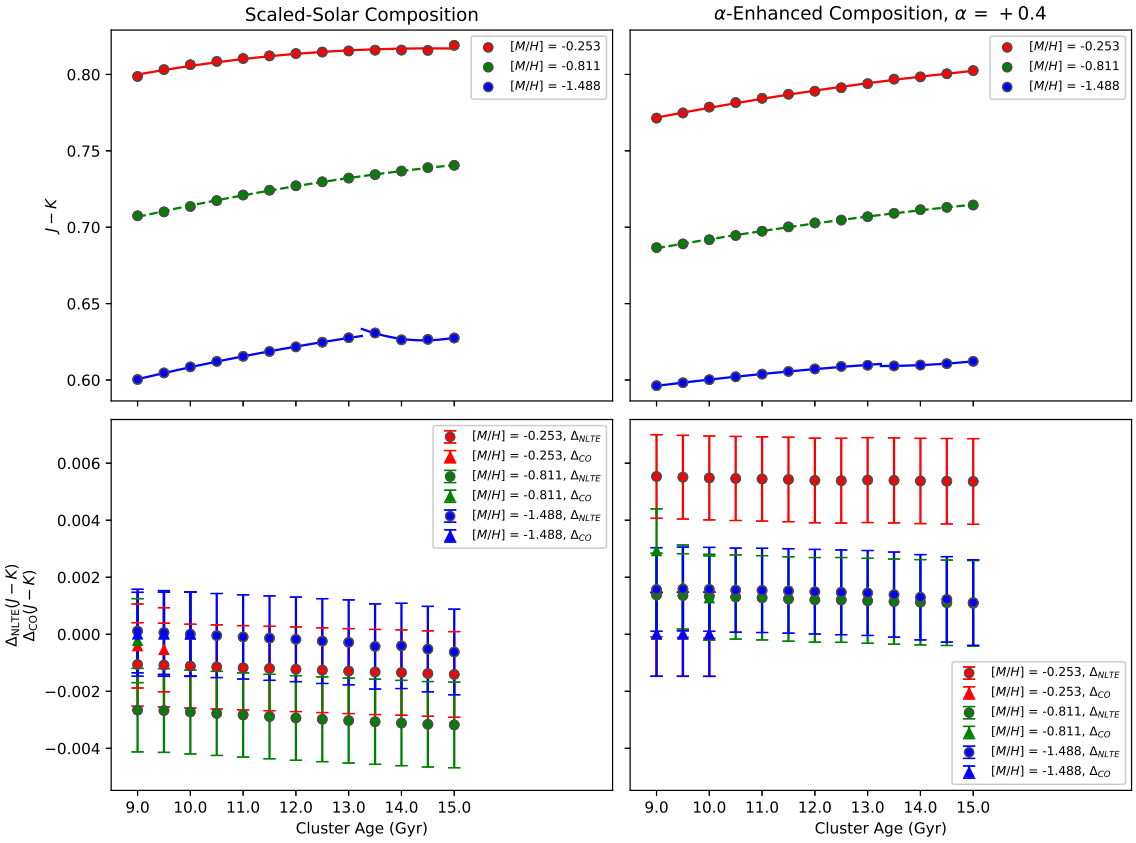

Figure 3.10 Same as Figure 3.5, but for $J - K$.

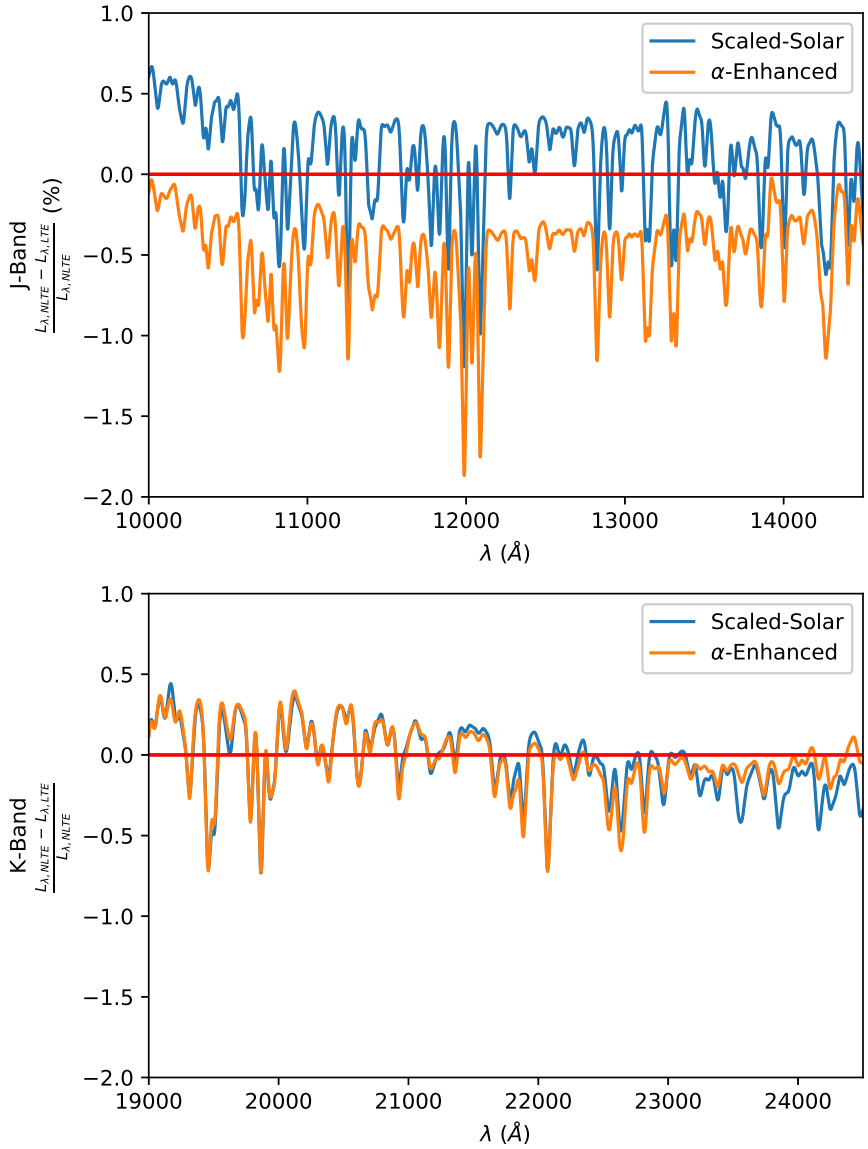

Figure 3.11 $\Delta_{\rm NLTE}(L_\lambda)$ for α-enhanced and scaled-solar 12.0 Gyr, $[M/H]$ = -0.253 clusters. Luminosity spectra have been convolved to a spectral resolution of R $\sim$ 1000 for ease of viewing, and normalized to K-band.

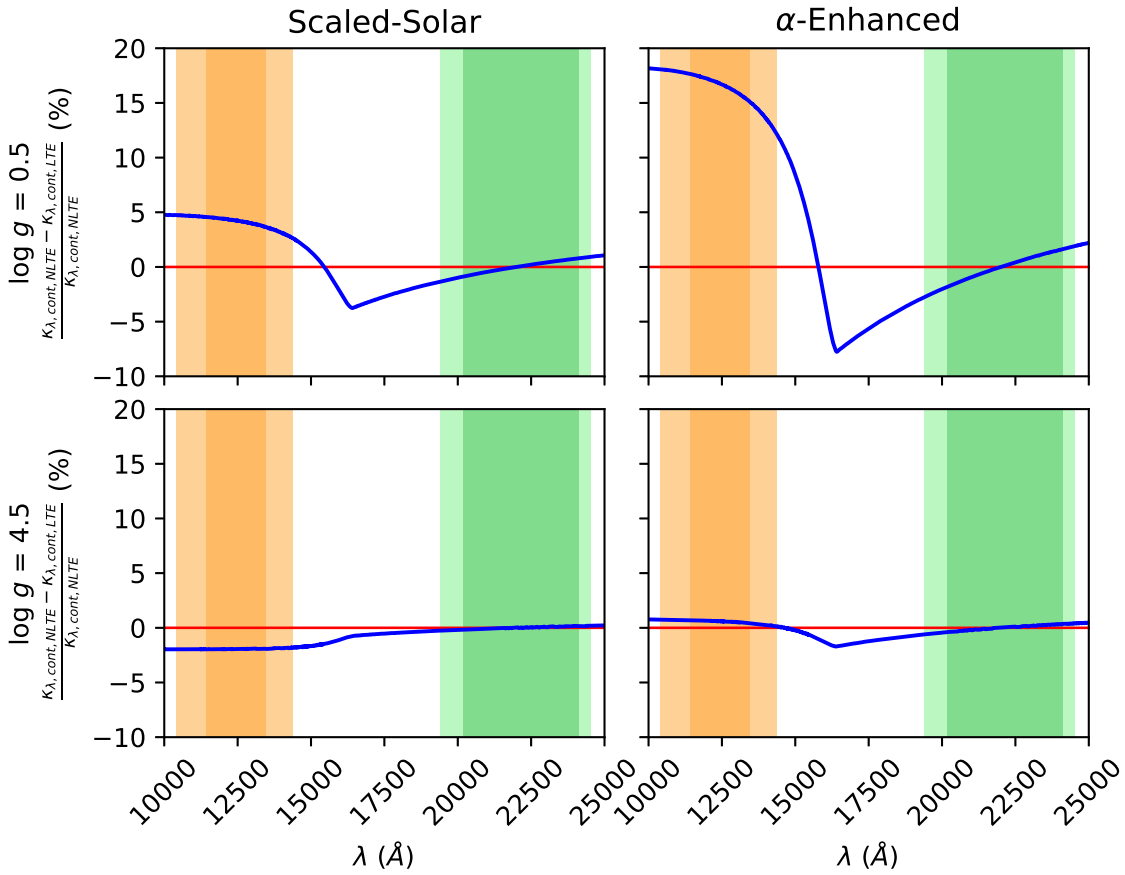

Figure 3.12 $\Delta_{\rm NLTE}(\kappa_{\lambda,\rm cont})$ for scaled-solar and α-enhanced stars of $T_{\rm eff}$ = 4000 K, $[M/H]$ = 0.0, and log g = 0.5 and 4.5. Opacities have been normalized to the integrated K-band values. Shaded regions indicate the J (orange) and K (green) passbands. Darker regions indicate where filter transmission is > 50%.

values for scaled-solar and α-enhanced $[M/H]$ = 0.0 giant and dwarf stars, with log g = 0.5 and 4.5, respectively.

The large change in opacity around 1.6 μm suggests that the cause of the increase in J-band $\Delta_{\rm NLTE}(\kappa_{\lambda,\rm cont})$ is primarily H^- opacity. Figure 3.13 displays the $\Delta_{\rm NLTE}(p_{\rm H^-})$ and $\Delta_{\rm NLTE}(p_{\rm e^-})$ values of the same four $[M/H]$ = 0.0 stars as previous, where $p_{\rm H^-}$ and $p_{\rm e^-}$ are the partial pressures for H^- and free electrons, respectively. The α-enhanced stars and scaled-solar giant show $\Delta_{\rm NLTE}(p_{\rm H^-}) > 0$ throughout the upper atmosphere,

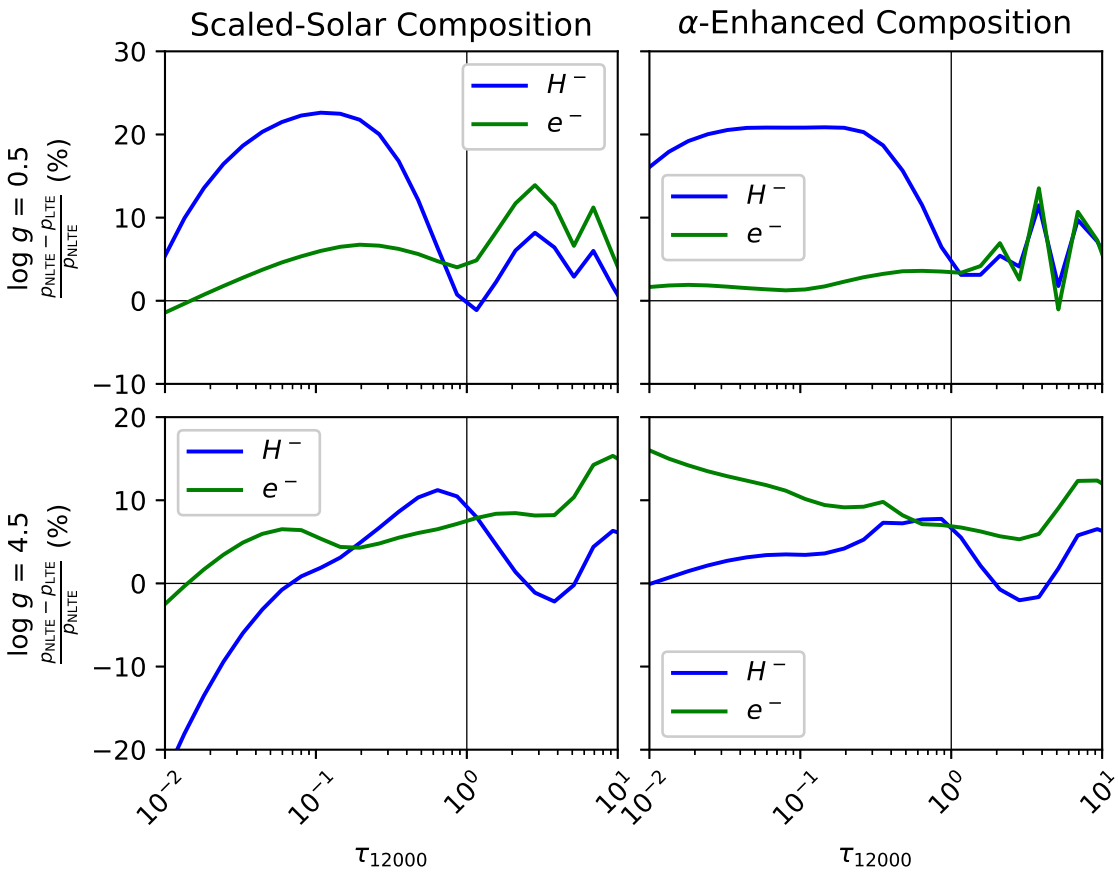

Figure 3.13 $\Delta_{\rm NLTE}(p_{\rm H^-})$ and $\Delta_{\rm NLTE}(p_{\rm e^-})$ for scaled-solar and α-enhanced stars of $T_{\rm eff}$ = 4000 K, $[M/H] = 0.0$, and log g = 0.5 and 4.5.

while the scaled solar dwarf does not.

Old Metal Poor Clusters

As the stars evolve in these clusters, the HB extends blueward of the MS turnoff becoming the bluest stars in the cluster. Figure 3.14 displays four example CMDs, showing the evolution of populations for metal-rich ($[M/H] = -0.253$) and metal-poor ($[M/H] = -1.488$) clusters, with both α-enhanced and scaled-solar abundance distributions. Horizontal branches are seen to remain tightly clumped for metal-rich

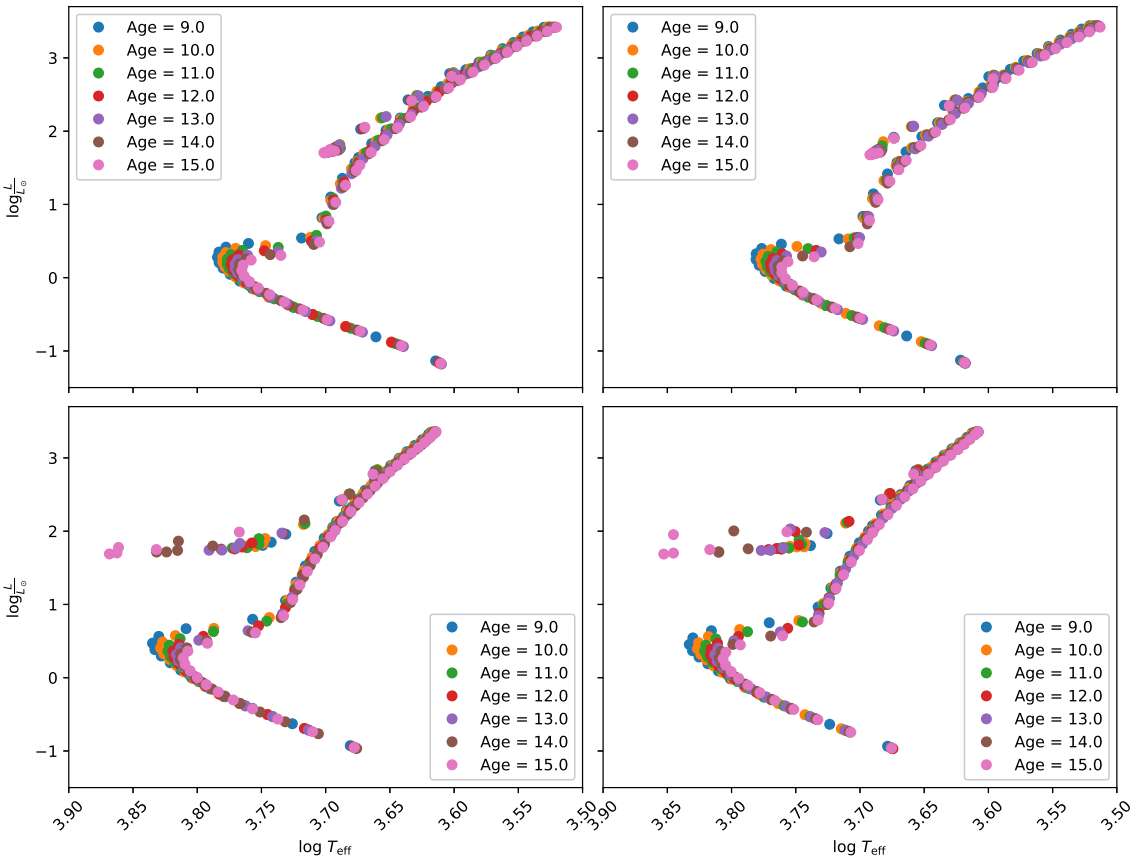

Figure 3.14 Comparison of the evolution of HB morphologies. *Top Row*: Clusters of constant $[M/H] = -0.253$. *Bottom Row*: Clusters of constant $[M/H] = -1.488$. *Left Column*: α-enhanced clusters. *Right Column*: Scaled-solar clusters.

clusters at all ages, while expanding blueward with age for metal-poor clusters.

Horizontal branch morphologies are mainly dependent upon three parameters (Gratton *et al.*, 2010). In order of impact on the morphology, they are: 1) the overall cluster metallicity, 2) the cluster age, and 3) the cluster He abundance. Cluster metallicity and age both control the separation between the cool edge of the HB and RGB, with greater separation seen for older, more metal-poor clusters, while He abundance affects the width of the HB, with greater elongation seen for higher He

abundance (Milone, 2013). Our HBs continue to extend blueward with increasing age in these metal poor clusters, dominating the B and V passbands and causing the shift towards bluer IL colours. In these metal poor clusters the colour-age relation is fit with two separate parabolas, one for ages 9.0 to 13.0 Gyr, and another for 13.0 to 15.0 Gyr (see Figures 3.5 to 3.10).

3.3.2 colours vs Cluster Metallicity

Figures 3.15 to 3.20 present the IL values of the six indices, and $\Delta_{\rm NLTE}(colour)$ and $\Delta_{\rm CO}(colour)$, as functions of cluster metallicity. In addition to the same general properties listed in Section 3.3.1, the six indices display the following properties as functions of cluster metallicity:

1. All indices are seen to redden with increasing metallicity
2. For all indices except $B-V$ and scaled-solar $J-K$, $\Delta_{\rm NLTE}(colour)$ values increase as a function of cluster metallicity
3. The results for *alpha*-enhanced $\Delta_{\rm NLTE}(B-V)$ and scaled-solar $\Delta_{\rm NLTE}(J-K)$ simulations peak at $[M/H]=-0.963$

3.3.3 Age-Metallicity Degeneracy

Current modelling of Galactic GC IL has demonstrated an age-metallicity degeneracy in photometric colours. Worthey (1994) has shown that a percentage change of

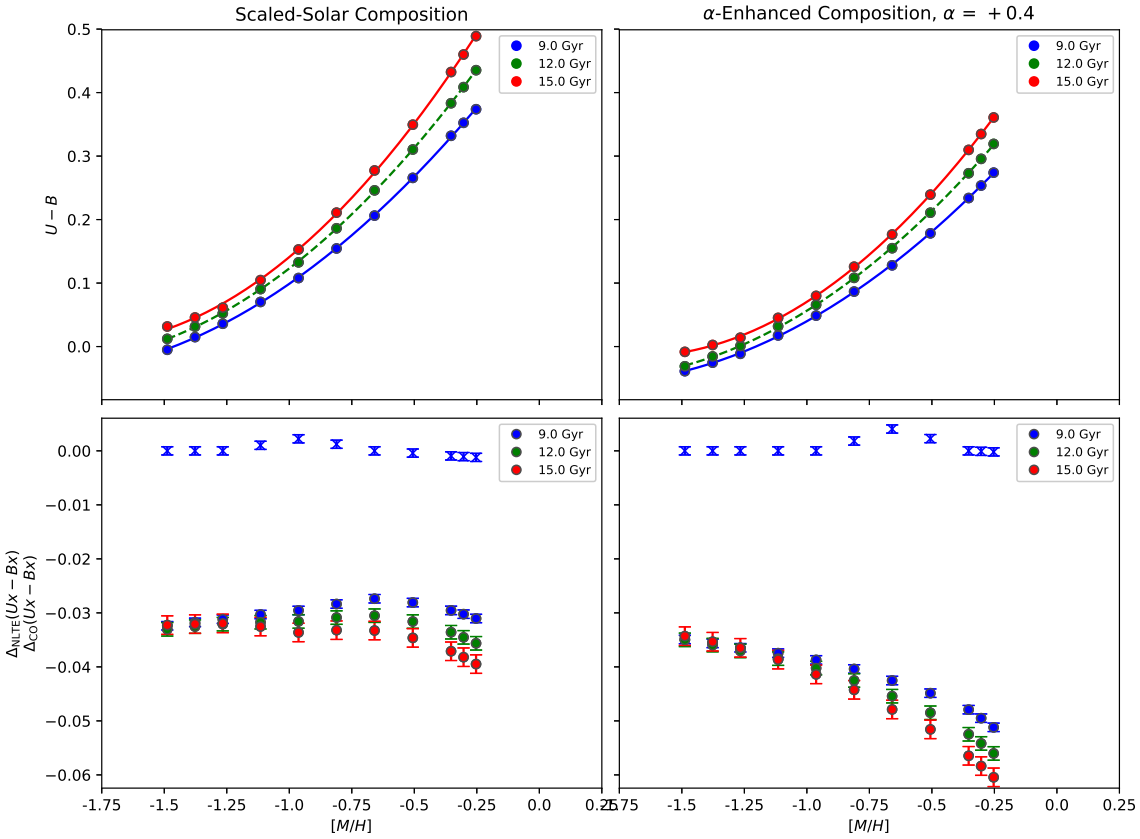

Figure 3.15 *Top* - Photometric LTE $U-B$ colour values *vs* cluster $[M/H]$. *Bottom* - $\Delta_{\rm NLTE}$ (circles) and $\Delta_{\rm CO}$ (triangles) *vs* cluster $[M/H]$. Only a sample of the ages are shown for ease of viewing. Error bars for isochrone discretizeation uncertainty are too small to be seen at this scale. Best fitting second order polynomials are plotted as solid lines for isochrone IL spectra, and dashed lines for interpolated IL spectra.

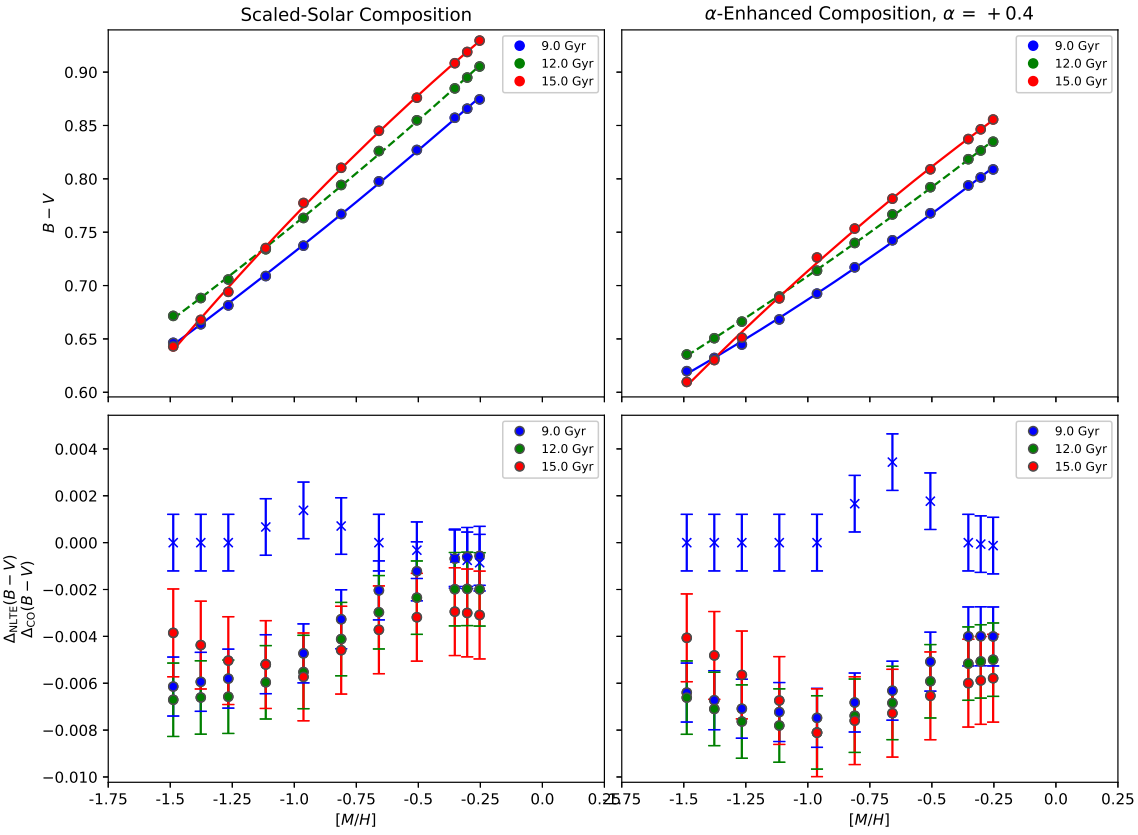

Figure 3.16 Same as Figure 3.15, but for $B - V$.

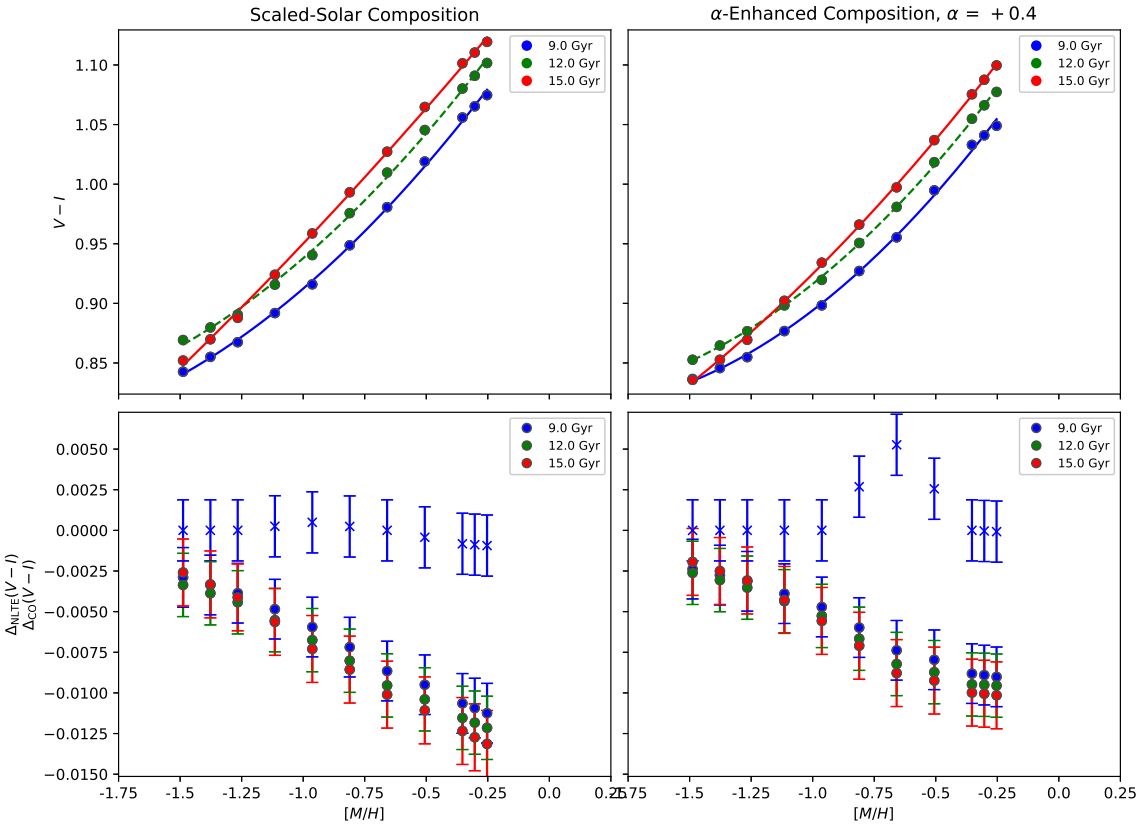

Figure 3.17 Same as Figure 3.15, but for $V - I$.

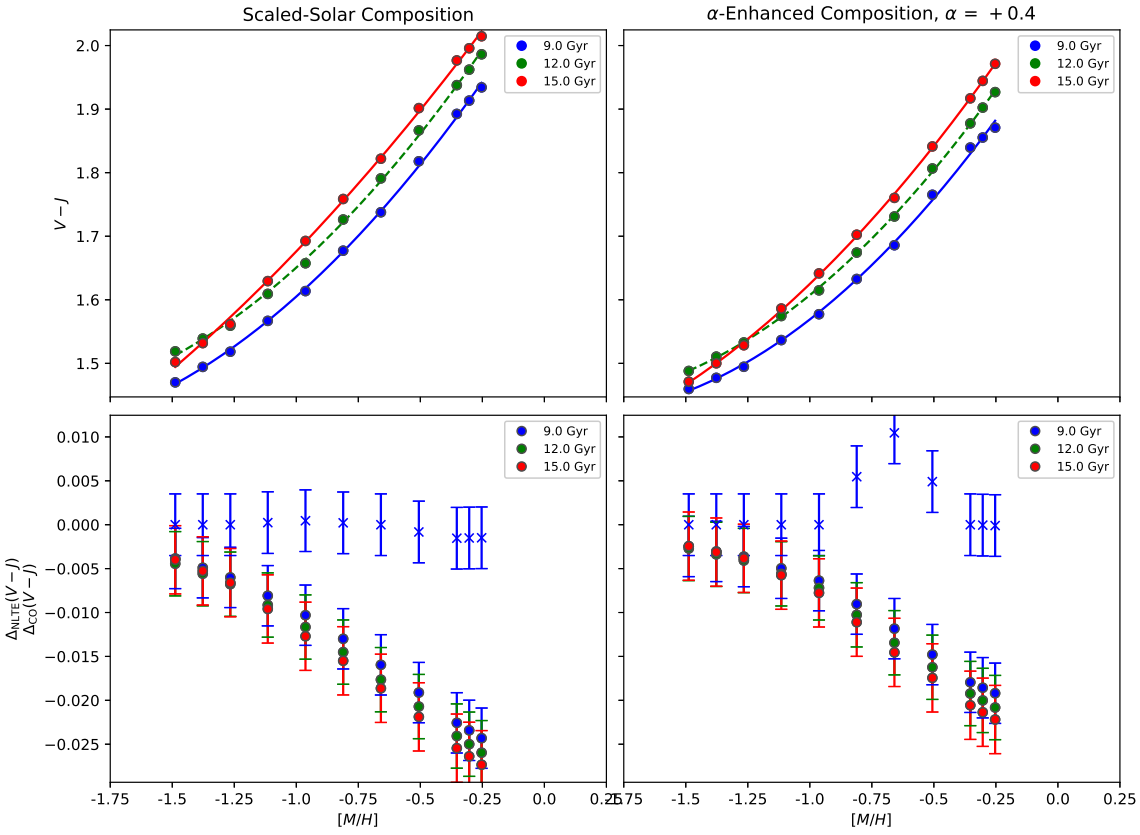

Figure 3.18 Same as Figure 3.15, but for $V - J$.

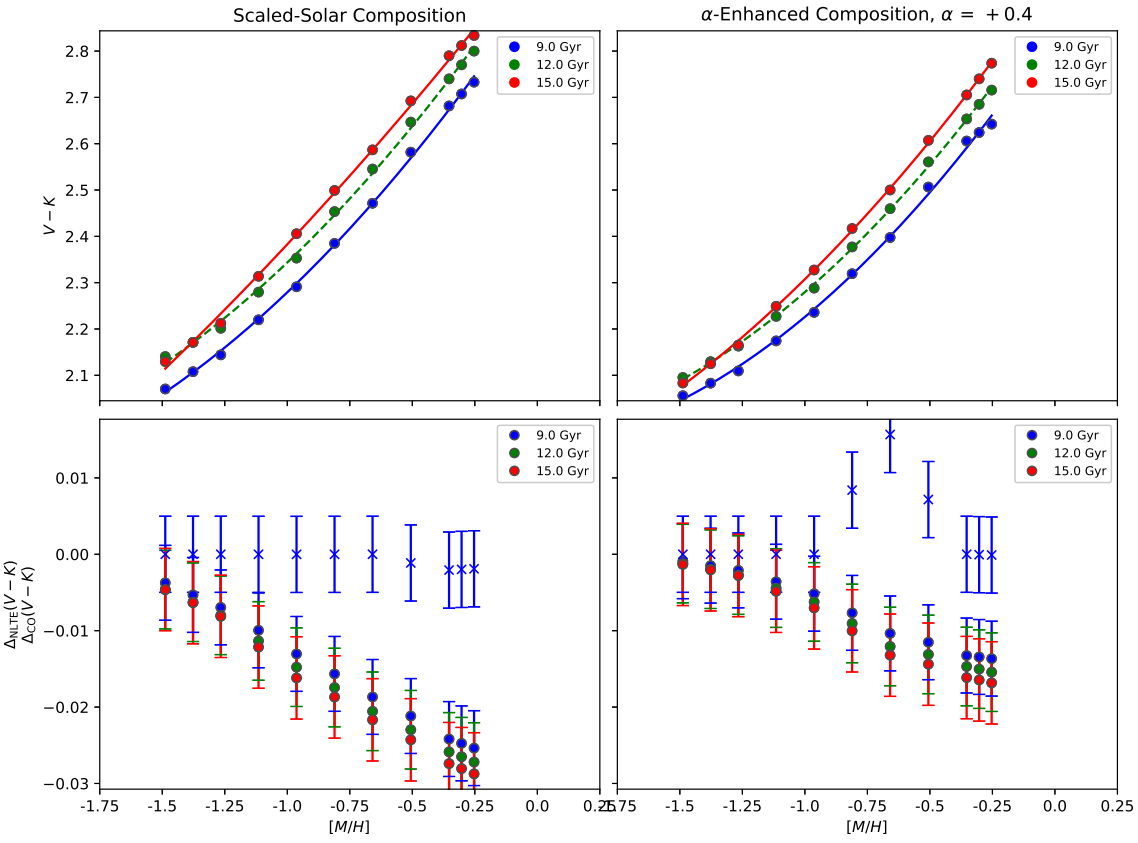

Figure 3.19 Same as Figure 3.15, but for $V - K$.

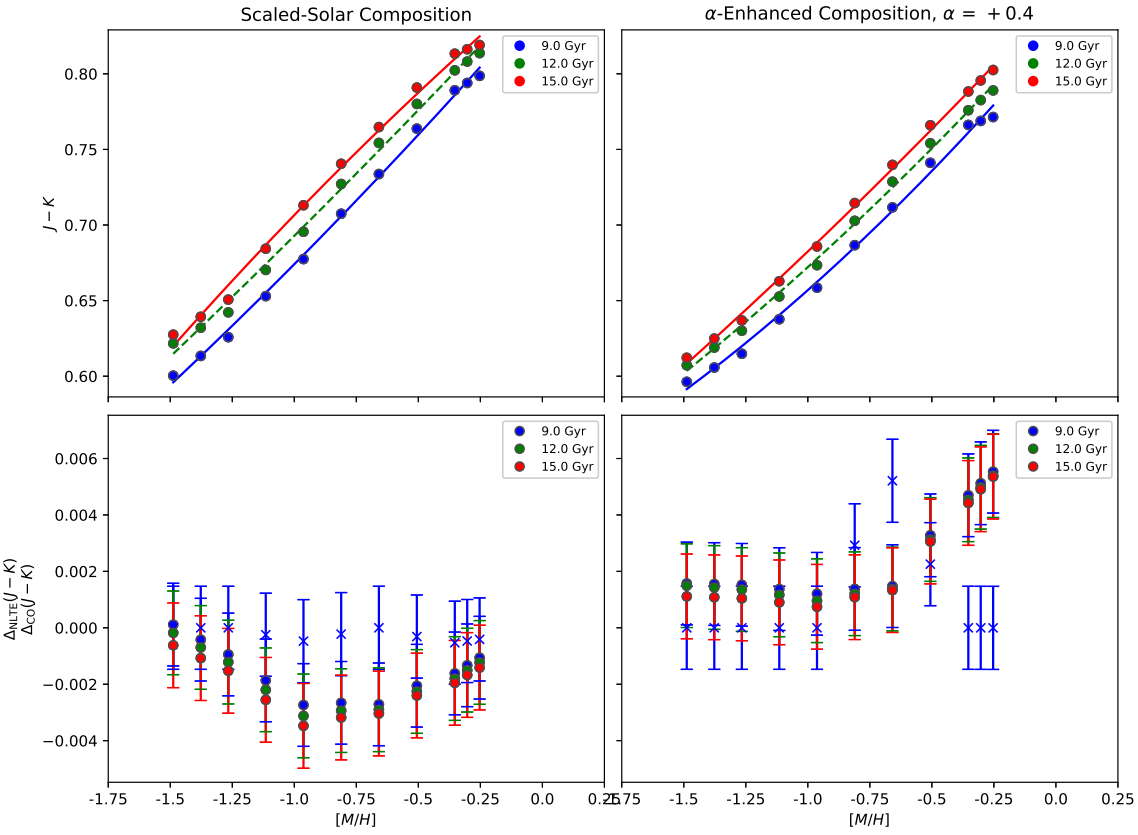

Figure 3.20 Same as Figure 3.15, but for $J - K$.

$\Delta Age/\Delta Z \approx 3/2$ between two populations will cause them to appear almost identical in most indices. But this degeneracy was quantified with LTE atmospheric models and spectra, not NLTE. To demonstrate how NLTE impacts the age-metallicity degeneracy, we parameterize our six indices with fourth order polynomial surfaces of the form

$$colour = \sum_{i=0}^{2} \sum_{j=0}^{2} k_{ij} \cdot Age^{i} \cdot [M/H]^{j} \tag{3.1}$$

where the k_{ij}'s are constants. As above, we restrict the fit to second order in age and metallicity, and only include third and fourth order cross terms of the form $X^i \cdot Y^j$, where $i, j \leq 2$ and $i + j \leq 4$. The k_{ij} constants are presented in Tables 3.2 and 3.3. Two measures of the impact of NLTE are taken: 1) $\Delta_{\rm NLTE}([M/H])$ as a function of age, and 2) $\Delta_{\rm NLTE}(age)$ as a function of metallicity. The residuals of these surface fits are less than 0.001 mag for all indices.

Galactic GCs

To investigate how the degeneracy varies with colour for a given index, we substitute the observed colour values of three well studied Galactic GCs, NGC 5139 (ω Cen), NGC 104 (47 Tuc), and NGC 6205 (M13), into equation 4.4. The resulting curves map the degenerate age-metallicity combinations that produce the input cluster colours. We note that none of our curves reproduce the 3/2 degeneracy of Worthey. See Table 3.4 for a list of cluster parameters and colours. It is important to note that our synthetic IL colours are intrinsic values and need to be reddened before

Table 3.2 Constant k_{ij} values for surfaces fit to our six colour indices, according to equation 4.4.

Index	k_{00}	k_{01}	k_{02}	k_{10}	k_{11}
$U-B_{N,\alpha}$	$2.138\cdot10^{-1}$	$5.249\cdot10^{-1}$	$2.536\cdot10^{-1}$	$1.008\cdot10^{-2}$	$-2.601\cdot10^{-2}$
$U-B_{N,\odot}$	$2.715\cdot10^{-1}$	$4.638\cdot10^{-1}$	$1.561\cdot10^{-1}$	$2.205\cdot10^{-2}$	$-2.673\cdot10^{-3}$
$U-B_{L,\alpha}$	$2.492\cdot10^{-1}$	$5.342\cdot10^{-1}$	$2.564\cdot10^{-1}$	$1.273\cdot10^{-2}$	$-2.386\cdot10^{-2}$
$U-B_{L,\odot}$	$2.799\cdot10^{-1}$	$4.438\cdot10^{-1}$	$1.487\cdot10^{-1}$	$2.547\cdot10^{-2}$	$2.543\cdot10^{-3}$
$B-V_{N,\alpha}$	$7.119\cdot10^{-1}$	$9.804\cdot10^{-3}$	$-1.904\cdot10^{-1}$	$2.239\cdot10^{-2}$	$3.764\cdot10^{-2}$
$B-V_{N,\odot}$	$7.430\cdot10^{-1}$	$-1.226\cdot10^{-1}$	$-3.229\cdot10^{-1}$	$2.927\cdot10^{-2}$	$6.380\cdot10^{-2}$
$B-V_{L,\alpha}$	$7.055\cdot10^{-1}$	$-1.835\cdot10^{-2}$	$-2.135\cdot10^{-1}$	$2.351\cdot10^{-2}$	$4.066\cdot10^{-2}$
$B-V_{L,\odot}$	$7.288\cdot10^{-1}$	$-1.606\cdot10^{-1}$	$-3.510\cdot10^{-1}$	$3.129\cdot10^{-2}$	$6.936\cdot10^{-2}$
$V-I_{N,\alpha}$	$9.789\cdot10^{-1}$	$1.246\cdot10^{-1}$	$-1.123\cdot10^{-1}$	$2.089\cdot10^{-2}$	$3.476\cdot10^{-2}$
$V-I_{N,\odot}$	$9.434\cdot10^{-1}$	$-4.985\cdot10^{-2}$	$-2.437\cdot10^{-1}$	$3.200\cdot10^{-2}$	$6.672\cdot10^{-2}$
$V-I_{L,\alpha}$	$9.880\cdot10^{-1}$	$1.324\cdot10^{-1}$	$-1.133\cdot10^{-1}$	$2.115\cdot10^{-2}$	$3.472\cdot10^{-2}$
$V-I_{L,\odot}$	$9.540\cdot10^{-1}$	$-4.275\cdot10^{-2}$	$-2.469\cdot10^{-1}$	$3.235\cdot10^{-2}$	$6.704\cdot10^{-2}$
$V-J_{N,\alpha}$	$1.775\cdot10^{0}$	$3.429\cdot10^{-1}$	$-1.071\cdot10^{-1}$	$3.219\cdot10^{-2}$	$4.488\cdot10^{-2}$
$V-J_{N,\odot}$	$1.670\cdot10^{0}$	$-4.338\cdot10^{-2}$	$-3.799\cdot10^{-1}$	$6.455\cdot10^{-2}$	$1.239\cdot10^{-1}$
$V-J_{L,\alpha}$	$1.796\cdot10^{0}$	$3.724\cdot10^{-1}$	$-9.792\cdot10^{-2}$	$3.280\cdot10^{-2}$	$4.453\cdot10^{-2}$
$V-J_{L,\odot}$	$1.696\cdot10^{0}$	$-1.373\cdot10^{-2}$	$-3.741\cdot10^{-1}$	$6.529\cdot10^{-2}$	$1.237\cdot10^{-1}$
$V-K_{N,\alpha}$	$2.576\cdot10^{0}$	$5.991\cdot10^{-1}$	$-6.759\cdot10^{-2}$	$3.655\cdot10^{-2}$	$3.928\cdot10^{-2}$
$V-K_{N,\odot}$	$2.409\cdot10^{0}$	$2.601\cdot10^{-2}$	$-4.680\cdot10^{-1}$	$8.477\cdot10^{-2}$	$1.541\cdot10^{-1}$
$V-K_{L,\alpha}$	$2.589\cdot10^{0}$	$6.181\cdot10^{-1}$	$-6.176\cdot10^{-2}$	$3.713\cdot10^{-2}$	$3.835\cdot10^{-2}$
$V-K_{L,\odot}$	$2.434\cdot10^{0}$	$5.076\cdot10^{-2}$	$-4.655\cdot10^{-1}$	$8.541\cdot10^{-2}$	$1.532\cdot10^{-1}$
$J-K_{N,\alpha}$	$8.010\cdot10^{-1}$	$2.562\cdot10^{-1}$	$3.955\cdot10^{-2}$	$4.353\cdot10^{-3}$	$-5.599\cdot10^{-3}$
$J-K_{N,\odot}$	$7.386\cdot10^{-1}$	$6.939\cdot10^{-2}$	$-8.816\cdot10^{-2}$	$2.022\cdot10^{-2}$	$3.020\cdot10^{-2}$
$J-K_{L,\alpha}$	$7.924\cdot10^{-1}$	$2.456\cdot10^{-1}$	$3.616\cdot10^{-2}$	$4.332\cdot10^{-3}$	$-6.173\cdot10^{-3}$
$J-K_{L,\odot}$	$7.383\cdot10^{-1}$	$6.449\cdot10^{-2}$	$-9.149\cdot10^{-2}$	$2.012\cdot10^{-2}$	$2.955\cdot10^{-2}$

comparison with observed values. To do so, we take the $B-V$ colour excesses of each observed cluster, $E(B-V)$, from Harris 1996 (2010 ed) and convert them to other indices using the galactic absorption law of Cardelli, Clayton, & Mathis (1989).

Table 3.3 Additional constant k_{ij} values for surfaces fit to our six colour indices, according to equation 4.4.

Index	k_{12}	k_{20}	k_{21}	k_{22}
$U-B_{N,\alpha}$	$-2.851\cdot10^{-2}$	$3.094\cdot10^{-4}$	$1.948\cdot10^{-3}$	$1.520\cdot10^{-3}$
$U-B_{N,\odot}$	$-1.015\cdot10^{-2}$	$3.181\cdot10^{-5}$	$1.111\cdot10^{-3}$	$7.564\cdot10^{-4}$
$U-B_{L,\alpha}$	$-2.763\cdot10^{-2}$	$2.843\cdot10^{-4}$	$1.941\cdot10^{-3}$	$1.498\cdot10^{-3}$
$U-B_{L,\odot}$	$-7.299\cdot10^{-3}$	$-4.387\cdot10^{-5}$	$9.303\cdot10^{-4}$	$6.316\cdot10^{-4}$
$B-V_{N,\alpha}$	$4.198\cdot10^{-2}$	$-6.916\cdot10^{-4}$	$-1.821\cdot10^{-3}$	$-2.040\cdot10^{-3}$
$B-V_{N,\odot}$	$6.336\cdot10^{-2}$	$-9.279\cdot10^{-4}$	$-2.896\cdot10^{-3}$	$-2.914\cdot10^{-3}$
$B-V_{L,\alpha}$	$4.534\cdot10^{-2}$	$-7.258\cdot10^{-4}$	$-1.950\cdot10^{-3}$	$-2.194\cdot10^{-3}$
$B-V_{L,\odot}$	$6.834\cdot10^{-2}$	$-9.968\cdot10^{-4}$	$-3.134\cdot10^{-3}$	$-3.138\cdot10^{-3}$
$V-I_{N,\alpha}$	$3.666\cdot10^{-2}$	$-6.006\cdot10^{-4}$	$-1.640\cdot10^{-3}$	$-1.768\cdot10^{-3}$
$V-I_{N,\odot}$	$5.837\cdot10^{-2}$	$-1.137\cdot10^{-3}$	$-3.164\cdot10^{-3}$	$-2.736\cdot10^{-3}$
$V-I_{L,\alpha}$	$3.710\cdot10^{-2}$	$-6.060\cdot10^{-4}$	$-1.652\cdot10^{-3}$	$-1.799\cdot10^{-3}$
$V-I_{L,\odot}$	$5.921\cdot10^{-2}$	$-1.140\cdot10^{-3}$	$-3.184\cdot10^{-3}$	$-2.780\cdot10^{-3}$
$V-J_{N,\alpha}$	$4.885\cdot10^{-2}$	$-7.643\cdot10^{-4}$	$-1.960\cdot10^{-3}$	$-2.303\cdot10^{-3}$
$V-J_{N,\odot}$	$9.788\cdot10^{-2}$	$-2.322\cdot10^{-3}$	$-5.788\cdot10^{-3}$	$-4.554\cdot10^{-3}$
$V-J_{L,\alpha}$	$4.872\cdot10^{-2}$	$-7.687\cdot10^{-4}$	$-1.945\cdot10^{-3}$	$-2.308\cdot10^{-3}$
$V-J_{L,\odot}$	$9.813\cdot10^{-2}$	$-2.336\cdot10^{-3}$	$-5.795\cdot10^{-3}$	$-4.583\cdot10^{-3}$
$V-K_{N,\alpha}$	$4.930\cdot10^{-2}$	$-8.070\cdot10^{-4}$	$-1.892\cdot10^{-3}$	$-2.446\cdot10^{-3}$
$V-K_{N,\odot}$	$1.204\cdot10^{-1}$	$-3.138\cdot10^{-3}$	$-7.482\cdot10^{-3}$	$-5.720\cdot10^{-3}$
$V-K_{L,\alpha}$	$4.865\cdot10^{-2}$	$-8.099\cdot10^{-4}$	$-1.855\cdot10^{-3}$	$-2.429\cdot10^{-3}$
$V-K_{L,\odot}$	$1.202\cdot10^{-1}$	$-3.147\cdot10^{-3}$	$-7.467\cdot10^{-3}$	$-5.733\cdot10^{-3}$
$J-K_{N,\alpha}$	$4.498\cdot10^{-4}$	$-4.264\cdot10^{-5}$	$6.803\cdot10^{-5}$	$-1.428\cdot10^{-4}$
$J-K_{N,\odot}$	$2.251\cdot10^{-2}$	$-8.165\cdot10^{-4}$	$-1.695\cdot10^{-3}$	$-1.166\cdot10^{-3}$
$J-K_{L,\alpha}$	$-7.162\cdot10^{-5}$	$-4.115\cdot10^{-5}$	$8.937\cdot10^{-5}$	$-1.216\cdot10^{-4}$
$J-K_{L,\odot}$	$2.210\cdot10^{-2}$	$-8.115\cdot10^{-4}$	$-1.673\cdot10^{-3}$	$-1.150\cdot10^{-3}$

Results

Our degenerate age-metallicity curves and $\Delta_{\rm NLTE}$ values are presented in Figures 3.21 to 3.23. Degenerate curves for colours not included in the figures fall outside of the parameter space of our library of IL spectra. The degenerate curves exhibit the following properties with age as the independent variable:

1. With the exception of the degenerate curves derived from $U-B$, $\Delta_{\rm NLTE}([M/H]) \leq$

0.06 at all ages.

2. For $U-B$, $\Delta_{\rm NLTE}([M/H]) \leq 0.15$ for α-enhanced models and $\Delta_{\rm NLTE}([M/H]) \leq 0.115$ for scaled-solar models.

3. With the exception of α-enhanced $J-K$ for NGC 104, $\Delta_{\rm NLTE}([M/H]) \geq 0$.

4. Generally, indices comprised of bluer filters show larger values for $\Delta_{\rm NLTE}([M/H])$ with the exception of $B-V$ for both NGC 104 and NGC 5139.

5. Degenerate curves derived from bluer indices show that $\Delta_{\rm NLTE}([M/H], \alpha) > \Delta_{\rm NLTE}([M/H], solar)$, while redder indices show that $\Delta_{\rm NLTE}([M/H], solar) > \Delta_{\rm NLTE}([M/H], \alpha)$, and $V-I$ shows both trends.

With $[M/H]$ as the independent variable, we find:

1. $-2.0 < \Delta_{\rm NLTE}(age) < 2.0$ Gyr, except for $V-I$ for NGC 104, and $U-B$ in general

2. $\Delta_{\rm NLTE}(age)$ values for a given $[M/H]$ in $B-V$ and $V-I$ are degenerate, and may be either $\Delta_{\rm NLTE}(age) < 0$ or $\Delta_{\rm NLTE}(age) > 0$, with approximately equivalent magnitudes

For the three observed clusters, the impact of NLTE modelling can be assessed directly. By assuming the ages listed in Table 3.4, our degeneracy curves show that the metallicities of the clusters, derived from IL $B-V$, would be increased by up to 0.05 dex when modelled in NLTE, depending on the degree of α-enhancement. If

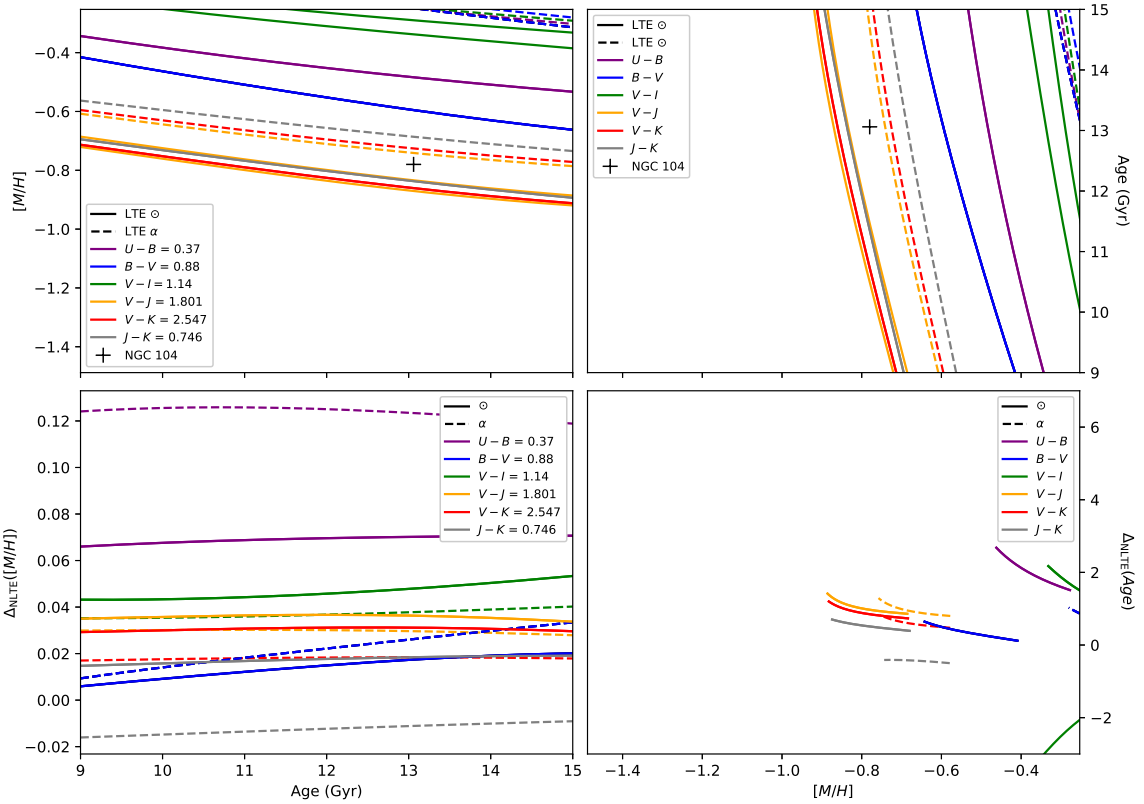

Figure 3.21 Degenerate age-metallicity combinations that produce the observed colour values of NGC 104, and $\Delta_{\rm NLTE}$ values. The black cross marks the actual age and metallicity of NGC 104 (Forbes, 2010).

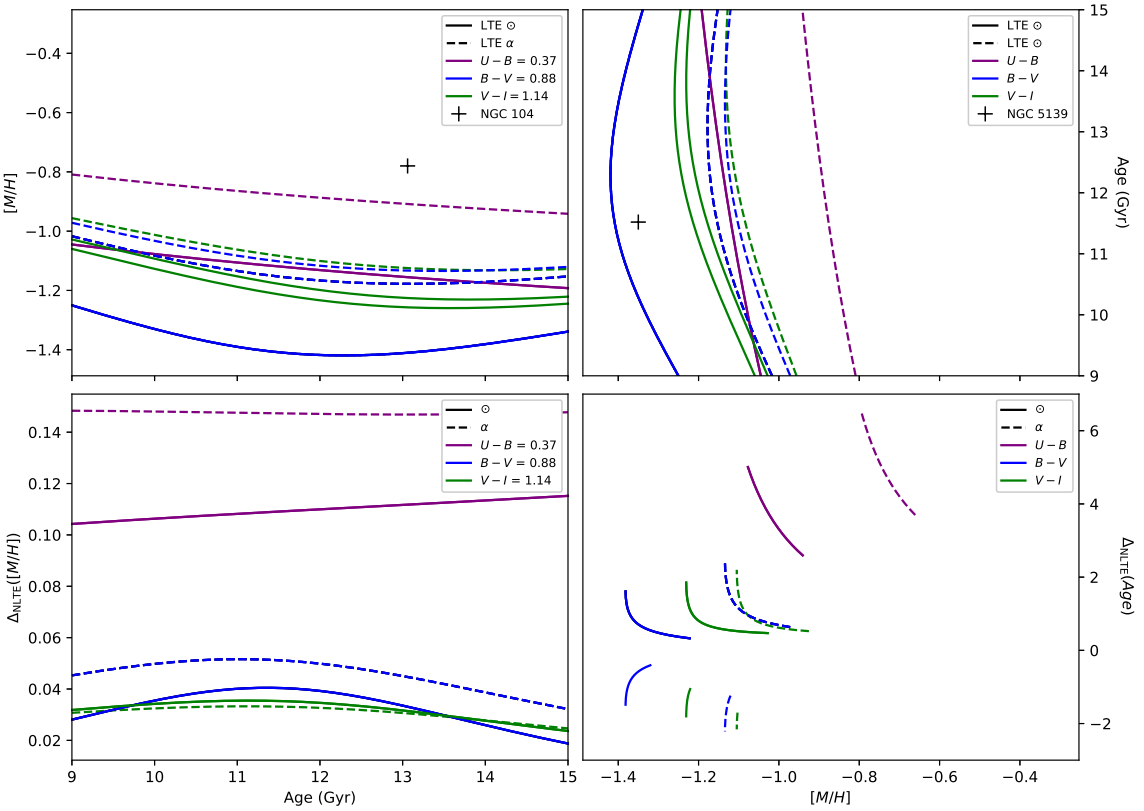

Figure 3.22 Same as Figure 3.21, but for NGC 5139.

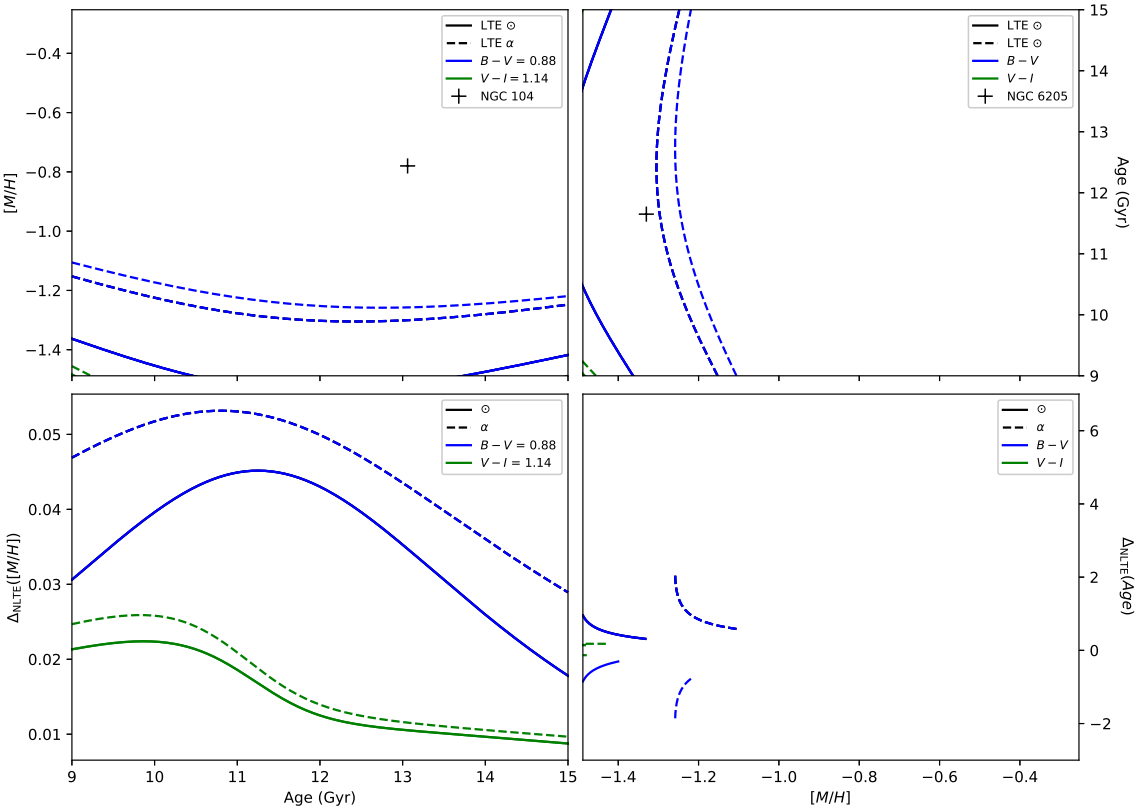

Figure 3.23 Same as Figure 3.21, but for NGC 6205.

instead we assume the metallicities of the three clusters, $\Delta_{\rm NLTE}(Age)$ is not single valued for all colour indexes, and ages derived from NLTE colours may be either younger or older than those from LTE colours. We are unable to derive a value of $\Delta_{\rm NLTE}(Age)$ for NGC 104 from IL $B-V$ at the degree of α-enhancement we have computed. Instead, $V-K$ indicates an increase of $\Delta_{\rm NLTE}(Age) \approx 0.75$ Gyr, while $J-K$ indicates $\Delta_{\rm NLTE}(Age) \approx \pm 0.5$ Gyr. For the remaining two clusters, $\Delta_{\rm NLTE}(Age)$s derived from IL $B-V$ have magnitudes less than 0.5 Gyr.

3.4 SPECTRAL LINE SENSITIVITY

3.4.1 Analysis

Spectral lines in the wavelength range $\lambda = 12000$ Å to 20000 Å are investigated to find those which are sensitive to GC age or metallicity. For a spectral line to be considered sensitive to a parameter in this work, it must follow two trends as that parameter is adjusted. The depth at line center, $F_{\lambda_0}/F_{\lambda}^{C}$, must change proportionally to the parameter of interest over the full range, and it must change by a detectable amount.

To prepare the IL spectra for identification of sensitive spectral features, the high resolution IL SEDs are convolved to a spectral resolution of R $\sim$ 30000, typical of observed high resolution IL spectra used for cluster parameter determination (McWilliam & Bernstein, 2008), Doppler broadened with a velocity dispersion and

continuum rectified. Continuum rectification of the IL spectra is performed with a two pass process. In the first pass, the synthetic IL SEDs are normalized by dividing by the corresponding synthetic IL continuum SED. In the second pass, the normalized spectra are broken into 1000 Å regions and rectified by a second order polynomial, fit to several regions free of spectral lines, identified by visual inspection.

Our goal is to identify features that vary consistently with $[M/H]$ or age in a way that is distinct from that of the local F_λ^C value, and are not blended with close neighbors. The variation with $[M/H]$ or age is quantified as the rate at which $F_{\lambda_0}/F_\lambda^C$ changes with respect to the parameter of interest, $\frac{\partial(F_{\lambda_0}/F_\lambda^C)}{\partial X}$, where X is either the age or $[M/H]$. To avoid falsely identifying features that are blended with nearby lines, we measure the slope of the flux at one half of a characteristic width (CW) to either side of line center. If the magnitudes of the slopes for a line are within 5% of each other, as for the Ca λ19967.3 line in the top panel of Figure 3.24, we consider the line to be a clean feature and mark it for further analysis. If a line does not meet this criteria, as illustrated in the bottom panel of Figure 3.24, it is rejected as a blended feature. A second pass filtering of blended features by visual inspection is performed later in the procedure to remove any blends that survive this first pass filtration.

The rectified spectra are sampled every 0.28 Å, one eighth of the characteristic width, $\Delta\lambda_{CW}$ of spectral lines at this resolution, chosen so that each side of a spectral line will be sampled a minimum of four times. For each sampling point, λ_i, $\frac{\partial F_\lambda}{\partial \lambda}$ is

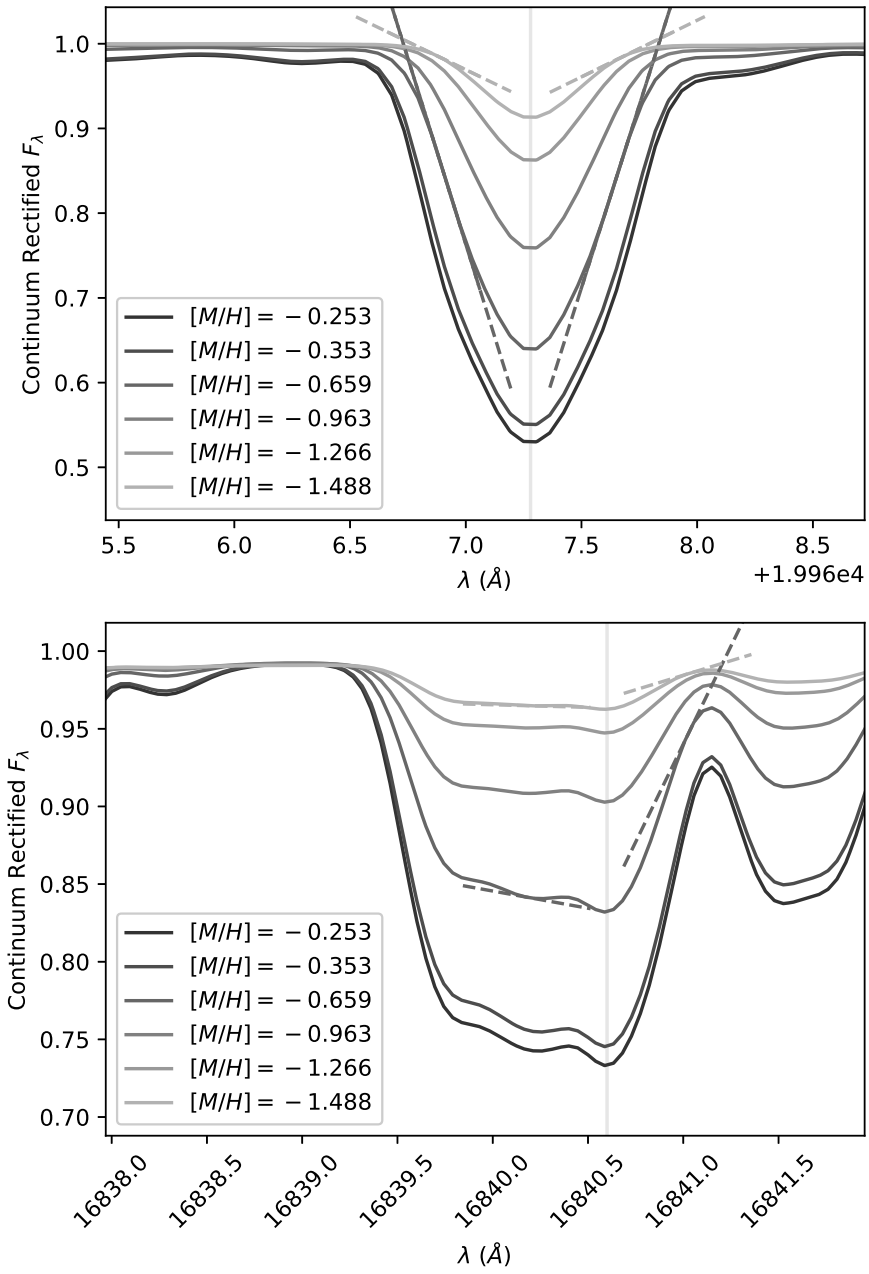

Figure 3.24 Sample clean and blended features flagged as possibly sensitive to cluster $[M/H]$. In both panels, the light gray vertical line marks line center for the flagged feature, and the dashed lines are the slopes to either side of line center. *Top panel*: CA λ19967.2796 line. *Bottom panel*: Unidentified blended feature, included for illustrative purposes.

approximated by

$$\frac{\partial F_\lambda}{\partial \lambda} \approx \frac{1}{5} \sum_{j=1}^{5} \frac{F_{\lambda_{i+j}} - F_{\lambda_{i-j}}}{\lambda_{i+j} - \lambda_{i-j}} \ . \tag{3.2}$$

For a given λ_i, these $\frac{\partial F_\lambda}{\partial \lambda}$ values are fit with two first order polynomials, one as a function of age, and one as a function of $[M/H]$. The slopes of these fits are taken to be $\frac{\partial}{\partial X}(\frac{\partial F_\lambda}{\partial \lambda})$. We consider any sampling point where $\frac{\partial}{\partial X}(\frac{\partial F_\lambda}{\partial \lambda}) > 0.8 \cdot \frac{\partial}{\partial X}(\frac{\partial F_\lambda}{\partial \lambda})_{max}$ to be a feature sensitive to the related cluster parameter, age or $[M/H]$.

Identification of which atomic species and transitions are responsible for generating synthetic IL spectral features is not a straightforward procedure. For an individual stellar spectrum, PHOENIX calculates the strongest atomic and molecular contributors to the overall opacity at each λ sampling point. Which species are the strongest contributors at a given wavelength can be dependent on the parameters of that star, and in general will vary among members of the cluster. Because the IL spectrum is the co-added spectra of all the individual cluster members, PHOENIX may potentially identify as many atomic and molecular species as the main opacity source for a given wavelength as there are cluster members.

Cluster members with similar parameters are likely to report the same species as the strongest absorber for a given wavelength. This reduces the possible number of species responsible for generating a spectral feature to a manageable quantity. We narrow the possibilities further by investigating how much flux each star contributes to the integrated light in different wavebands. Figures 3.25 and 3.26 show the relative contribution of each star to total cluster flux for different photometric wavebands

of two α-enhanced clusters. Scaled-solar clusters show similar behaviors. For the wavelength range of interest, RGB and AGB stars dominate the cluster flux, and whatever opacity sources are identified as the strongest absorbers in RGB stars are considered to be the strongest absorbers in this wavelength range of the IL spectra.

Identified lines are categorized into sets by which modelling parameter they are most sensitive to. We compile sets of features sensitive to cluster age and to metallicity, separating them by composition (scaled-solar or α-enhanced) and NLTE or LTE modelling treatment. The sets of sensitive features are then reduced with a two pass process after line source identification is performed. 1) Any identification where the difference between the line center as reported by PHOENIX and the local minimum of flux is $\Delta\lambda > 0.2$ Å is considered to be a false identification, and removed. 2) The set is further reduced by removing any remaining obviously blended features. Line blends are identified by visual inspection and removed if found to occur within $2 \cdot \Delta\lambda_{CW}$ of each identified sensitive feature. These sets of identified sensitive lines need further investigation to ensure there are no blends with weak features, confirm the line source identification, and confirm the quality of the oscillator strengths. We consider the identified sensitive lines to be potential GC diagnostic features until this further work is completed.

We quantify the overall sensitivity of a feature by measuring the equivalent width (EW) of the line within $\lambda_0 \pm \Delta\lambda_{CW}$, and fit either a first or second order polynomial to the EWs as a function of age or metallicity. The polynomial order of the fit is

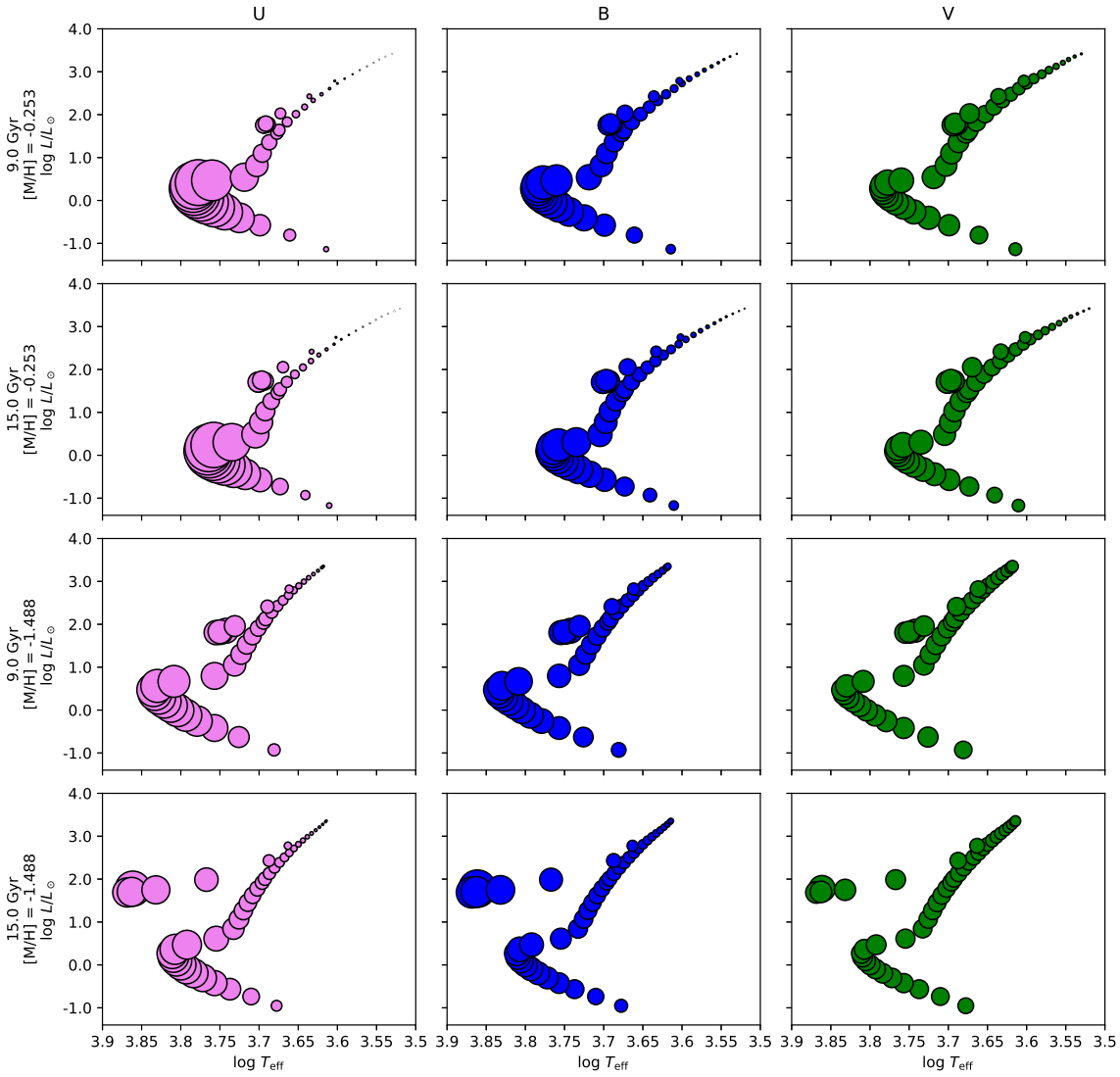

Figure 3.25 Relative contributions to total cluster flux by individual cluster members for four different synthetic clusters with $\alpha = +0.4$. Rows have constant cluster parameters, columns are constant photometric waveband. *Top row:* cluster age = 9.0 Gyr, [M/H] = -0.253, *upper-middle row:* cluster age = 15.0 Gyr, [M/H] = -0.253, *lower-middle row:* cluster age = 9.0 Gyr, [M/H] = -1.488, *bottom row:* cluster age = 15.0 Gyr, [M/H] = -1.488. *Left column: U*-band, *middle column: B*-band, *right column: V*-band. Radii of markers are proportional to the percentage of total cluster flux emitted in that waveband by the representative star.

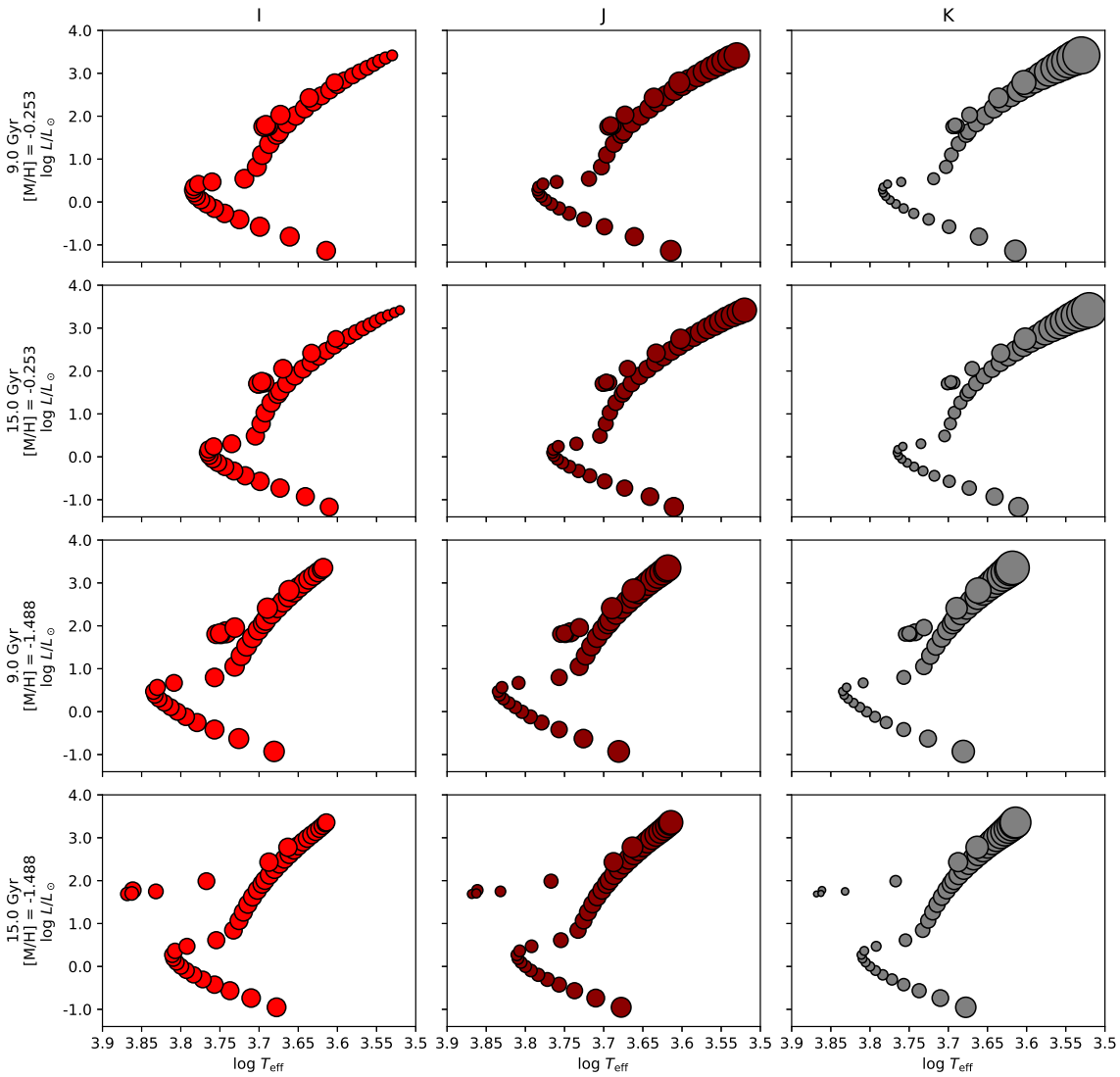

Figure 3.26 Same as Figure 3.25, but for *Left column: I*-band, *middle column: J*-band, and *right column: K*-band filters.

determined in each case by whichever function minimizes the residuals of the fit.

3.4.2 Results

Identification

We have identified 60 lines sensitive to cluster age and 38 lines sensitive to cluster metallicity in the range λ = 12000 to 22000 Å, for 14 different atomic species: Al I, Ca I, C I, Co I, Cr I, Fe I, Fe II, Mg I, Mn I, Na I, Ni I, S I, Si I, and Ti I. The total number of lines for each species is presented in Table 3.5. For potential cluster age diagnostics, the species with the greatest number of identified lines is Fe I, with 27 age sensitive lines, followed by Ca I, with eight sensitive lines. For potential metallicity diagnostics, the most prevalent species is Ca I, with nine metallicity sensitive lines, followed by Fe I, with seven sensitive lines. In general, the strengths of spectral lines in our IL spectra were found to be significantly more sensitive to cluster metallicity than to cluster age, with $\frac{\partial}{\partial Age}(\frac{\partial F_\lambda}{\partial \lambda})_{max} = 0.007$ and $\frac{\partial}{\partial [M/H]}(\frac{\partial F_\lambda}{\partial \lambda})_{max} = 0.230$. Figure 3.27 displays the Ca I λ19314.4964 line of scaled-solar IL spectra at varying model ages and metallicities.

Tables 3.6 and 3.7 display the full lists of age and metallicity sensitive features, respectively, indicating if a feature was found to be sensitive in NLTE or LTE spectra, and for scaled-solar or α-enhanced clusters. All lines are listed in vacuum wavelengths. Our identification process did not flag any age sensitive features for $[M/H]$ = -0.253 or -0.353, after having removed blended features and discarded atomic species iden-

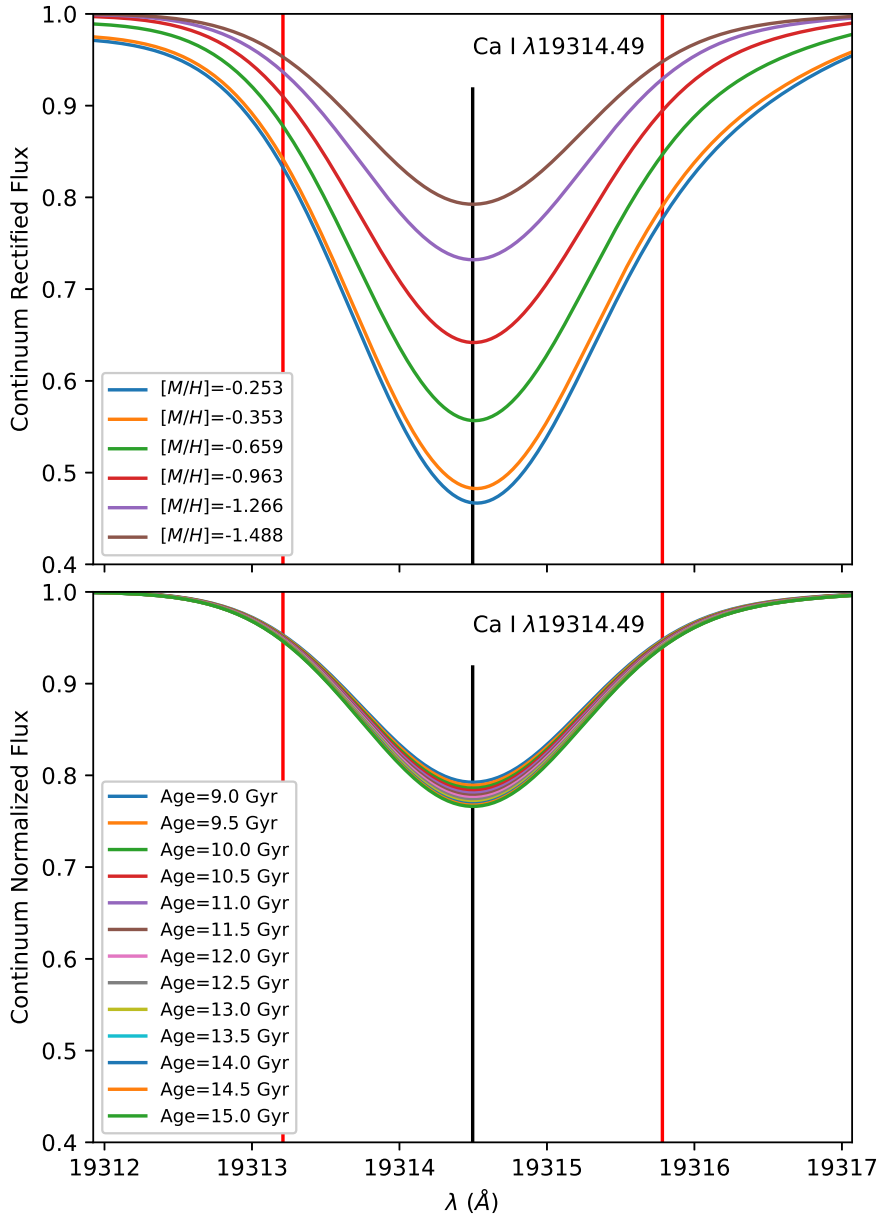

Figure 3.27 The Ca I λ19314.4964 line of scaled-solar IL spectra at varying model ages and metallicities. Vertical black line indicates line center of the PHOENIX identification tag, while red lines indicate the characteristic width of spectral lines for R $\sim$ 30000. *Top* - Model age = 9.0 Gyr. *Bottom* - Model $[M/H]$ = -1.488.

tifications located more than 0.2 Å from line center. All of the lines identified for $[M/H]$ = -0.659 are from α-enhanced IL spectra, with the exception of the Cr I λ16903.5128 line, which was also found to be sensitive to age in the LTE scaled-solar IL spectrum. However, lines identified for $[M/H]$ = -0.963, -1.266, and -1.488 were found in both scaled-solar and α-enhanced IL spectra. These $[M/H]$ = -0.659 α-enhanced IL spectra were generated from stellar spectra equivalent to $[Fe/H]$ = -1.009 for non-α elements. We identify the greatest number of age sensitive lines for clusters of $[M/H] \approx$ -0.9 $\pm$ 0.3, suggesting a peak in IL spectra age sensitivity around $[M/H] \approx$ -1.0. We do not identify any lines that are consistently sensitive to age for both NLTE and LTE, scaled-solar and α-enhanced compositions, across all cluster metallicities, suggesting cluster age is a secondary parameter in determining line strength in IL IR spectra. Overall, we observe a slight trend of age sensitive lines identified in NLTE IL spectra to occur at higher metallicities than lines identified in LTE.

Table 3.4 Properties of selected Galactic GCs. Cluster IDs, positions, M_V, $E(B-V)$, $U-B$, $B-V$, and $V-I$ taken from Harris 1996 (2010 ed). Age and $[Fe/H]$ from Forbes (2010). Other colours derived from magnitudes from Skrutskie *et al.* (2006), except [a] which is from Forbes *et al* (2008). No J magnitude data was included in the reference for NGC 5139.

ID	Age (Gyr)	$[Fe/H]$	M_V	$E(B-V)$	$U-B$	$B-V$	$V-I$	$V-J$	$V-K$	$J-K$
NGC 104	13.06	-0.78	-9.42	0.040	0.370	0.880	1.140	1.801	2.547	0.746
NGC 5139	11.52	-1.35	-10.26	0.120	0.190	0.790	1.050		4.480[a]	
NGC 6205	11.65	-1.33	-8.55	0.020	-0.020	0.680	0.860	1.348	1.946	0.598

Table 3.5 Numbers of atomic IR sensitive lines for cluster age and metallicity, broken down by atomic species.

Species	# of Age Sensitive Lines	# of $[M/H]$ Sensitive Lines
Al I	1	5
Ca I	8	9
C I	6	1
Co I	1	—
Cr I	1	2
Fe I	27	7
Fe II	1	—
Mg I	1	2
Mn I	1	4
Na I	—	1
Ni I	1	—
S I	3	1
Si I	4	3
Ti I	5	3
Total	60	38

Table 3.6: Globular cluster age sensitve lines. Column headings indicate at which metallicity values a line was found to be sensitive to cluster age. The letters N and L indicate that the line was sensitive to age in NLTE and LTE spectra, respectively. The subscript symbols $_\odot$ and $_\alpha$ indicate scaled-solar and α-enhanced clusters, respectively. Lines are listed with vacuum wavelenghts.

Species	λ_0 (Å)	$[M/H]$ -0.253	$[M/H]$ -0.353	$[M/H]$ -0.659	$[M/H]$ -0.963	$[M/H]$ -1.266	$[M/H]$ -1.488
Al I	15972.6514	···	···	N_α, L_α	···	···	···
Ca I	14469.2903	···	···	N_α, L_α	···	···	···
Ca I	16543.1061	···	···	N_α, L_α	$N_\odot$, $L_\odot$	$L_\odot$	···
Ca I	19314.4964	···	···	···	···	$N_{\odot,\alpha}$, $L_\odot$	$N_{\odot,\alpha}$, $L_{\odot,\alpha}$
Ca I	19458.2943	···	···	···	···	$N_{\odot,\alpha}$, $L_\odot$	$N_{\odot,\alpha}$, $L_{\odot,\alpha}$
Ca I	19511.0685	···	···	···	···	$N_\odot$, $L_\odot$	$N_\odot$, $L_{\odot,\alpha}$
Ca I	19782.1678	···	···	···	···	···	$N_{\odot,\alpha}$, $L_\odot$
Ca I	19867.6130	···	···	N_α	N_α	$N_{\odot,\alpha}$, $L_\odot$	$N_{\odot,\alpha}$, $L_{\odot,\alpha}$
Ca I	19922.6329	···	···	···	$N_\odot$, $L_\odot$	$N_\odot$, $L_\odot$	···
C I	13919.2393	···	···	N_α, L_α	N_α, $L_{\odot,\alpha}$	···	···
C I	13927.8510	···	···	N_α, L_α	···	···	···
C I	13936.5238	···	···	N_α, L_α	···	···	···
C I	14626.5518	···	···	N_α, L_α	$N_{\odot,\alpha}$, $L_{\odot,\alpha}$	···	···
C I	17351.1442	···	···	N_α, L_α	···	···	···
C I	17432.9039	···	···	N_α, L_α	···	···	···
Co I	14614.4095	···	···	N_α, L_α	$N_{\odot,\alpha}$, $L_{\odot,\alpha}$	···	···
Cr I	16903.5128	···	···	N_α, $L_{\odot,\alpha}$	$N_\odot$, $L_\odot$	$L_\odot$	···
Fe I	13951.8275	···	···	N_α, L_α	$L_\odot$	···	···
Fe I	13956.8162	···	···	N_α, L_α	$N_{\odot,\alpha}$, $L_{\odot,\alpha}$	N_α, $L_{\odot,\alpha}$	···
Fe I	14519.1286	···	···	N_α, L_α	$N_{\odot,\alpha}$, $L_{\odot,\alpha}$	···	···
Fe I	14645.2491	···	···	···	$N_\odot$, $L_\odot$	···	···
Fe I	14664.7769	···	···	···	$N_\odot$, $L_\odot$	$L_\odot$	···
Fe I	14670.3800	···	···	···	$N_\odot$, $L_\odot$	$L_\odot$	···
Fe I	14698.7799	···	···	N_α, L_α	$N_\odot$, $L_\odot$	···	···
Fe I	14713.4272	···	···	N_α, L_α	N_α, $L_{\odot,\alpha}$	$L_\odot$	···
Fe I	15068.9975	···	···	N_α, L_α	···	···	···
Fe I	15282.5550	···	···	···	$N_\odot$, $L_\odot$	$L_\odot$	···
Fe I	15287.8284	···	···	N_α, L_α	···	···	···
Fe I	15388.3077	···	···	L_α	L_α	···	···
Fe I	15423.5564	···	···	N_α, L_α	$N_{\odot,\alpha}$, $L_{\odot,\alpha}$	N_α, $L_{\odot,\alpha}$	L_α
Fe I	15438.8024	···	···	N_α, L_α	N_α, L_α	···	···
Fe I	15902.0013	···	···	N_α, L_α	$N_{\odot,\alpha}$, $L_{\odot,\alpha}$	N_α, $L_{\odot,\alpha}$	L_α
Fe I	16030.4168	···	···	···	$L_\odot$	···	···
Fe I	16030.9779	···	···	L_α	···	···	···

Species	λ_0 (Å)	$[M/H]$ -0.253	$[M/H]$ -0.353	$[M/H]$ -0.659	$[M/H]$ -0.963	$[M/H]$ -1.266	$[M/H]$ -1.488
Fe I	16078.8697	···	···	L_α	L_α	L_α	L_α
Fe I	16388.6163	···	···	L_α	···	···	···
Fe I	16414.8755	···	···	N_α, L_α	···	···	···
Fe I	16442.0152	···	···	L_α	···	···	···
Fe I	16528.3644	···	···	N_α	$N_{\odot,\alpha}$, $L_\odot$	N_α, $L_\odot$	···
Fe I	16913.8863	···	···	N_α, L_α	$N_{\odot,\alpha}$, $L_{\odot,\alpha}$	N_α, $L_{\odot,\alpha}$	···
Fe I	17189.0741	···	···	N_α, L_α	···	···	···
Fe I	17317.8186	···	···	N_α, L_α	$N_{\odot,\alpha}$, $L_{\odot,\alpha}$	···	···
Fe I	17823.4311	···	···	N_α	···	···	···
Fe I	18028.4658	···	···	L_α	···	···	···
Fe II	17418.7628	···	···	N_α, L_α	···	···	···
Mg I	14604.9935	···	···	N_α, L_α	N_α, L_α	N_α, L_α	···
Mn I	12903.2991	···	···	···	···	N_α	N_α
Ni I	13984.2963	···	···	N_α, L_α	$N_\odot$, $L_\odot$	$L_\odot$	···
S I	15426.4872	···	···	···	···	$L_\odot$	···
S I	15474.0431	···	···	N_α, L_α	L_α	···	···
S I	16452.5250	···	···	N_α, L_α	N_α, L_α	L_α	···
Si I	13921.9399	···	···	N_α, L_α	$L_\odot$	···	···
Si I	15391.2702	···	···	L_α	L_α	···	···
Si I	16459.0251	···	···	···	···	$N_{\odot,\alpha}$, $L_{\odot,\alpha}$	$N_{\odot,\alpha}$, $L_{\odot,\alpha}$
Si I	16755.6407	···	···	···	$L_\odot$	···	···
Ti I	13932.3435	···	···	N_α, L_α	N_α, $L_{\odot,\alpha}$	N_α, $L_{\odot,\alpha}$	···
Ti I	13976.8167	···	···	N_α, L_α	$N_{\odot,\alpha}$, $L_{\odot,\alpha}$	N_α, $L_{\odot,\alpha}$	···
Ti I	15151.9538	···	···	L_α	L_α	L_α	···
Ti I	15431.1853	···	···	L_α	···	···	···
Ti I	21903.3565	···	···	N_α	$N_\odot$, $L_\odot$	···	···

Table 3.7: Similar to Table 3.6, but for features sensitive to cluster metallicity. Column headings indicate at which age a line was found to be sensitive to metallicity. Only whole number age sampling points are included for ease of viewing.

Species	λ_0 (Å)	Age = 9.0 Gyr	Age = 10.0 Gyr	Age = 11.0 Gyr	Age = 12.0 Gyr	Age = 13.0 Gyr	Age = 14.0 Gyr	Age = 15.0 Gyr
Al I	13126.9979	N_α	N_α	N_α	N_α	N_α	N_α	N_α
Al I	13154.3502	$N_{\odot,\alpha}$	$N_{\odot,\alpha}$	$N_{\odot,\alpha}$	$N_{\odot,\alpha}$	$N_{\odot,\alpha}$	$N_{\odot,\alpha}$	$N_{\odot,\alpha}$
Al I	16767.9355	$L_\odot$	$L_\odot$	$L_\odot$	$L_\odot$	$L_\odot$	$L_\odot$	$L_\odot$
Al I	21098.7839	$L_{\odot,\alpha}$	L_α	...	...	...	...	...
Al I	21169.5304	N_α	N_α	N_α	N_α	N_α	N_α, $L_{\odot,\alpha}$	N_α, $L_\odot$
Ca I	16155.1756	$L_{\odot,\alpha}$	$L_{\odot,\alpha}$	$L_{\odot,\alpha}$	$L_{\odot,\alpha}$	$L_{\odot,\alpha}$	$L_{\odot,\alpha}$	$L_{\odot,\alpha}$
Ca I	16543.1061	$L_\odot$	$L_\odot$	$L_\odot$	$L_\odot$	$L_\odot$	$L_\odot$	$L_{\odot,\alpha}$
Ca I	19314.4964	$N_{\odot,\alpha}$, $L_{\odot,\alpha}$	N_α, $L_\odot$	N_α	N_α	N_α	...	...
Ca I	19458.2943	$N_{\odot,\alpha}$, $L_{\odot,\alpha}$	$N_{\odot,\alpha}$, $L_{\odot,\alpha}$	$N_{\odot,\alpha}$, $L_{\odot,\alpha}$	$N_{\odot,\alpha}$, $L_{\odot,\alpha}$	$N_{\odot,\alpha}$, $L_{\odot,\alpha}$	$N_{\odot,\alpha}$, L_α	$N_{\odot,\alpha}$, L_α
Ca I	19511.0685	$N_\odot$, $L_{\odot,\alpha}$	$N_\odot$, $L_{\odot,\alpha}$	$N_\odot$, $L_{\odot,\alpha}$	$N_\odot$, $L_{\odot,\alpha}$	$N_\odot$, $L_{\odot,\alpha}$	$N_\odot$, $L_{\odot,\alpha}$	$N_\odot$, $L_{\odot,\alpha}$
Ca I	19858.5157	$N_{\odot,\alpha}$, $L_{\odot,\alpha}$	$N_{\odot,\alpha}$, $L_{\odot,\alpha}$	$N_{\odot,\alpha}$, $L_{\odot,\alpha}$	$N_{\odot,\alpha}$, $L_{\odot,\alpha}$	$N_{\odot,\alpha}$, $L_{\odot,\alpha}$	$N_{\odot,\alpha}$, $L_{\odot,\alpha}$	$N_{\odot,\alpha}$, $L_{\odot,\alpha}$
Ca I	19867.6130	$N_{\odot,\alpha}$, L_α	$N_{\odot,\alpha}$, $L_{\odot,\alpha}$	$N_{\odot,\alpha}$, $L_{\odot,\alpha}$	$N_{\odot,\alpha}$, $L_{\odot,\alpha}$	$N_{\odot,\alpha}$, $L_{\odot,\alpha}$	$N_{\odot,\alpha}$, $L_{\odot,\alpha}$	$N_{\odot,\alpha}$, $L_{\odot,\alpha}$
Ca I	19939.1655	$N_{\odot,\alpha}$, $L_{\odot,\alpha}$	$N_{\odot,\alpha}$, $L_{\odot,\alpha}$	$N_\odot$, $L_{\odot,\alpha}$	$N_\odot$, $L_{\odot,\alpha}$	$N_\odot$, $L_{\odot,\alpha}$	$N_\odot$, $L_{\odot,\alpha}$	$N_\odot$, $L_{\odot,\alpha}$
Ca I	19967.2796	N_α, $L_{\odot,\alpha}$	N_α, $L_{\odot,\alpha}$	N_α, $L_{\odot,\alpha}$	N_α, $L_{\odot,\alpha}$	N_α, $L_{\odot,\alpha}$	N_α, $L_{\odot,\alpha}$	N_α, $L_{\odot,\alpha}$
C I	14783.6522	...	...	L_α	L_α	L_α	L_α	L_α
Cr I	16903.5128	$L_{\odot,\alpha}$	$L_{\odot,\alpha}$	$L_{\odot,\alpha}$	$L_{\odot,\alpha}$	$L_{\odot,\alpha}$	$L_{\odot,\alpha}$	$L_{\odot,\alpha}$
Cr I	18589.1938	...	...	...	...	$L_\odot$	$L_\odot$	$L_\odot$
Fe I	14713.4272	...	...	...	...	$L_\odot$	$L_\odot$	$L_\odot$
Fe I	16069.1208	...	...	...	...	...	$L_\odot$	$L_\odot$
Fe I	16106.8069	$L_\odot$	$L_\odot$	$L_\odot$	$L_\odot$	$L_\odot$	$L_\odot$	$L_\odot$
Fe I	16229.6687	...	L_α	L_α	L_α	L_α	L_α	L_α
Fe I	16586.5556	...	...	...	...	...	...	$L_\odot$
Fe I	17317.8186	...	$L_\odot$	$L_\odot$	...	...	...	...

Species	λ_0 (Å)	Age = 9.0 Gyr	Age = 10.0 Gyr	Age = 11.0 Gyr	Age = 12.0 Gyr	Age = 13.0 Gyr	Age = 14.0 Gyr	Age = 15.0 Gyr
Fe I	18992.1916	L_α	L_α	...	...	...	...	...
Mg I	18902.7786	N_α, L_α	N_α, L_α	N_α, L_α	L_α	L_α	L_α	L_α
Mg I	18926.9234	L_α	L_α	...	...	...	...	...
Mn I	12903.2991	N_α	N_α	N_α	N_α	N_α	N_α	N_α
Mn I	13630.4807	$N_{\odot,\alpha}$	$N_{\odot,\alpha}$	$N_{\odot,\alpha}$	$N_{\odot,\alpha}$	$N_{\odot,\alpha}$	$N_{\odot,\alpha}$	$N_{\odot,\alpha}$
Mn I	13646.6697	$N_\odot$	$N_\odot$	$N_\odot$	$N_\odot$	$N_\odot$	$N_\odot$	...
Mn I	13867.9858	N_α	N_α	N_α	N_α	N_α	N_α	N_α
Na I	18470.5290	...	...	...	...	...	L_α	L_α
S I	15474.0431	...	L_α	L_α	L_α	L_α	L_α	L_α
Si I	16459.0251	L_α	...	...	...	...	...	...
Si I	17230.2740	L_α	L_α	L_α	L_α	L_α	L_α	...
Si I	17628.1393	$L_\odot$	$L_\odot$	...	...	...	...	...
Ti I	15339.0365	...	...	...	$L_\odot$	$L_\odot$	$L_\odot$	$L_\odot$
Ti I	21788.8723	N_α	N_α	N_α	N_α	N_α	N_α	N_α
Ti I	21903.3565	$N_\odot$	$N_\odot$	$N_\odot$	$N_\odot$, $L_\odot$	$N_\odot$, $L_\odot$	$N_\odot$, $L_\odot$	$N_\odot$, $L_\odot$

A single line has been identified that is consistently sensitive to metallicity at all ages, for all NLTE and LTE, scaled-solar and α-enhanced combinations; the Ca I λ19858.5157 line. Several other Ca I lines show a strong sensitivity to metallicity, namely the λ19458.2943, λ19511.0685, λ19867.6130, λ19939.1655, and λ19967.2796 lines, but did not meet the sensitivity criteria for one or more of the above combinations of composition and modelling treatment, most often the NLTE α-enhanced IL spectra. Overall, metallicity sensitive lines have a roughly even distribution across cluster ages, with no clear age preference. We observe no discernible difference in the NLTE and LTE distributions of metallicity sensitive lines across cluster ages. A total of 12 lines were identified that serve as both potential metallicity and potential age diagnostics. They include five Ca I lines, two Fe I, and one each of Cr I, Mn I, S I, Si I, and Ti I, as listed in Table 3.8.

Table 3.8 Spectral IL IR lines that are sensitive to both cluster age and metallicity.

Species	λ_0 (Å)	Species	λ_0 (Å)	Species	λ_0 (Å)
Ca I	16543.1061	Ca I	19867.6130	Mn I	12903.2991
Ca I	19314.4964	Cr I	16903.5128	S I	15474.0431
Ca I	19458.2943	Fe I	14713.4272	Si I	16459.0251
Ca I	19511.0685	Fe I	17317.8186	Ti I	21903.3565

Equivalent Widths

Continuing the investigation of the age-metallicity degeneracy of globular clusters, we have taken two sample spectral lines, the Fe I λ17317.8186 line and the

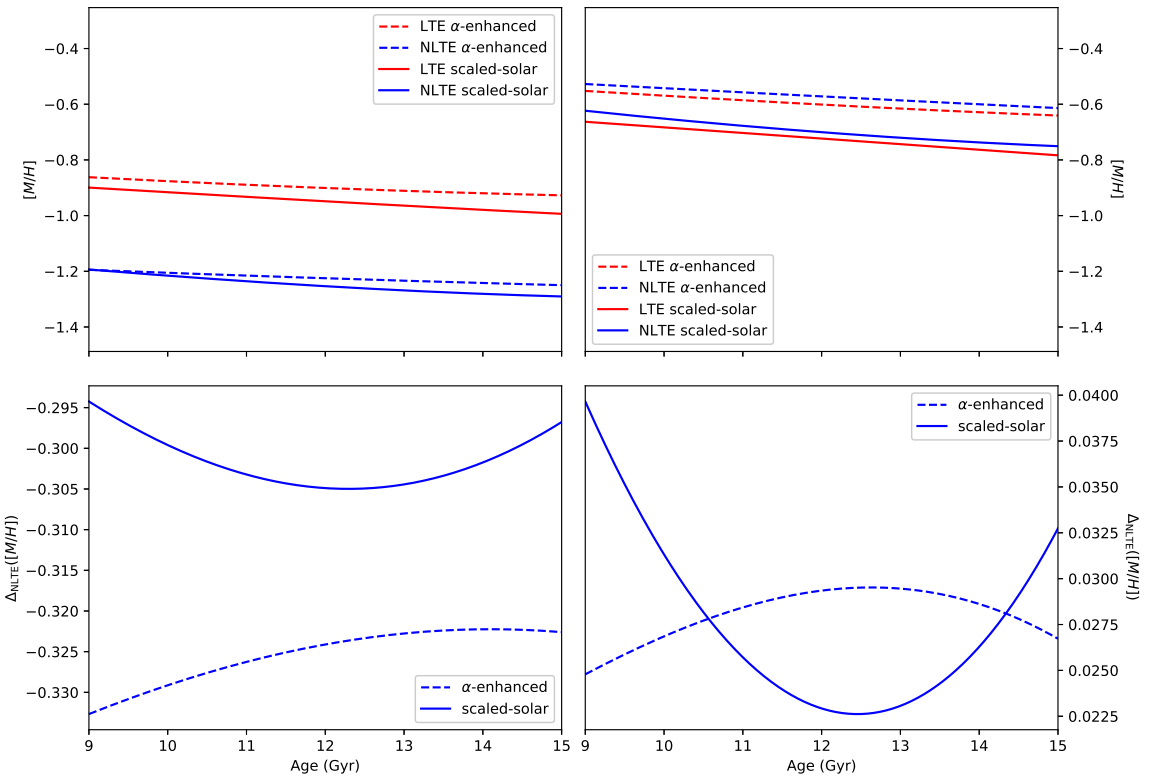

Figure 3.28 Degenerate age-metallicity combinations that produce EWs of 0.50 Å for the Ca I λ19314.4964 line (left) and 0.25 Å for the Fe I λ17317.8186 line (right), and associated $\Delta_{\rm NLTE}$ values (bottom).

Ca I λ19314.4964 line, and fit their EWs with a fourth order polynomial surface of the same form as equation 4.4. To illustrate the example, we assume EWs of 0.25 and 0.50 Å for the lines, respectively, and continue with the analysis in a similar manner as in Section 3.3.3, substituting EW for colour index. Figure 3.28 displays the results. For this selection of lines and EWs, we see that if an age is assumed from an independent source, NLTE effects can change the derived metallicity by $-0.332 \lesssim \Delta_{\rm NLTE}([M/H]) \lesssim 0.040$. We note that there is no degeneracy observed between NLTE and LTE at constant metallicity for any value in our parameter space.

In Figures 3.29 and 3.30 we present the $\Delta_{\rm NLTE}(EW)$ values over our full parameter

space for the same two sample spectral lines as above. Contour plots for the remaining spectral lines in our sample identified as sensitive in both LTE and NLTE spectra are included in Appendix A. Differences in EW caused by NLTE effects fall in the range $-0.15 \leq \Delta_{\rm NLTE}(EW) \leq 0.25$ Å . In general, $\Delta_{\rm NLTE}(EW)$ becomes relatively insensitive to age for features at wavelengths longer than $\lambda \approx 18000$ Å, regardless of abundance distribution. The difference may be either positive, negative, or both for an individual line, depending on the age and $[M/H]$ of the cluster, but for a given species $\Delta_{\rm NLTE}(EW)$ is generally seen to exhibit larger negative values at shorter wavelengths and larger positive values at longer wavelengths. McWilliam & Bernstein (2008) demonstrate that a trend in EW is indicative of an incorrect microturbulent velocity distribution within the population, suggesting that our selection of two discrete values may be responsible. Additionally, we observe a loose trend that features at $\lambda \lesssim 15000$ Å, $\Delta_{\rm NLTE}(EW)$ decreases with increasing $[M/H]$, and at $\lambda \gtrsim 18000$ Å, $\Delta_{\rm NLTE}(EW)$ increases with increasing $[M/H]$.

3.5 SUMMARY

We have expanded our library of α-enhanced stellar atmospheric models and synthetic spectra presented in Paper I to five new metallicities and computed a complimentary library of scaled-solar compositions. In addition to this, we have prepared a corresponding library of synthetic continua, for a total of 6600 each of synthetic spectra and continua. We leveraged this expanded library to generate new IL spectra

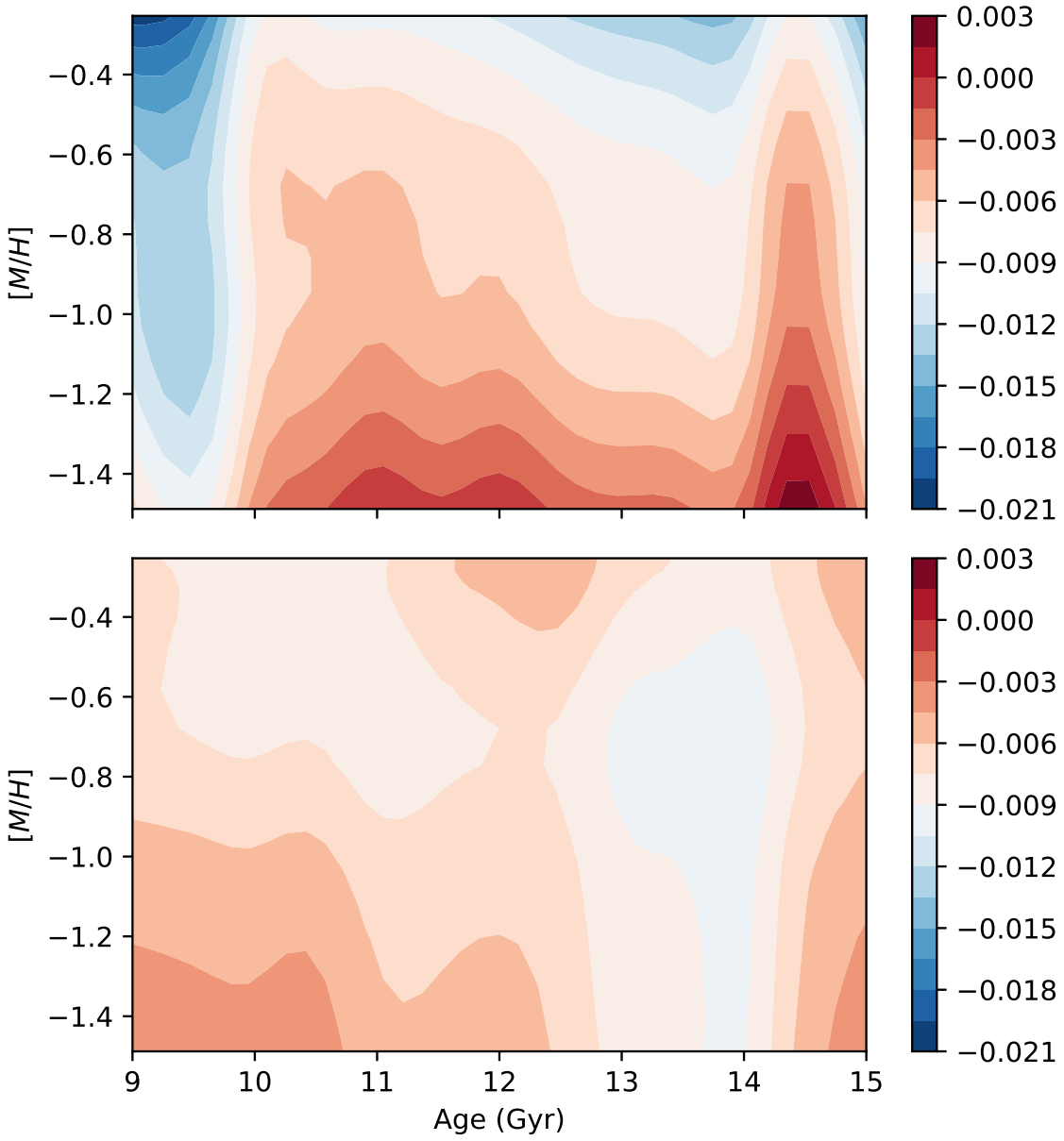

Figure 3.29 Contour plot of $\Delta_{\rm NLTE}(EW)$ for the Fe I λ17317.8186 line over the full parameter space of our IL spectra library. The contours sample $\Delta_{\rm NLTE}(EW)$ every 0.0015 Å . *Top*: Scaled-solar spectra. *Bottom*: α-enhanced spectra.

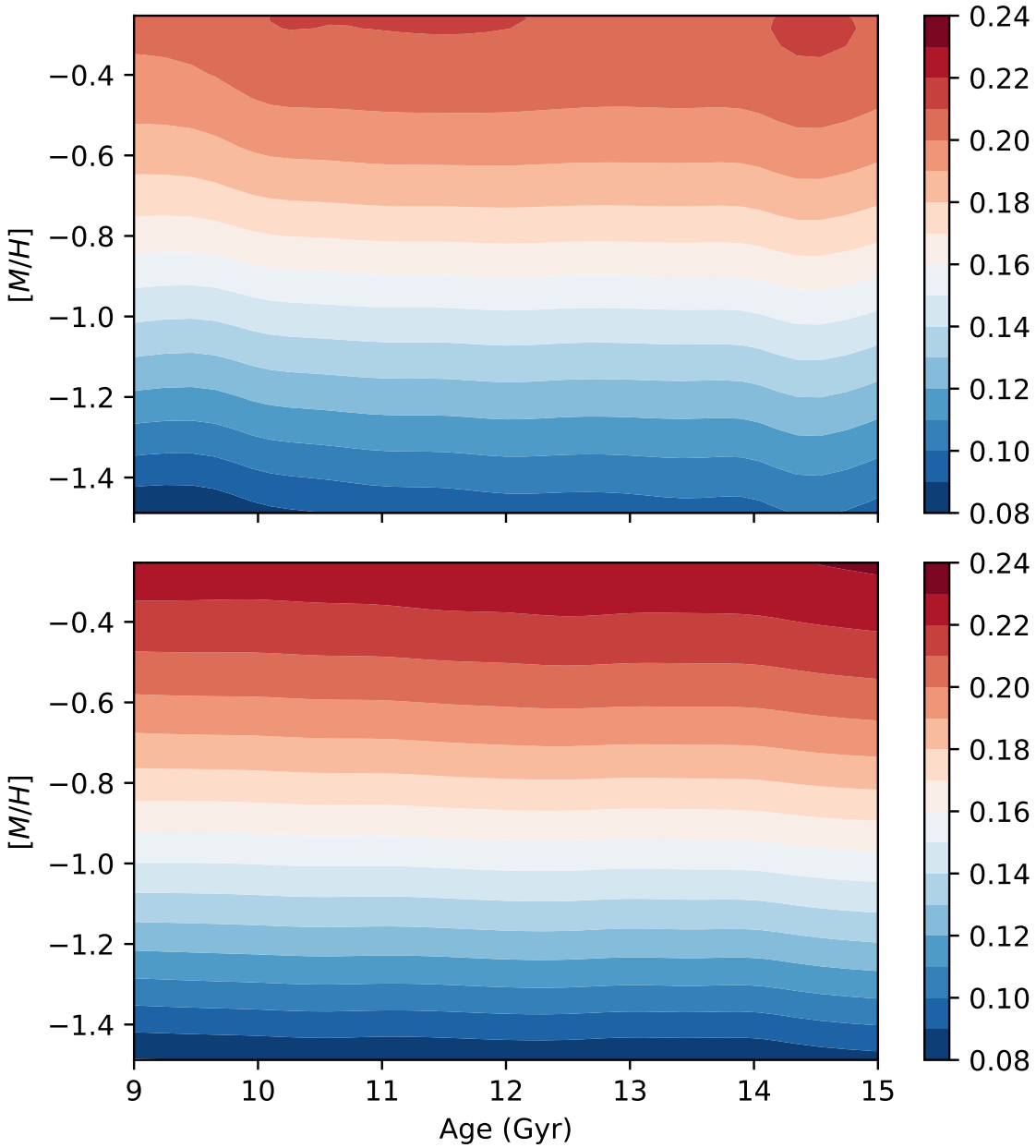

Figure 3.30 Similar to Figure 3.29, but for the Ca I λ19314.4964 line, with contours sampling $\Delta_{\rm NLTE}(EW)$ every 0.01 Å .

and continua for new isochrone metallicities, linearly interpolated in the metallicity and α-enhancement dimensions, and compute a set of IL spectra and continua from convective core overshoot isochrones; a total of 910 each of IL spectra and continua, and 105 core overshoot IL spectra and continua.

For this expanded collection of IL spectra, photometric colours in six indices ($U-B$, $B-V$, $V-I$, $V-J$, $V-K$, and $J-K$) were shown to exhibit the following properties:

1. Integrated light colours of α-enhanced clusters are bluer than scaled-solar clusters by up to 0.15 mag

2. colours redden with ages up to 13.0 Gyr; older than 13.0 Gyr, clusters with $[M/H] > -1.0$ continue to redden, while clusters with $[M/H] < -1.0$ reverse and get bluer with age

3. colours redden with increasing metallicity

4. NLTE colours are bluer than LTE by up to 0.06 mag, except for $J-K$ values of α-enhanced clusters, where NLTE colours are redder than LTE

5. As a function of age, $\Delta_{\rm NLTE}(colour)$ values are constant within uncertainty, except for $\Delta_{\rm NLTE}(U-B)$ which increases with age

6. As a function of metallicity, $\Delta_{\rm NLTE}(colour)$ increase, except for $\Delta_{\rm NLTE}(B-V)$ and scaled-solar $\Delta_{\rm NLTE}(J-K)$ which peak at $[M/H]$ = -0.963

7. Core overshoot has no impact on IL colours within uncertainty, with the exception of $[M/H]$ = -0.506, -0.659, and -0.811 α-enhanced clusters, where core overshoot reddens $U-B$ by up to 0.05 mag and other colours by up to 0.015 mag

We note that bluer α-enhanced colours have previously been demonstrated both for single stars (Cassisi *et al*, 2004), and for SSPs (Coelho *et al.*, 2007). Coelho *et al.* also demonstrate the reddening of colours with cluster age, but do not compute models at low enough metallicity to investigate the old age blueing we have observed for metal poor clusters. Kučinskas *et al* (2006) have demonstrated bluer NLTE colours for late type giants, but do not observe the redder NLTE colours for $J-K$ values that we find here.

Our investigation of the age-metallicity degeneracy led us to generate curves which map combinations of age and metallicity that reproduce colour values of three Galactic GCs according to equation 4.4. These curves exhibit the following properties:

1. $U-B$ colours produce values of $|\Delta_{\rm NLTE}([M/H])| \leq 0.15$ dex, while all other indices produce $|\Delta_{\rm NLTE}([M/H])| \leq 0.06$ dex

2. NLTE produces more metal rich curves as functions of age than LTE, with the exception of the α-enhanced $J-K$ curves

3. With the exception of $B-V$, values of $\Delta_{\rm NLTE}([M/H])$ increase with decreasing index wavelength

4. Shorter wavelength indices show $\Delta_{\rm NLTE}([M/H], \alpha) > \Delta_{\rm NLTE}([M/H], {\rm solar})$, while longer wavelength indices show the reverse, crossing over at $V - I$

5. As functions of $[M/H]$, the curves show $-2.0 < \Delta_{\rm NLTE}(age) < 2.0$, except for $U - B$ and the NGC 104 $V - I$ curves

6. For $B - V$ and $V - I$, $\Delta_{\rm NLTE}(age)$ is double valued, with approximately equal magnitudes and opposite signs

7. Derived metallicities of the three clusters in our sample were shown to increase by up to 0.05 dex when modelled in NLTE

We have identified a total of 86 lines sensitive to cluster age or metallicity, 12 of which are sensitive to both. These lines represent 14 different atomic species, the majority of which are Fe I and Ca I lines. The strength of features was found to be significantly more sensitive to $[M/H]$ than age, showing a much larger change in both EW and depth at line center. Differences in EW appear to be insensitive to age for $\lambda \gtrsim 18000$ Å, and $\Delta_{\rm NLTE}(EW)$ is negative at shorter wavelengths and positive at longer wavelengths for most species at most metallicities. We observe a trend that for $\lambda \lesssim 15000$ Å, $\Delta_{\rm NLTE}(EW)$ decreases with increasing $[M/H]$, and for $\lambda \gtrsim 18000$ Å, $\Delta_{\rm NLTE}(EW)$ increases with increasing $[M/H]$.

4 Optical Line Sensitivity and Comparison with Observed Galactic Globular Clusters

4.1 INTRODUCTION

Globular cluster (GC) abundance analysis is one of the most important tools for probing galaxy evolution history. While high-resolution chemical abundance analysis of individual stars in Galactic GCs has been pursued for 40 years (e.g., Cohen (1978); Pilachowski, Canterna, & Wallerstein (1980)), it is only recently that the technology and methodology have advanced to the point where extragalactic GCs, whose individual stars are too faint to be resolved, may be studied for similar purposes using high-resolution integrated light (IL) spectra (McWilliam & Bernstein, 2008; Colucci *et al.*, 2009). Previous estimates of extragalactic GC abundances have been limited to broadband photometric colours (e.g., Forte, Strom, & Strom (1981); Geisler, Lee, & Kim (1996); Goudfrooij *et al.* (2006)), and low-resolution Lick indices (e.g., Faber *et al.* (1985); Worthey *et al.* (1994); Trager (2004)).

Regardless of which observational technique one uses when deriving parameters of observed GCs, it is important to know which observables or features can serve as diagnostics of those parameters. For example, it is of no use to measure the equivalent width (EW) of a spectral line if it does not depend on the metallicity ($[M/H]$) of a

cluster, nor the B-V colour index if it does not depend on the age. Previous GC IL spectral analysis works have presented lists of many spectral lines that can serve as age and metallicity diagnostics (e.g., Colucci *et al.* (2009); Sakari *et al.* (2013)). Even if a feature is sensitive to a parameter of interest, it may not be sensitive over all possible values that the parameter may take. If an Fe I line saturates at $[M/H] = -1.0$, it would not be a good diagnostic for clusters more metal-rich than this. In Young & Short (2018), hereafter Paper II, we investigate the sensitivity of IR spectral features to cluster ages and metallicities, and find that the majority of identified features are sensitive only over a subset of the possible values, with most showing greater age sensitivity in more metal poor clusters, and greater metallicity sensitivity in younger clusters.

Nearly all IL analyses to date has been performed assuming local thermodynamic equilibrium (LTE) when modelling stellar atmospheres. For individual stars, abundances inferred from non-local thermodynamic equilibrium (NLTE) modelling can differ significantly (up to 0.3 dex) from those of LTE modelling (Short & Hauschildt, 2009). Hence, it seems reasonable that abundances derived from IL spectra would also experience NLTE effects. Indeed, Lapenna *et al.* (2014) and Mucciarelli *et al.* (2015) have demonstrated the presence of NLTE effects in AGB stars in the GC 47 Tuc, and we have shown in Young & Short (2017), hereafter Paper I, and in Paper II, that assuming LTE may introduce an error in the inferred age of a GC of more than 2.0 Gyr for a given metallicity, and in the inferred metallicity of more than 0.05

dex for a given age.

In Papers I and II, we have focused exclusively on differentials in modelling techniques and assumptions, highlighting the effects NLTE has on derived cluster parameters and comparing to the magnitude of the effect from adopting or neglecting core-overshoot in the underlying isochrone models to assess the significance. Here we take the next step by comparing our models with observed IL spectra of GCs. Colucci, Bernstein & McWilliam (2017), hereafter CBM17, have recently made publicly available a set of 12 observed GC high-resolution IL spectra used in their IL modelling studies. These spectra present a valuable opportunity for a practical test of our differential techniques.

4.1.1 Current Work

Our primary goal is to investigate the effects of modelling the opacity sources of stellar atmospheres and spectra in NLTE on the IL spectra of synthetic GCs, as well as on the ages and metallicities derived from them. We identify optical spectral features that may potentially be used as diagnostics of cluster age, metallicity, and degree of α-enhancement guided by both LTE and NLTE spectra. We also use our library of synthetic GC IL spectra to derive ages and metallicities, focusing on the differences between NLTE and LTE, of the 11 Galactic and one extragalactic GCs of CBM17 by fitting spectral line profiles of the identified sensitive lines, and over 600 diagnostic lines from the literature. The production of the synthetic spectra using the

PHOENIX atmospheric modelling and spectrum synthesis code is detailed in Paper I, and the expanded parameters of the library are described in Paper II.

4.2 SPECTRAL LINE SENSITIVITY

4.2.1 Analysis

Spectral lines in the wavelength range $\lambda = 4000$ to 9000 Å are investigated to find those which are sensitive to GC age or metallicity. We consider a line to be sensitive to a parameter if it follows two trends as the parameter is adjusted. The depth at line center, $F_{\lambda_0}/F_\lambda^C$, where λ_0 is the wavelength at line center and F_λ^C is the adjacent continuum flux, must change proportionally to the parameter of interest over the full range, and it must change by a detectable amount. Our goal is to identify features where F_{λ_0} varies consistently with $[M/H]$ or age in a way that is distinct from that of F_λ^C, and are not blended with close neighbors. The variation with $[M/H]$ or age is quantified as the rate at which $F_{\lambda_0}/F_\lambda^C$ changes with respect to the parameter of interest, $\frac{\partial(F_{\lambda_0}/F_\lambda^C)}{\partial age}$ or $\frac{\partial(F_{\lambda_0}/F_\lambda^C)}{\partial[M/H]}$. To avoid falsely identifying features that are blended with nearby lines, we measure the slope of the flux at one half of a CW to either side of line center. If the magnitudes of the slopes for a line are within 5% of each other, we consider the line to be a clean feature and mark it for further analysis. If a line does not meet this criteria, it is rejected as a blended feature. A second pass filtering of blended features by visual inspection is performed later in the procedure

to remove any blends that survive this first pass filtration. For further discussion of our sensitivity criteria, preparation of the IL spectra, and line identification process, see Paper II.

Identified lines are categorized by which modelling parameter they are most sensitive to. We compile sets of features identified as sensitive to cluster age or metallicity, separating them by abundance distribution (scaled-solar or α-enhanced) and modelling treatment (NLTE or LTE). These sets of sensitive features are then reduced according to two criteria after line source identification is performed: 1) Identifications where the difference between the line center as reported by PHOENIX and the local minimum of flux is $\Delta\lambda > 0.1$ $\mathring{A}$ is considered to be a false identification and is removed; 2) Each set is further filtered by removing any blended features. Line blends are identified by visual inspection and removed if found to occur within two characteristic line widths, $\Delta\lambda_{CW}$, of each identified sensitive feature.

We quantify the NLTE impact on the overall sensitivity of a feature by measuring the equivalent width (EW) of the line within $\lambda_0 \pm \Delta\lambda_{CW}$ in both NLTE and LTE, and fit either a first or second order polynomial to the difference of EWs as a function of age or metallicity. The polynomial order is determined in each case by whichever function minimizes the residuals of the fit.

4.2.2 Results

Identification

We have identified 55 lines sensitive to cluster age and 117 lines sensitive to cluster metallicity in the range $\lambda = 4000$ to 9000 $\mathring{A}$, attributed to 14 different atomic species: Al I, Ba II, Ca I, C I, Cr I, Fe I, K I, Mn I, Na I, Ni I, Sc I, Ti I, Ti II, and V I. The total number of lines for each species, sensitive to each parameter, is presented in Table 4.1. The species with the greatest number of identified lines is Fe I, as expected, with 25 age- and 55 $[M/H]$-sensitive lines, followed by Ca I, with eight age- and 23 $[M/H]$-sensitive lines. In general, the strengths of spectral lines in our IL spectra were found to be five to six times more sensitive to cluster metallicity than to cluster age, with $\frac{\partial}{\partial Age}(\frac{\partial F_\lambda}{\partial \lambda})_{max} = 0.098$ and $\frac{\partial}{\partial [M/H]}(\frac{\partial F_\lambda}{\partial \lambda})_{max} = 0.625$. Sensitivity of these features to both age and metallicity is anywhere from two to 14 times higher than for near-IR lines, where $\frac{\partial}{\partial Age}(\frac{\partial F_\lambda}{\partial \lambda})_{max} = 0.007$ and $\frac{\partial}{\partial [M/H]}(\frac{\partial F_\lambda}{\partial \lambda})_{max} = 0.230$ (Paper II).

Tables 4.2 and 4.3 display the full lists of age- and metallicity-sensitive features, respectively, indicating if a feature was found to be sensitive in NLTE or LTE spectra, and for scaled-solar or α-enhanced clusters. All lines are presented in vacuum wavelengths. Our identification process did not flag any unblended age sensitive lines for $[M/H]$ = -0.353 clusters, and only two and four lines for $[M/H]$ = -0.659 and -0.253 clusters, respectively. Three of the four $[M/H]$ = -0.253 lines were found in LTE scaled-solar spectra, while the other line and both $[M/H]$ = -0.659 lines were found in NLTE α-enhanced spectra. All of the lines identified for $[M/H]$ = -0.963

Table 4.1 Numbers of optical atomic potential diagnostic lines for cluster age and metallicity, broken down by atomic species.

Species	# of Age Sensitive Lines	# of $[M/H]$ Sensitive Lines
Al I	···	1
Ba II	2	···
C I	1	1
Ca I	8	23
Cr I	3	8
Fe I	25	55
K I	···	1
Mn I	1	2
Na I	···	3
Ni I	2	4
Sc I	1	···
Ti I	5	19
Ti II	1	···
V I	6	···
Total	55	117

are from α-enhanced IL spectra, with the majority found in NLTE spectra. However, lines identified for $[M/H]$ = -1.266 and -1.488 were found in both scaled-solar and α-enhanced IL spectra. We identify the greatest number of age sensitive lines for clusters of $[M/H]$ = -1.266, suggesting a peak in IL spectral age-sensitivity. This is slightly more metal-poor than near-IR wavelengths, where the peak in age sensitivity is seen around $[M/H] \approx$ -1.0 (Paper II). We do not identify any lines that are consistently sensitive to age for both abundance distributions and modelling treatments and across all cluster metallicities, suggesting cluster age is a secondary parameter in determining line strength in IL spectra.

Table 4.2: Potential GC age diagnostic lines. Column headings indicate at which metallicity values a line was found to be sensitive to cluster age. The letters N and L indicate that the line was sensitive to age in NLTE and LTE spectra, respectively. The subscript symbols $_\odot$ and $_\alpha$ indicate scaled-solar and α-enhanced clusters, respectively. Lines are listed with vacuum wavelengths.

Species	λ_0 (Å)	$[M/H]$ -0.253	$[M/H]$ -0.353	$[M/H]$ -0.659	$[M/H]$ -0.963	$[M/H]$ -1.266	$[M/H]$ -1.488
Ba II	4555.3064	···	···	···	···	···	N_α,L_α
Ba II	4935.4545	···	···	···	···	···	N_α,L_α
Ca I	4227.9185	···	···	···	···	N_α	···
Ca I	4284.2148	···	···	···	N_α	···	···
Ca I	4300.1968	···	···	···	N_α	···	···
Ca I	4436.2028	···	···	···	N_α	···	···
Ca I	4456.0280	···	···	···	N_α	···	···
Ca I	6574.5931	···	···	···	N_α	$N_{\alpha,\odot}$,$L_{\alpha,\odot}$	$N_\odot$,$L_\odot$
Ca I	7412.6475	···	···	N_α	···	···	···
Ca I	7585.5010	N_α	···	···	···	···	···
C I	7366.7650	···	···	N_α	···	···	···
Cr I	4217.5475	···	···	···	···	···	N_α
Cr I	5205.9555	···	···	···	N_α	···	···
Cr I	5347.2865	$L_\odot$	···	···	···	···	···
Fe I	4006.3749	···	···	···	N_α	···	···
Fe I	4031.6282	···	···	···	···	···	N_α
Fe I	4046.9553	···	···	···	N_α	N_α	···
Fe I	4064.7422	···	···	···	L_α	$L_{\alpha,\odot}$	···
Fe I	4072.8879	···	···	···	L_α	$L_{\alpha,\odot}$	···
Fe I	4133.2243	···	···	···	N_α	···	···
Fe I	4188.9760	···	···	···	N_α	···	···
Fe I	4237.1285	···	···	···	L_α	···	···
Fe I	4384.7771	···	···	···	···	L_α	···
Fe I	4405.9870	···	···	···	L_α	···	···
Fe I	4462.9045	···	···	···	···	···	N_α
Fe I	5108.8701	···	···	···	···	···	L_α
Fe I	5446.5547	$L_\odot$	···	···	···	···	···
Fe I	6947.1200	···	···	···	···	···	$N_\odot$
Fe I	7725.3347	···	···	···	···	N_α	···
Fe I	7915.0432	···	···	···	···	$N_{\alpha,\odot}$,$L_{\alpha,\odot}$	$N_\odot$,$L_\odot$
Fe I	8049.8314	···	···	···	···	$N_{\alpha,\odot}$,$L_{\alpha,\odot}$	$N_\odot$,$L_\odot$
Fe I	8077.3685	···	···	···	···	$N_{\alpha,\odot}$,$L_{\alpha,\odot}$	$N_\odot$,$L_\odot$
Fe I	8207.1903	···	···	···	···	$N_\odot$	$N_\odot$,$L_\odot$
Fe I	8241.391	···	···	···	···	$N_{\alpha,\odot}$	$N_\odot$

Species	λ_0 (Å)	$[M/H]$ -0.253	$[M/H]$ -0.353	$[M/H]$ -0.659	$[M/H]$ -0.963	$[M/H]$ -1.266	$[M/H]$ -1.488
Fe I	8470.7337	···	···	···	···	N_α	$N_\odot$
Fe I	8614.1709	···	···	···	···	N_α	$N_\odot$
Fe I	8623.9708	···	···	···	···	···	$N_\odot$
Fe I	8759.5902	···	···	···	···	N_α	$N_\odot$
Fe I	8840.8552	···	···	···	···	N_α	$N_\odot$
Mn I	4035.6215	···	···	···	L_α	···	···
Ni I	5354.8797	$L_\odot$	···	···	···	···	···
Ni I	7716.4364	···	···	···	···	···	$N_\odot$
Sc I	6307.4010	···	···	···	···	$N_\odot$	···
Ti I	4537.1896	···	···	···	N_α	···	···
Ti I	7211.4221	···	···	···	···	$N_{\alpha,\odot}$,$L_\odot$	···
Ti I	8366.5376	···	···	···	N_α	N_α,$L_{\alpha,\odot}$	···
Ti I	8399.2056	···	···	···	N_α	$N_{\alpha,\odot}$,$L_{\alpha,\odot}$	$L_\odot$
Ti I	8685.3667	···	···	···	···	$L_\odot$	···
Ti II	4396.2671	···	···	···	L_α	···	···
V I	6191.0779	···	···	···	···	$N_{\alpha,\odot}$,$L_\odot$	···
V I	6200.9109	···	···	···	···	$N_\odot$	$N_\odot$
V I	6225.9604	···	···	···	···	$N_\odot$	···
V I	6276.3852	···	···	···	···	$N_\odot$	···
V I	6286.8881	···	···	···	···	$N_\odot$	$N_\odot$
V I	6298.2272	···	···	···	···	$N_\odot$,$L_\odot$	···

Table 4.3: Similar to Table 4.2, but for features sensitive to cluster metallicity. Column headings indicate at which age a line was found to be sensitive to cluster metallicity. Only whole number ages are included for ease of viewing.

Species	λ_0 (Å)	Age = 9.0 Gyr	Age = 10.0 Gyr	Age = 11.0 Gyr	Age = 12.0 Gyr	Age = 13.0 Gyr	Age = 14.0 Gyr	Age = 15.0 Gyr
Al I	8776.3063	$N_\odot$	$N_\odot$	$N_\odot$	$N_\odot$	$N_\odot$	$N_\odot$	$N_\odot$
C I	5302.3454	$L_\odot$	...	...	...	...	...	...
Ca I	4456.0280	N_α	N_α	N_α	N_α	N_α	N_α	N_α
Ca I	4582.7501	$N_{\alpha,\odot}$, $L_{\alpha,\odot}$	$N_{\alpha,\odot}$, $L_{\alpha,\odot}$	$N_{\alpha,\odot}$, $L_{\alpha,\odot}$	$N_{\alpha,\odot}$, $L_{\alpha,\odot}$	$N_{\alpha,\odot}$, $L_{\alpha,\odot}$	$N_{\alpha,\odot}$, $L_{\alpha,\odot}$	$N_{\alpha,\odot}$, $L_{\alpha,\odot}$
Ca I	4587.2480	L_α	L_α	L_α	L_α	L_α	N_α, L_α	N_α, L_α
Ca I	4686.5785	N_α, L_α	N_α, L_α	N_α, L_α	N_α, L_α	N_α, L_α	N_α, L_α	N_α, L_α
Ca I	5350.9534	L_α	L_α	L_α	L_α	L_α	L_α	...
Ca I	5583.5163	N_α, $L_{\alpha,\odot}$	N_α, $L_{\alpha,\odot}$	N_α, $L_{\alpha,\odot}$	N_α, $L_{\alpha,\odot}$	$N_{\alpha,\odot}$, $L_{\alpha,\odot}$	N_α, $L_{\alpha,\odot}$	N_α, $L_{\alpha,\odot}$
Ca I	5596.0150	$N_\odot$	$N_\odot$	$N_\odot$	$N_\odot$	$N_\odot$	$N_\odot$	$N_\odot$
Ca I	5600.0344	N_α, $L_{\alpha,\odot}$	N_α, L_α	N_α, L_α	N_α, L_α	N_α	...	...
Ca I	5602.8323	$N_{\alpha,\odot}$, $L_{\alpha,\odot}$	$N_{\alpha,\odot}$, $L_{\alpha,\odot}$	$N_{\alpha,\odot}$, $L_{\alpha,\odot}$	$N_{\alpha,\odot}$, $L_{\alpha,\odot}$	$N_{\alpha,\odot}$, $L_{\alpha,\odot}$	$N_{\alpha,\odot}$, $L_{\alpha,\odot}$	$N_{\alpha,\odot}$, $L_{\alpha,\odot}$
Ca I	5604.3985	$L_\odot$	$L_\odot$	$L_\odot$	$L_\odot$	...	$L_\odot$	$L_\odot$
Ca I	5859.0749	$N_{\alpha,\odot}$, $L_{\alpha,\odot}$	$N_{\alpha,\odot}$, L_α	$N_{\alpha,\odot}$, L_α	$N_{\alpha,\odot}$, L_α	$N_{\alpha,\odot}$, L_α	$N_{\alpha,\odot}$, L_α	$N_{\alpha,\odot}$, L_α
Ca I	6165.4598	L_α	L_α	L_α	L_α	L_α	...	...
Ca I	6440.8544	$N_\odot$	...	...	...	...	...	...
Ca I	6451.5906	N_α, L_α	N_α, L_α	N_α, L_α	N_α, L_α	N_α, L_α	N_α, L_α	N_α, L_α
Ca I	6464.3515	N_α	N_α	N_α	N_α	N_α	N_α	N_α
Ca I	6473.4500	$N_{\alpha,\odot}$, $L_{\alpha,\odot}$	$N_{\alpha,\odot}$, $L_{\alpha,\odot}$	$N_{\alpha,\odot}$, $L_{\alpha,\odot}$	$N_{\alpha,\odot}$, $L_{\alpha,\odot}$	$N_{\alpha,\odot}$, $L_{\alpha,\odot}$	$N_{\alpha,\odot}$, $L_\odot$	$N_{\alpha,\odot}$, $L_\odot$
Ca I	6495.5751	$N_{\alpha,\odot}$	N_α	N_α	N_α	N_α	N_α	N_α
Ca I	6501.4465	N_α	N_α	N_α	N_α	N_α	N_α	N_α
Ca I	6574.5931	$N_\odot$, $L_{\alpha,\odot}$	$N_\odot$, $L_{\alpha,\odot}$	$L_{\alpha,\odot}$	L_α	L_α	L_α	L_α
Ca I	6719.5366	$N_{\alpha,\odot}$, L_α	$N_{\alpha,\odot}$, L_α	$N_{\alpha,\odot}$	$N_{\alpha,\odot}$	$N_{\alpha,\odot}$	$N_\odot$	$N_\odot$
Ca I	7150.1202	$N_\odot$	$N_\odot$	$N_\odot$	$N_\odot$	$N_\odot$	$N_\odot$	...

Species	λ_0 (Å)	Age = 9.0 Gyr	Age = 10.0 Gyr	Age = 11.0 Gyr	Age = 12.0 Gyr	Age = 13.0 Gyr	Age = 14.0 Gyr	Age = 15.0 Gyr
Ca I	7204.1855	$N_{\alpha,\odot}$, L_α	$N_\odot$, L_α	$N_\odot$, L_α	$N_\odot$, L_α	$N_\odot$, L_α	$N_\odot$	$N_\odot$
Ca I	7328.1652	$N_{\alpha,\odot}$, L_α	$N_{\alpha,\odot}$, L_α	$N_{\alpha,\odot}$, L_α	$N_{\alpha,\odot}$, L_α	$N_{\alpha,\odot}$, L_α	$N_{\alpha,\odot}$, L_α	$N_{\alpha,\odot}$, L_α
Cr I	4566.7774	N_α, $L_{\alpha,\odot}$	N_α, $L_{\alpha,\odot}$	N_α, $L_{\alpha,\odot}$	N_α, $L_{\alpha,\odot}$	N_α, $L_{\alpha,\odot}$	N_α, $L_{\alpha,\odot}$	N_α, $L_{\alpha,\odot}$
Cr I	4627.4700	L_α	L_α	L_α	L_α	L_α	L_α	$L_{\alpha,\odot}$
Cr I	4915.1156	L_α	L_α	L_α	L_α	L_α	L_α	L_α
Cr I	5347.2865	···	L_α	L_α	N_α, L_α	N_α, L_α	N_α, L_α	N_α, L_α
Cr I	5349.8004	L_α	L_α	L_α	L_α	L_α	L_α	···
Cr I	5411.2750	L_α	L_α	L_α	L_α	L_α	L_α	L_α
Cr I	7402.2660	$N_\odot$, $L_{\alpha,\odot}$	$N_\odot$, $L_{\alpha,\odot}$	$N_\odot$, L_α	$N_\odot$, L_α	$N_\odot$, L_α	$N_\odot$	$N_\odot$
Cr I	7464.4195	$L_\odot$	$L_\odot$	$L_\odot$	$L_\odot$	$L_\odot$	$L_\odot$	$L_\odot$
Fe I	4006.3749	N_α	N_α	N_α	N_α	N_α	N_α	N_α
Fe I	4023.0037	N_α	N_α	···	···	···	N_α	N_α
Fe I	4056.0124	···	N_α	···	···	···	N_α	N_α
Fe I	4246.4520	L_α	L_α	L_α	L_α	L_α	L_α	L_α
Fe I	4261.6730	···	···	···	···	···	N_α	N_α
Fe I	4477.2736	N_α	N_α	N_α	N_α	N_α	N_α	N_α
Fe I	4612.5704	N_α	N_α	···	···	···	N_α	N_α
Fe I	4634.2079	N_α, L_α	N_α, L_α	N_α, L_α	N_α, L_α	N_α, L_α	N_α, L_α	N_α, L_α
Fe I	4655.9119	N_α, $L_{\alpha,\odot}$	N_α, $L_{\alpha,\odot}$	N_α, $L_{\alpha,\odot}$	$N_{\alpha,\odot}$, $L_{\alpha,\odot}$	$N_{\alpha,\odot}$, $L_{\alpha,\odot}$	$N_{\alpha,\odot}$, $L_{\alpha,\odot}$	$N_{\alpha,\odot}$, $L_\odot$
Fe I	4734.9150	L_α	L_α	L_α	L_α	L_α	L_α	L_α
Fe I	4830.4700	···	···	···	···	$N_\odot$	···	···
Fe I	4947.7690	N_α	N_α	N_α	N_α	N_α	N_α	N_α
Fe I	4980.0815	$N_\odot$	$N_\odot$	$N_\odot$	$N_\odot$	$N_\odot$	$N_\odot$	$N_\odot$
Fe I	4990.3411	L_α	L_α	L_α	···	···	···	···
Fe I	5003.9783	$L_\odot$	$L_\odot$	$L_\odot$	$L_\odot$	$L_\odot$	$L_\odot$	$L_\odot$
Fe I	5061.4892	$L_{\alpha,\odot}$	$L_{\alpha,\odot}$	$L_{\alpha,\odot}$	$L_{\alpha,\odot}$	$L_{\alpha,\odot}$	$L_\odot$	$L_\odot$
Fe I	5098.4178	L_α	L_α	L_α	L_α	$N_\odot$, L_α	···	···

Species	λ_0 (Å)	Age = 9.0 Gyr	Age = 10.0 Gyr	Age = 11.0 Gyr	Age = 12.0 Gyr	Age = 13.0 Gyr	Age = 14.0 Gyr	Age = 15.0 Gyr
Fe I	5138.8137	...	...	...	...	...	...	...
Fe I	5203.7850	$N_\odot$	$N_\odot$	$N_\odot$	$N_\odot$	$N_\odot$	$N_\odot$	$N_\odot$
Fe I	5274.8421	L_α	L_α	L_α	L_α	L_α	L_α	L_α
Fe I	5303.7746	N_α, L_α	N_α	N_α	N_α	$N_{\alpha,\odot}$	$N_{\alpha,\odot}$	$N_{\alpha,\odot}$
Fe I	5323.5200	$N_\odot$	$N_\odot$	$N_\odot$	$N_\odot$	$N_\odot$	$N_\odot$	...
Fe I	5334.3831	$L_\odot$	...	...	...	...	...	...
Fe I	5402.0026	$N_\odot$, L_α	$N_\odot$, L_α	$N_\odot$, L_α	$N_\odot$, L_α	$N_\odot$, L_α	$N_\odot$	$N_\odot$
Fe I	5446.5547	...	...	...	$N_\odot$	$N_\odot$	$N_\odot$	...
Fe I	5556.4379	$N_\odot$	$N_\odot$, L_α	$N_\odot$, L_α	$N_\odot$, L_α	$N_\odot$, L_α	$N_\odot$	$N_\odot$
Fe I	5565.1461	$L_\odot$	...	...	...	...	...	...
Fe I	5710.9605	$L_\odot$	$L_\odot$	$L_\odot$	$L_\odot$	$L_\odot$	$L_\odot$	$L_\odot$
Fe I	5915.7496	L_α	L_α	L_α	L_α	L_α	...	...
Fe I	5986.4718	L_α	L_α	L_α	L_α	L_α	...	...
Fe I	6067.1606	N_α	N_α	N_α	...	...	...	...
Fe I	6338.5764	$N_\odot$	$N_\odot$	$N_\odot$	$N_\odot$	$N_\odot$	$N_\odot$	$N_\odot$
Fe I	6423.1246	N_α	N_α	N_α	N_α	N_α	N_α	...
Fe I	6548.0461	$N_{\alpha,\odot}$, L_α	$N_{\alpha,\odot}$	$N_{\alpha,\odot}$	$N_{\alpha,\odot}$	$N_{\alpha,\odot}$	$N_{\alpha,\odot}$	$N_\odot$
Fe I	6665.2815	$N_{\alpha,\odot}$	$N_{\alpha,\odot}$	$N_\odot$	$N_\odot$	$N_\odot$	$N_\odot$	$N_\odot$
Fe I	6947.1200	$N_{\alpha,\odot}$	$N_\odot$	$N_\odot$	$N_\odot$	$N_\odot$	...	...
Fe I	7018.3256	$L_{\alpha,\odot}$	...	...	...	...	...	...
Fe I	7391.4333	$N_\odot$	$N_\odot$	$N_\odot$	$N_\odot$	$N_\odot$	$N_\odot$	$N_\odot$
Fe I	7497.1291	N_α, L_α	N_α	N_α	N_α	N_α	N_α	N_α
Fe I	7513.0887	$N_{\alpha,\odot}$	$N_{\alpha,\odot}$	$N_{\alpha,\odot}$	$N_{\alpha,\odot}$	$N_{\alpha,\odot}$	$N_{\alpha,\odot}$	$N_{\alpha,\odot}$
Fe I	7585.8765	$N_{\alpha,\odot}$, L_α	$N_{\alpha,\odot}$, L_α	$N_{\alpha,\odot}$, L_α	$N_{\alpha,\odot}$, L_α	$N_{\alpha,\odot}$, L_α	$N_{\alpha,\odot}$	$N_\odot$
Fe I	7782.6987	$N_\odot$	$N_\odot$	$N_\odot$	$N_\odot$	$N_\odot$	$N_\odot$	...
Fe I	7834.3519	$N_\odot$	$N_\odot$	$N_\odot$	$N_\odot$	...	...	...
Fe I	7939.3241	$N_{\alpha,\odot}$	$N_{\alpha,\odot}$	N_α	N_α	N_α	...	...

Species	λ_0 (Å)	Age = 9.0 Gyr	Age = 10.0 Gyr	Age = 11.0 Gyr	Age = 12.0 Gyr	Age = 13.0 Gyr	Age = 14.0 Gyr	Age = 15.0 Gyr
Fe I	8001.1449	$N_{\alpha,\odot}$	$N_{\alpha,\odot}$	$N_{\alpha,\odot}$	$N_{\alpha,\odot}$	$N_{\odot}$	$N_{\odot}$	$N_{\odot}$
Fe I	8048.2578	$N_{\alpha,\odot}$	$N_{\odot}$	$N_{\odot}$	$N_{\odot}$	$N_{\odot}$	$N_{\odot}$	$N_{\odot}$
Fe I	8049.8314	L_{α}	L_{α}	L_{α}	L_{α}	L_{α}	...	...
Fe I	8077.3685	L_{α}	L_{α}	L_{α}	L_{α}	L_{α}	...	...
Fe I	8087.3947	$N_{\odot}$	$N_{\odot}$	$N_{\odot}$	$N_{\odot}$	$N_{\odot}$	$N_{\odot}$	...
Fe I	8222.6385	N_{α}	N_{α}	N_{α}	N_{α}	N_{α}	...	...
Fe I	8241.3910	$N_{\alpha,\odot}$, L_{α}	N_{α}, L_{α}	N_{α}, L_{α}	...	...	...	...
Fe I	8614.1709	$N_{\alpha,\odot}$	$N_{\alpha,\odot}$	N_{α}	N_{α}	...	...	...
Fe I	8623.9708	$N_{\odot}$	$N_{\odot}$	$N_{\odot}$	$N_{\odot}$	...	...	...
Fe I	8759.5902	$N_{\alpha,\odot}$	$N_{\alpha,\odot}$	$N_{\alpha,\odot}$	$N_{\alpha,\odot}$	$N_{\alpha,\odot}$	$N_{\alpha,\odot}$	$N_{\alpha,\odot}$
Fe I	8795.7585	$N_{\odot}$	$N_{\odot}$	$N_{\odot}$	...	...	...	...
Fe I	8840.8552	$N_{\alpha,\odot}$	$N_{\alpha,\odot}$	$N_{\alpha,\odot}$	$N_{\alpha,\odot}$	$N_{\alpha,\odot}$	$N_{\alpha,\odot}$	$N_{\alpha,\odot}$
K I	7701.0921	$N_{\alpha,\odot}$, L_{α}	$N_{\odot}$, L_{α}	$N_{\odot}$, L_{α}	$N_{\odot}$, L_{α}	$N_{\odot}$	$N_{\odot}$	$N_{\odot}$
Mn I	5396.1689	L_{α}	L_{α}	L_{α}	L_{α}	L_{α}	L_{α}	...
Mn I	6018.3053	...	...	$N_{\odot}$	$N_{\odot}$	$N_{\odot}$	...	...
Na I	5689.7837	N_{α}, $L_{\alpha,\odot}$	N_{α}, $L_{\alpha,\odot}$	N_{α}, $L_{\alpha,\odot}$	$N_{\alpha,\odot}$, $L_{\alpha,\odot}$	$N_{\alpha,\odot}$, $L_{\alpha,\odot}$	$N_{\alpha,\odot}$, $L_{\odot}$	N_{α}, $L_{\odot}$
Na I	8185.5069	$N_{\alpha,\odot}$, $L_{\alpha,\odot}$	$N_{\alpha,\odot}$, $L_{\alpha,\odot}$	$N_{\alpha,\odot}$, $L_{\alpha,\odot}$	$N_{\alpha,\odot}$, $L_{\alpha,\odot}$	$N_{\alpha,\odot}$, $L_{\alpha,\odot}$	$N_{\alpha,\odot}$, $L_{\alpha,\odot}$	$N_{\alpha,\odot}$, $L_{\alpha,\odot}$
Na I	8197.0771	$N_{\alpha,\odot}$, L_{α}	$N_{\alpha,\odot}$, L_{α}	$N_{\alpha,\odot}$, L_{α}	$N_{\alpha,\odot}$, L_{α}	$N_{\alpha,\odot}$, L_{α}	$N_{\alpha,\odot}$	$N_{\alpha,\odot}$
Ni I	4606.2717	L_{α}	L_{α}	L_{α}	L_{α}	L_{α}	L_{α}	...
Ni I	5354.8797	$N_{\odot}$, $L_{\alpha,\odot}$	$N_{\odot}$, $L_{\alpha,\odot}$	$N_{\odot}$, $L_{\odot}$	$N_{\odot}$, $L_{\odot}$	$N_{\odot}$, $L_{\odot}$	$N_{\odot}$, $L_{\odot}$	$N_{\odot}$, $L_{\odot}$
Ni I	5593.8106	$L_{\alpha,\odot}$	$L_{\alpha,\odot}$	$L_{\alpha,\odot}$	$L_{\alpha,\odot}$	$L_{\alpha,\odot}$	$L_{\odot}$	$L_{\odot}$
Ni I	7716.4364	$N_{\odot}$	$N_{\odot}$	...	...	...	...	...
Ti I	4328.1764	N_{α}	N_{α}	N_{α}	N_{α}	N_{α}	N_{α}	N_{α}
Ti I	4640.9602	N_{α}	N_{α}	N_{α}	N_{α}	N_{α}	N_{α}	N_{α}
Ti I	4692.6445	L_{α}	L_{α}	L_{α}	L_{α}	L_{α}	L_{α}	L_{α}
Ti I	4793.8233	$N_{\odot}$, $L_{\alpha,\odot}$	$N_{\odot}$, $L_{\alpha,\odot}$	$N_{\odot}$, $L_{\alpha,\odot}$	$N_{\odot}$, $L_{\alpha,\odot}$	$N_{\odot}$, $L_{\alpha,\odot}$	$N_{\odot}$, $L_{\alpha,\odot}$	$N_{\odot}$, $L_{\alpha,\odot}$
Ti I	4901.3896	L_{α}	L_{α}	...	...	...	...	...

Species	λ_0 (Å)	Age = 9.0 Gyr	Age = 10.0 Gyr	Age = 11.0 Gyr	Age = 12.0 Gyr	Age = 13.0 Gyr	Age = 14.0 Gyr	Age = 15.0 Gyr
Ti I	4992.4574	N_α	N_α	N_α	N_α	N_α	N_α	N_α
Ti I	5645.7002	$L_\odot$	$L_\odot$	$L_\odot$	$L_\odot$	$L_\odot$	$L_\odot$	$L_\odot$
Ti I	5868.0784	$N_{\alpha,\odot}$, $L_{\alpha,\odot}$	$N_{\alpha,\odot}$, L_α	$N_{\alpha,\odot}$, L_α	$N_{\alpha,\odot}$, L_α	$N_{\alpha,\odot}$, L_α	$N_{\alpha,\odot}$, L_α	$N_\odot$
Ti I	5900.9285	L_α	L_α	...	...	...	...	...
Ti I	6086.9109	L_α	L_α	$N_\odot$, L_α	$N_\odot$, L_α	$N_\odot$, L_α	$N_\odot$	...
Ti I	7211.4221	$N_{\alpha,\odot}$, L_α	$N_{\alpha,\odot}$, L_α	$N_{\alpha,\odot}$	$N_\odot$	$N_\odot$	$N_\odot$	...
Ti I	7246.8520	N_α, L_α	N_α, L_α	N_α, L_α	N_α, L_α	N_α, L_α	N_α	...
Ti I	7253.7071	L_α	L_α	L_α	L_α	L_α	...	...
Ti I	7346.7179	L_α	L_α	L_α	L_α	L_α	...	...
Ti I	7359.7552	$N_\odot$, L_α	$N_\odot$, L_α	$N_\odot$, L_α	$N_\odot$, L_α	$N_\odot$, L_α	$N_\odot$	$N_\odot$
Ti I	7366.1278	$L_{\alpha,\odot}$	$L_{\alpha,\odot}$	$L_\odot$	$N_\odot$, $L_\odot$	$N_\odot$, $L_\odot$	$L_\odot$	...
Ti I	8399.2056	$N_{\alpha,\odot}$, $L_{\alpha,\odot}$	$N_{\alpha,\odot}$, $L_{\alpha,\odot}$	$N_{\alpha,\odot}$, $L_{\alpha,\odot}$	$N_{\alpha,\odot}$, $L_{\alpha,\odot}$	$N_{\alpha,\odot}$, $L_{\alpha,\odot}$	$N_{\alpha,\odot}$, $L_{\alpha,\odot}$	$N_{\alpha,\odot}$, L_α
Ti I	8414.6702	$L_\odot$	...	...	...	...	...	...
Ti I	8685.3667	$N_{\alpha,\odot}$, $L_\odot$	$N_{\alpha,\odot}$, $L_\odot$	$N_{\alpha,\odot}$, $L_\odot$	$N_{\alpha,\odot}$, $L_\odot$	$N_{\alpha,\odot}$, $L_\odot$	N_α	N_α

Three lines have been identified that are sensitive to metallicity at all ages, regardless of abundance distribution or modelling treatment; the Ca I λ4582.8 and λ5602.8 lines and the Na I λ8185.5 line. A total of 63 other lines show a sensitivity to metallicity at all ages, but did not meet the sensitivity criteria for one or more of the combinations of abundance distribution and modelling treatment, most often the LTE scaled-solar IL spectra. Overall, the sensitivity of metallicity sensitive lines is inversely proportional to cluster age in both LTE and NLTE spectra (with a greater effect for LTE), with fewer sensitive lines seen for greater cluster ages. Additionally, a total of 18 lines were identified that serve as both potential metallicity and potential age diagnostics, including ten Fe I lines, three Ti I, two each of Ca I and Ni I lines, and a single Cr I line, as listed in Table 4.4.

Table 4.4 Spectral IL optical lines that are sensitive to both cluster age and metallicity.

Species	λ_0 (Å)	Species	λ_0 (Å)	Species	λ_0 (Å)
Ca I	4456.0280	Fe I	8049.8314	Fe I	8840.8552
Ca I	6574.5931	Fe I	8077.3685	Ni I	5354.8797
Cr I	5347.2865	Fe I	8241.3910	Ni I	7716.4364
Fe I	4006.3749	Fe I	8614.1709	Ti I	7211.4221
Fe I	5446.5547	Fe I	8623.9708	Ti I	8399.2056
Fe I	6947.1200	Fe I	8759.5902	Ti I	8685.3667

Equivalent Widths

We introduce the notation

$$\Delta_{\rm NLTE}(X) = X_{\rm NLTE} - X_{\rm LTE} \tag{4.1}$$

to mean the difference introduced in a derived quantity X by NLTE effects. In Figures 4.1 to 4.4 we present the $\Delta_{\rm NLTE}(EW)$ values over our full parameter space for four representative spectral lines, the Ca I λ5602.8323 line, the Fe I λ8077.3685 line, the Na I λ8185.5069 line, and the Ti I λ8399.2056 line. The primary source of uncertainty in our EW measurements is the uncertainty from the sigma-clipping continuum rectifications. Contour plots for the remaining spectral lines in our sample identified as sensitive in both LTE and NLTE spectra are included in Appendix A. Differences in EW caused by NLTE effects fall in the range $-0.03 \leq \Delta_{\rm NLTE}(EW) \leq 0.08$ Å . In general, $\Delta_{\rm NLTE}(EW)$ is relatively insensitive to age for most species regardless of abundance distribution, with the exceptions of Fe I, Cr I, V I, and some Ti I features. Fe I uniquely shows a greater sensitivity to metallicity in scaled-solar IL spectra than in α-enhanced spectra, while also exhibiting a mild age sensitivity for both abundance distributions at certain metallicities. The $\Delta_{\rm NLTE}(EW)$ values may be either positive, negative, or both for a given line depending on the age and $[M/H]$. We observe a loose trend for the age insensitive features where $\Delta_{\rm NLTE}(EW)$ increases with increasing $[M/H]$.

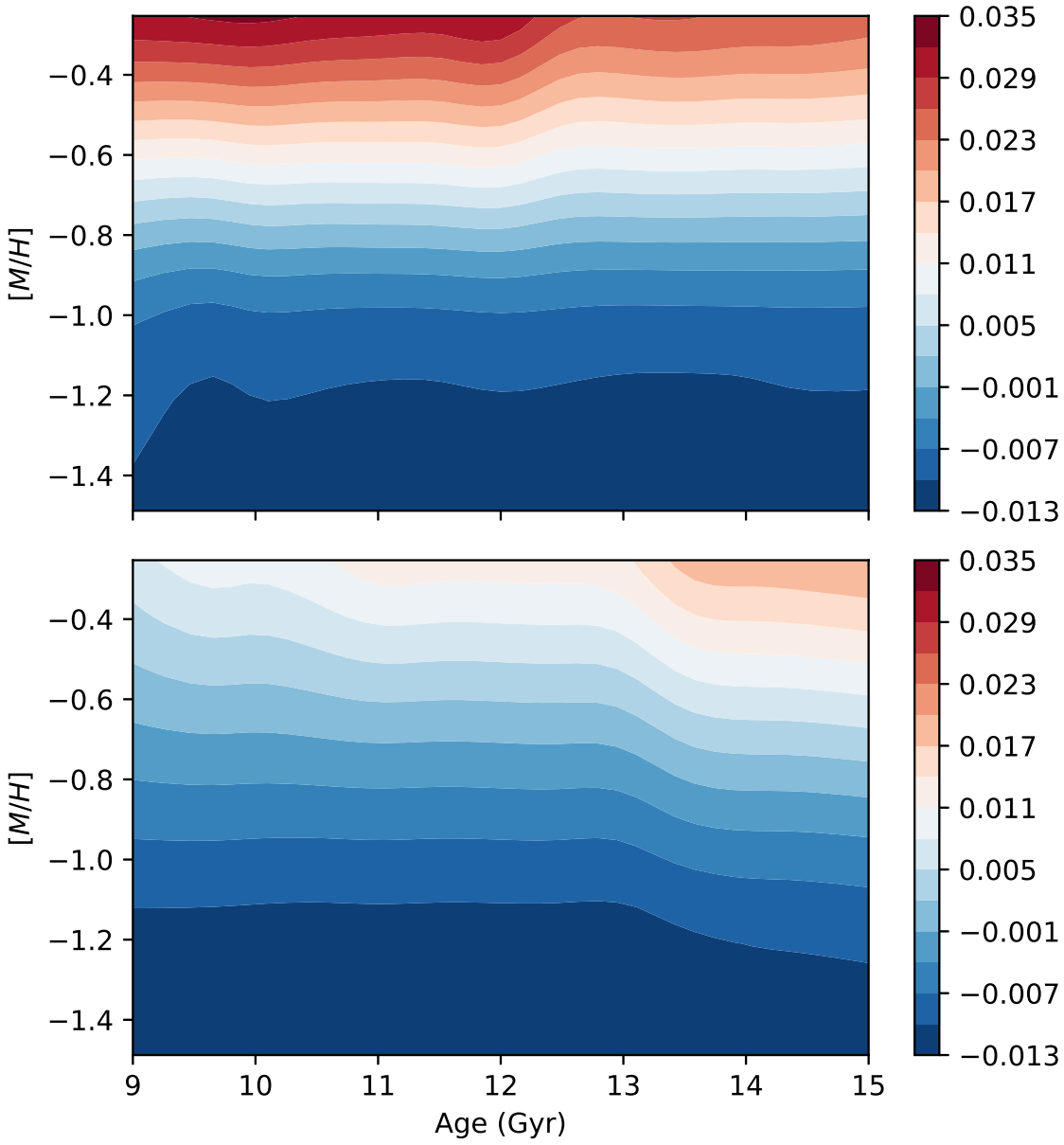

Figure 4.1 Contour plot of $\Delta_{\rm NLTE}(EW)$ for the Ca I λ5602.8323 line over the full parameter space of our IL spectra library. The countours sample $\Delta_{\rm NLTE}(EW)$ every 0.003 Å . *Top*: Scaled-solar spectra. *Bottom*: α-enhanced spectra.

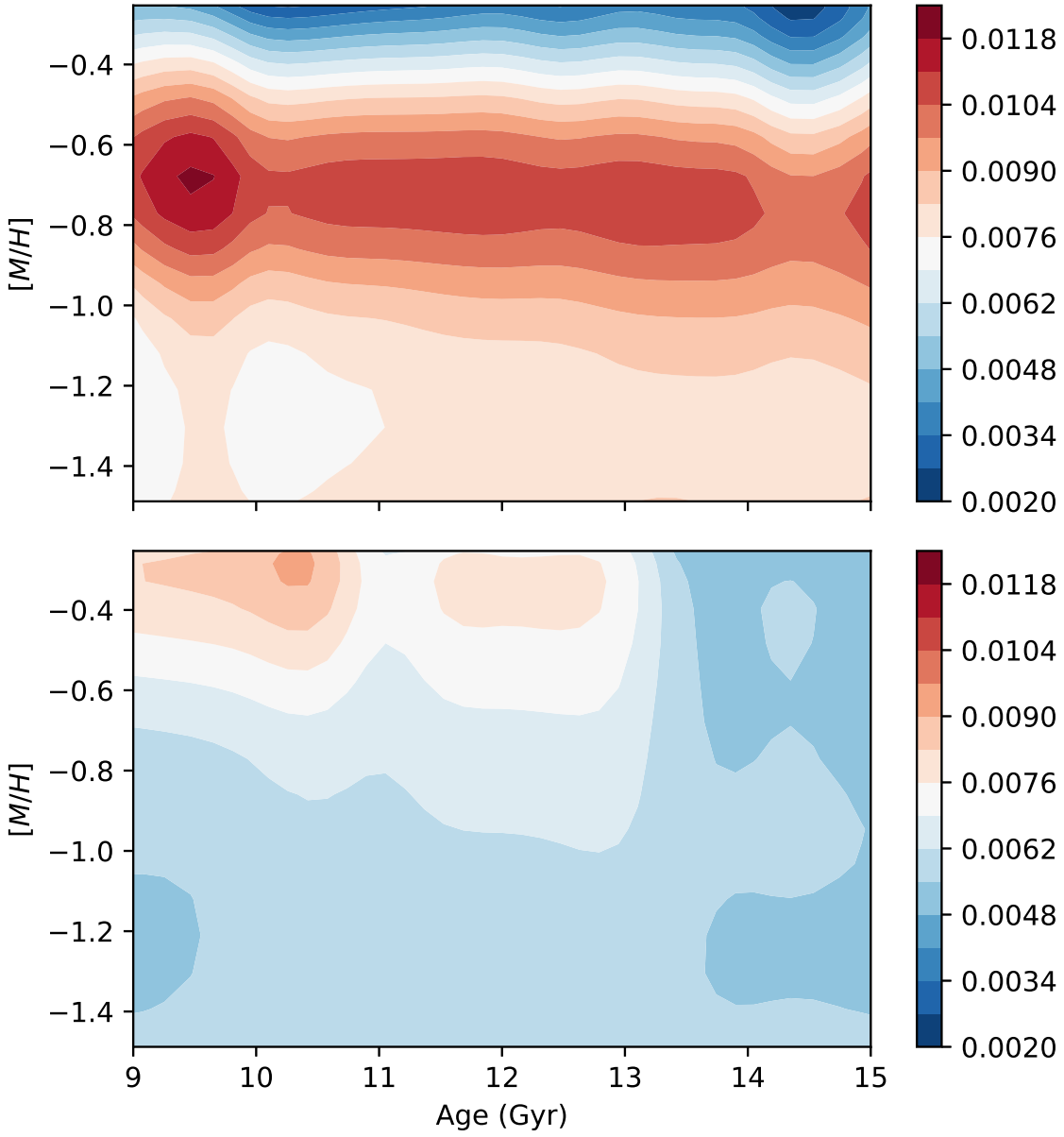

Figure 4.2 Similar to Figure 4.1, but for the Fe I λ8077.3685 line, with contours sampling $\Delta_{\rm NLTE}(EW)$ every 0.0007 Å .

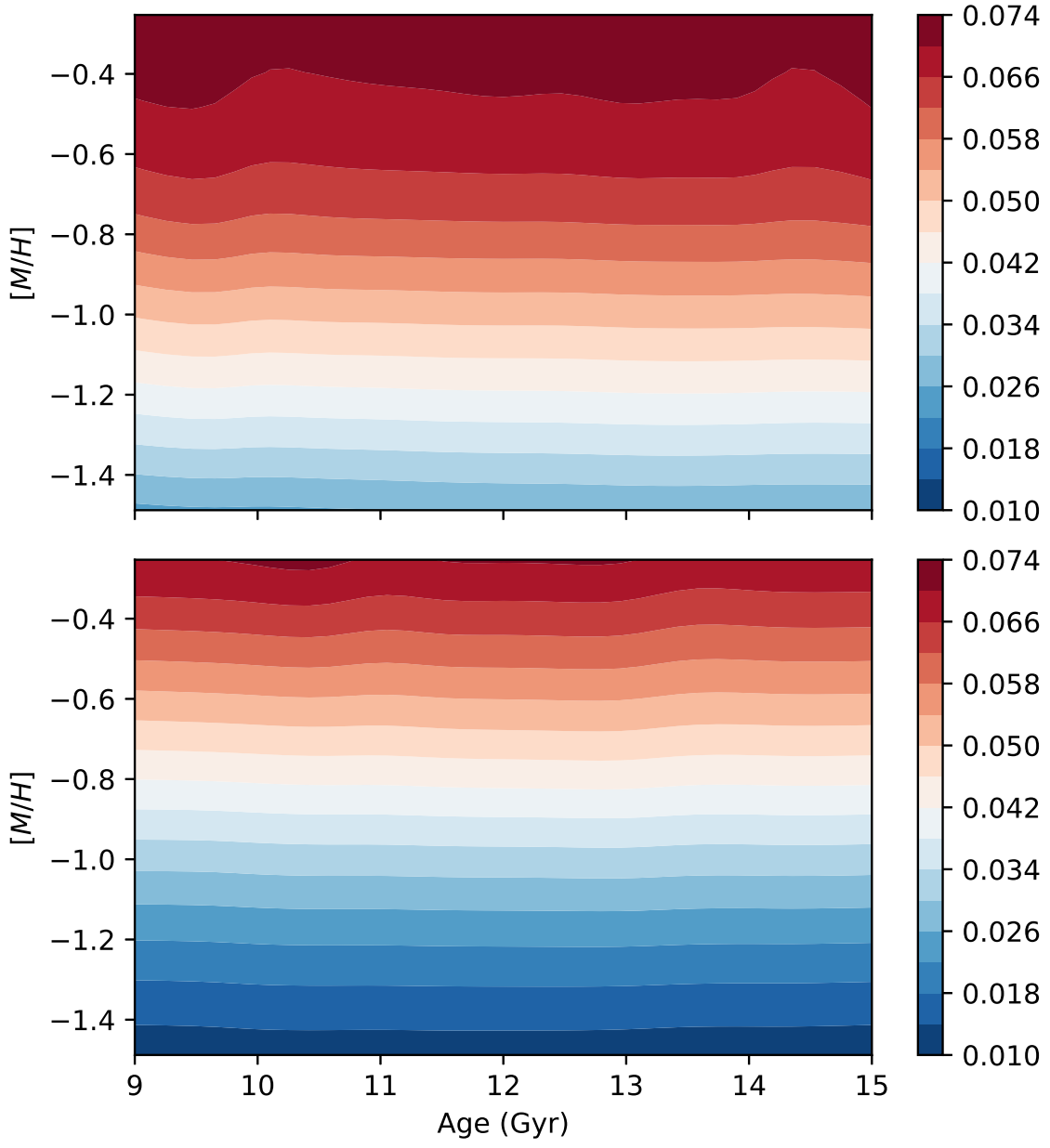

Figure 4.3 Similar to Figure 4.1, but for the Na I λ8185.5069 line, with contours sampling $\Delta_{\rm NLTE}(EW)$ every 0.004 Å .

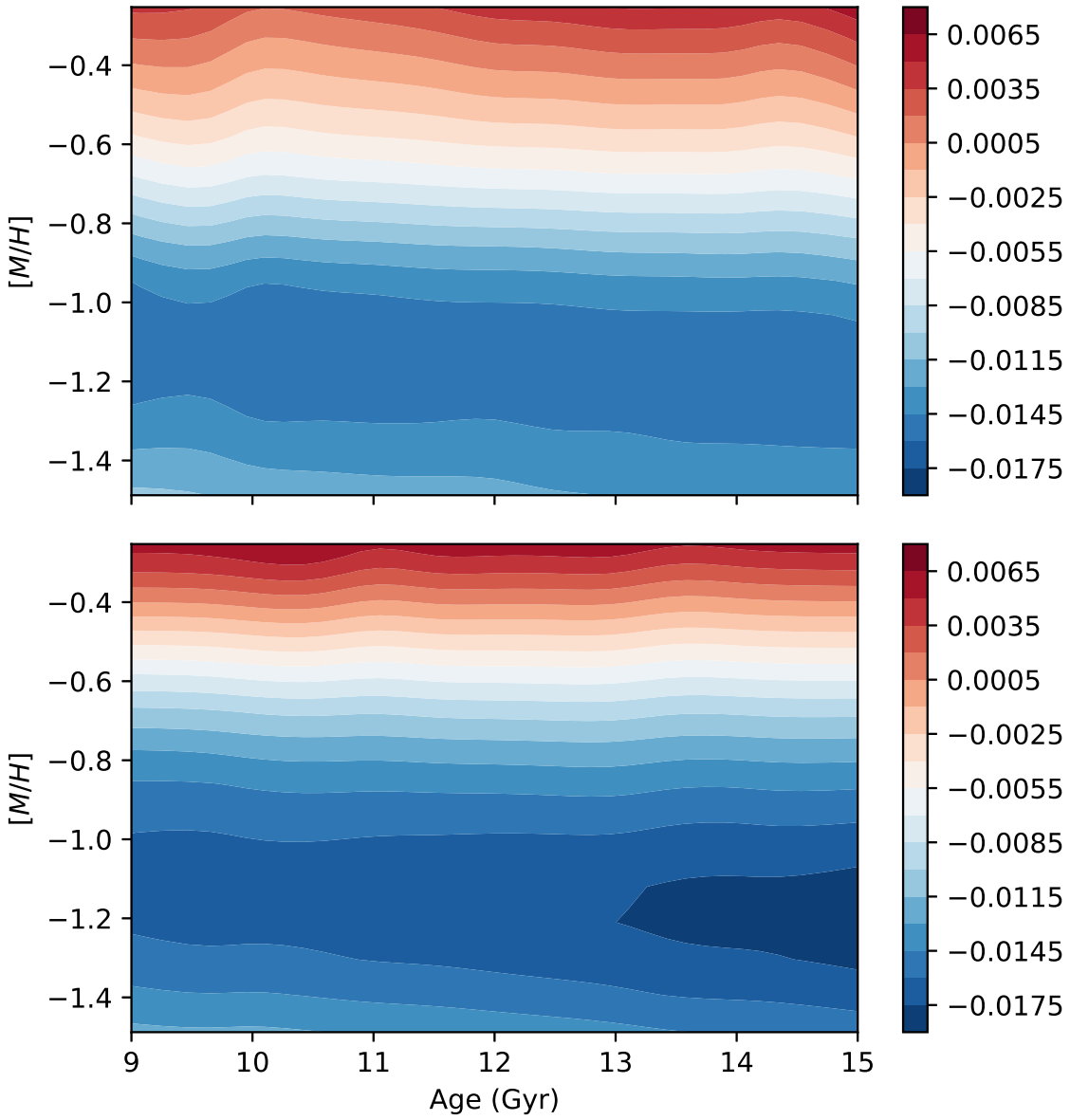

Figure 4.4 Similar to Figure 4.1, but for the Ti I λ8399.2056 line, with contours sampling $\Delta_{\rm NLTE}(EW)$ every 0.01 Å .

4.3 OBSERVATIONAL DATA

We have obtained the high resolution IL spectra of the 12 GCs presented in and made publicly available in CBM17. The high spectral resolution of these spectra, R $\sim$ 30000 to 40000, offers a unique opportunity for unprecedented precision in determination of cluster properties such as cluster age or $[M/H]$. Details of the observations and post-processing can be found in CBM17 and references therein, and are summarized here. The data were obtained using a combination of the echelle spectrograph on the 2.5 m du Pont telescope at Las Campanas and the MIKE spectrograph on the Magellan Clay Telescope. Further details of the observations are listed in Table 4.5.

Table 4.5 Observation details of the 12 GC spectra obtained from CBM17.

ID	R.A. (J2000)	Dec. (J2000)	$r_{\rm core}$ ($'$)	Telescope	Scan Area (" × ")	$T_{\rm exp}$ (s)	S/N (pixel^{-1})
NGC 104	$00^{\rm h}24^{\rm m}05.2^{\rm s}$	-72°04'51"	3.2	Du Pont	32 × 32	11030	100
NGC 2808	$09^{\rm h}12^{\rm m}02.6^{\rm s}$	-64°51'47"	0.8	Du Pont	32 × 32	10730	81
NGC 362	$01^{\rm h}03^{\rm m}14.3^{\rm s}$	-70°50'54"	0.8	Du Pont	32 × 32	11021	89
NGC 6093	$16^{\rm h}17^{\rm m}02.5^{\rm s}$	-22°58'30"	0.6	Du Pont	32 × 32	7350	52
NGC 6397	$17^{\rm h}40^{\rm m}41.3^{\rm s}$	-53°40'25"	2.9	Du Pont	32 × 32	18374	57
NGC 6752	$19^{\rm h}10^{\rm m}52.0^{\rm s}$	-59°59'05"	1.9	Du Pont	32 × 32	11021	130
NGC 6388	$17^{\rm h}36^{\rm m}17.0^{\rm s}$	-44°44'06"	0.5	Magellan	30 × 30	3600	200
NGC 6440	$17^{\rm h}48^{\rm m}52.7^{\rm s}$	-20°21'37"	0.5	Magellan	10 × 10	25200	162
NGC 6441	$17^{\rm h}50^{\rm m}13.1^{\rm s}$	-37°03'05"	0.6	Magellan	10 × 10	3600	119
NGC 6528	$18^{\rm h}04^{\rm m}49.6^{\rm s}$	-30°03'23"	0.4	Magellan	10 × 10	10800	104
NGC 6553	$18^{\rm h}09^{\rm m}17.6^{\rm s}$	-25°54'31"	1.0	Magellan	30 × 30	2700	103
Fornax 3	$02^{\rm h}04^{\rm m}52.5^{\rm s}$	-34°16'08"	0.04	Magellan	···	6000	70

The authors have already performed basic data reduction of the spectra prior to making them publicly available. The du Pont spectra were reduced with the echelle package in IRAF including routines for overscan, bias, and flat-field corrections, and subtraction of inter-order scattered light, while the Magellan spectra were reduced using the MIKE IDL pipeline. Sky spectra were collected, scaled, and subtracted from the exposures. Approximations of the echelle spectrograph blaze functions for each order were obtained from observations of a bright G-star and used to normalize the IL flux. No attempts were made to remove telluric lines from the spectra; however the authors did compare telluric template stars to determine that no lines were measured near telluric lines. At the authors' suggestion, we limit the spectra from their full wavelength ranges (3700 to 7800 $\mathring{A}$ for the du Pont and 3700 to 9800 $\mathring{A}$ for the Magellan spectra) to 4100 to 7500 $\mathring{A}$, avoiding the majority of telluric absorption features altogether and maximizing S/N.

4.4 SPECTRAL ANALYSIS

To prepare both the observed IL spectra and our library of synthetic IL spectra for line profile fitting, we convert the wavelengths of the observed spectra from air wavelengths to vacuum wavelengths, reduce the extremely-high spectral resolution synthetic spectra ($R \sim 300000$) to the spectral resolution of CBM17 ($R \sim 30000$), artificially broaden the synthetic spectra according to each observed cluster's velocity dispersion, V_σ, continuum rectify both the synthetic and observed spectra in a

consistent manner, and correct the observed spectra for their radial velocities. For the air-to-vacuum wavelength conversion, we calculate the index of refraction at each wavelength according to the formula presented by Morton (2000).

A list of the velocity dispersions used for these preparations, as well as cluster ages and metallicities, is displayed in Table 4.6. The synthetic spectra are convolved first to the desired spectral resolution, and then separately once more for each observed cluster according to their velocity dispersion. We apply the radial velocity corrections to each echelle order of the observed spectra independently and confirm the accuracy of the correction, while allowing for additional correction, after continuum rectification is performed.

We rectify both the synthetic and observed spectra with a two-step process. First, the continuum level is normalized by adapting the corrected sigma-clipping method of STATCONT (Sánchez-Monge *et al.*, 2018). Sigma-clipping is a straightforward iterative process that can be used to find the continuum level in spectra that are not heavily blanketed by lines. The process is: 1) Calculate the standard deviation (σ) and the median (m) of the data; 2) Remove all data points that are smaller or larger than $m \pm \alpha\sigma$, where α is a parameter set by the user; 3) Repeat from step 1 until a selected tolerance level, defined as $(\sigma_{\rm old} - \sigma_{\rm new})/\sigma_{\rm new}$, is met. The corrected sigma-clipping method of STATCONT allows for continuum level determination of absorption- or emission-dominated spectra by adding or subtracting the uncertainty in the determined continuum level, respectively. The second step of our rectification

Table 4.6 Observed cluster properties. Ages and $[M/H]$ values in columns two and three are from Forbes (2010), except where otherwise indicated ([a] Boyles *et al.* (2011), [b] Koleva *et al.* (2008), [c] Harris 1996 (2010 ed), [d] Leaman (2012)), while v_σ values in column four are from Zaritsky *et al.* (2014). Parameters in columns five, six, and seven are from CBM17.

ID	Age (Gyr)	$[M/H]$	v_σ (km s^{-1})	Age$_{CBM}$ (Gyr)	$[M/H]_{CBM}$	$v_{\sigma,CBM}$ (km s^{-1})
NGC 104	13.06	-0.78	11.5±0.2	10.0±3.0	-0.65±0.05	12.6±1.2
NGC 362	10.37	-1.09	9.2±0.4	14.0±1.0	-1.14±0.04	9.1±1.2
NGC 2808	10.2[a]	-1.14[b]	13.0±0.5	11.5±1.5	-1.04±0.04	13.7±1.1
NGC 6093	12.54	-1.47	9.5±0.5	12.5±2.5	-1.65±0.09	11.9±3.3
NGC 6388	···	-0.55[c]	18.4±0.6	9.0±4.0	-0.33±0.13	23.1±2.5
NGC 6397	···	-1.76	···	11.0±4.0	-2.05±0.03	···
NGC 6440	···	-0.36[c]	13.3±0.7	9.0±4.0	-0.34±0.08	15.9±1.7
NGC 6441	···	-0.53[d]	16.5±0.7	9.0±6.0	-0.46±0.11	18.1±2.8
NGC 6528	···	-0.11[c]	5.8±0.5	8.5±1.5	-0.31±0.06	6.4±1.4
NGC 6553	···	-0.18[c]	7.0±0.5	10.0±3.0	-0.35±0.03	7.8±1.9
NGC 6752	11.78	-1.24	6.6±0.4	11.0±4.0	-1.58±0.03	7.0±1.5
Fornax 3	···	···	···	14.0±1.0	-2.27±0.05	9.9±2.6

process is to remove any remaining curvature by fitting a second order polynomial to points within $1 \pm \sigma_{\rm scm}$, where $\sigma_{\rm scm}$ is the uncertainty inherent in the sigma clipping method.

Our core analysis method allows us to measure the age and metallicity of an observed GC by fitting the line profiles of selected absorption lines. From the literature we have compiled a list of over 600 spectral lines at optical and NIR wavelengths that serve as potential diagnostics of age and metallicity (Colucci *et al.*, 2009, 2011, 2012; McWilliam & Bernstein, 2008; Sakari *et al.*, 2013), 470 of which we model in NLTE. Of these 470 lines, 359 are found to be in our wavelength range of interest. We combine this list with the lines identified in our sensitivity analysis, for a total of 445 diagnostic features in the wavelength range $\lambda = 4100$ to 7500 $\mathring{A}$, 31 of which were both present in the literature lists and identified by our analysis. These 31 lines are listed in Table 4.7.

To determine the best fitting synthetic population, we utilize the chi-squared minimization technique of the FIREFLY code (Wilkinson *et al.*, 2017). We have adapted the code to use our synthetic spectra, and only find a single best fitting SSP, rather than a linear combination of SSPs, as identifying multiple cluster populations is beyond the scope of this work. The reduced chi-squared statistic is calculated as

$$\chi^2_\nu = \frac{1}{\nu} \sum_\lambda \frac{(F_{\rm data}(\lambda) - F_{\rm model_i}(\lambda))^2}{\sigma(\lambda)^2}, \tag{4.2}$$

where $F_{\rm data}(\lambda)$ and $F_{\rm model}(\lambda)$ are the fluxes of the observed and synthetic spectra as

Table 4.7 Diagnostic spectral lines previously reported in the literature that we identified as sensitive.

Species	λ_0 (Å)	Species	λ_0 (Å)	Species	λ_0 (Å)
Ba II	4935.4545	Ca I	7150.1202	Fe I	6548.0461
Ca I	4456.0280	Ca I	7328.1652	Mn I	5396.16895396.1689
Ca I	5350.9534	Fe I	4133.2243	Mn I	6018.3053
Ca I	5583.5163	Fe I	4261.6730	Na I	5689.7837
Ca I	5602.8323	Fe I	4261.6730	Ti I	4992.4574
Ca I	5859.0749	Fe I	4462.9045	Ti I	5868.0784
Ca I	6440.8544	Fe I	4634.2079	Ti I	7211.4221
Ca I	6464.3515	Fe I	4655.9119	Ti I	7253.7071
Ca I	6473.4500	Fe I	5303.7746	Ti II	4396.2671
Ca I	6495.5751	Fe I	6338.5764	···	···
Ca I	6574.5931	Fe I	6423.1246	···	···

functions of wavelength, respectively, $\sigma(\lambda)$ is the error in the observed spectra, and ν is the number of degrees of freedom. We take the error to be $\sigma(\lambda) = F_{\rm data}(\lambda)/SN$, the observed flux at a given wavelength divided by the signal-to-noise of the observed spectrum, and express the degrees of freedom as $\nu = N - m$, where N is the number of wavelength sampling points used in calculating the statistic, and m is the number of parameters being fit (two in our case, the cluster age and $[M/H]$). The uncertainty in our chi-squared values is taken as

$$\sigma_{\chi^2_\nu} = \frac{1}{2\nu}\sum_{\lambda}\frac{\Big(\big(1+\frac{1}{SN}\big)F_{\rm data}(\lambda) - F_{\rm model_i}(\lambda)\Big)^2 - \Big(\big(1-\frac{1}{SN}\big)F_{\rm data}(\lambda) - F_{\rm model_i}(\lambda)\Big)^2}{\sigma(\lambda)^2}, \tag{4.3}$$

representing the range of possible values the statistic can take by scaling the observed flux higher or lower by a factor of $1/SN$. For each potential diagnostic feature fit,

a three dimensional surface of chi-squared values is computed as a function of both the cluster age and metallicity for each combination of modelling treatment, NLTE or LTE, and abundance distribution, α-enhanced or scaled-solar. This surface is parameterized with a fourth order polynomial of the form

$$colour = \sum_{i=0}^{2} \sum_{j=0}^{2} k_{ij} \cdot Age^{i} \cdot [M/H]^{j} \tag{4.4}$$

where the k_{ij}'s are constant coefficients. The surface is minimized to obtain the best fitting age and metallicity combination for that feature. An example surface for NGC 104 is shown in Figure 4.5.

The observed spectra are investigated by eye to determine if a given diagnostic or potential diagnostic line is present and detectable relative to the noise. This results in differing numbers of diagnostic lines per cluster available for analysis. For each observed spectrum, rather than fit individual line profiles, we fit a number of 10 Å windows which contain a minimum of three diagnostic lines. These windows are selected to avoid telluric features and to avoid molecular features, which PHOENIX does not model in NLTE. Two example windows for NGC 104 overplotted with 13.0 Gyr IL spectra of varying metallicity are shown in Figure 4.6. Additional representative 10 Å windows for each of the 12 clusters are included in Appendix B.

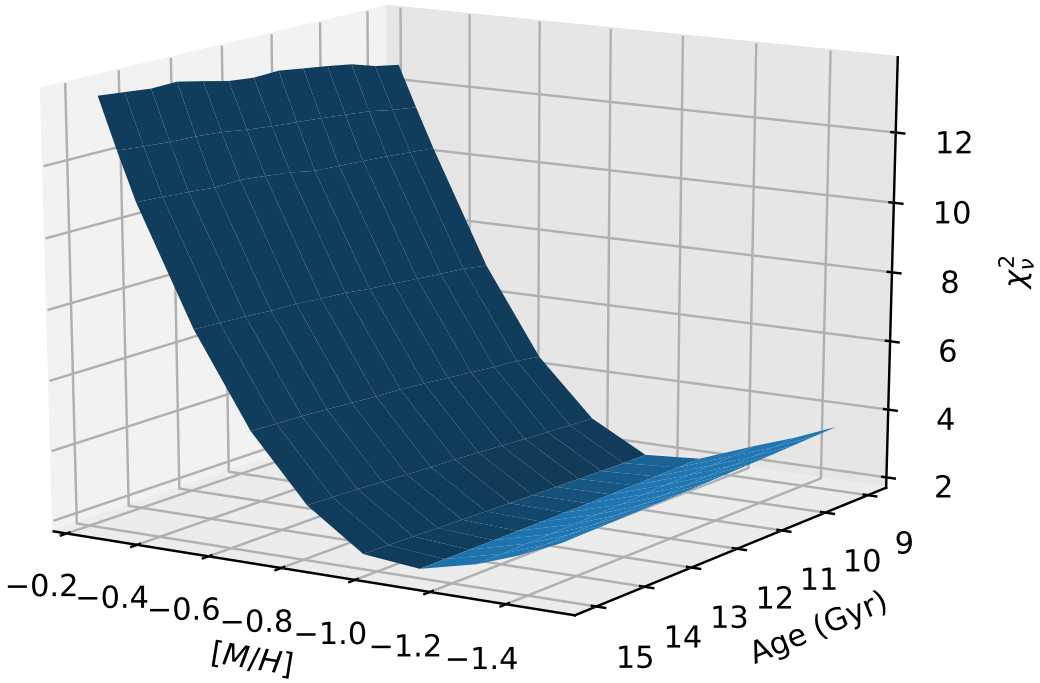

Figure 4.5 NGC 104 reduced chi-squared surface for the 10 $\mathring{A}$ window spanning $\lambda =$ 6703.8 to 6713.8 $\mathring{A}$. This window contains three Fe I lines, λ6705.4268, λ6706.9563, and λ6712.1757.

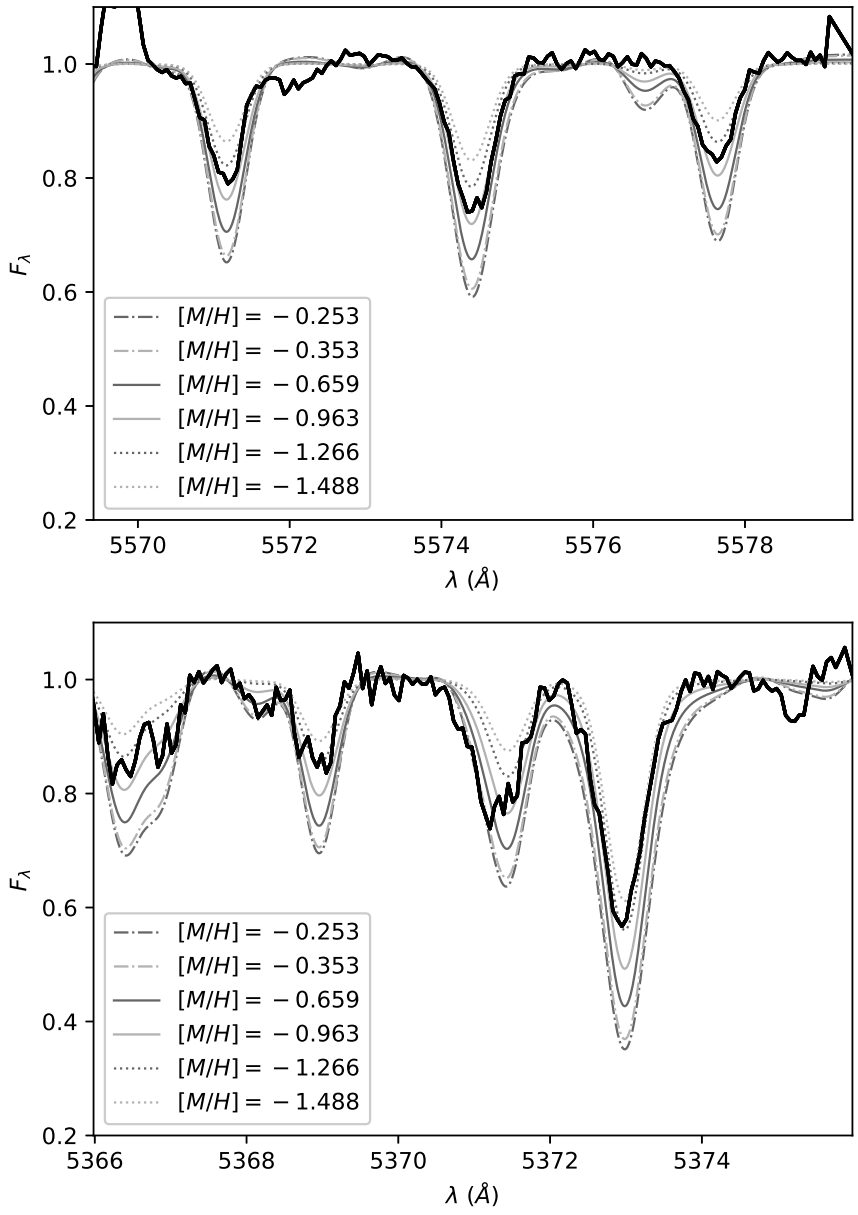

Figure 4.6 Example 10 $\mathring{A}$ windows for NGC 104 with 13.0 Gyr NLTE α-enhanced IL spectra overplotted. *Top*: The window contains three Fe I lines, the Fe I λ5571.1777, Fe I λ5574.3986 and Fe I λ5577.6474 lines. The best fitting IL synthetic spectrum is $[M/H] = -0.963$. *Bottom*: The window contains three more Fe I lines, Fe I λ5368.9687, Fe I λ5371.4674 and Fe I λ5372.9948. The best fitting IL synthetic spectrum is $[M/H] = -1.266$.

4.5 RESULTS

4.5.1 Derived Ages and Metallicities

We obtain a separate estimate of the age and metallicity for each 10 $\mathring{A}$ window fit with synthetic spectra. For windows present in overlapping regions of echelle orders, estimates are obtained for each order. The derived ages and metallicities are averaged over all windows for a given cluster, and are presented with their standard deviations in Tables 4.8 and 4.9, respectively. For NGCs 6093, 6397, 6752, and Fornax 3, we were unable to obtain age estimates. The calculated chi-squared statistics for these clusters were equivalent within uncertainty along the age axes of the surfaces, and we were consequently unable to minimize them in the age dimension. The derived metallicities for NGC 6397 and Fornax 3 are considered to be upper limits as the best fitting values for all features were the most metal poor synthetic spectra of our library.

The CBM17 ages of for all clusters fall within one standard deviation (1σ) of our values, with the exception of NGC 6528, where ours are found to be more than 2σ larger for LTE derived values, and more than 5σ larger for NLTE derived values. Ages derived from the different abundance distributions are well within 1σ of one another, and similarly, so are those derived from the different modelling treatments. Ages derived from NLTE spectra show a reduced spread in the distribution of values for a cluster when compared with LTE, where the difference of the standard deviations are $\Delta_{\mathrm{NLTE},\%}(\sigma_{\mathrm{Age}}) \approx$ -20 to -50 %.

Table 4.8 Derived ages of the 11 GCs for all combinations of modelling treatment (NLTE & LTE), and abundance distribution (scaled-solar & α-enhanced). Column headers indicate the modelling treatment and abundance distribution (α for α-enhanced and $\odot$ for scaled-solar). Presented values are the average $\pm$ the standard deviation over all fitted windows for a cluster. Missing values indicate where chi-squared coefficients were equivalent within uncertainty and no minimum was detectable.

ID	Age (Gyr) (NLTE, α)	Age (Gyr) (LTE, α)	Age (Gyr) (NLTE, $\odot$)	Age (Gyr) (LTE, $\odot$)
NGC 104	12.9 ± 0.7	12.6 ± 1.2	12.9 ± 0.7	12.8 ± 1.2
NGC 362	12.7 ± 0.6	12.4 ± 1.1	12.7 ± 0.9	12.5 ± 1.3
NGC 2808	11.3 ± 0.8	11.1 ± 1.1	11.5 ± 0.5	11.0 ± 1.1
NGC 6093	...	...	...	...
NGC 6388	10.2 ± 0.7	10.2 ± 1.0	10.3 ± 0.6	10.1 ± 1.2
NGC 6397	...	...	...	...
NGC 6440	10.0 ± 0.5	9.8 ± 1.1	10.3 ± 0.7	10.0 ± 1.0
NGC 6528	13.0 ± 0.6	13.0 ± 1.1	13.1 ± 0.5	13.0 ± 1.1
NGC 6553	11.0 ± 0.8	11.8 ± 1.0	11.1 ± 0.8	11.0 ± 1.1
NGC 6752	...	...	...	...
Fornax 3	...	...	...	...

Table 4.9 Same as Table 4.8, but for derived metallicities. Values for NGC 6397 and Fornax 3 are upper limits.

ID	$[M/H]$ (NLTE, α)	$[M/H]$ (LTE, α)	$[M/H]$ (NLTE, $\odot$)	$[M/H]$ (LTE, $\odot$)
NGC 104	-0.90 ± 0.05	-0.96 ± 0.26	-1.15 ± 0.05	-1.19 ± 0.26
NGC 362	-1.15 ± 0.05	-1.27 ± 0.24	-1.40 ± 0.05	-1.50 ± 0.25
NGC 2808	-1.21 ± 0.06	-1.29 ± 0.26	-1.44 ± 0.06	-1.51 ± 0.28
NGC 6093	-1.41 ± 0.06	-1.43 ± 0.22	-1.66 ± 0.07	-1.70 ± 0.26
NGC 6388	-1.20 ± 0.05	-1.30 ± 0.21	-1.44 ± 0.05	-1.52 ± 0.23
NGC 6397	< -1.49	< -1.49	< -1.79	< -1.79
NGC 6440	-0.86 ± 0.07	-0.93 ± 0.30	-1.08 ± 0.08	-1.12 ± 0.33
NGC 6528	-0.35 ± 0.03	-0.36 ± 0.15	-0.50 ± 0.06	-0.49 ± 0.25
NGC 6553	-0.45 ± 0.05	-0.45 ± 0.21	-0.62 ± 0.07	-0.61 ± 0.29
NGC 6752	-1.38 ± 0.03	-1.43 ± 0.13	-1.62 ± 0.04	-1.68 ± 0.15
Fornax 3	< -1.49	< -1.49	< -1.79	< -1.79

Similar to the derived ages, we find that the metallicities derived from fitting NLTE synthetic spectra to the observed clusters show less spread in the distributions than those from fitting LTE spectra, with $\Delta_{\mathrm{NLTE},\%}(\sigma_{[\mathrm{M/H}]}) \approx$ -66 to -75 %. We do find that scaled-solar spectra produce metallicity estimates that are more metal poor than the α-enhanced spectra by $\sim$ 0.2 to 0.25 dex, exceeding 2σ or 3σ in NLTE, and in some cases exceeding 1σ in LTE. We find the CBM17 values fall within 1σ of our LTE derived metallicities for every cluster except NGC 6388 and NGC 6440, where our estimates are more metal poor than the CBM 17 values by more than 3σ and 2σ, respectively. The standard deviations of the metallicity values derived from LTE spectra are such that the abundance distribution cannot be determined in the remaining clusters, with both the scaled-solar and α-enhanced values being within 1σ of the CBM17 values. In some of these cases, the metallicities derived from NLTE spectra are better able to distinguish between abundance distributions. Clusters NGC 362, NGC 2808, and NGC 6553 are fall within 3σ or less of the α-enhanced distributions, while exceeding 3σ for scaled-solar distributions, and NGC 6752 falls within 1σ of the scaled-solar value but exceeds 3σ of the α-enhanced value. Clusters NGC 6093 and NGC 6528 are less strongly distinguished, falling within 1σ of the scaled-solar and α-enhanced values, respectively, but also within 3σ of the other distribution in either case. The remaining CBM17 values do not fall within 3σ of the NLTE derived metallicities for either abundance distribution.

4.6 SUMMARY

We have identified a total of 154 lines sensitive to cluster age or metallicity, 18 of which are sensitive to both. These lines represent 14 different atomic species, the majority of which are Fe I, Ca I, and Ti I lines. The strength of features was found to be significantly more sensitive to $[M/H]$ than age, showing a much larger change in both EW and depth at line center. Differences in EW are $-0.03 \leq \Delta_{\rm NLTE}(EW) \leq 0.08$, and appear to be insensitive to age for species other than Fe I, Cr I, V I, and Ti I. We observe a trend that for age insensitive species, $\Delta_{\rm NLTE}(EW)$ increases with increasing $[M/H]$.

A collection of 12 GC IL spectra were obtained from CBM17, and fit with our synthetic IL spectra to derive ages and metallicities. Derived ages were found to be in agreement with CBM17 values within 1σ, with the exception of NGC 6528, where the CBM17 values were found to exceed our values by 2σ to 5σ, depending on modelling treatment. Metallicities derived from LTE spectra were found to agree with CBM17 values within 1σ, except for NGC 6388 and NGC 6440, for which our values were found to be more metal poor than CBM17 by more than 3σ and 2σ, respectively. We were unable to distinguish between scaled-solar and α-enhanced abundance distributions with LTE spectra, but were able to distinguish four clusters confidently with NLTE spectra, and two additional clusters with a lesser degree of confidence. CBM17 metallicities for NGCs 362, 2808, and 6528 are within 3σ or less of our α-enhanced values and exceed 3σ of the scaled-solar values, while NGC 6752

was within 1σ of our scaled-solar value, and exceeded 3σ of our α-enhanced value. NGCs 6093 and 6528 agreed within 1σ of our scaled-solar and α-enhanced values, respectively, but also within 3σ of the opposite abundance distributions. The LTE and NLTE derived values of both ages and metallicities were found to agree with each other within 1σ in all cases, but find the NLTE derived values to exhibit less spread in their individual distributions, with $\Delta_{\mathrm{NLTE,\%}}(\sigma_{\mathrm{Age}}) \approx$ -20 to -75 % depending on abundance distribution and parameter of interest.

5 Conclusions

In this work, we investigated the impact of NLTE modelling on photometric IL colours, the EWs of potential diagnostic spectral lines in IL spectra, and derived ages and metallicities of 12 Galactic GCs, and also presented several results regarding aspects of the general methodology that may prove useful in advising futures studies. Our investigation of the resolution of the CMD discretization has demonstrated that synthetic IL spectra display a dependency on the resolution, which is more prominent at shorter wavelengths. We find that the 25 to 35 boxes recommended in the literature do not provide enough resolution to critically sample the upper main sequence and horizontal branch. A minimum of 40 to 50 boxes is necessary to minimize this resolution dependency.

Initial analysis suggests that NLTE effects in main sequence stars have approximately equivalent influence on IL spectra as do those in more evolved stars at UV and optical wavelengths. At IR wavelengths, NLTE effects in main sequence stars are diminished to the point of having negligible impact on the IL. This diminishing appears to be independent of CMD discretization resolution for the resolutions investigated here.

We have demonstrated that, for a fixed metallicity, age estimates which may be derived by fitting observed IL photometric colours with synthetic LTE colours were shown to differ from NLTE derived ages by up to 2.5 Gyr. These differences

are comparable with the limiting observational precision of photometric colours in the Harris Catalog. When the metallicity was allowed to vary, synthetic photometric colours were demonstrated to exhibit several global properties in both LTE and NLTE IL spectra. The choice of abundance distribution affected photometric colours of all indices, independent of age and metallicity. Colours of α-enhanced $\alpha = +0.4$ clusters were bluer than scaled-solar clusters by up to 0.15 mag. Regardless of abundance distribution, colours of all indices were seen to redden with increasing metallicity over the full parameter space, and redden with increasing age up to 13.0 Gyr. In clusters older than 13.0 Gyr, colours of clusters with $[M/H] > -1.0$ continued to redden with increasing age, while colours of clusters with $[M/H] < -1.0$ got bluer with increasing age.

The investigation of the impact of NLTE effects on the IL photometric colours revealed trends that varied over the parameter space. At all ages and metallicites, NLTE colours were seen to be bluer than LTE colours by up to 0.06 mag, with the exception of $J - K$ in α-enhanced clusters, where the NLTE colours were redder than LTE by -0.04 mag. NLTE effects were seen to be independent of cluster age for all indices except $U - B$, where $\Delta_{\rm NLTE}(U - B)$ was seen to increase with age. As a function of metallicity, $\Delta_{\rm NLTE}$ was seen to monotonically increase with increasing metallicity, with the exceptions of $\Delta_{\rm NLTE}(B-V)$ and scaled-solar $\Delta_{\rm NLTE}(J-K)$ which peaked at $[M/H]$ = -0.963. The significance of these NLTE effects was quantified by comparison with LTE IL spectra generated from isochrones modelled with convective

core overshoot. Core overshoot was seen to have no impact on IL colours within uncertainty at all ages, metallicities, and abundance distributions, with the exception of $[M/H]$ = -0.506, -0.659, and -0.811 α-enhanced clusters, where core overshoot reddened $U-B$ by up to 0.05 mag and other colours by up to 0.015 mag.

The NLTE impact on the age-metallicity degeneracy of Galactic GCs introduced an increase in metallicity of up to 0.15 dex for given ages, while NLTE effects introduced a change in age of $\pm$ 1 to 2 Gyr for given metallicities. These changes were generally larger at shorter wavelengths. The NLTE effects were also seen to be dependent upon abundance distribution, with $\Delta_{\rm NLTE}([M/H],\alpha) > \Delta_{\rm NLTE}([M/H],{\rm solar})$ for bluer indices, and the reverse for redder indices, crossing over for $V-I$. Under these conditions, the derived metallicities of 47 Tuc, ω Cen, and M13 increased by up to 0.05 dex when derived from NLTE colours.

Our investigations of the sensitivity of spectral features has revealed a total of 240 spectral lines that met our sensitivity criteria for either age or metallicity, 30 of which were sensitive to both parameters, and 31 of which have been previously identified in the literature as diagnostic features. The lines represented a total of 19 different species, with the majority identified as Fe I, Ca I, and Ti I lines. The lines were found to show significantly greater sensitivity to $[M/H]$ than age, and were also found to show greater sensitivity to either parameter over the wavelength range λ = 4000 to 9000 Å than over λ = 12000 to 22000 Å . Of our lines, 127 were identified as sensitive in NLTE IL spectra, 66 in LTE IL spectra, and 47 in both NLTE and LTE spectra.

Differences in the EWs of the sensitive lines due to NLTE effects were insensitive to age for species other than Fe I, Cr I, V I, and Ti I at short wavelengths, and insensitive to age for all species at wavelengths longer than $\lambda \gtrsim 18000$ Å . A general trend was observed in the age insensitive species that $\Delta_{\rm NLTE}(EW)$ increased with increasing $[M/H]$ in the range $4000 \lesssim \lambda \lesssim 9000$ Å, decreased with increasing $[M/H]$ for $12000 \lesssim \lambda \lesssim 15000$ Å, and increased again with increasing $[M/H]$ for $\lambda \gtrsim 18000$ Å . The impact of NLTE effects on sensitive line EWs was larger for longer wavelengths, with $-0.15 \leq \Delta_{\rm NLTE}(EW) \leq 0.25$ in the range$\lambda = 12000$ to 22000 Å and $-0.03 \leq \Delta_{\rm NLTE}(EW) \leq 0.08$ in the range$\lambda = 40000$ to 9000 Å, summed over all species.

For the 12 observed Galactic GCs, derived ages were found to be in agreement with CBM17 values within 1σ. The one exception was NGC 6528, where the CBM17 value was found to exceed our values by 2σ (LTE IL spectra) to 5σ (NLTE IL spectra). Metallicities derived from LTE spectra were found to agree with CBM17 values within 1σ, except for NGC 6388 and NGC 6440, for which our values were found to be more metal poor than CBM17 by greater than 3σ and 2σ, respectively. We were unable to distinguish between scaled-solar and α-enhanced abundance distributions with LTE spectra in all cases, but were able to distinguish the abundance distributions of six clusters with NLTE spectra, with varying degrees of confidence. The LTE and NLTE derived values of both age and metallicity were found to agree with each other within 1σ in all cases, but the NLTE derived values exhibited less spread in their individual

distributions, with $\Delta_{\mathrm{NLTE},\%}(\sigma) \approx$ -20 to -75 % depending on abundance distribution and parameter of interest.

While the detailed aspects of GC SPS using SSPs may not necessarily be accurate because of the existence of multiple populations and exotic objects such as blue stragglers and RR Lyrae variables, the methods and degrees of CMD discretization, and the 1D nature of stellar atmospheric modelling, we believe the calculations presented here represent a reasonable compromise between physical reality, numerical resolution, and the duration of modelling on current computational resources. The goal of this work was not to present a detailed model of GC SPS but, rather, to produce reasonable estimates of the impact NLTE modelling of stellar atmospheres and synthetic spectra may have on global parameters derived from GC IL.

As demonstrated, the magnitudes of NLTE effects on different GC IL observable quantities are of the same order as current limits of detectability in most cases. It will soon become necessary to fully adopt NLTE modelling in GC IL spectral synthesis for accurate determination of global cluster parameters, discarding LTE modelling. We are ideally situated to make this change in the coming years, as advances in observing technology push the limits of detectability lower while, simultaneously, advances in high-performance computing making NLTE calculations computationally affordable.

The next step in this work will be to adapt the current methodology to synthesize multiple GC populations as linear combinations of SSPs, and further investigate the list of potential diagnostic features to remove any blends with weak features, confirm

identifications, and confirm the quality of the reported oscillator strengths.

References

Aaronson, M. & Olszewski, E.W., 1986, AJ, 92, 580

Asplund, M., Grevesse, N., Sauval, A. J. et al., 2009, ARA&A, 47, 481

Bastian, N. & Lardo, C., 2018, ARA&A56, 1

Bellini, A., Renzini, A., Anderson, J., et al., 2015, ApJ, 805, 178-197

Bessel, M. S., 1988, PASP, 100, 1134

Bessel, M. S., 1990, PASP, 102, 1181

Bowman, W. P., Pilachowski, C. A., van Zee, L. et al., 2017, AJ, 154, 131

Boyles, J., Lorimer, D. R., Turk, P. J. et al., 2011, ApJ, 742, 51

Briley, M. M., Smith, V. V., & Lambert, D. L., 1994, ApJ, 424, L119-L122

Brodie, J. P., & Huchra, J. P., 1990, ApJ, 362, 503-521

Caffau, E., Ludwig, H-G., Steffen, M. et al., 2011, SoPh, 268, 255

Caldwell, N., Schiavon, R. P., Morrison, H. et al., 2011, AJ, 141, 18

Cardelli, J. A., Clayton, G. C., & Mathis, J. S., 1989, ApJ, 345, 245

Carretta, E. & Gratton, R. G., 1997, Å ps, 121, 95

Carretta, E., Bragaglia, A., Gratton, R. G. et al., 2010, Å p, 520, A95

Casetti-Dinescu, D.I., Girard, T.M., Korchagin, V.I. et al., 2010, AJ, 140, 1282

Cassisi, S., Salaris, M., Castelli, F. et al., 2004, ApJ, 616, 498

Cenarro, A. J., Peletier, R. F., Sánchez-Blázquez, P. et al., 2006, MNRAS, 374, 664

Coelho, P., Bruzual, G., Charlot, S. et al., 2017, MNRAS, 382, 498

Coelho, P. R. T., 2014, MNRAS, 440, 1027-1043

Cohen, R. E., Hempel, M., Mauro, F., et al., 2015, AJ, in press (arXiv:1509.01470v2)

Cohen, J. G., 1978, ApJ, 223, 487-508

Colucci, J. E., Bernstein, R. A., Cameron, S., et al., 2009, ApJ, 704, 385-414

Colucci, J. E., Bernstein, R. A., Cameron, S., et al., 2009, ApJ, 735, 55

Colucci, J. E., Bernstein, R. A., Cameron, S., et al., 2011, ApJ, 735, 55

Colucci, J. E., Bernstein, R. A., Cameron, S., et al., 2012, ApJ, 746, 29

Colucci, J. E., Bernstein, R. A., & McWilliam, A. 2017, ApJ, 834, 105

Cox, A. N., 2000, Allen's Astrophysical Quantities (4th ed.; New York, NY: Springer)

di Criscienzo, M., Caputo, F., Marconi, M. et al., 2006, MNRAS, 365, 1357

Dinescu, D.I., Girard, T.M., van Altena, W.F. et al., 2003, AJ, 125, 1373

D'Orazi, V., Gratton, R.G., Angelou, G.C. et al, 2015, MNRAS, 449, 4038

Drake, J. J. & Smith, G., 1991, MNRAS, 250, 89

Eadie, G. M., Springford, A. & Harris, W. E., 2017, ApJ, 838, 76

Elson, R. A. W., & Santiago, B. X., 1996, MNRAS, 278, 617

Faber, S. M. & Jackson, R. E., 1976, ApJ, 204, 668

Faber, S. M., Friel, E.D., Burstein, D. et al., 1985, ApJS, 57, 711

Faber, S. M., 1973, ApJ, 179, 731

Ferguson, J. W., Alexander, D. R., Allard, F. et al., 2005, ApJ, 623, 585

Forbes, D. A., & Bridges, T., 2010, MNRAS, 404, 1203

Forbes, D. A., Lasky, P., Graham, A. W. et al., 2008, MNRAS, 389, 1924

Forbes, D. A., 2010, MNRAS, 404, 1203

Forte, J. C., Strom, S. W., & Strom, K. M., 1981, ApJ, 245, L9

Geisler, D., Lee, M. G., & Kim, E., 1996, AJ, 111, 1529

Goudfrooij, P., Gilmore, D., Kissler-Patig, M., et al., 2006, MNRAS, 369

Gratton, R. G., Carretta, E., Bragaglia, A., et al., 2010, Å p, 517, A81

Graves, G. J. & Schiavon, R. P., 2008, ApJS, 177, 446

Grevesse, N., & Noels, A., 1993, in Origin and Evolution of the Elements, ed. N. Prantzos, E. Vangioni-Flam, & M. Cassé (Cambridge: Cambridge Univ. Press), 14

Grevesse, N., Scott, P., Asplund, M. *et al.*, 2015, Å p, 573, A27

Grevesse, N., Noels, A., & Sauval, A. J., 1996, ASP Conf. Ser., 99, 117-126

Harris, W.E., 1996, AJ, 112, 1487

Harris, W.E., 1996, AJ, 112, 1487

Herschel, W., Phil. Trans. R. Soc. London, 79, 212

Hidalgo, S. L., Pietrinferni, A., Cassisi, S. *et al.*, 2018, ApJ, 856, 125

Hubeny, I., 2017, MNRAS, 469, 841

Jang, S. Lee, Y-K., Joo, S-J. et al., 2014, MNRAS, 443, L15

Kinman, T., & Castelli, F., 2002, Å p, 391, 1039

Koleva, M. , Prugniel, Ph., Ocvirk, P. et al., MNRAS, 385, 1998

Kroupa, P., 2001, MNRAS, 322, 231-246

Kučinskas, A., Hauschildt, P. H., Brott, I. et al., 2006, Å p, 452, 1021

Lapenna, E., Mucciarelli, A., Lanzoni, B. et al, 2014, ApJ, 797, 124

Larsen, S. S., Brodie, J. P. & Strader, J., 2012, Å p, 546, A53

Larsen, S. S., Pugliese, G. & Brodie, J. P., 2018, arXiv pre-print, accepted for publication (Å p)

Leaman, R., AJ, 144, 183

Lee, H-C. & Worthey, G., 2005, ApJS, 160, 176

Martins, F., Schaerer, D. & Hillier, D. J., 2005, Å p, 436, 1049

Maschberger, Th., 2012, MNRAS, 429, 1725-1733

Mashonkina, L., Gehren, T., Shi, J.-R., et al., 2011, Å p, 528, A87

McWilliam, A., & Bernstein, R., 2008, ApJ, 684, 326-347

Milone, A. P., Marino, A. F., Mastrobuono-Battisti, A. et al., 2018, MNRAS, 479, 5005

Milone, A. P., 2013, Mem. Soc. Astron. Italiana, 84, 79

Monaco, L., Pancino, E., Ferraro, F. R. et al., 2004, MNRAS, 349, 1278

Morton, D., 2000, ApJS, 130, 403

Mucciarelli, A., Lapenna, E., Massari, D. et al, 2015, ApJ, 801,69

Muratov, A. L. & Gnedin, O. Y., 2010, ApJ, 718, 1266

Niederhofer, F., Bastian, N., Kozhurina-Platais, V. et al., 2016, MNRAS, 465, 4159

Oosterhoff, P. T., 1939, The Observatory, 62, 104

Peacock, M. B., Maccarone, T. J., Knigge, C. et al., 2010, MNRAS, 402, 803

Peng, E. W., Ford, H. C. & Freeman, K. C., 2004, ApJ, 602, 705

Perrett, K. M., Bridges, T. J., Hanes, D. A. et al., 2002, AJ, 123, 2490

Pietrinferni, A., Cassisi, S., Maurizio, S. *et al.*, 2006, ApJ, 642, 797-812

Pilachowski, C. A., Canterna, R., & Wallerstein, G., 1980, ApJ, 235, L21

Pilachowski, C. A., Olszewski, E. W. & Odell, A., 1983, PASP, 95, 713

Piotto, G., Milone, A. P., Bedin, L. R., et al., 2015, AJ, 149, 91-118

Puzia, T. H. & Sharina, M. E., 2008, ApJ, 674, 909

Racine, R., Oke, J. B., & Searle, L. 1978, ApJ, 223, 82

Ross, J. E. & Aller, L. H., 1976, Science, 191, 1223

Sánchez-Blázquez, P., Peletier, R. F., Jiménez-Vincente, J. et al., 2006, MNRAS, 371, 703

Sánchez-Monge, Á., Schilke, P., Ginsburg, A. et al., 2018, Å p, 609, A101

Sakari, C. M., Shetrone, M. D., Venn, K. et al., 2013, MNRAS, 434, 358

Sakari, C.M., Venn, K., Shetrone, M., et al., 2014, MNRAS, 443, 2285

Sakari, C. M., Shetrone, M. D., Schiavon, R. P. *et al.*, 2016, ApJ, 829, 116

Schiavon R. P., Faber S. M., Castilho B. V. et al., 2002, ApJ, 580, 850

Schiavon, R. P., Rose, J. A., & Courteau, S. et al., 2004, ApJ, 608, 33

Schiavon, R. P., Caldwell, N., Conroy, C. et al., 2013, ApJ, 776, L7

Scott, P., Grevesse, N., Asplund, M. *et al.*, 2015, Å p, 573, A25

Scott, P., Asplund, M., Grevesse, N. *et al.*, 2015, Å p, 573, A26

Shapley, H., 1916, The Obervatory, 39, 452

Shapley, H., 1914, ApJ, 40, 443

Short, C. I. & Hauschildt, P. H., 2009, ApJ, 596, 501

Short, C. I. & Hauschildt, P. H., 2009, ApJ, 691, 1634

Short, C. I., Campbell, E. A., Pickup, H. et al., 2012, ApJ, 747, 2

Skrutskie, M. F., Cutri, R. M., Stiening, R. et al., 2006, AJ, 131, 1163

Smith, V.V., Cunha, K., Shetrone, M.D., et al. 2013, ApJ, 765, 16

Sneden, C., Kraft, R. P., Prosser, C. F., et al., 1991, AJ, 102, 2001

Trager, S. C., 2004, in Origin and Evolution of the Elements, ed. A. McWilliam & M. Rauch (Cambridge: Cambridge Univ. Press), 391

Valcheva, A. T., Ovcharov, E. P., Lalova, A. D., et al., 2015, MNRAS, 446, 730-736

van Albada, T. S. & Baker, N., 1973, ApJ, 185, 477

Wagner-Kaiser, R., Stenning, D. C., Sarajedini, A. et al., 2016, MNRAS, 463, 3768

Whitmore, B. C., Sparks,W. B., Lucas, R., et al., 1995, ApJ, 454, L73

Wilkinson, D. M., Maraston, C., Goddard, D. et al., 2017, MNRAS, 472, 4297-4326

Worthey, G., Faber, S. M., Gonzalez, J. J. et al., 1994, ApJS, 94, 687

Worthey, G., 1994, ApJS, 95, 107

Yoon, S-J. & Lee, Y-K., 2002, Science, 297, 5581

Young, M. E. & Short, C. I., 2014, ApJ, 787, 43-55

Young, M. E. & Short, C. I., 2017, ApJ, 835, 292

Young, M. E. & Short, C. I., 2018, ApJ, *accepted for publication*

Zaritsky, D., Colucci, J. E., Pessev, P. M. et al., ApJ, 796, 71

Zinn, R., 1985, ApJ, 293, 424-444

Appendices

A Supplementary $\Delta_{\mathrm{NLTE}}(EW)$ Contour Plots

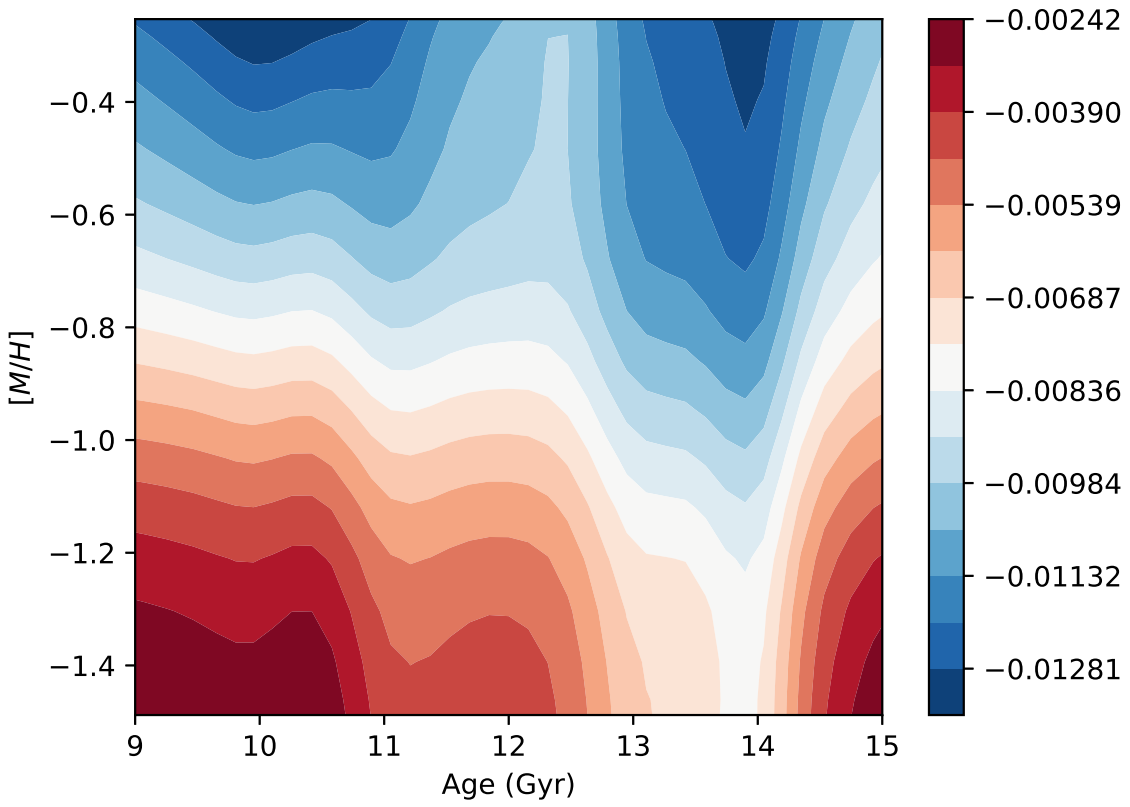

Figure A.1 Contour plot of $\Delta_{\rm NLTE}(EW)$ for the Al I λ15972.6514 line over the full parameter space of our synthetic IL spectra library for α-enhanced spectra. The countours sample $\Delta_{\rm NLTE}(EW)$ as indicated.

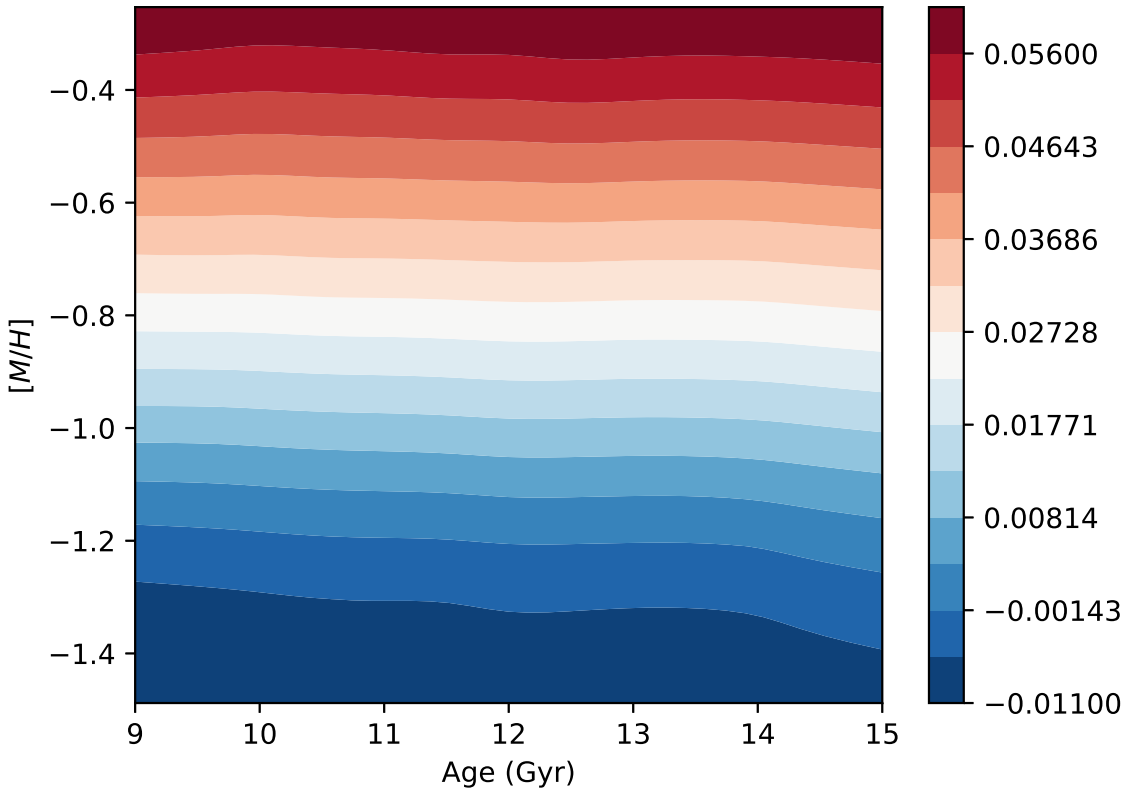

Figure A.2 Similar to A.1, but for the Al I λ21169.5304 line in α-enhanced IL spectra.

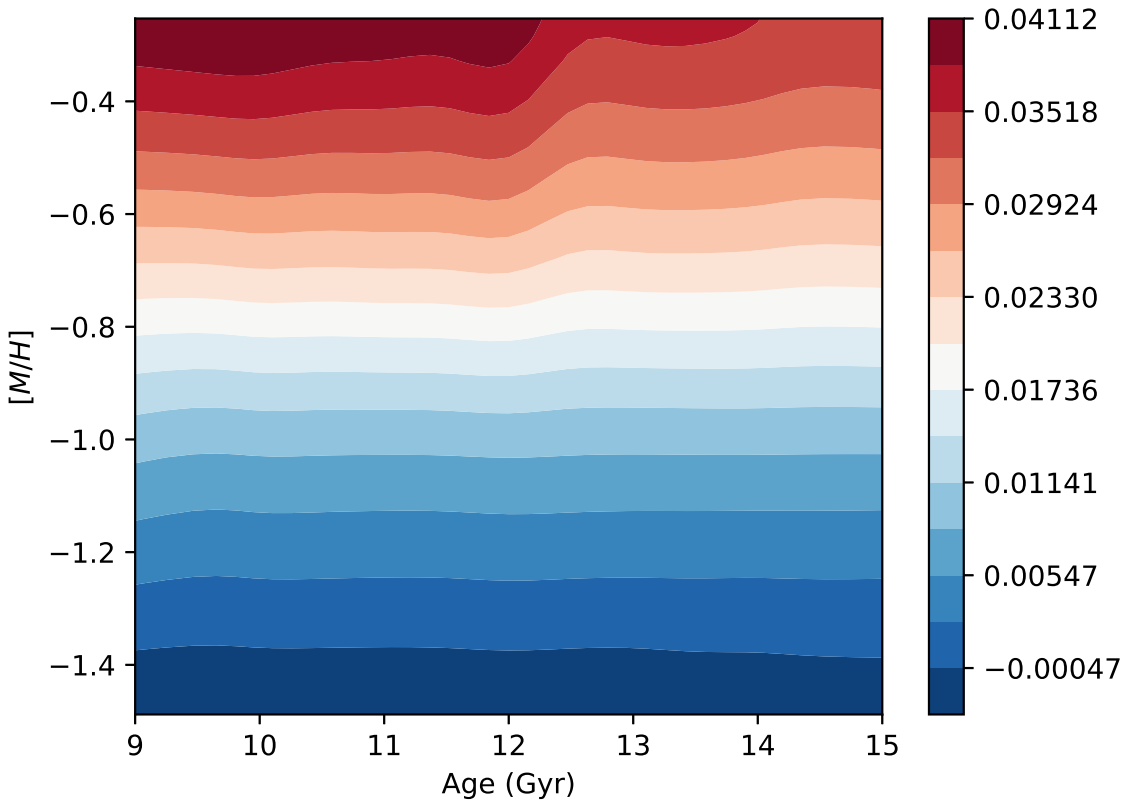

Figure A.3 Similar to A.1, but for the Ca I λ5859.0749 line in scaled-solar IL spectra.

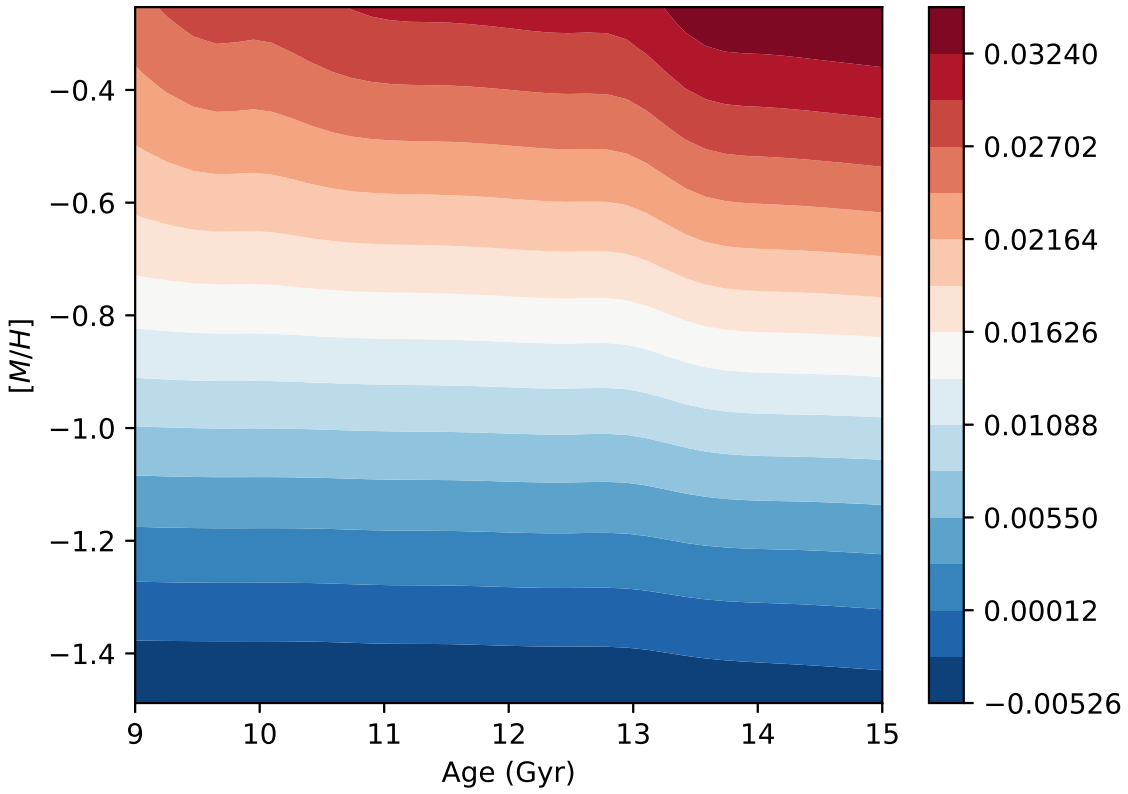

Figure A.4 Similar to A.1, but for the Ca I λ5859.0749 line in α-enhanced IL spectra.

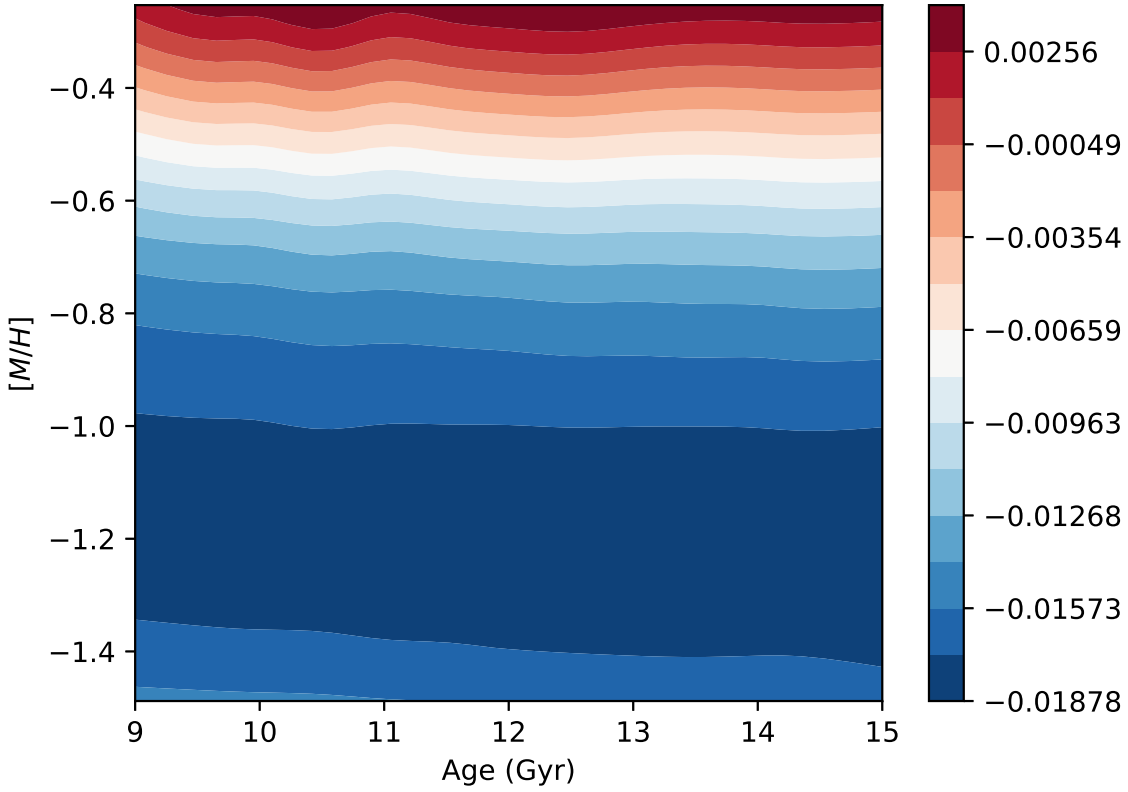

Figure A.5 Similar to A.1, but for the Ca I λ6451.5906 line in α-enhanced IL spectra.

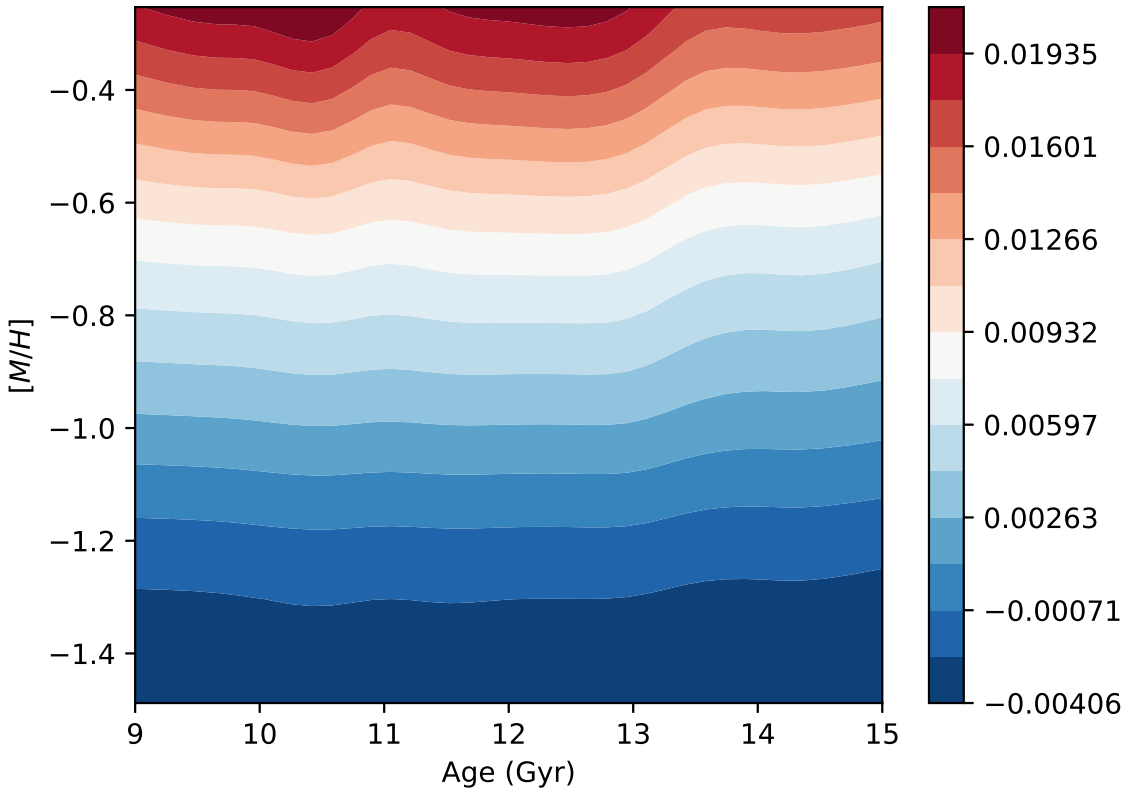

Figure A.6 Similar to A.1, but for the Ca I λ7204.1855 line in α-enhanced IL spectra.

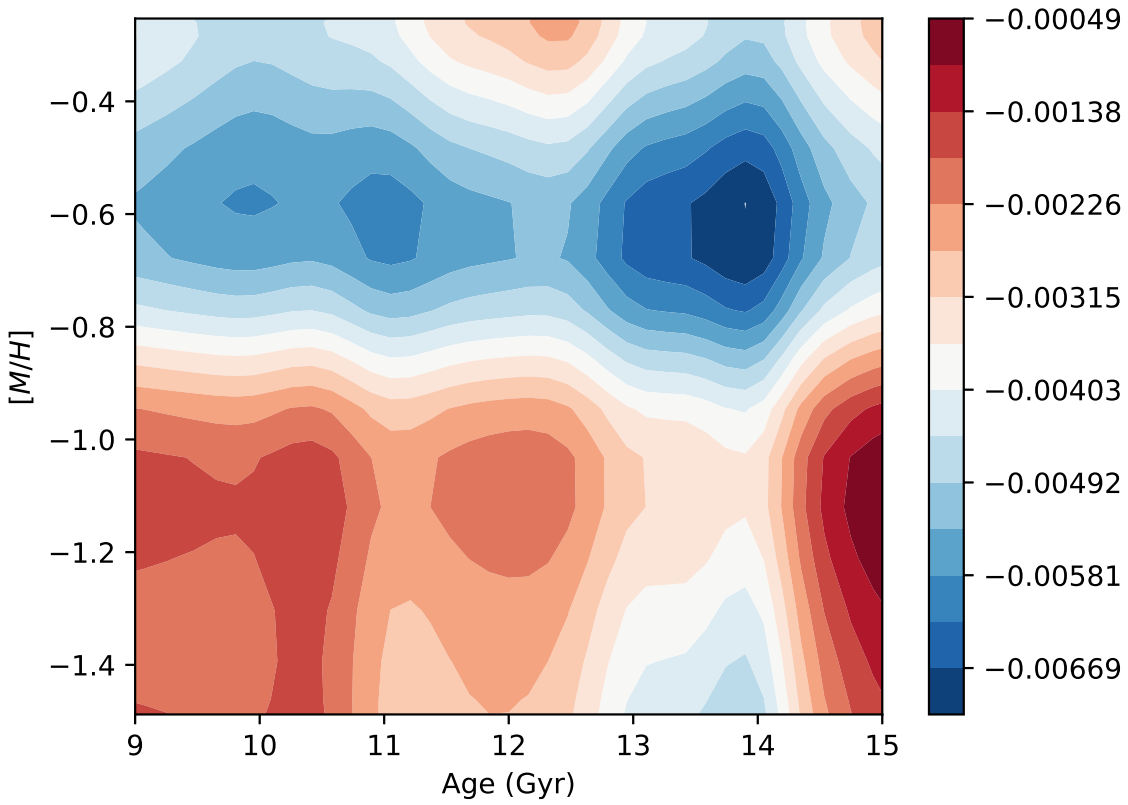

Figure A.7 Similar to A.1, but for the Ca I λ14469.2903 line in α-enhanced IL spectra.

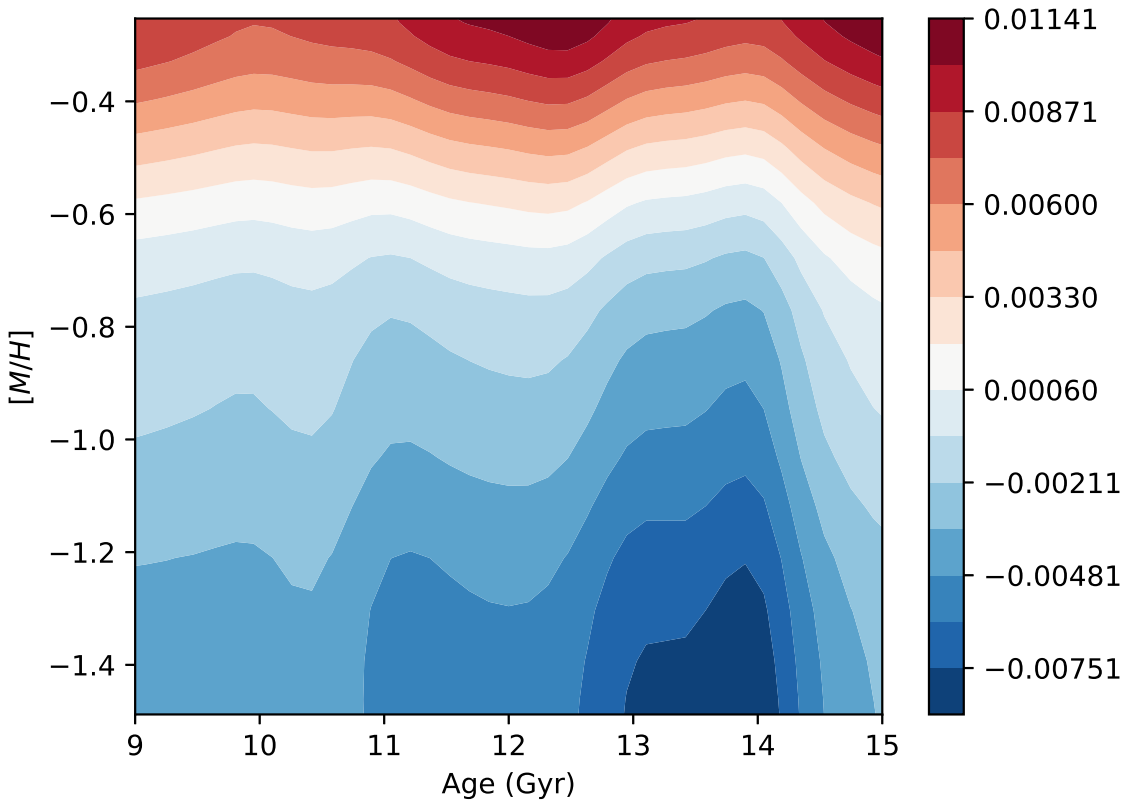

Figure A.8 Similar to A.1, but for the Ca I λ16543.1061 line in α-enhanced IL spectra.

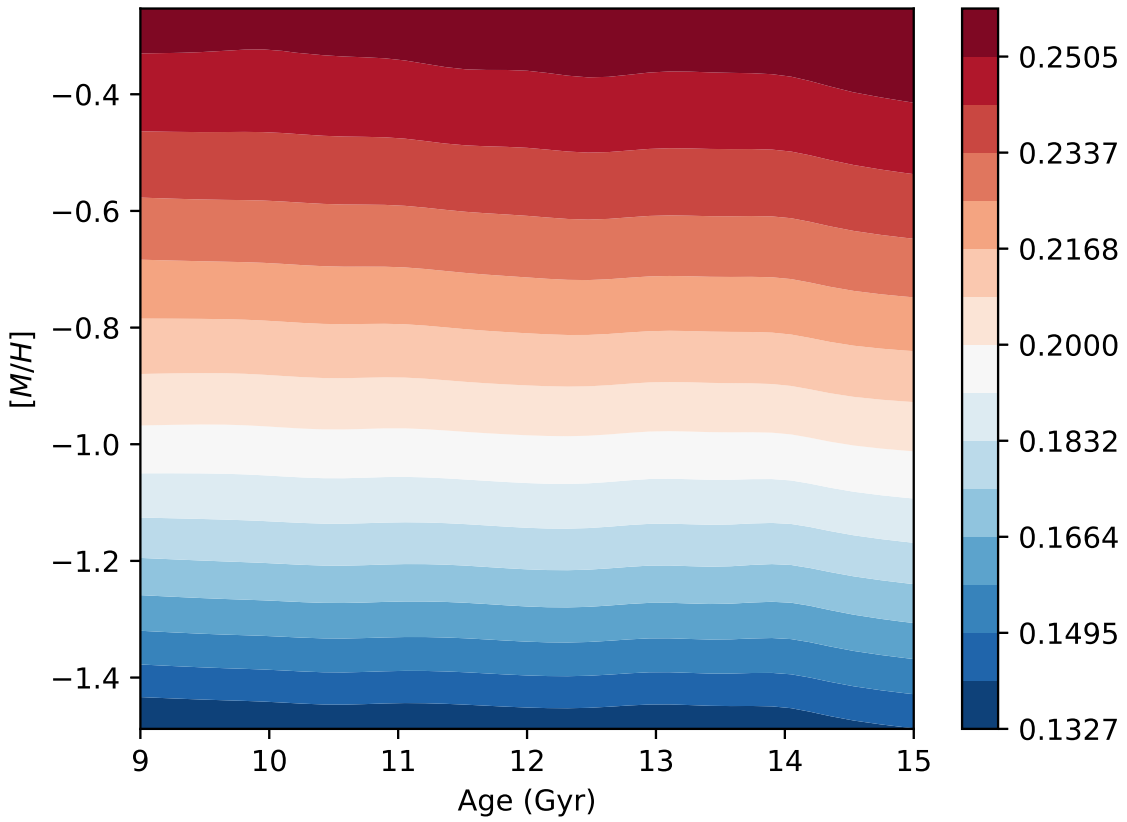

Figure A.9 Similar to A.1, but for the Ca I λ19458.2943 line in α-enhanced IL spectra.

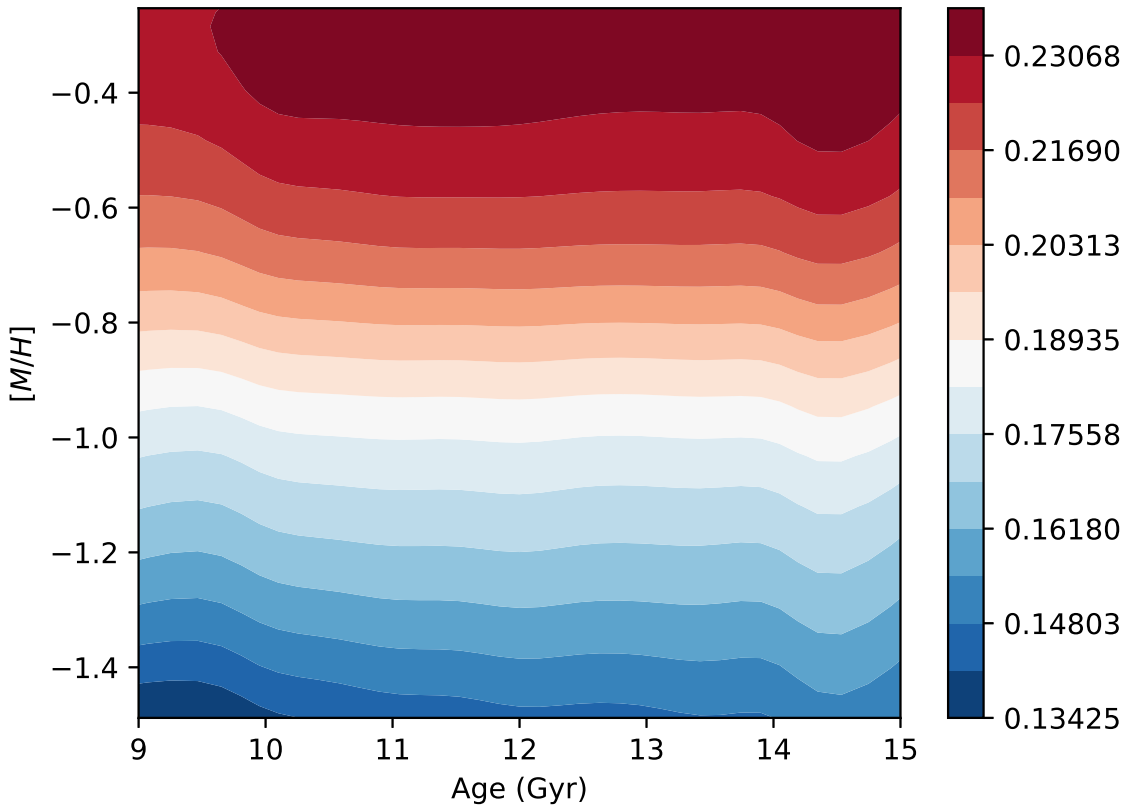

Figure A.10 Similar to A.1, but for the Ca I λ19458.2943 line in scaled-solar IL spectra.

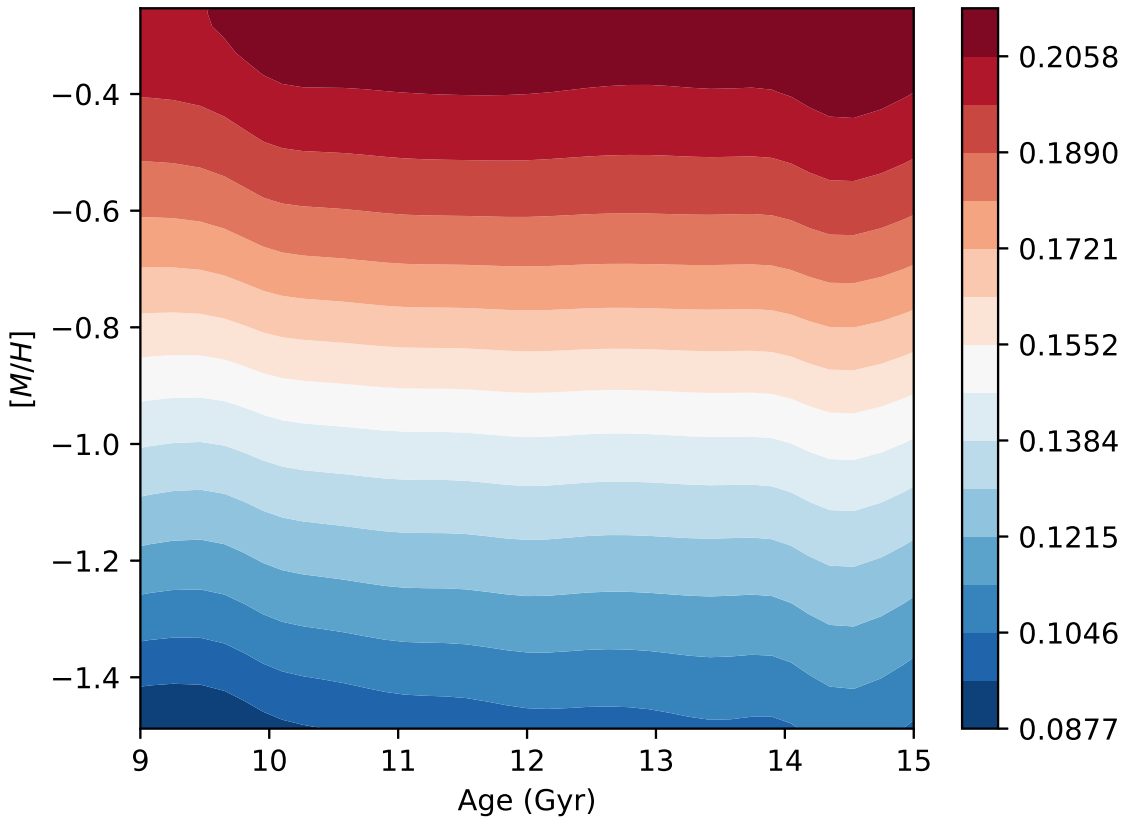

Figure A.11 Similar to A.1, but for the Ca I λ19511.0685 line in scaled-solar IL spectra.

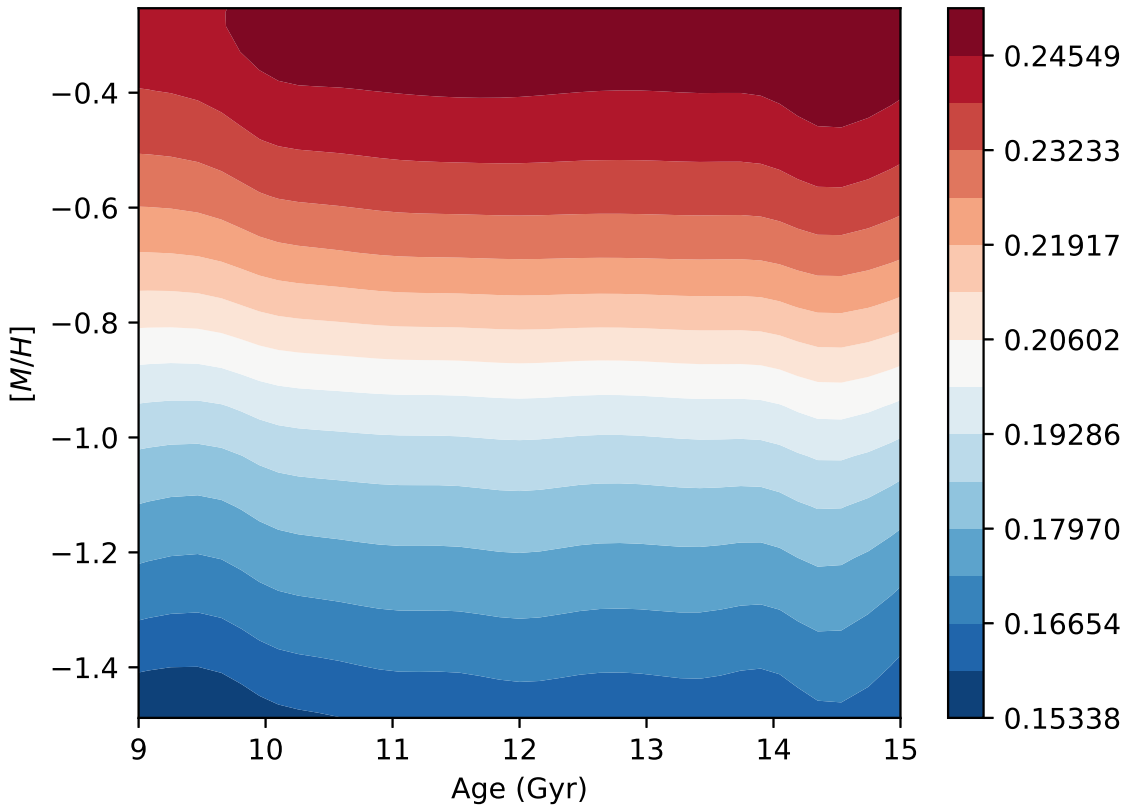

Figure A.12 Similar to A.1, but for the Ca I λ19782.1678 line in scaled-solar IL spectra.

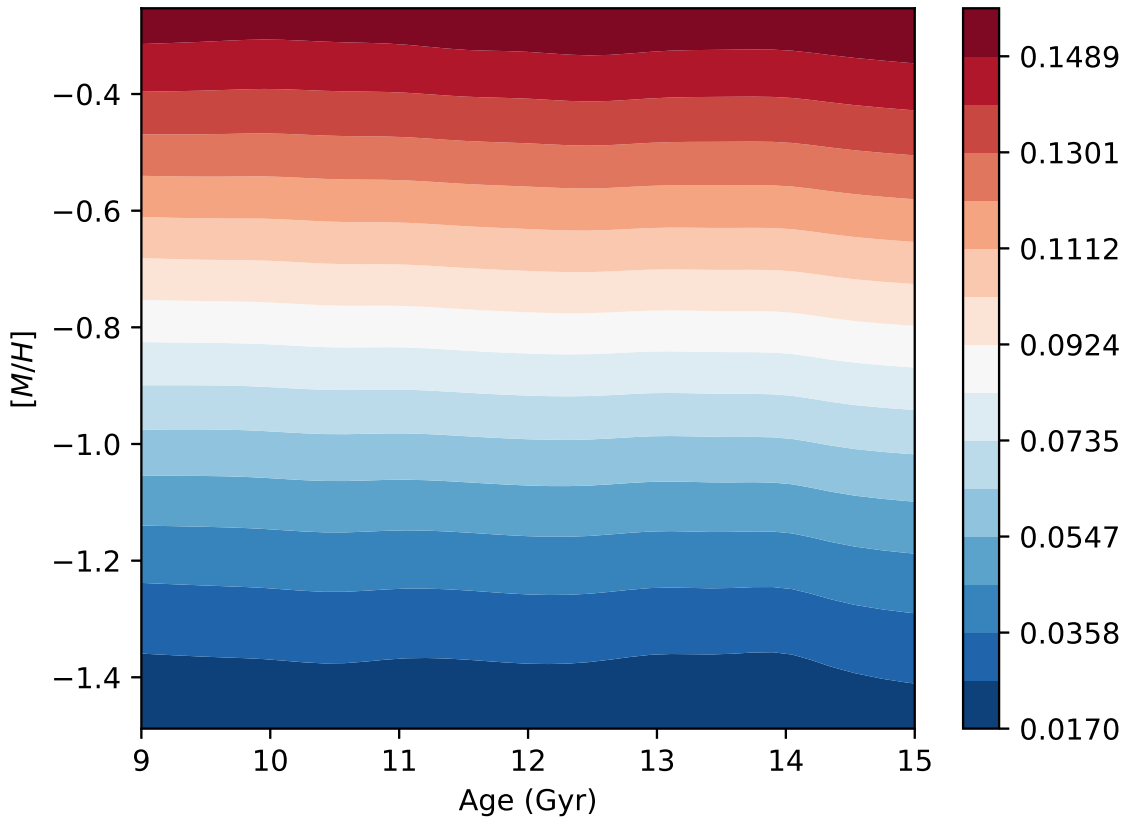

Figure A.13 Similar to A.1, but for the Ca I λ19858.5157 line in α-enhanced IL spectra.

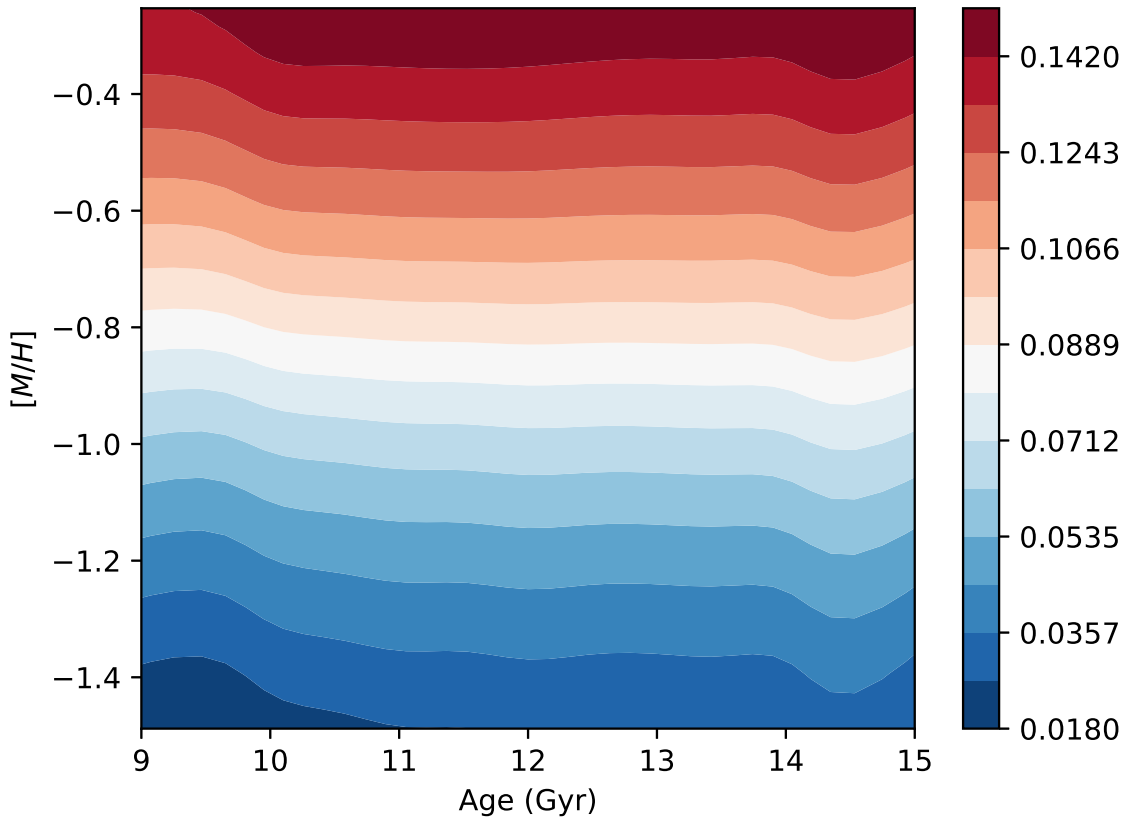

Figure A.14 Similar to A.1, but for the Ca I λ19858.5157 line in scaled-solar IL spectra.

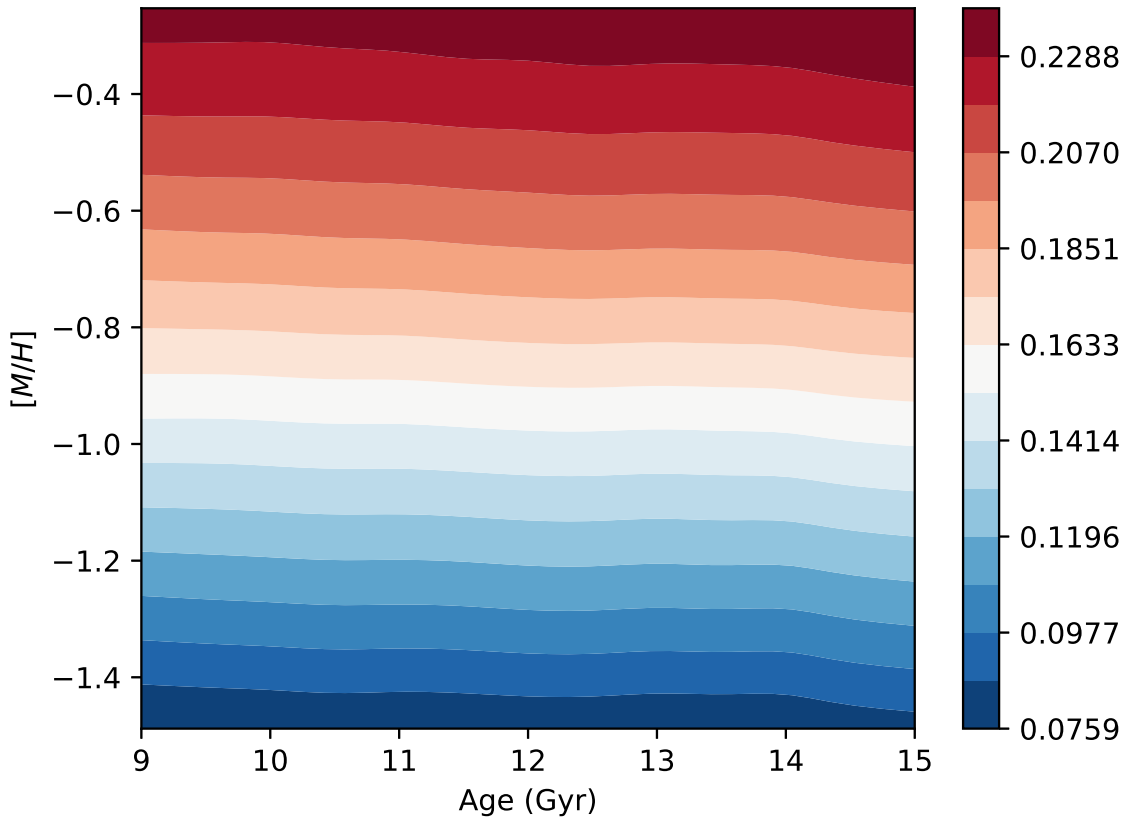

Figure A.15 Similar to A.1, but for the Ca I λ19867.6130 line in α-enhanced IL spectra.

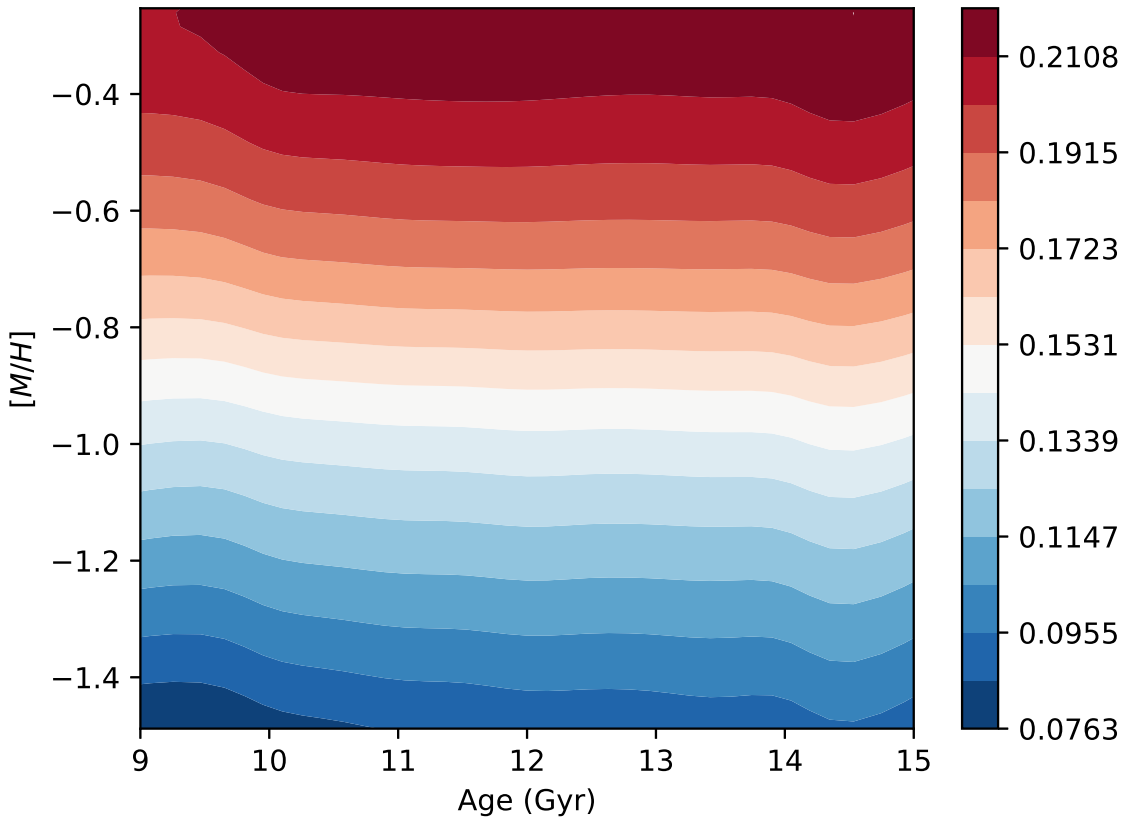

Figure A.16 Similar to A.1, but for the Ca I λ19867.6130 line in scaled-solar IL spectra.

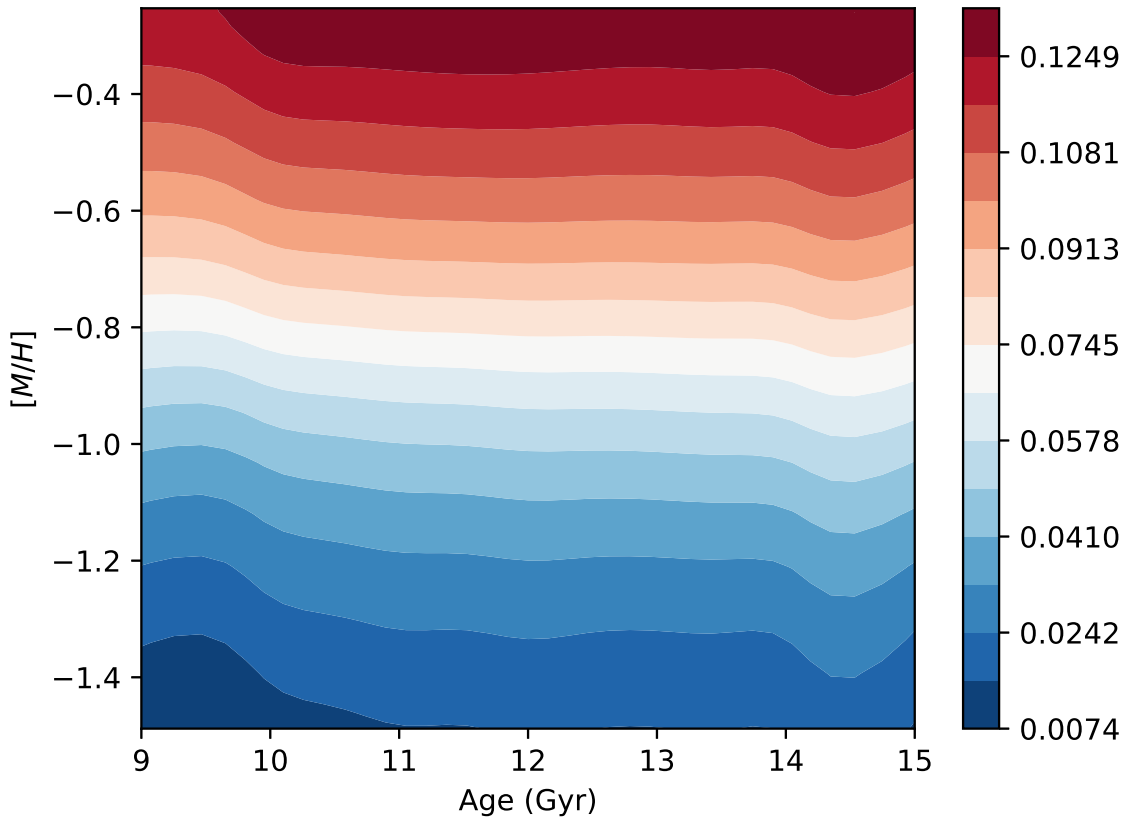

Figure A.17 Similar to A.1, but for the Ca I λ19922.6329 line in scaled-solar IL spectra.

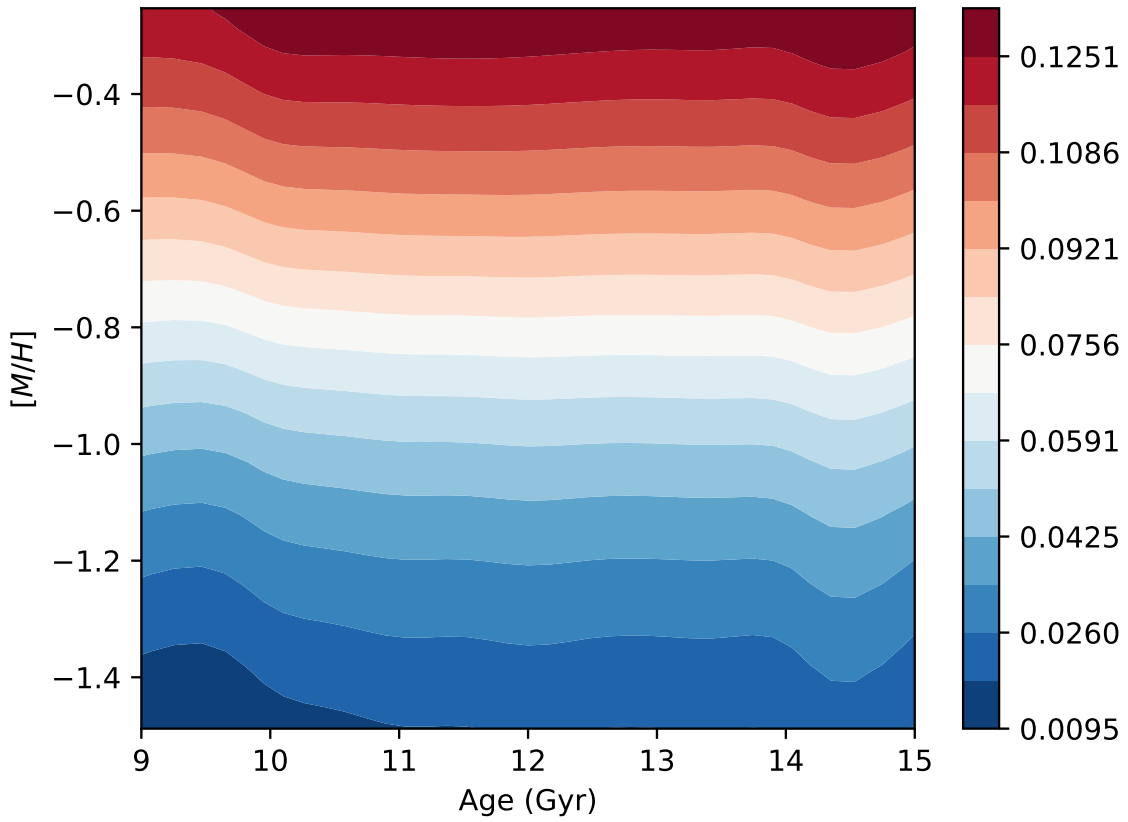

Figure A.18 Similar to A.1, but for the Ca I λ19939.1655 line in scaled-solar IL spectra.

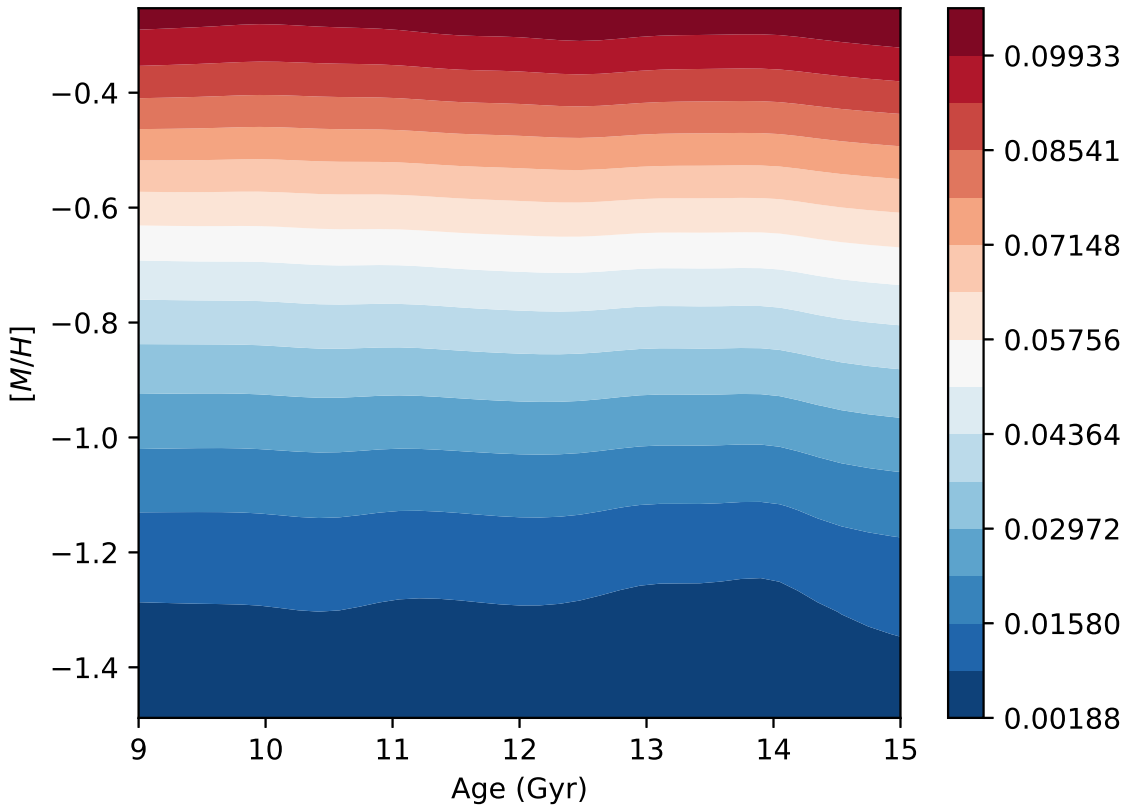

Figure A.19 Similar to A.1, but for the Ca I λ19967.2796 line in α-enhanced IL spectra.

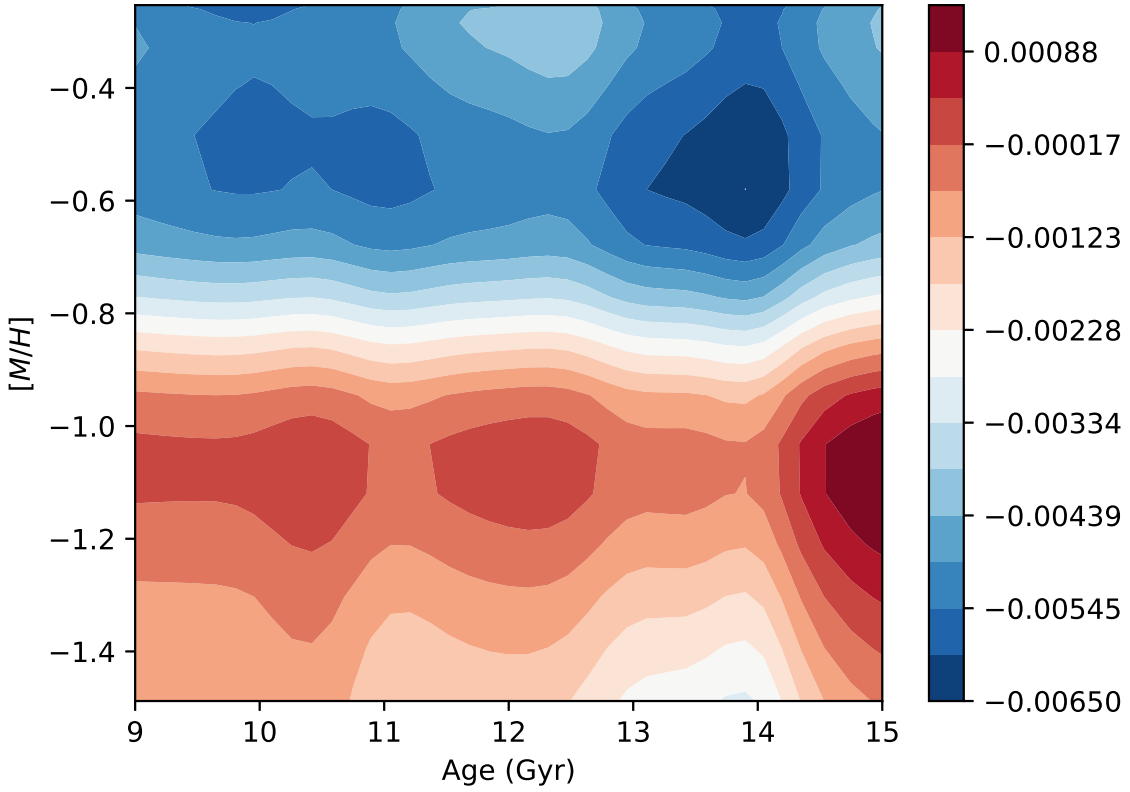

Figure A.20 Similar to A.1, but for the C I λ13919.2393 line in α-enhanced IL spectra.

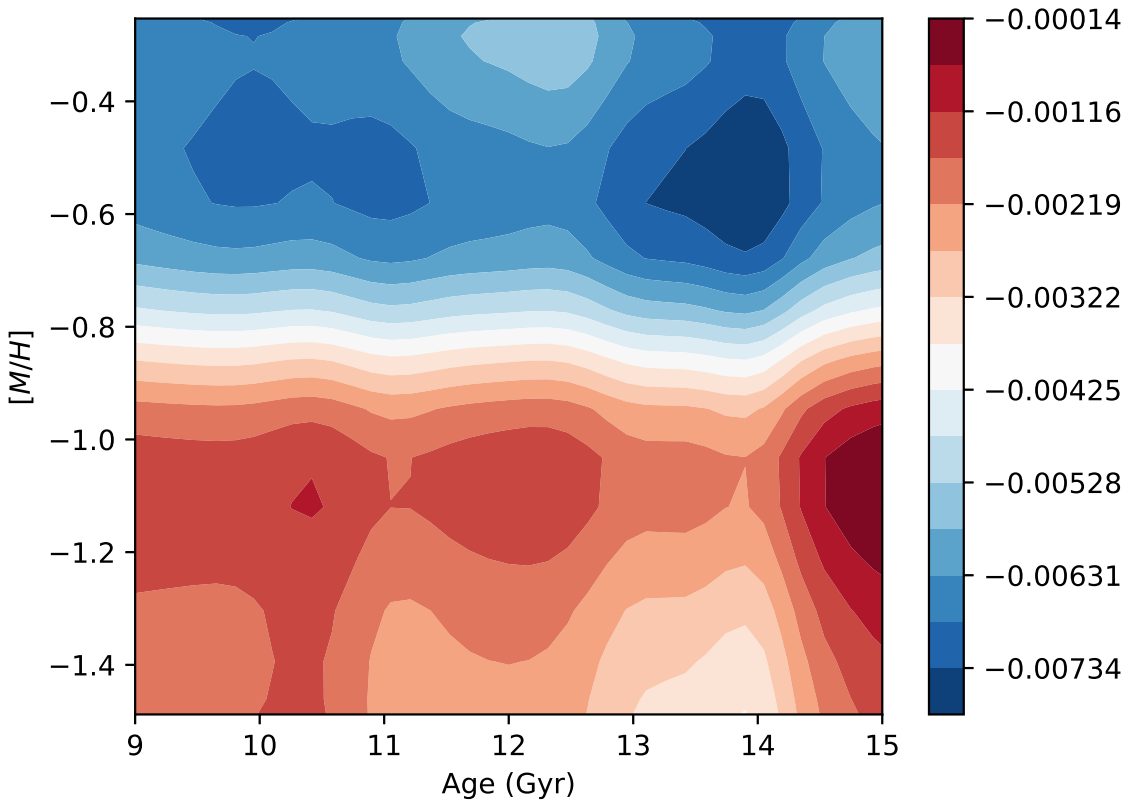

Figure A.21 Similar to A.1, but for the C I λ13927.8510 line in α-enhanced IL spectra.

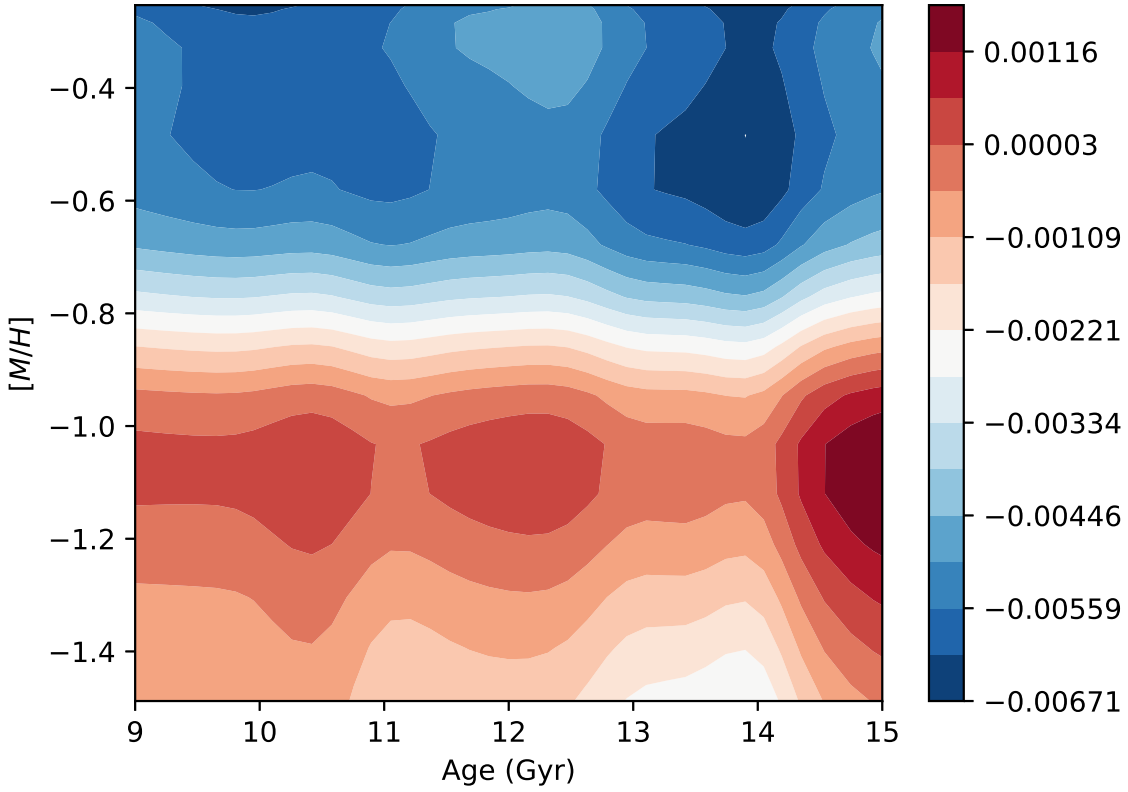

Figure A.22 Similar to A.1, but for the C I λ13936.5238 line in α-enhanced IL spectra.

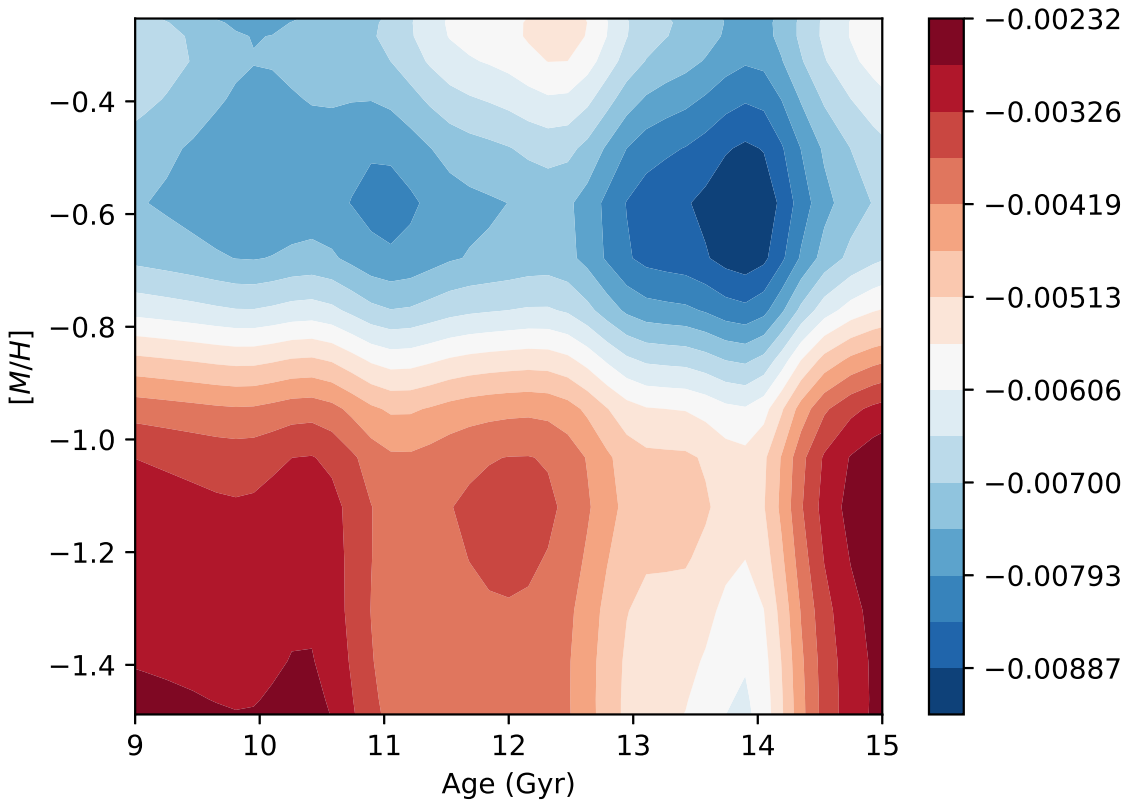

Figure A.23 Similar to A.1, but for the C I λ14626.5518 line in α-enhanced IL spectra.

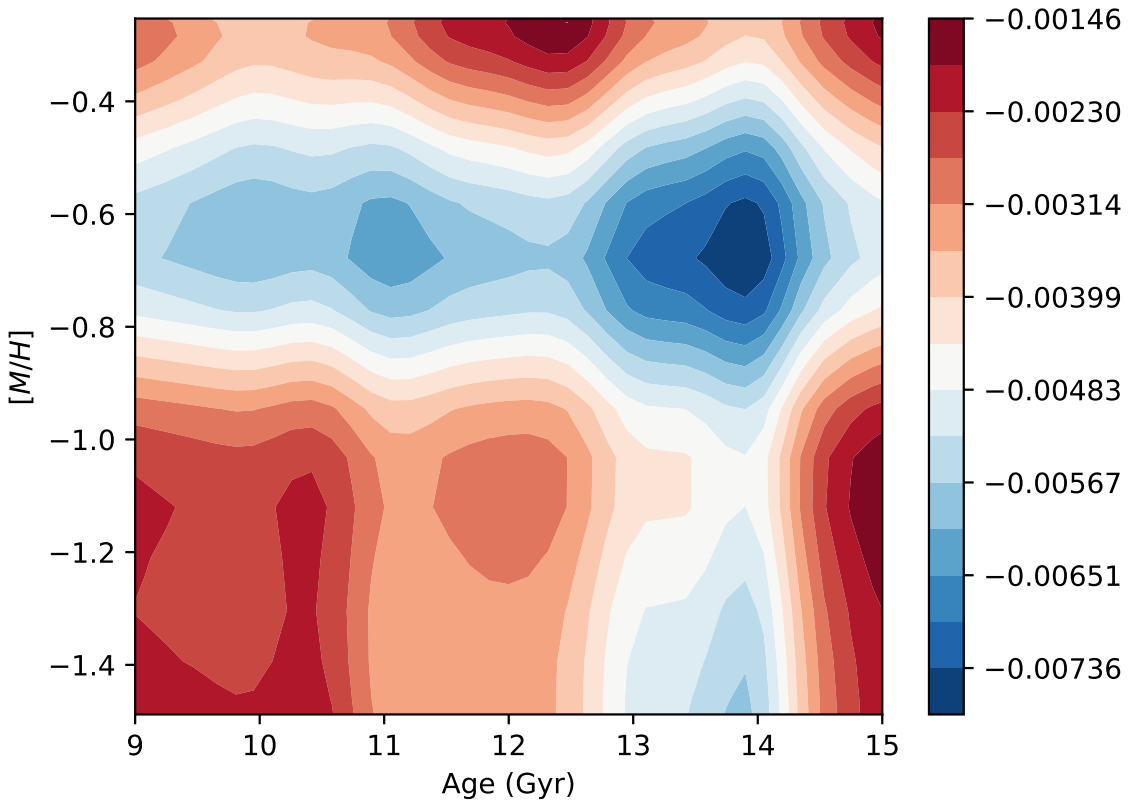

Figure A.24 Similar to A.1, but for the C I λ14783.6522 line in α-enhanced IL spectra.

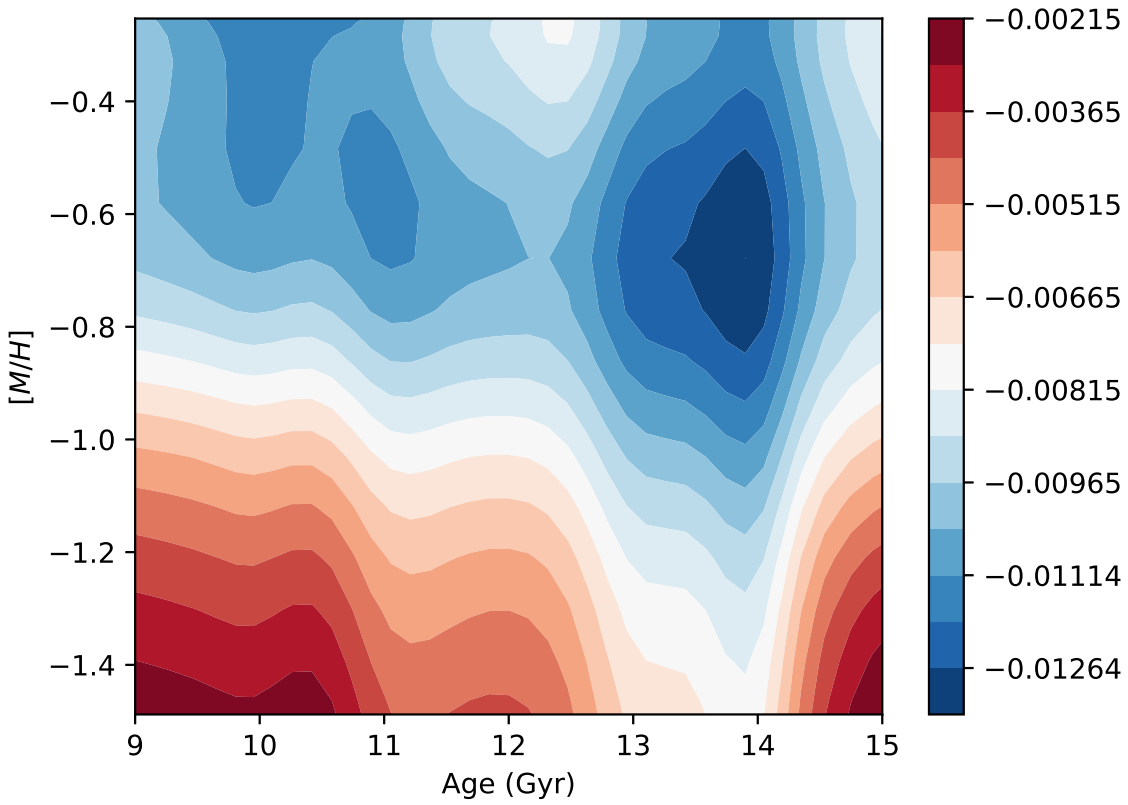

Figure A.25 Similar to A.1, but for the C I λ17351.1442 line in α-enhanced IL spectra.

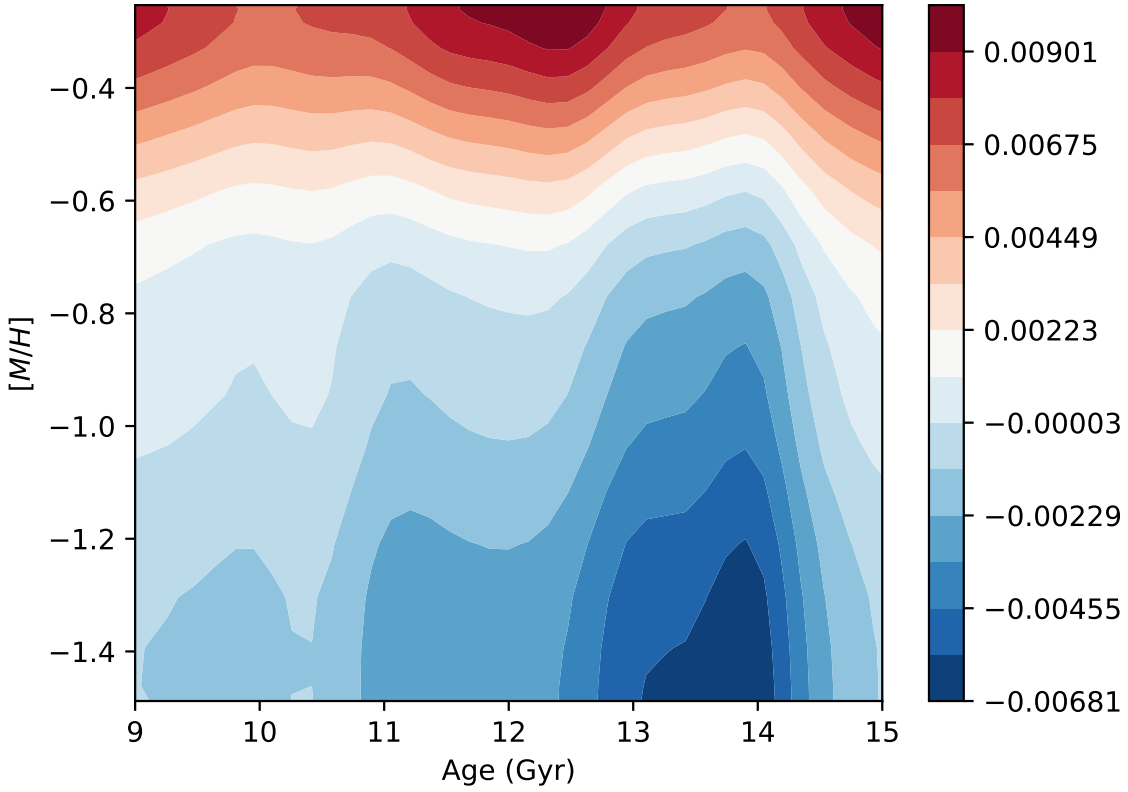

Figure A.26 Similar to A.1, but for the C I λ17432.9039 line in α-enhanced IL spectra.

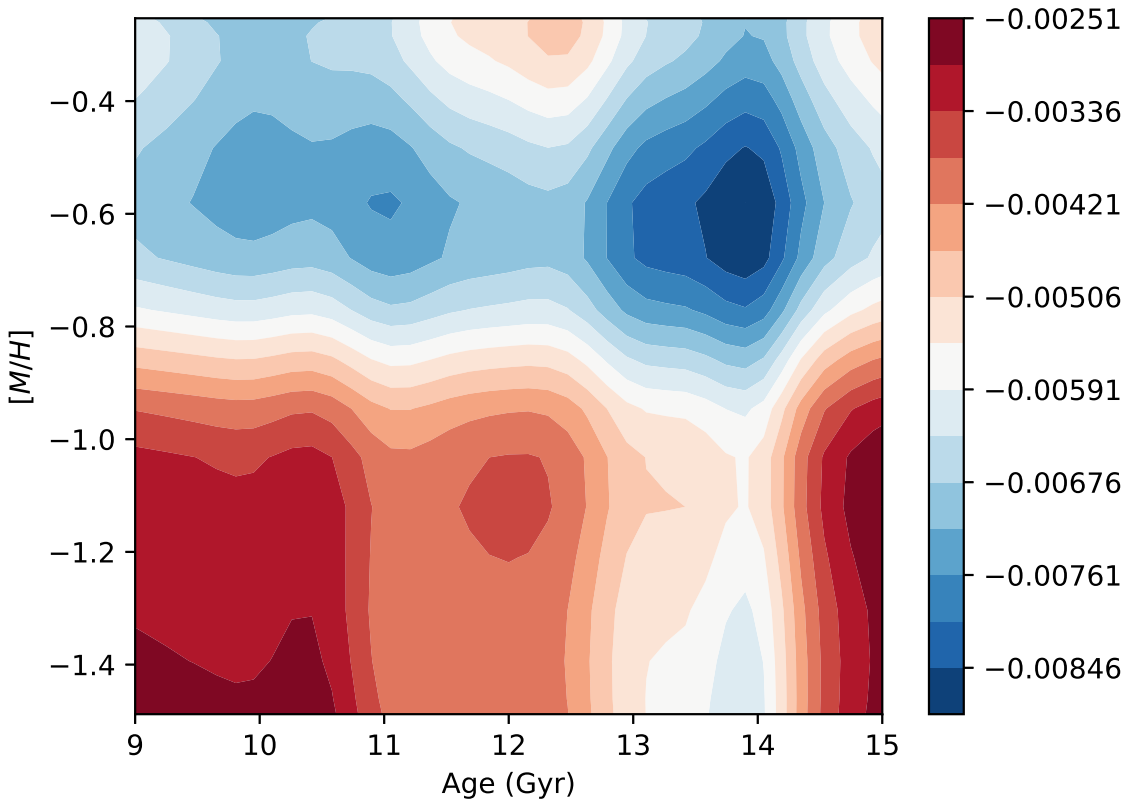

Figure A.27 Similar to A.1, but for the Co I λ14614.4095 line in α-enhanced IL spectra.

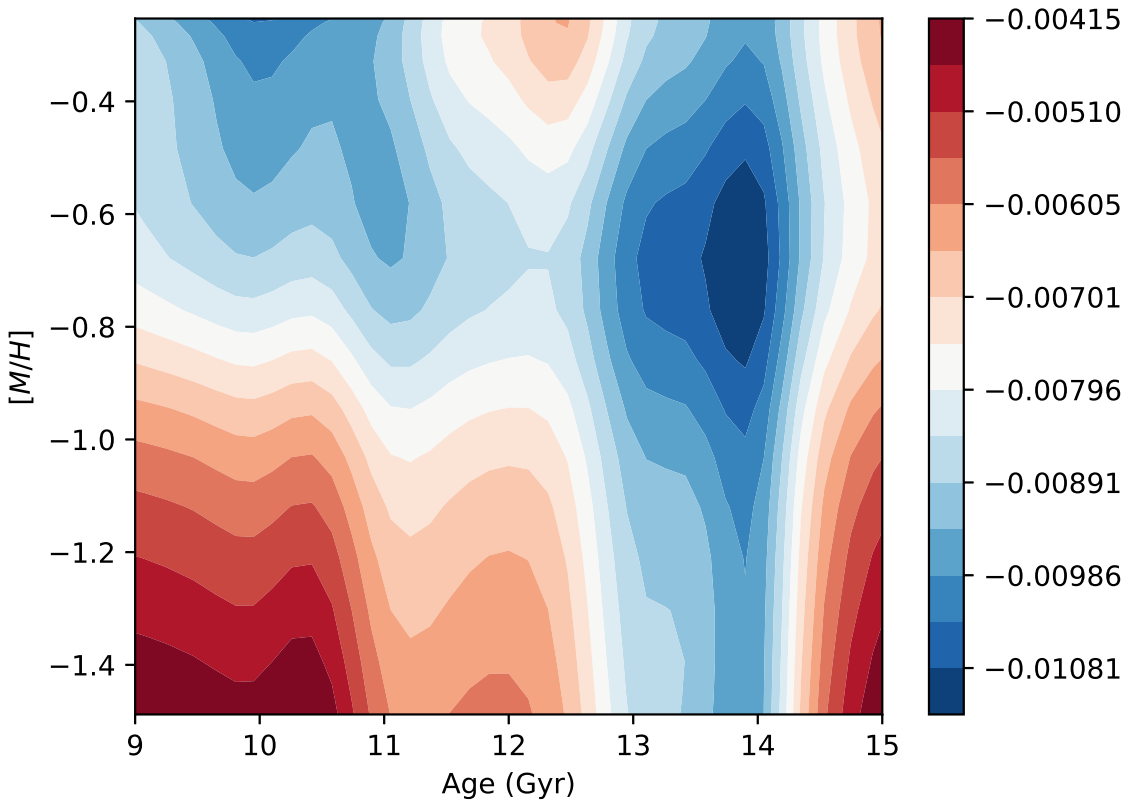

Figure A.28 Similar to A.1, but for the Cr I λ16903.5128 line in α-enhanced IL spectra.

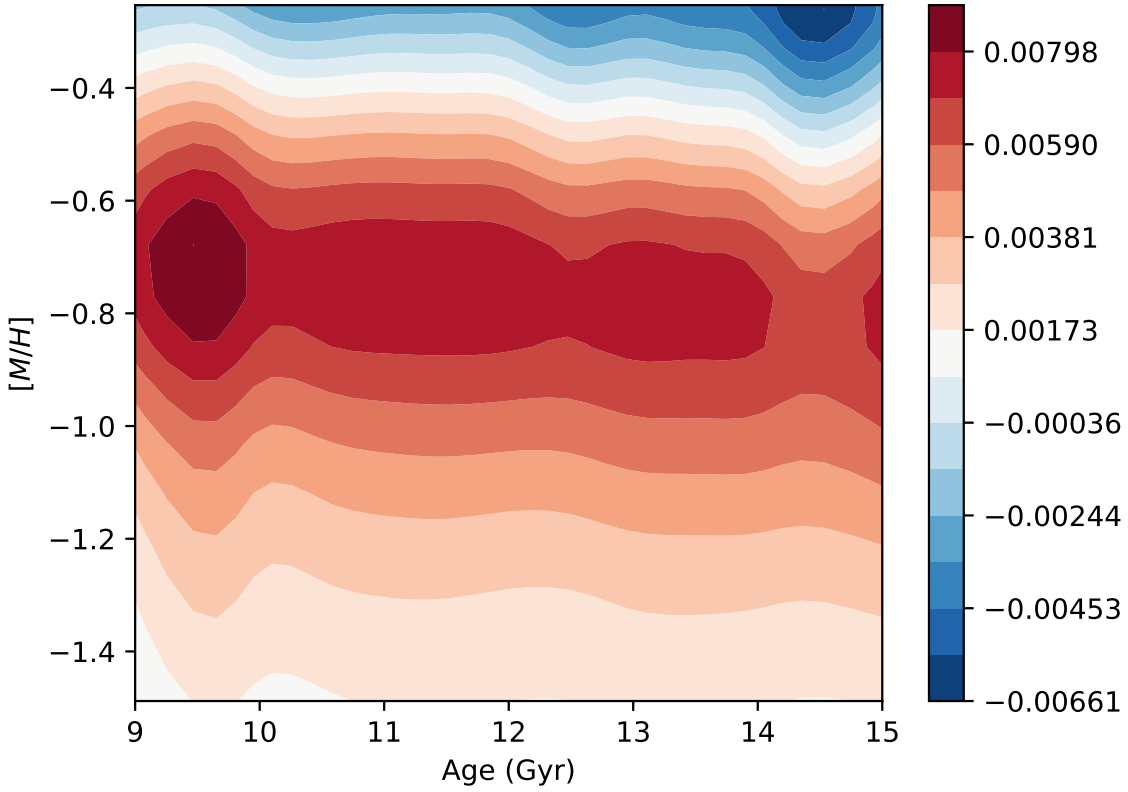

Figure A.29 Similar to A.1, but for the Cr I λ7402.2660 line in scaled-solar IL spectra.

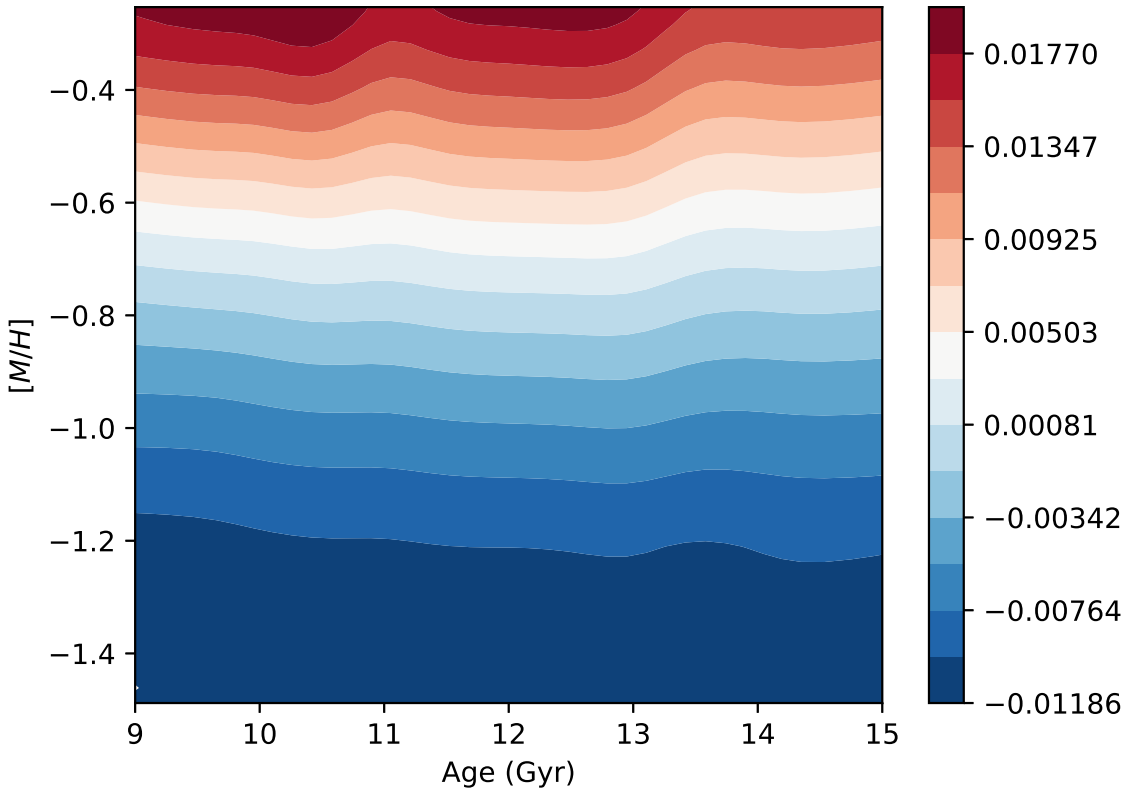

Figure A.30 Similar to A.1, but for the Fe I λ7585.8765 line in α-enhanced IL spectra.

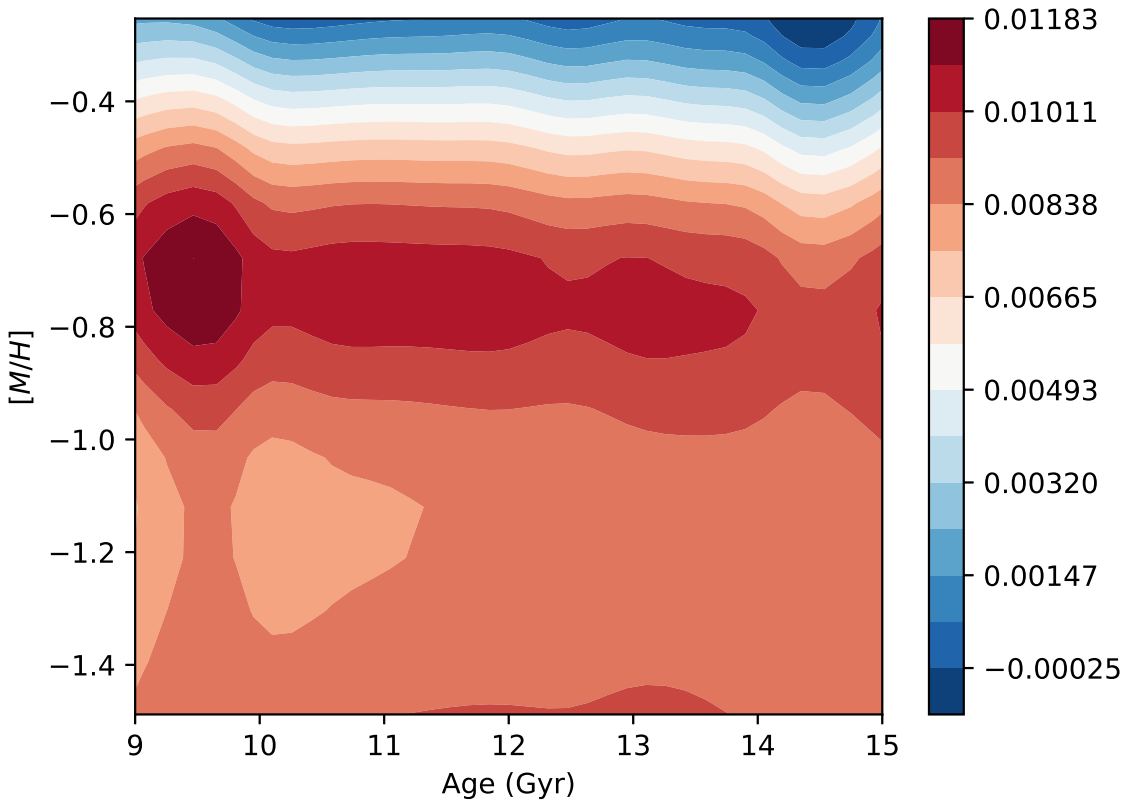

Figure A.31 Similar to A.1, but for the Fe I λ7915.0432 line in scaled-solar IL spectra.

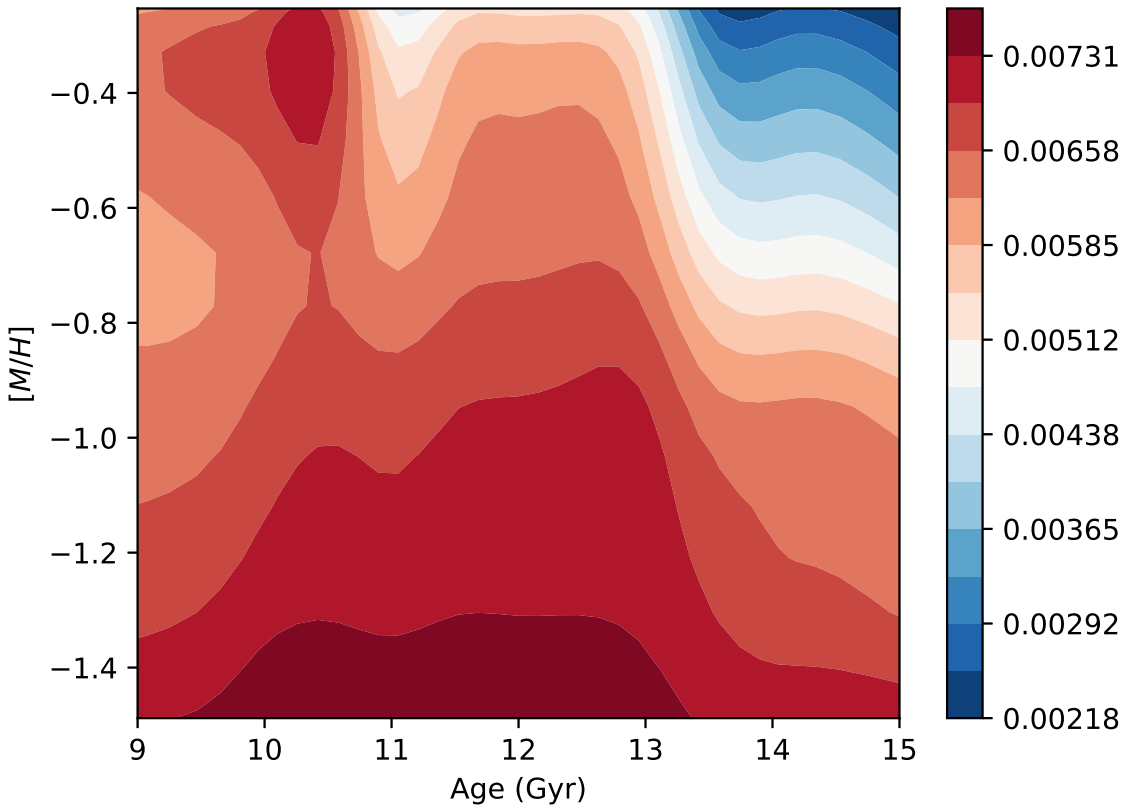

Figure A.32 Similar to A.1, but for the Fe I λ7915.0432 line in α-enhanced IL spectra.

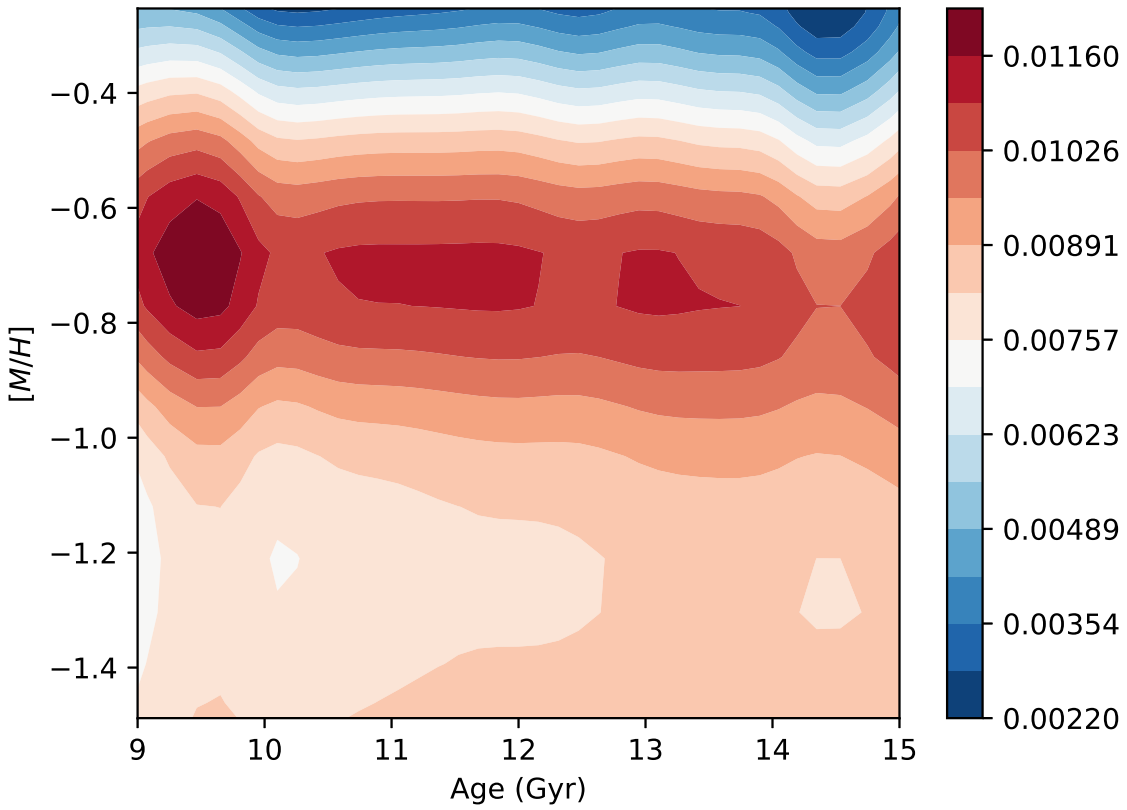

Figure A.33 Similar to A.1, but for the Fe I λ8049.8314 line in scaled-solar IL spectra.

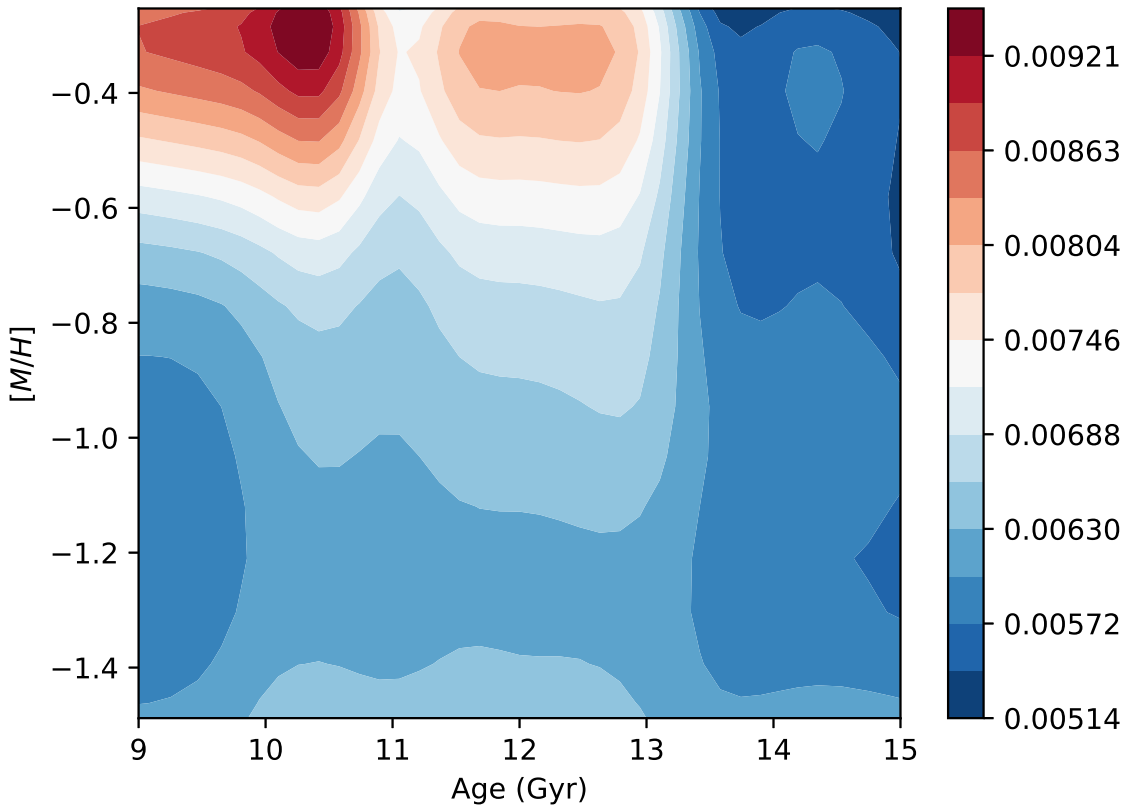

Figure A.34 Similar to A.1, but for the Fe I λ8049.8314 line in α-enhanced IL spectra.

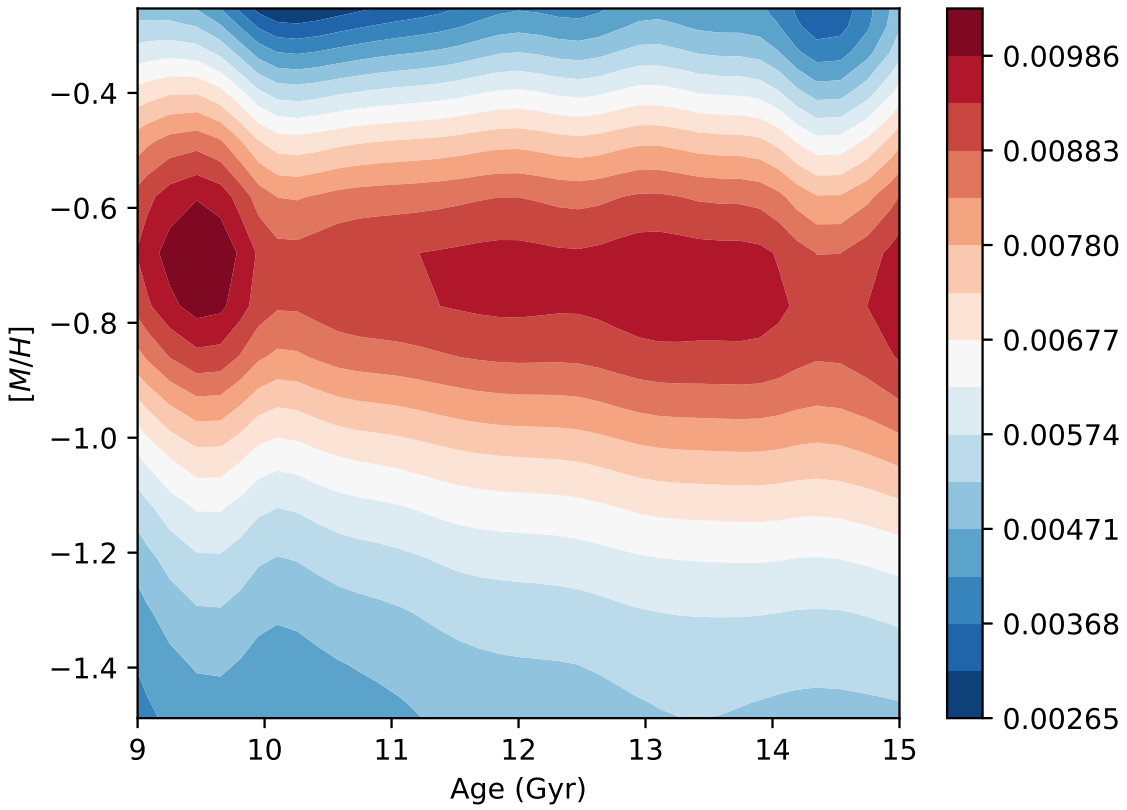

Figure A.35 Similar to A.1, but for the Fe I λ8207.1903 line in scaled-solar IL spectra.

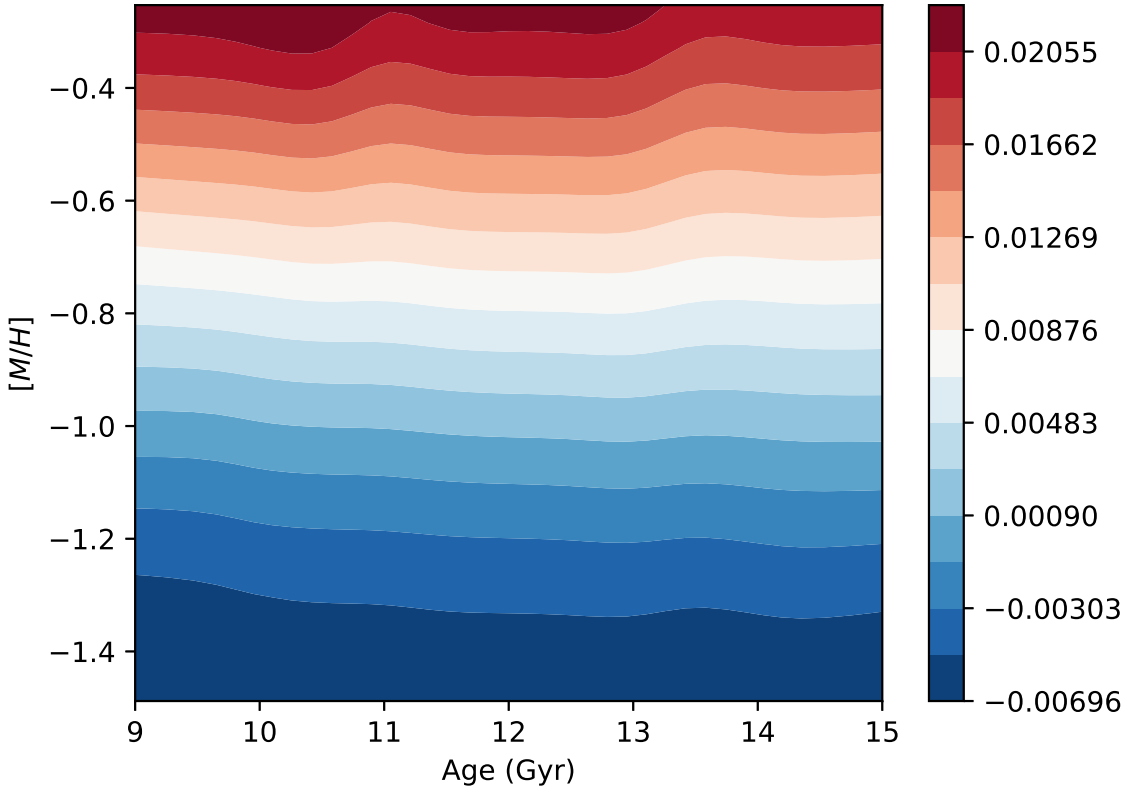

Figure A.36 Similar to A.1, but for the Fe I λ8241.3910 line in α-enhanced IL spectra.

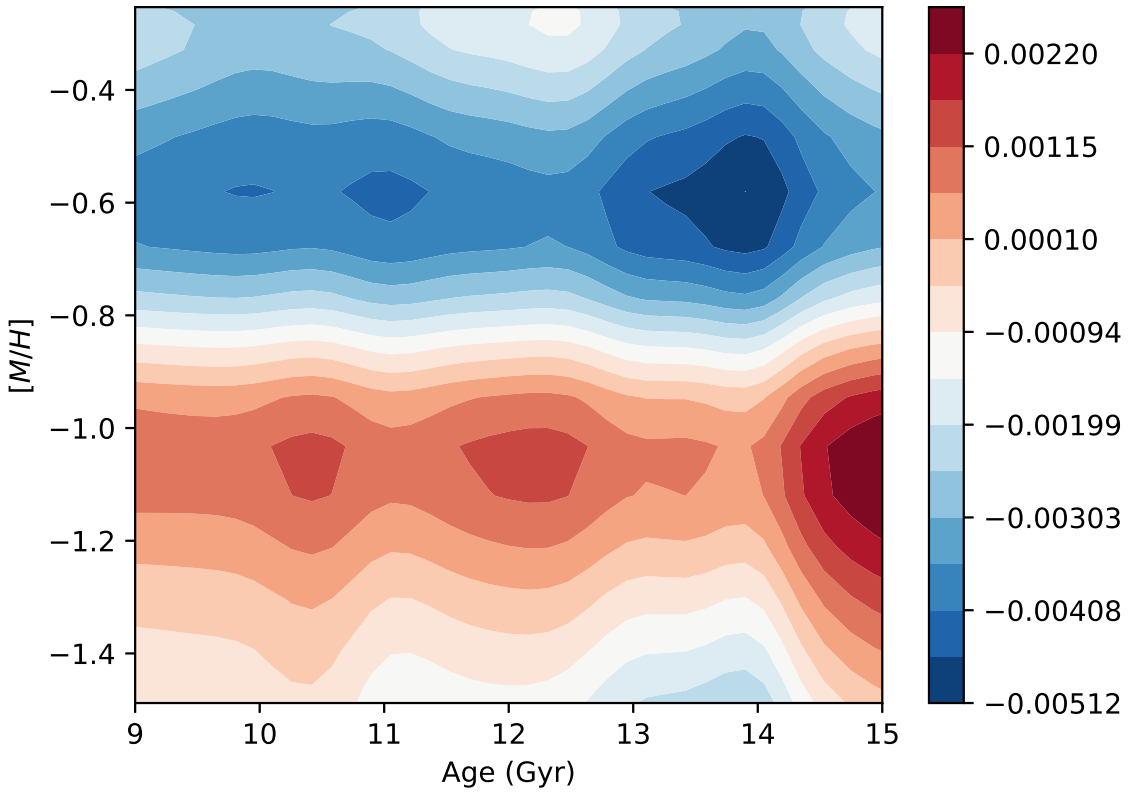

Figure A.37 Similar to A.1, but for the Fe I λ13951.8275 line in α-enhanced IL spectra.

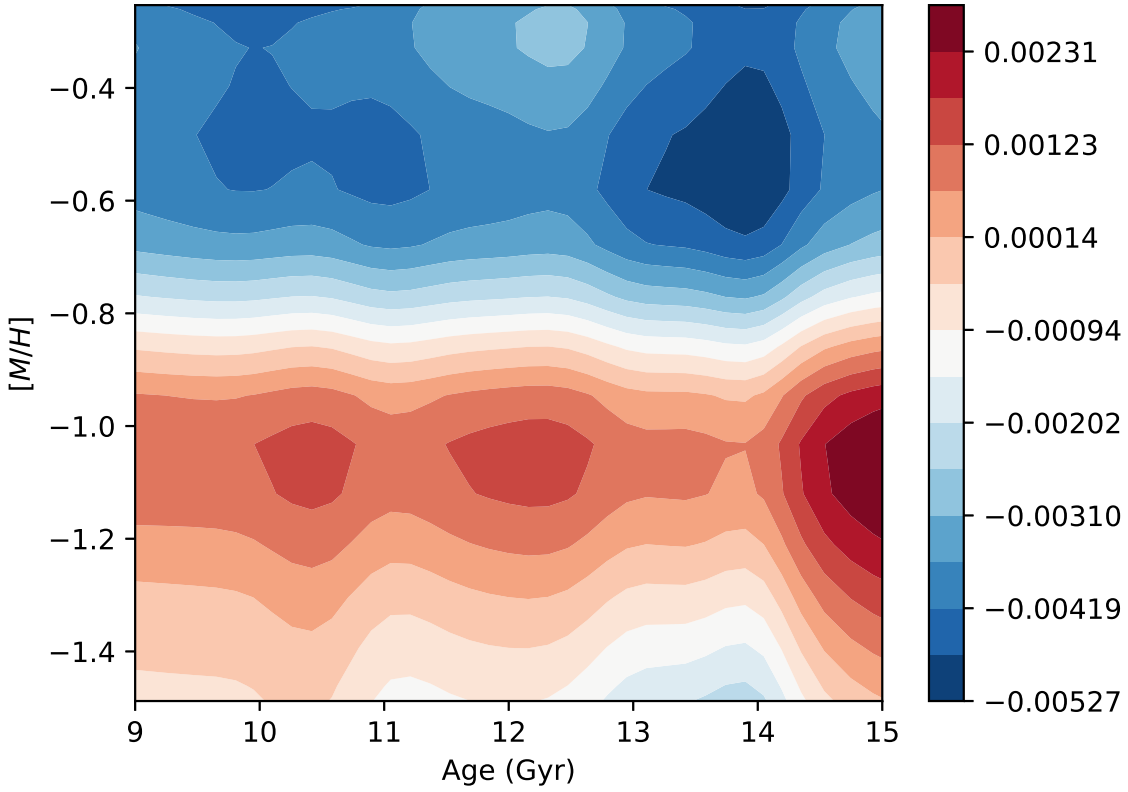

Figure A.38 Similar to A.1, but for the Fe I λ13956.8162 line in α-enhanced IL spectra.

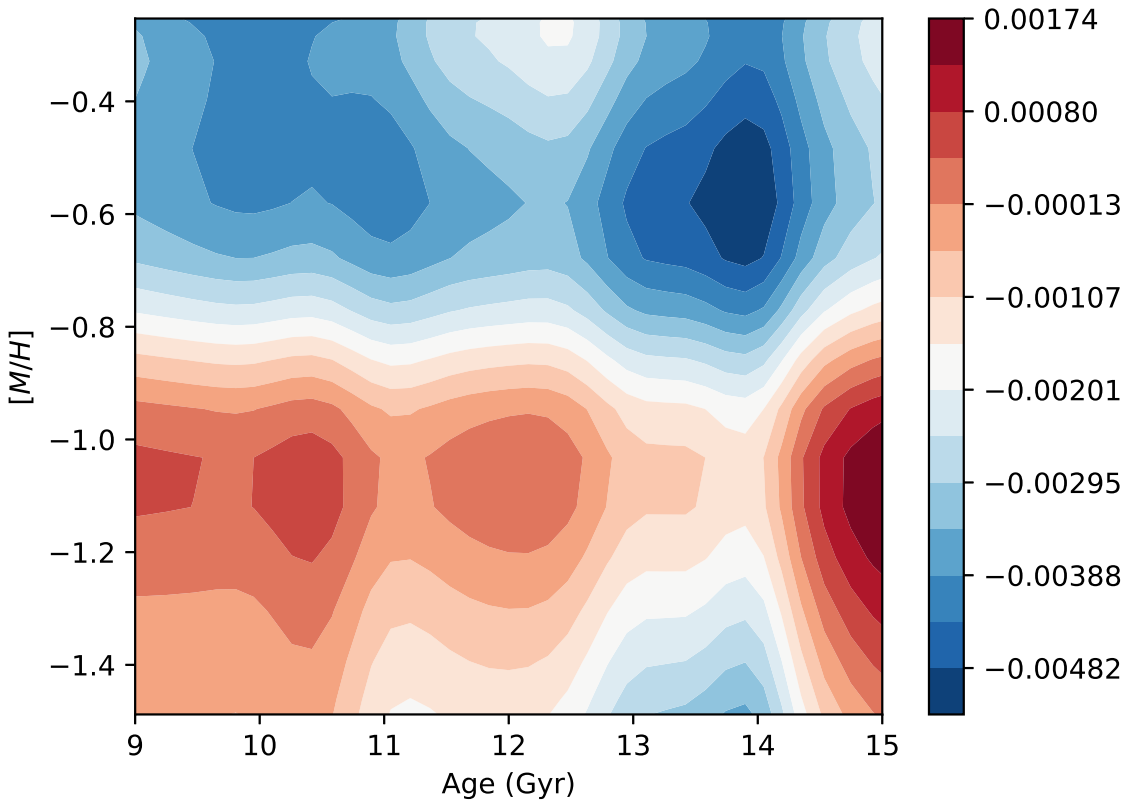

Figure A.39 Similar to A.1, but for the Fe I λ14519.1286 line in α-enhanced IL spectra.

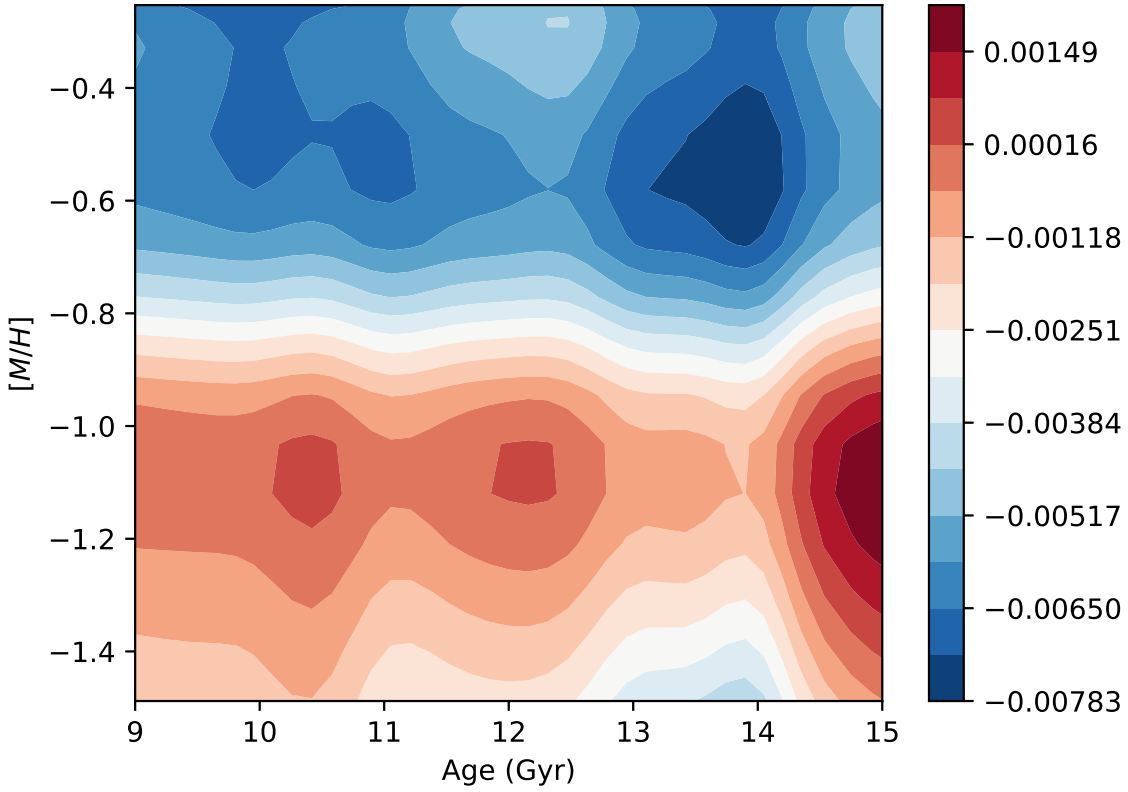

Figure A.40 Similar to A.1, but for the Fe I λ14698.7799 line in α-enhanced IL spectra.

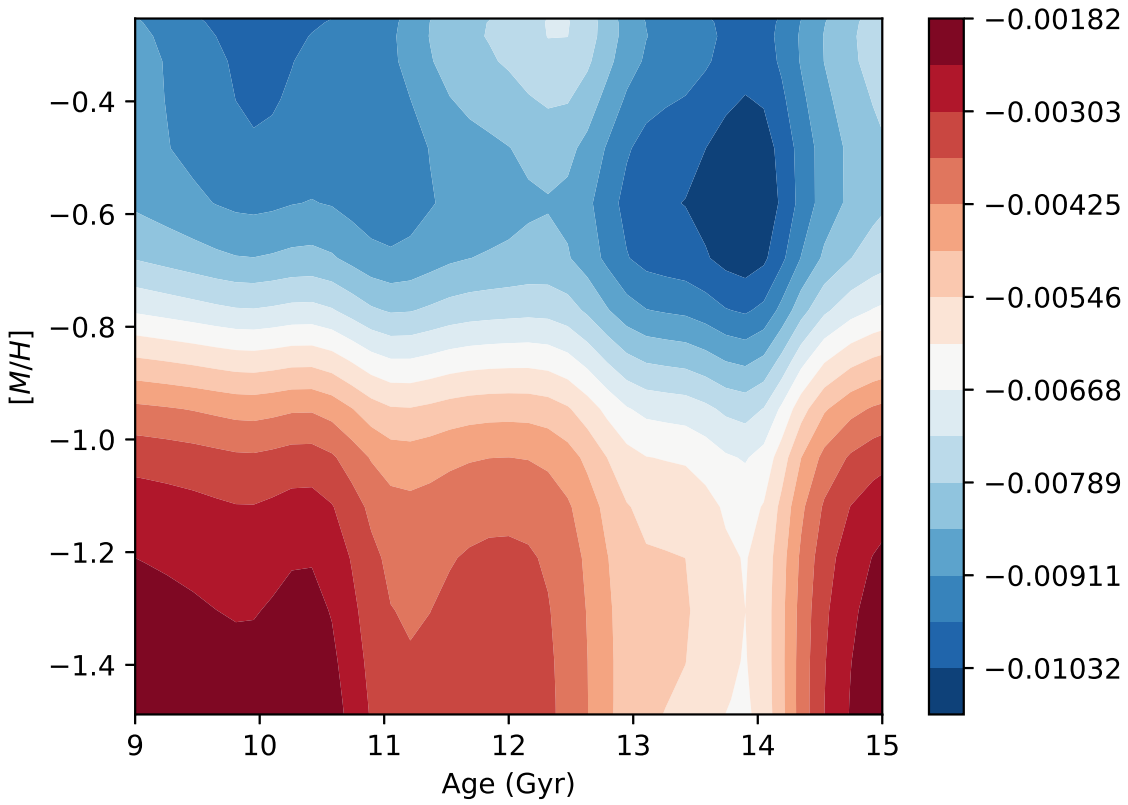

Figure A.41 Similar to A.1, but for the Fe I λ15068.9975 line in α-enhanced IL spectra.

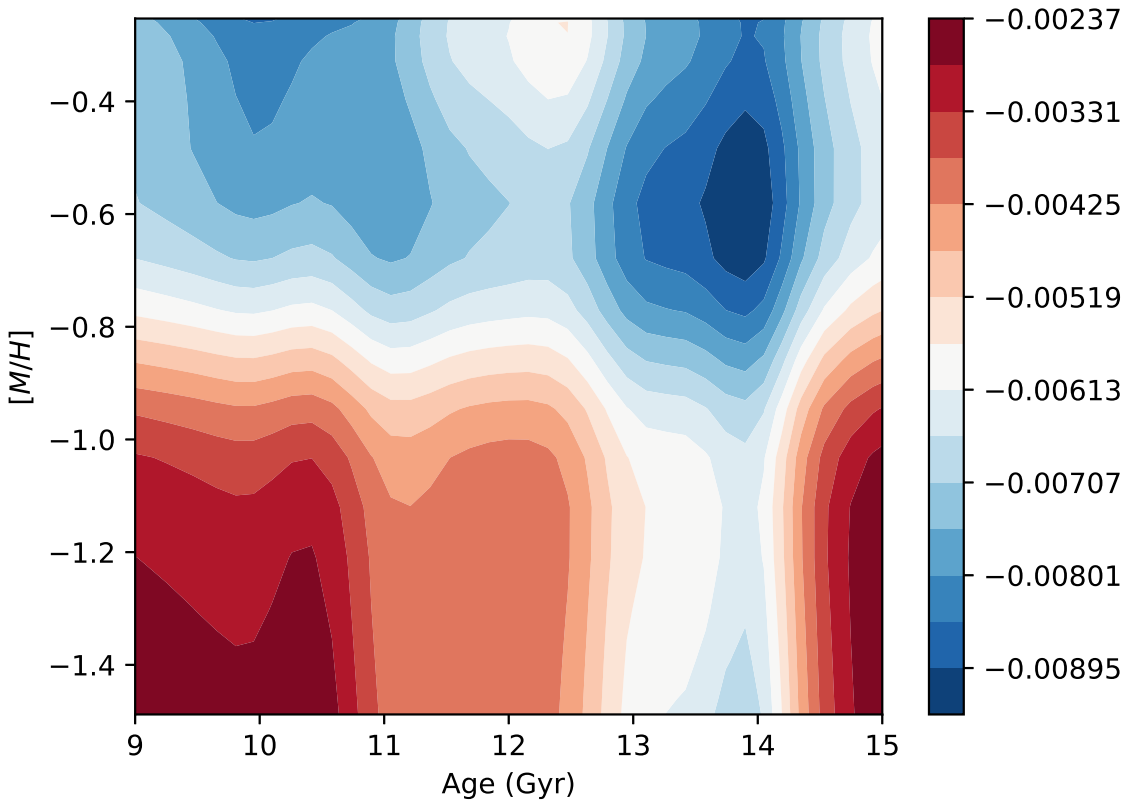

Figure A.42 Similar to A.1, but for the Fe I λ15287.8284 line in α-enhanced IL spectra.

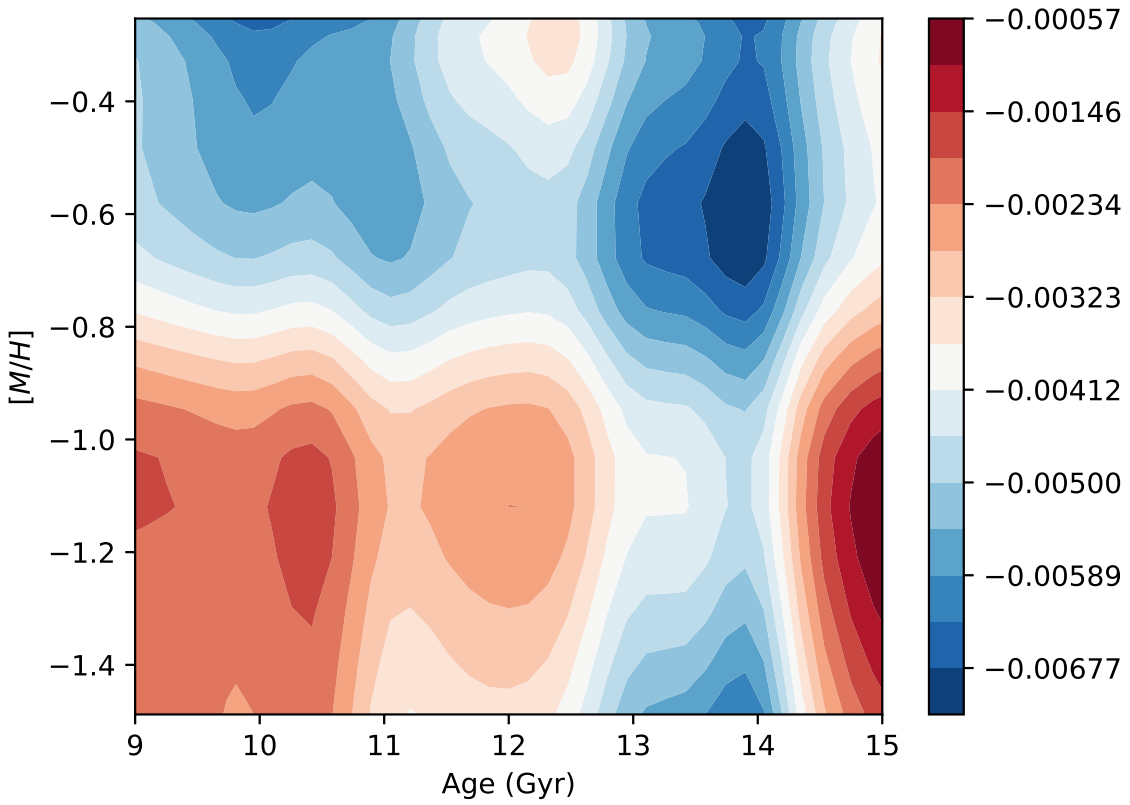

Figure A.43 Similar to A.1, but for the Fe I λ15423.5564 line in α-enhanced IL spectra.

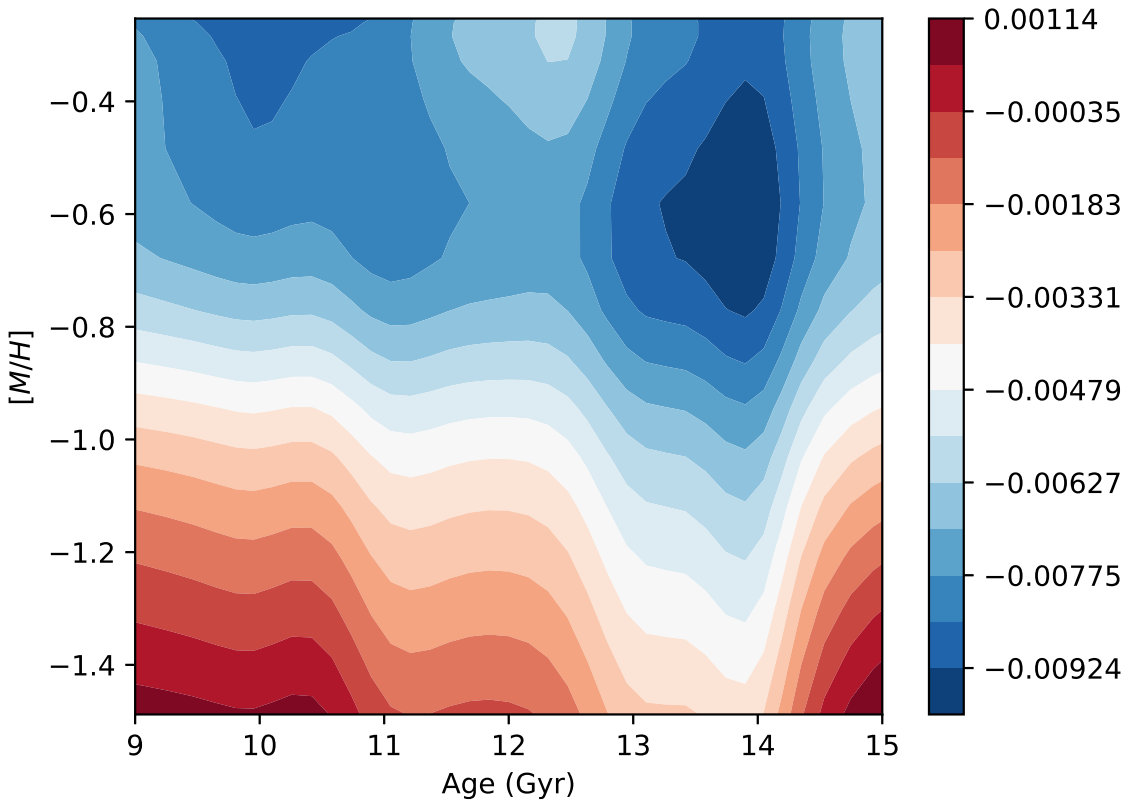

Figure A.44 Similar to A.1, but for the Fe I λ15438.8024 line in α-enhanced IL spectra.

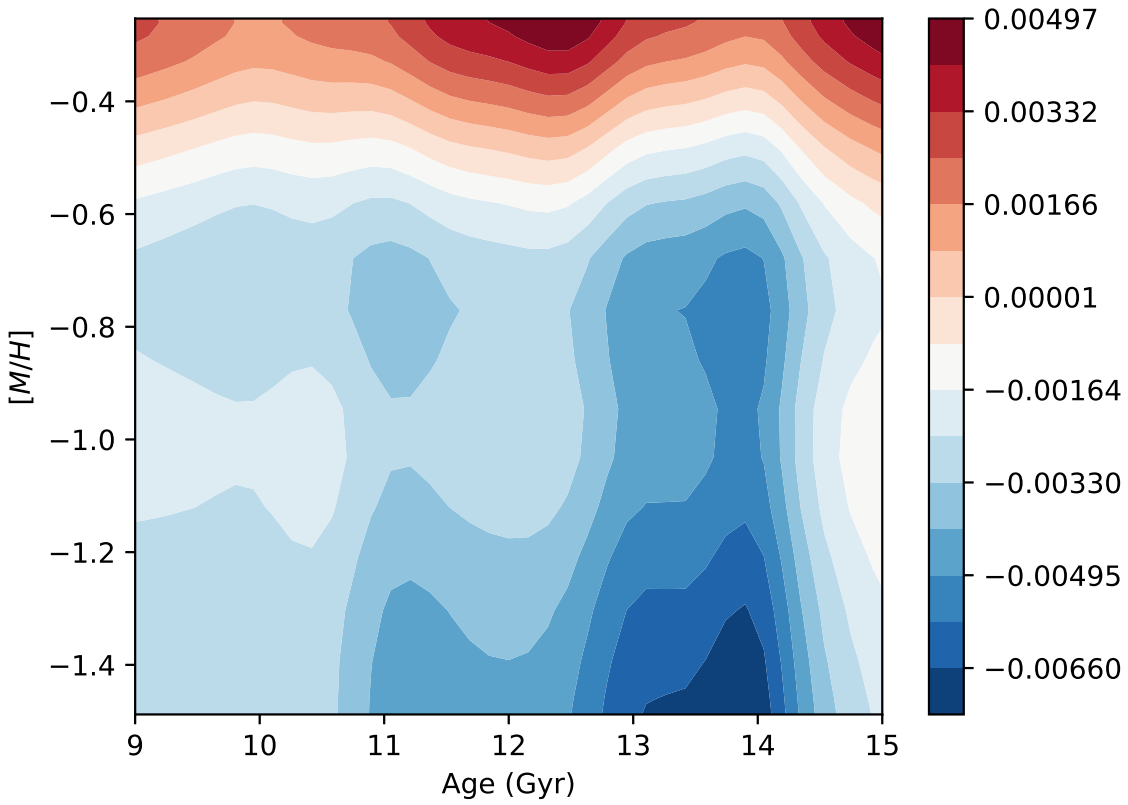

Figure A.45 Similar to A.1, but for the Fe I λ15902.0013 line in α-enhanced IL spectra.

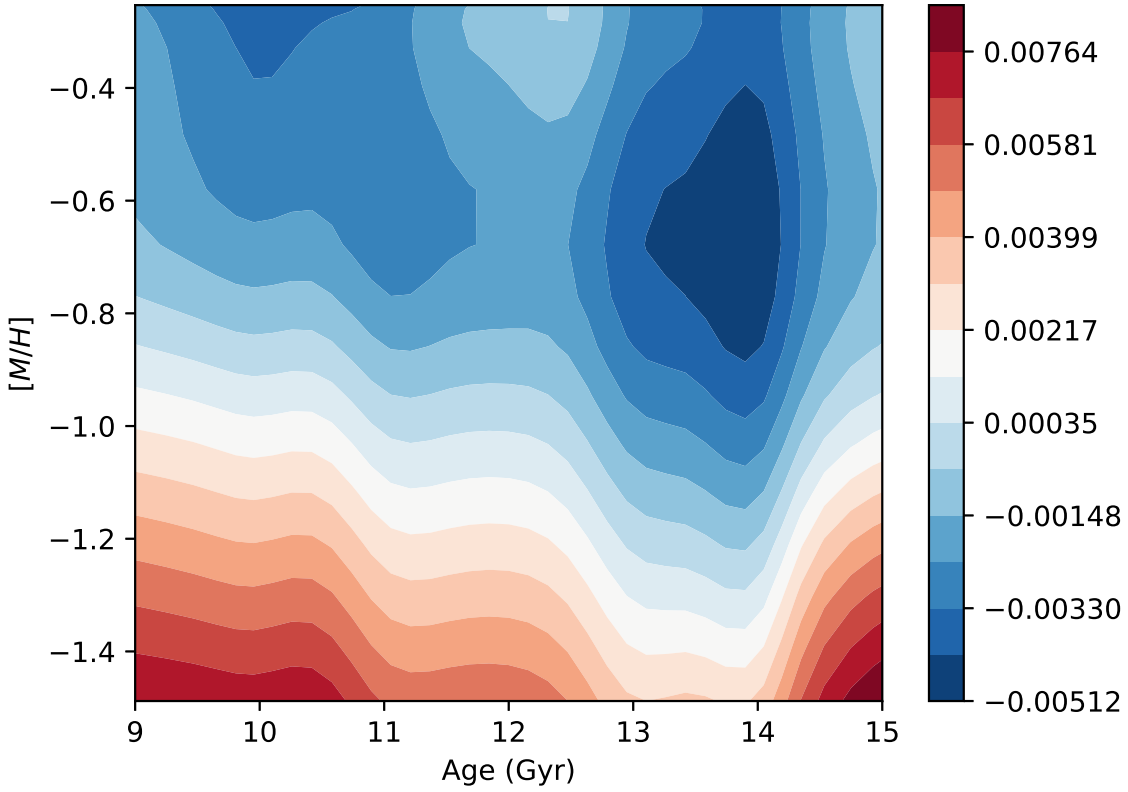

Figure A.46 Similar to A.1, but for the Fe I λ16414.8755 line in α-enhanced IL spectra.

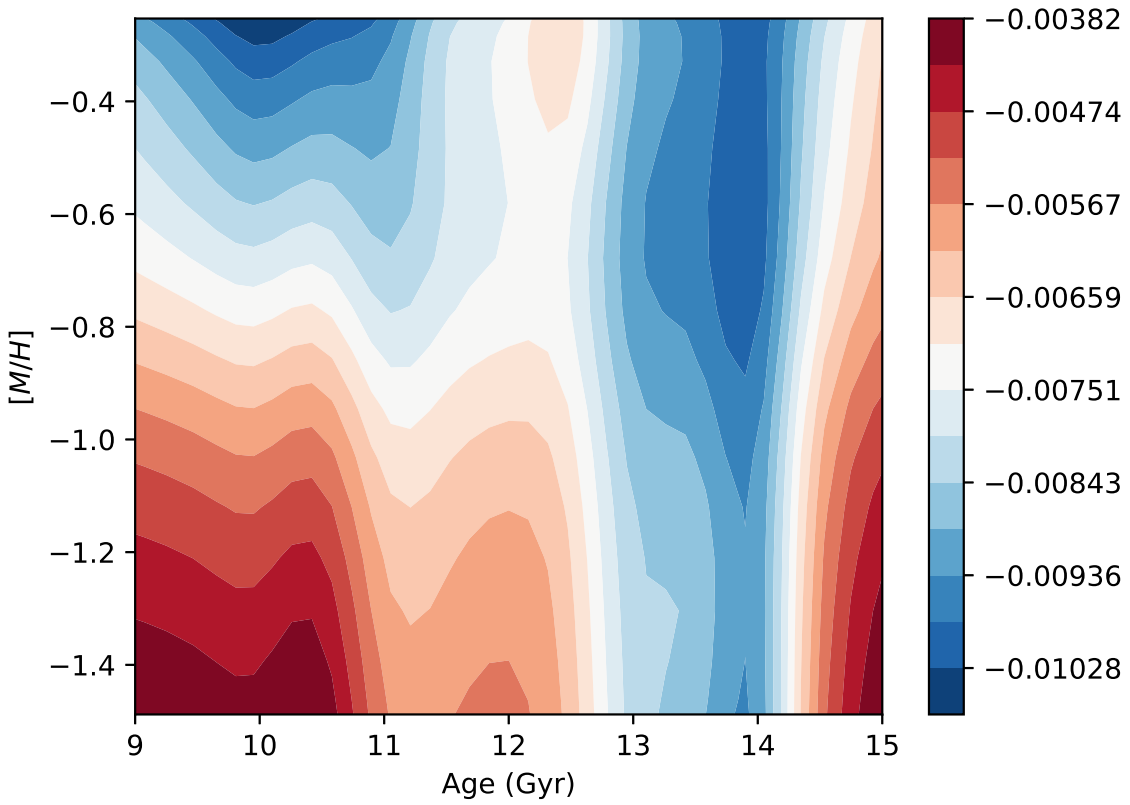

Figure A.47 Similar to A.1, but for the Fe I λ16913.8863 line in α-enhanced IL spectra.

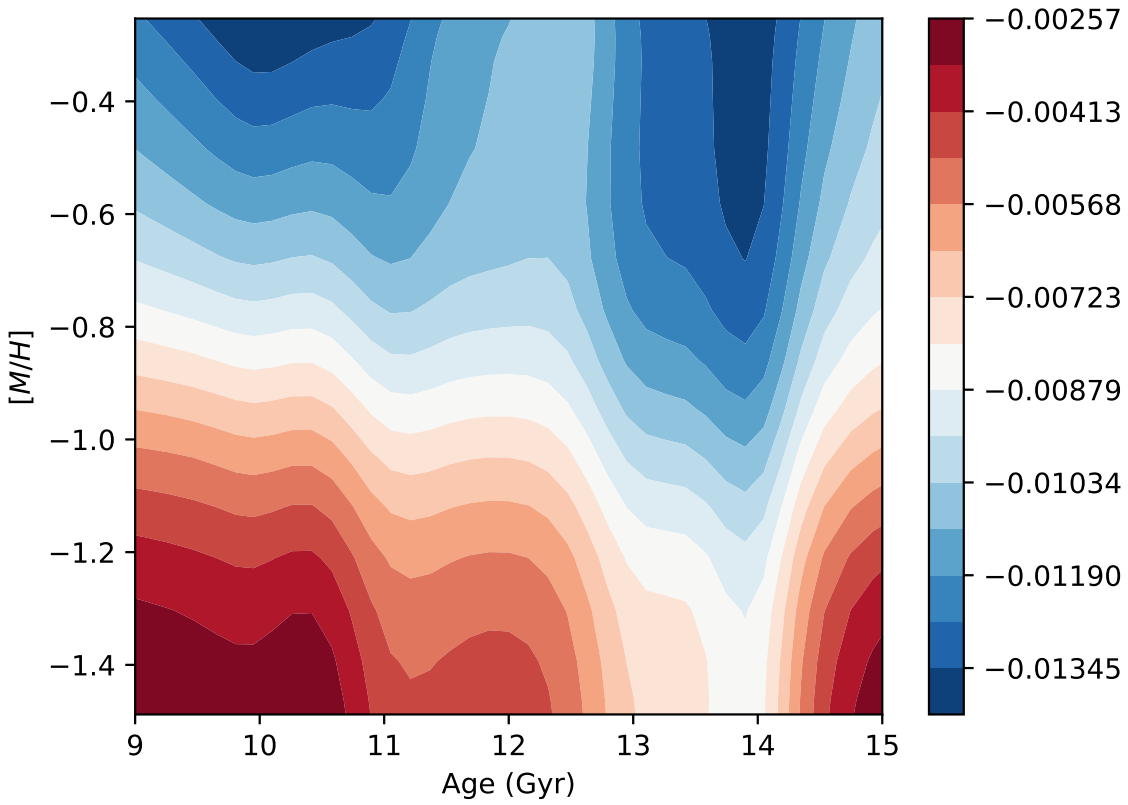

Figure A.48 Similar to A.1, but for the Fe I λ17189.0741 line in α-enhanced IL spectra.

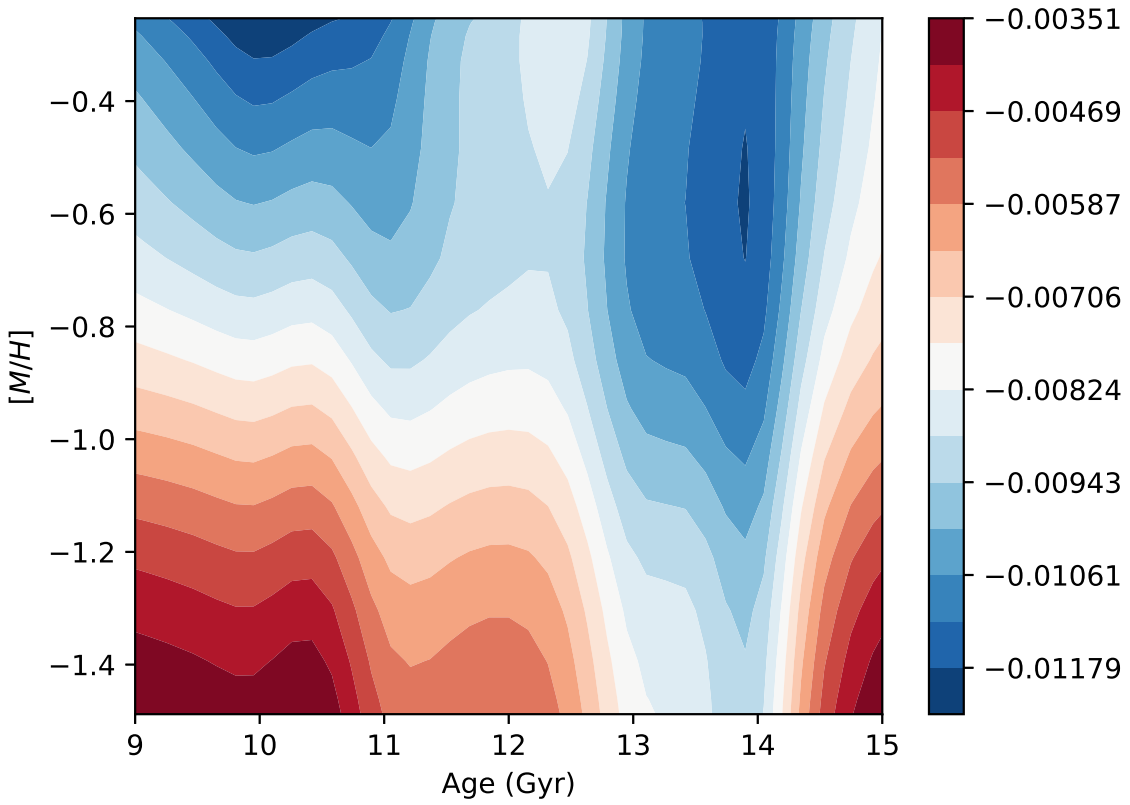

Figure A.49 Similar to A.1, but for the Fe II λ17418.7628 line in α-enhanced IL spectra.

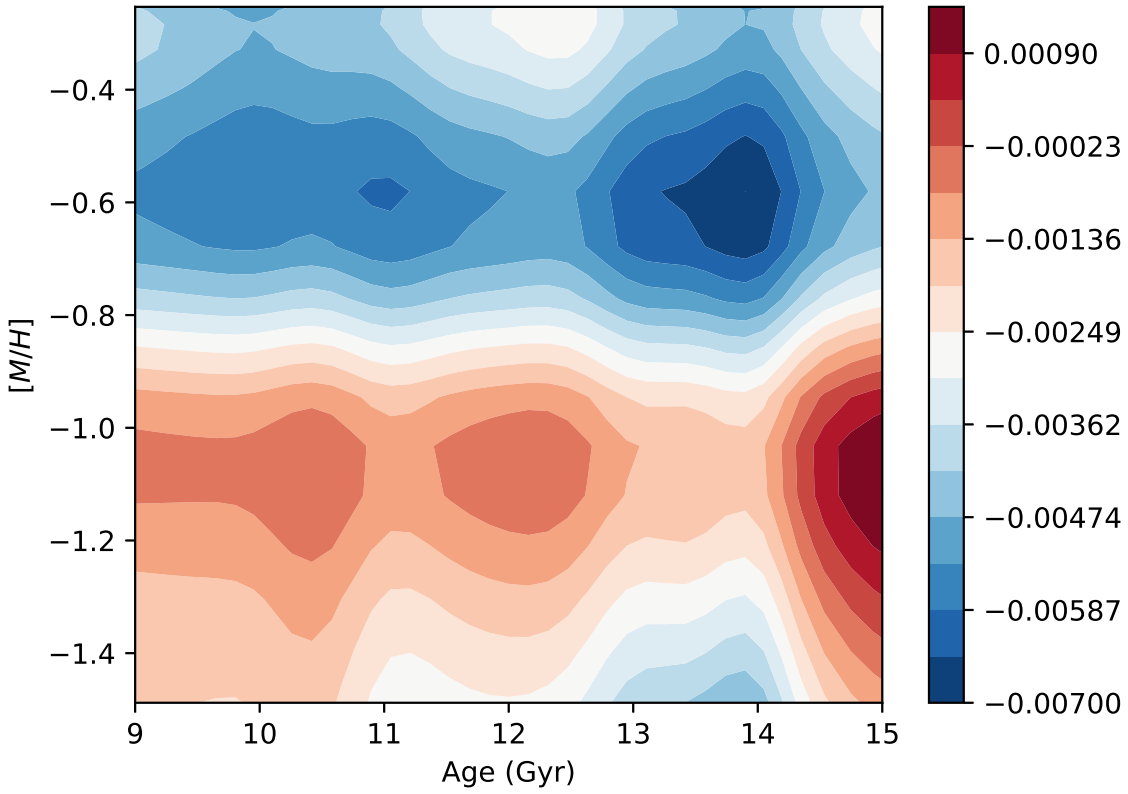

Figure A.50 Similar to A.1, but for the Mg I λ14604.9935 line in α-enhanced IL spectra.

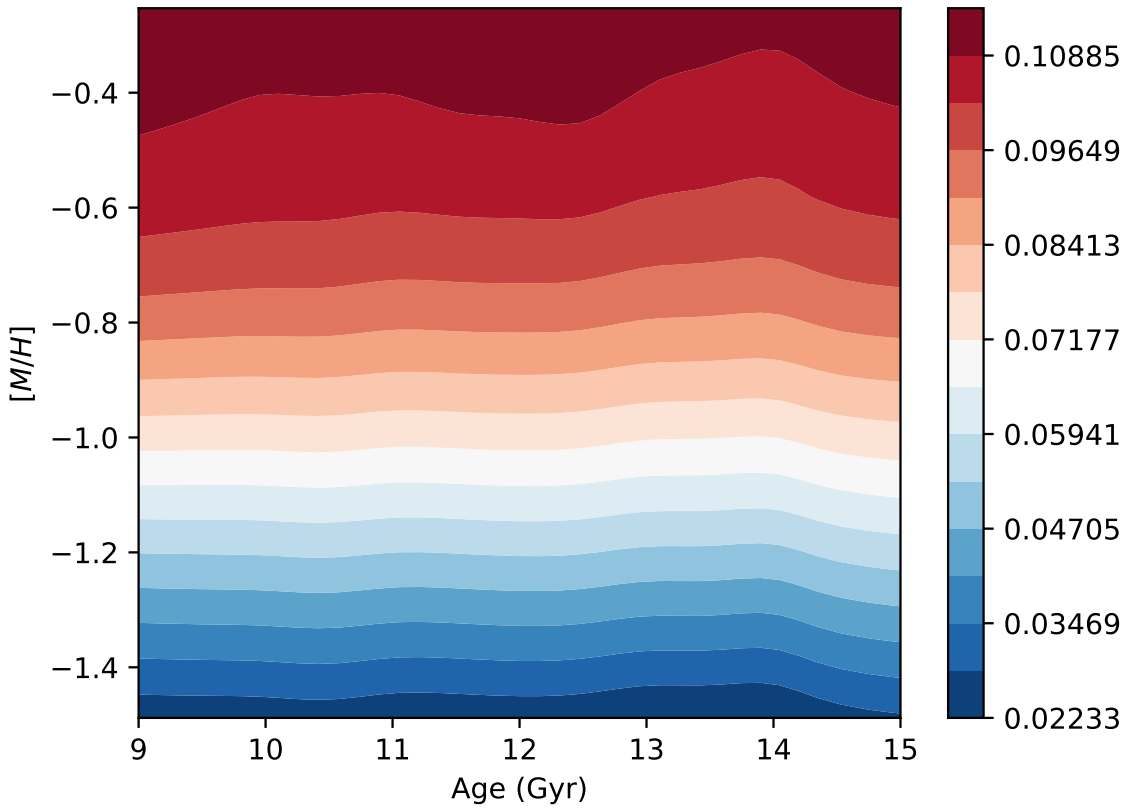

Figure A.51 Similar to A.1, but for the Mg I λ18902.7786 line in α-enhanced IL spectra.

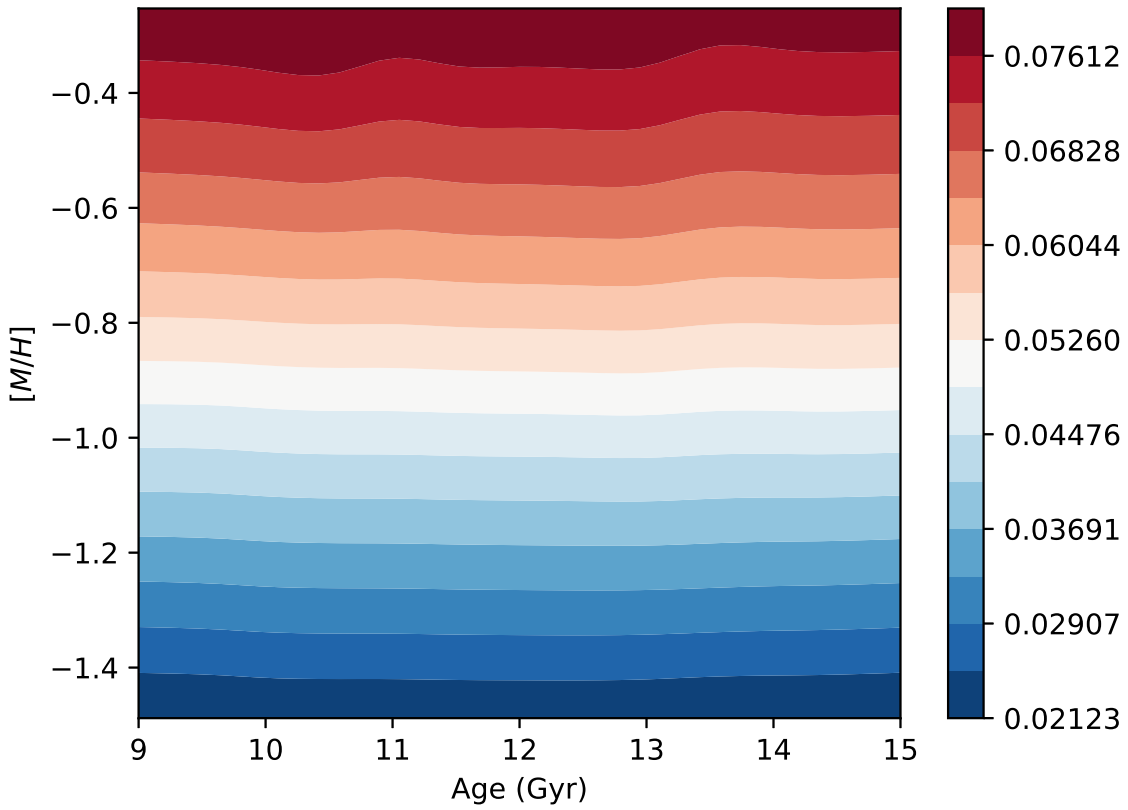

Figure A.52 Similar to A.1, but for the Na I λ8197.0771 line in α-enhanced IL spectra.

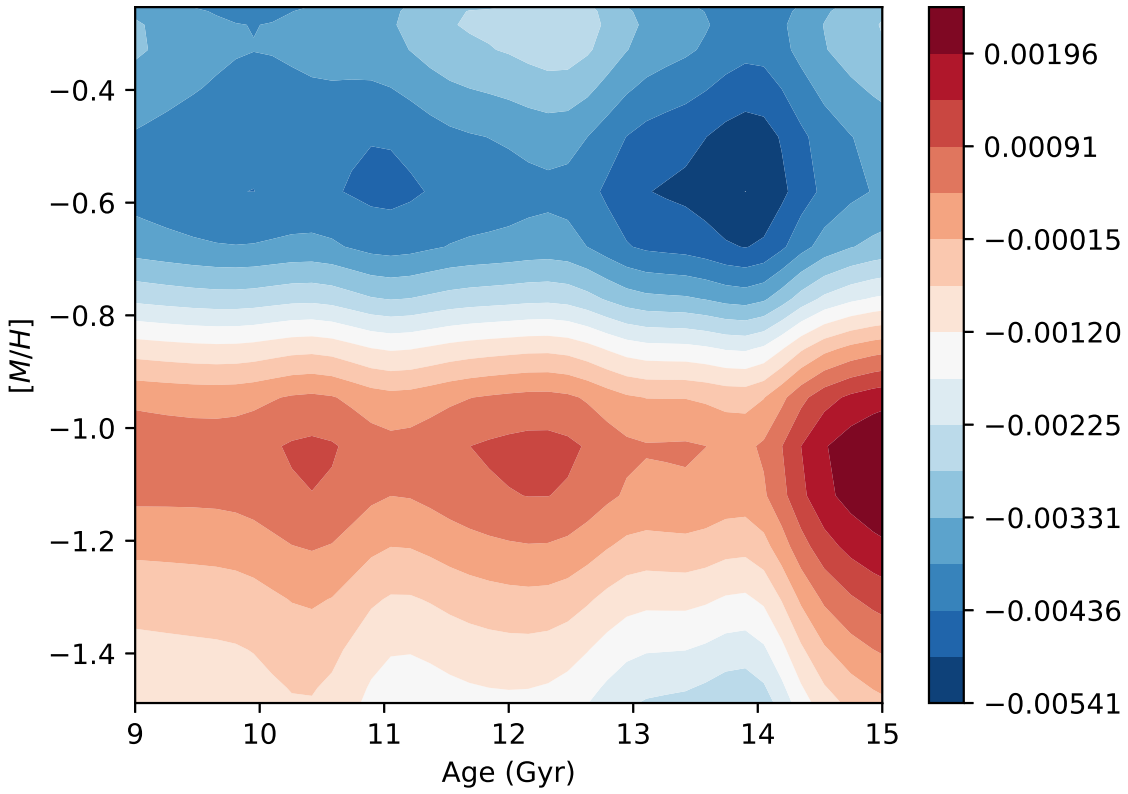

Figure A.53 Similar to A.1, but for the Ni I λ13984.2963 line in α-enhanced IL spectra.

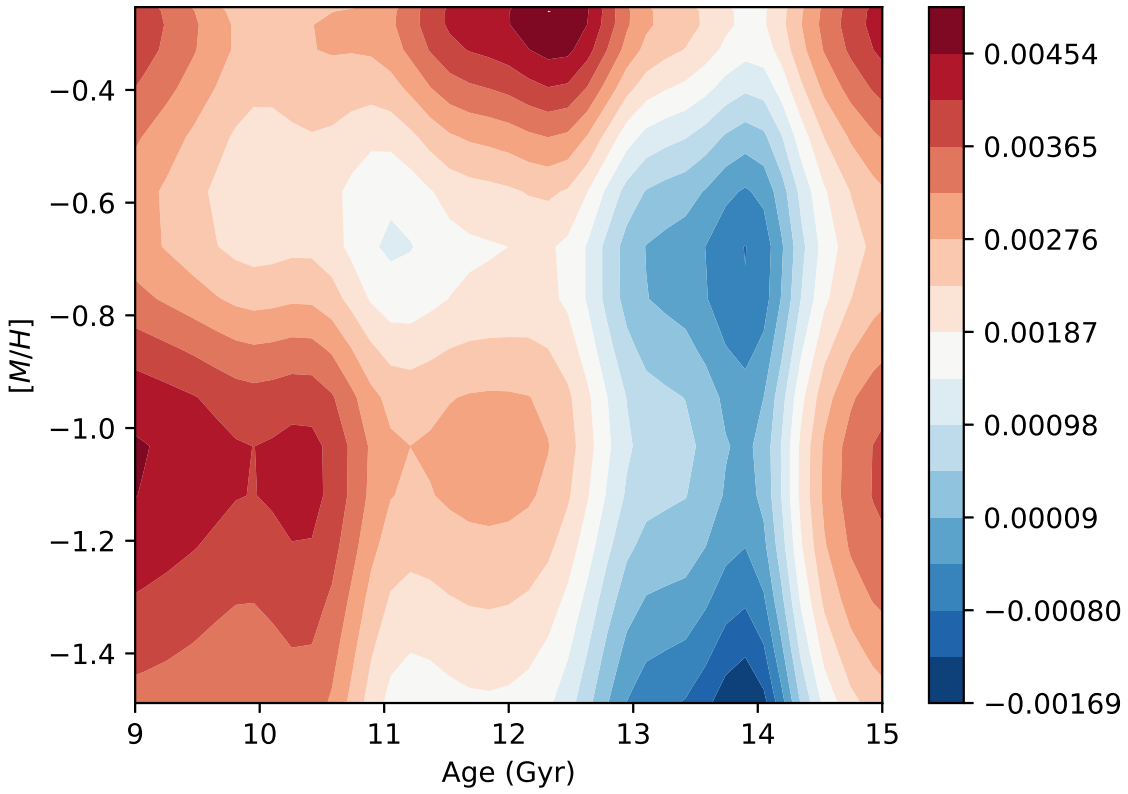

Figure A.54 Similar to A.1, but for the S I λ15474.0431 line in α-enhanced IL spectra.

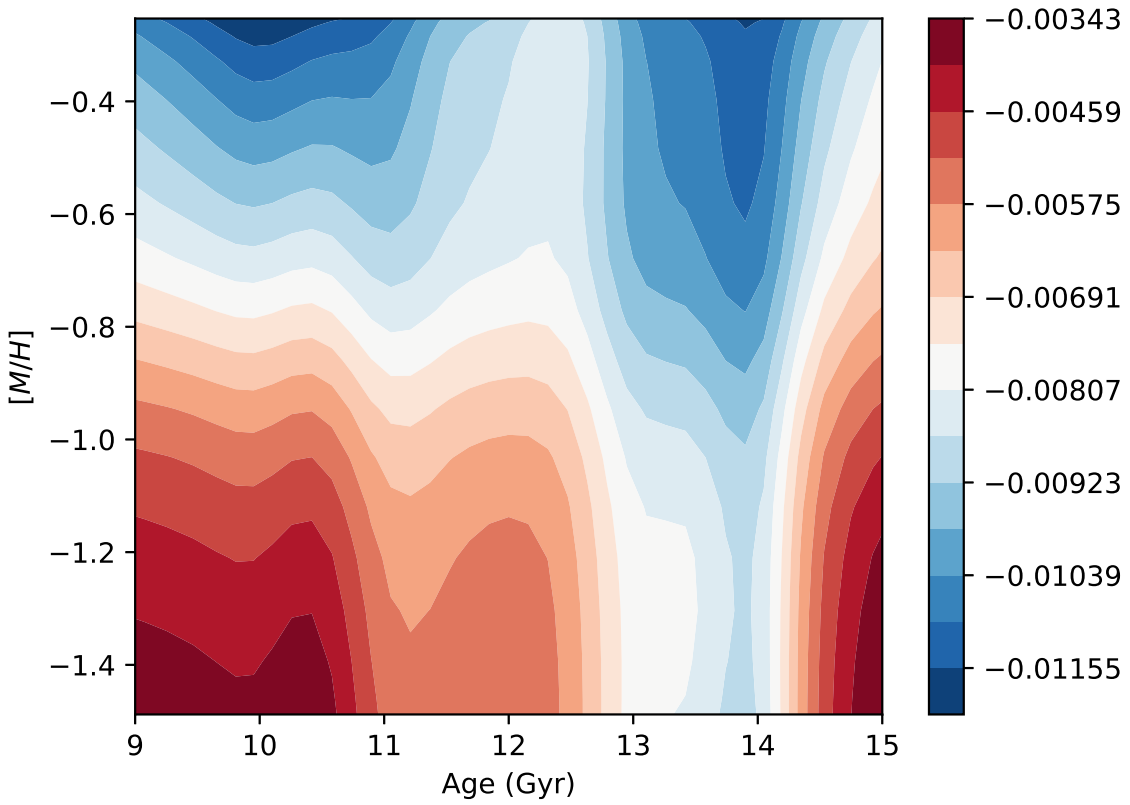

Figure A.55 Similar to A.1, but for the S I λ16452.5250 line in α-enhanced IL spectra.

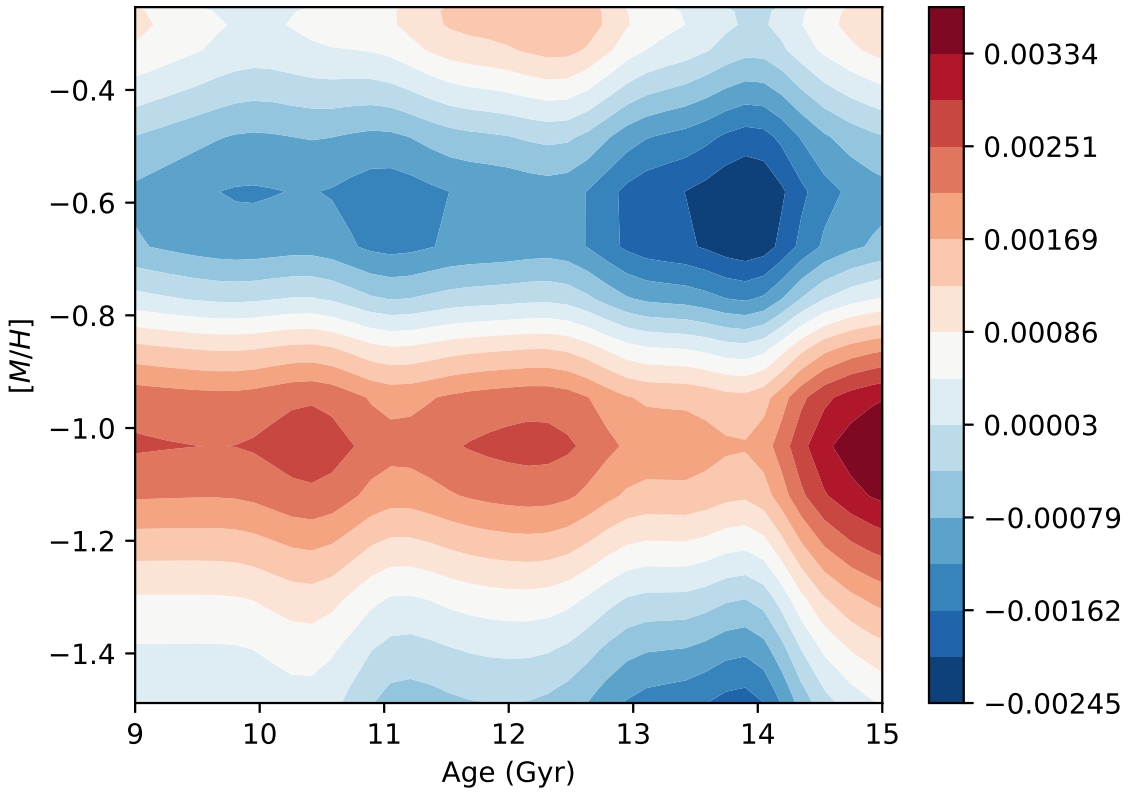

Figure A.56 Similar to A.1, but for the Si I λ13921.9399 line in α-enhanced IL spectra.

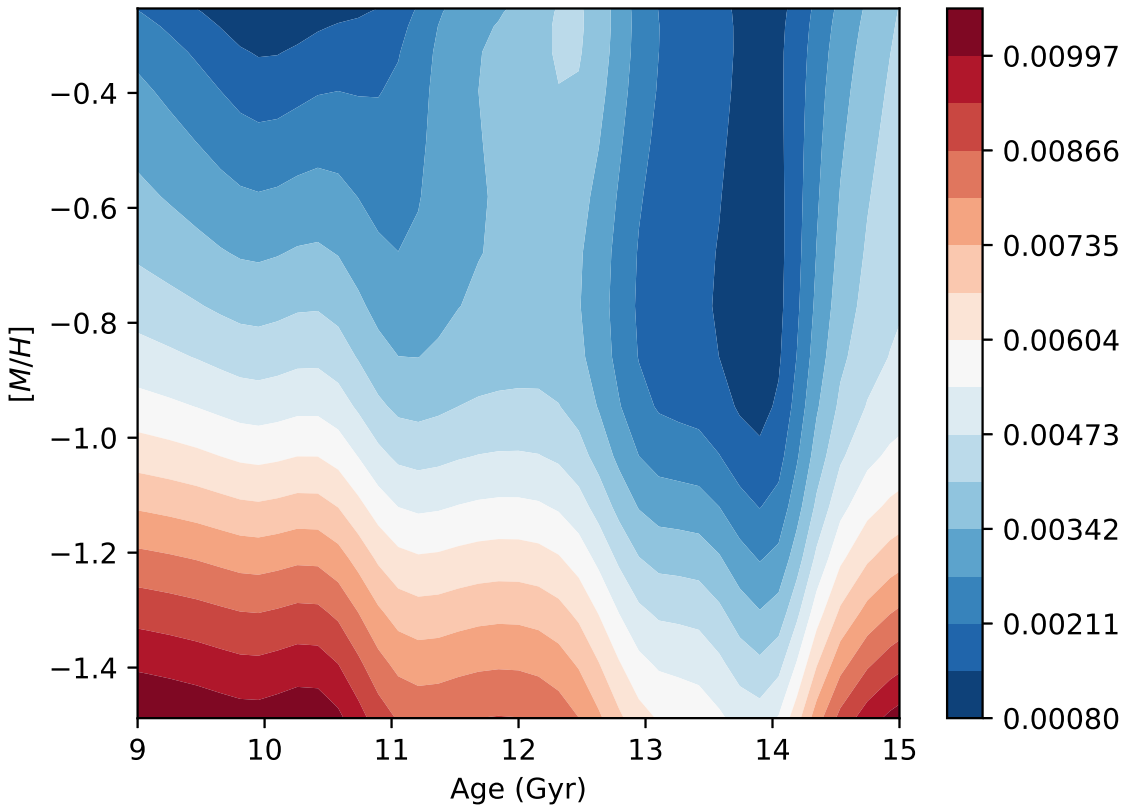

Figure A.57 Similar to A.1, but for the Si I λ16459.0251 line in α-enhanced IL spectra.

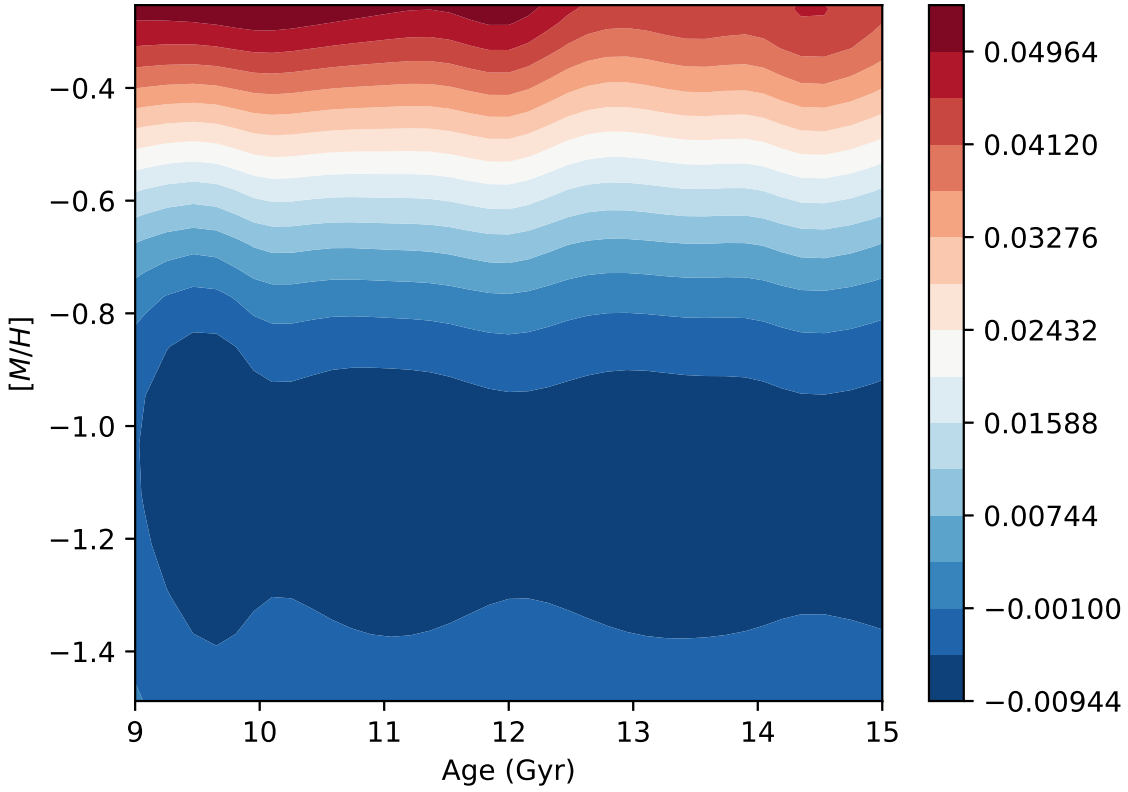

Figure A.58 Similar to A.1, but for the Ti I λ4793.8233 line in scaled-solar IL spectra.

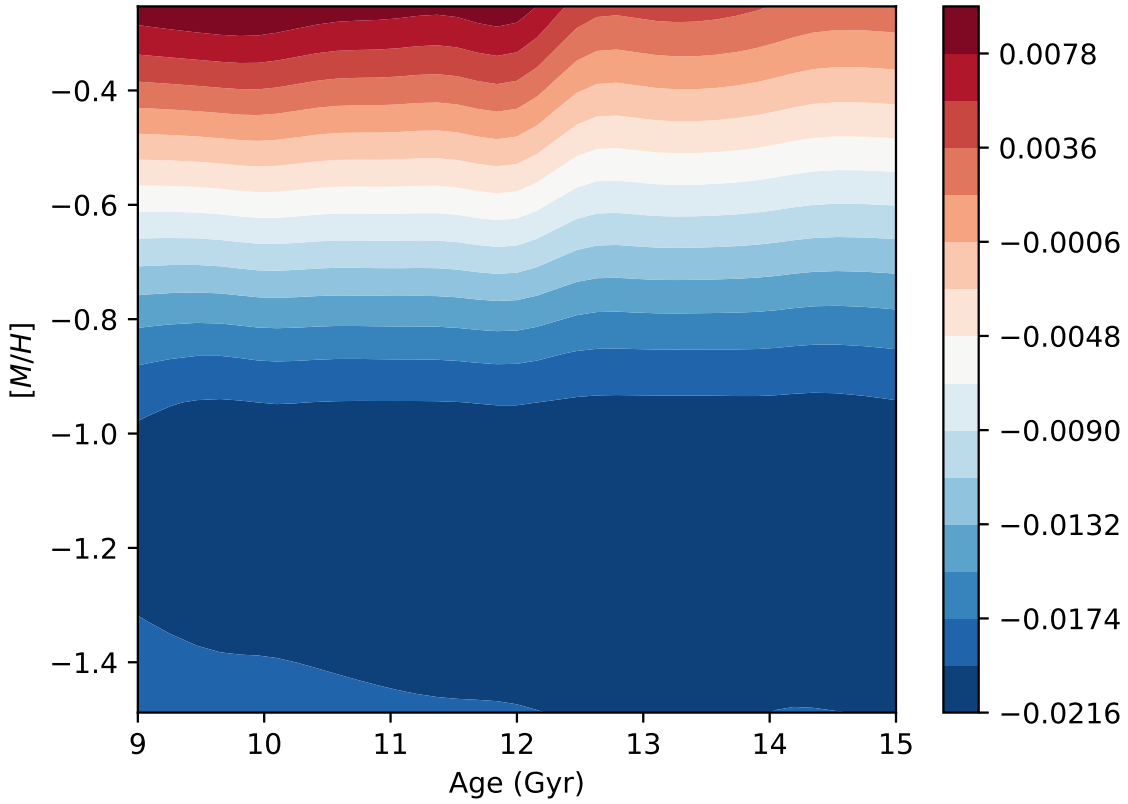

Figure A.59 Similar to A.1, but for the Ti I λ5868.0784 line in scaled-solar IL spectra.

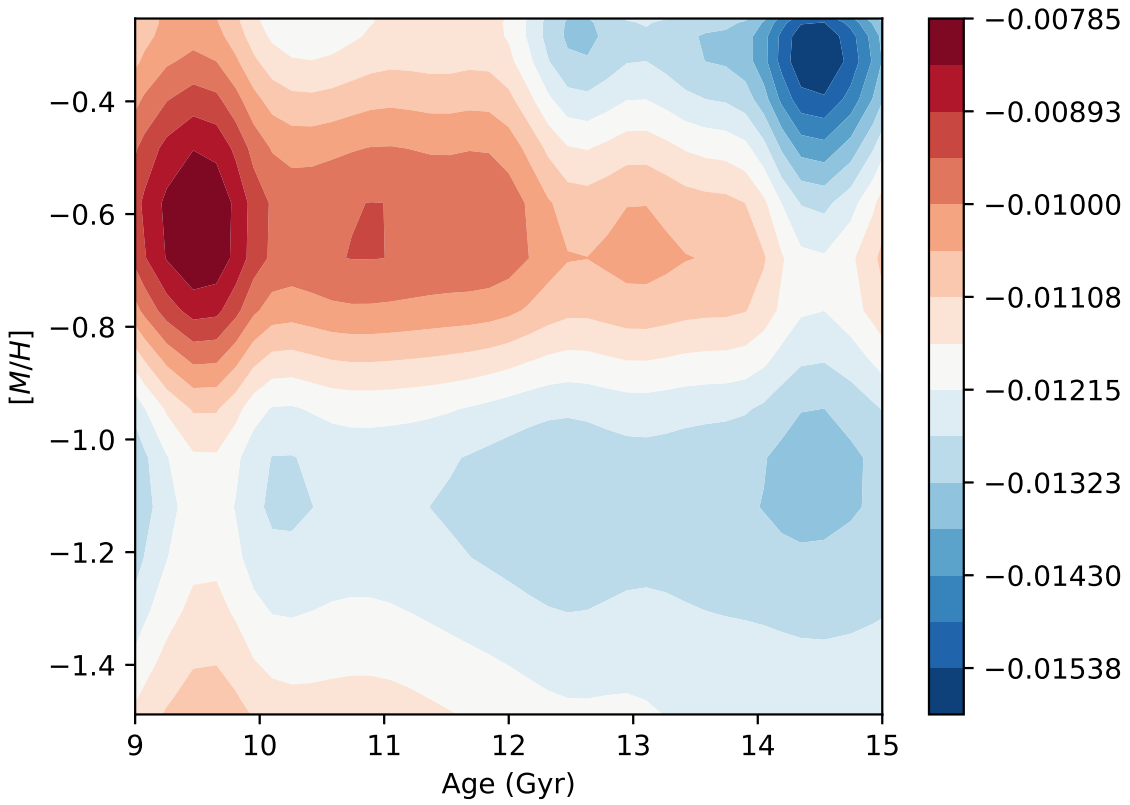

Figure A.60 Similar to A.1, but for the Ti I λ7211.4221 line in scaled-solar IL spectra.

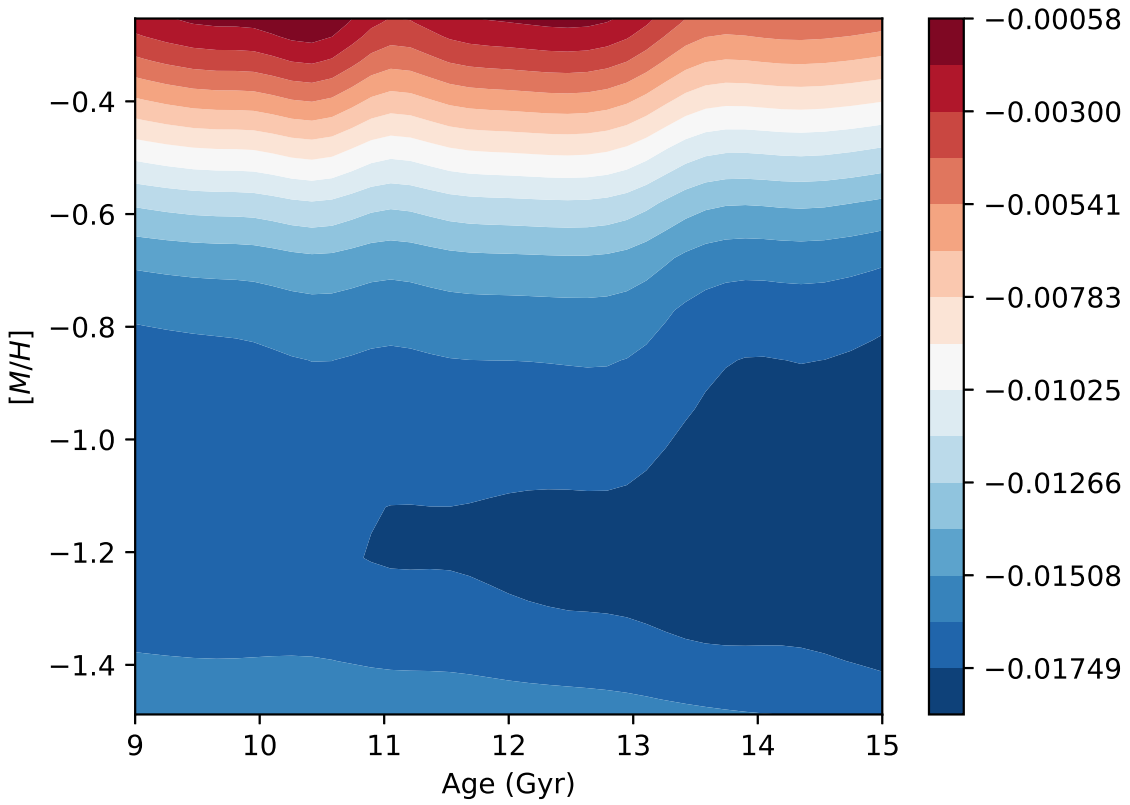

Figure A.61 Similar to A.1, but for the Ti I λ7211.4221 line in α-enhanced IL spectra.

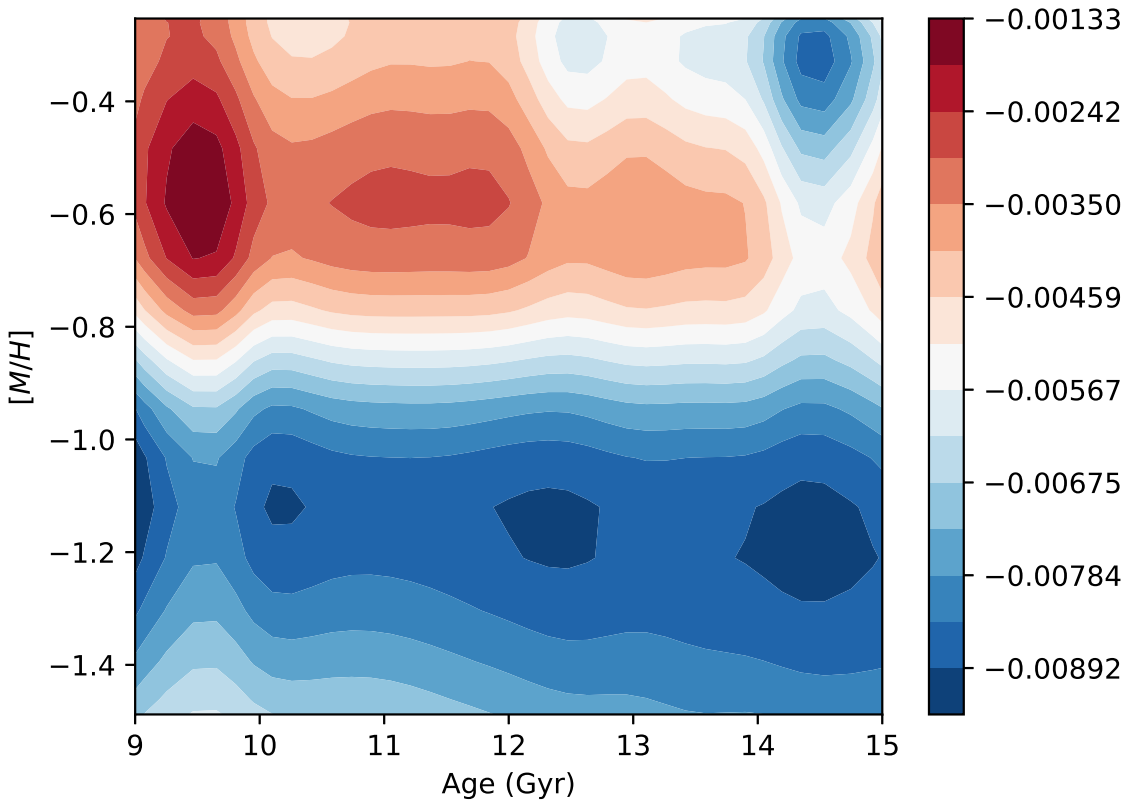

Figure A.62 Similar to A.1, but for the Ti I λ7366.1278 line in scaled-solar IL spectra.

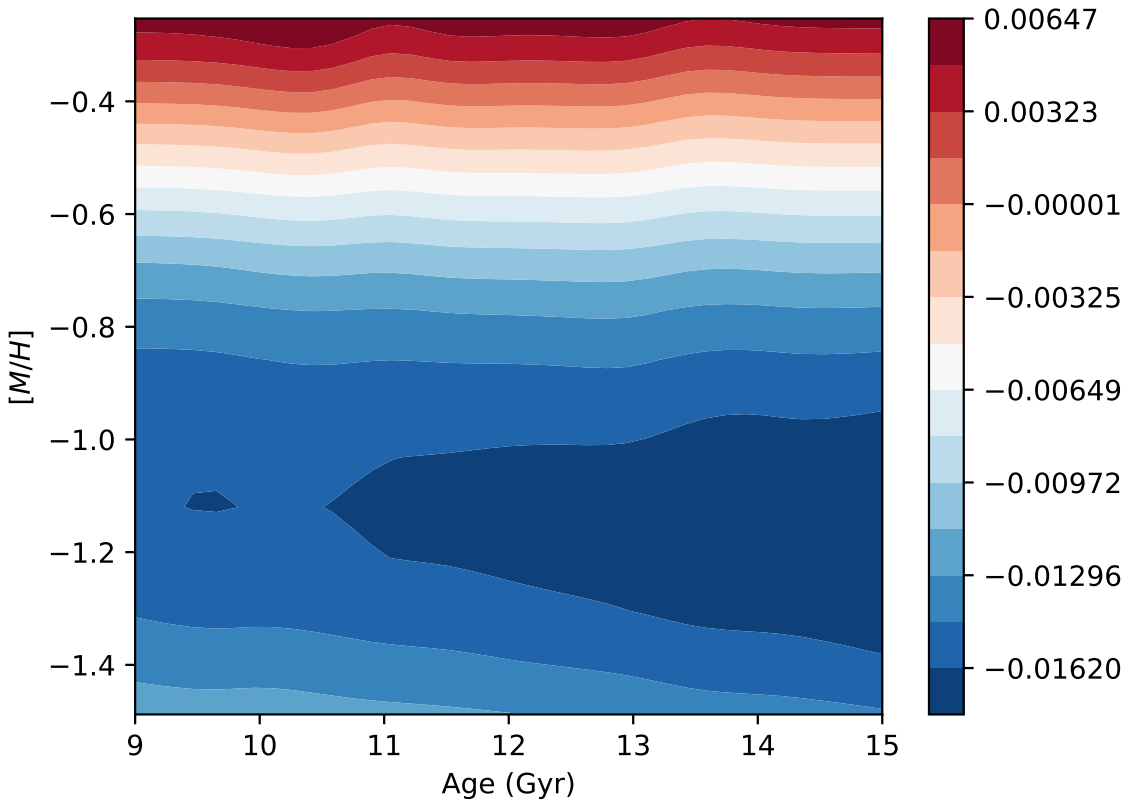

Figure A.63 Similar to A.1, but for the Ti I λ8366.5376 line in α-enhanced IL spectra.

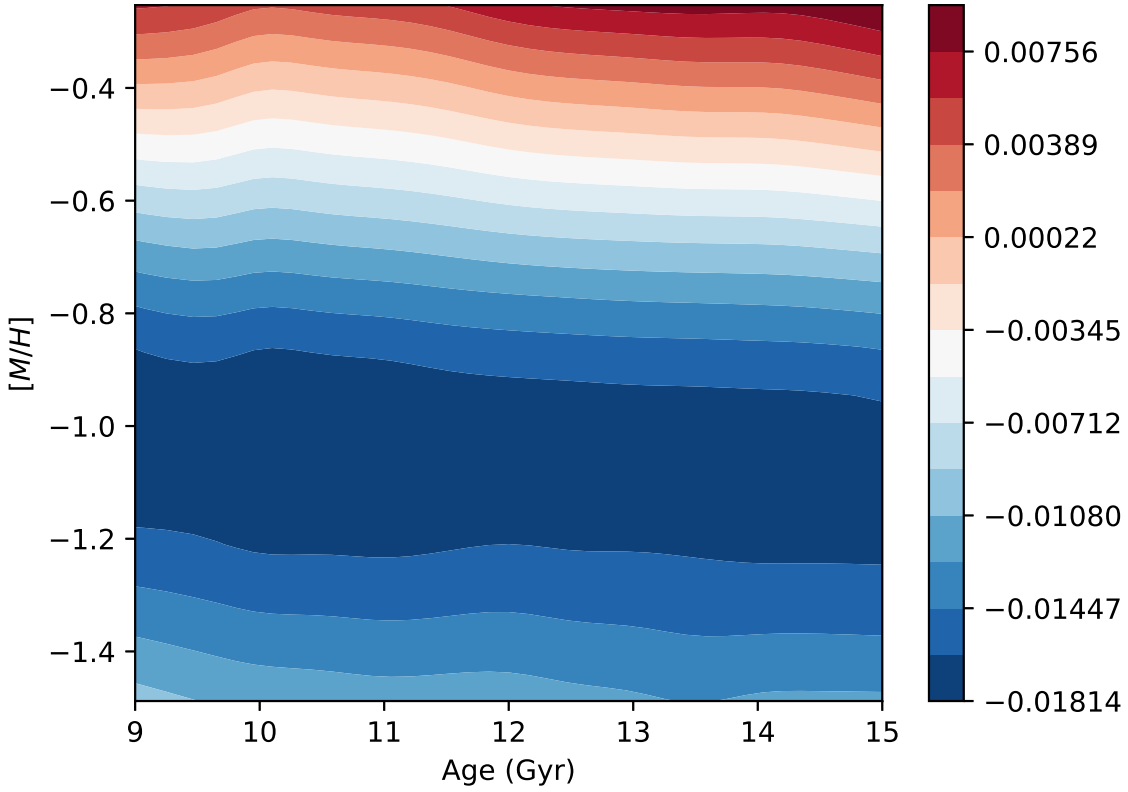

Figure A.64 Similar to A.1, but for the Ti I λ8685.3667 line in scaled-solar IL spectra.

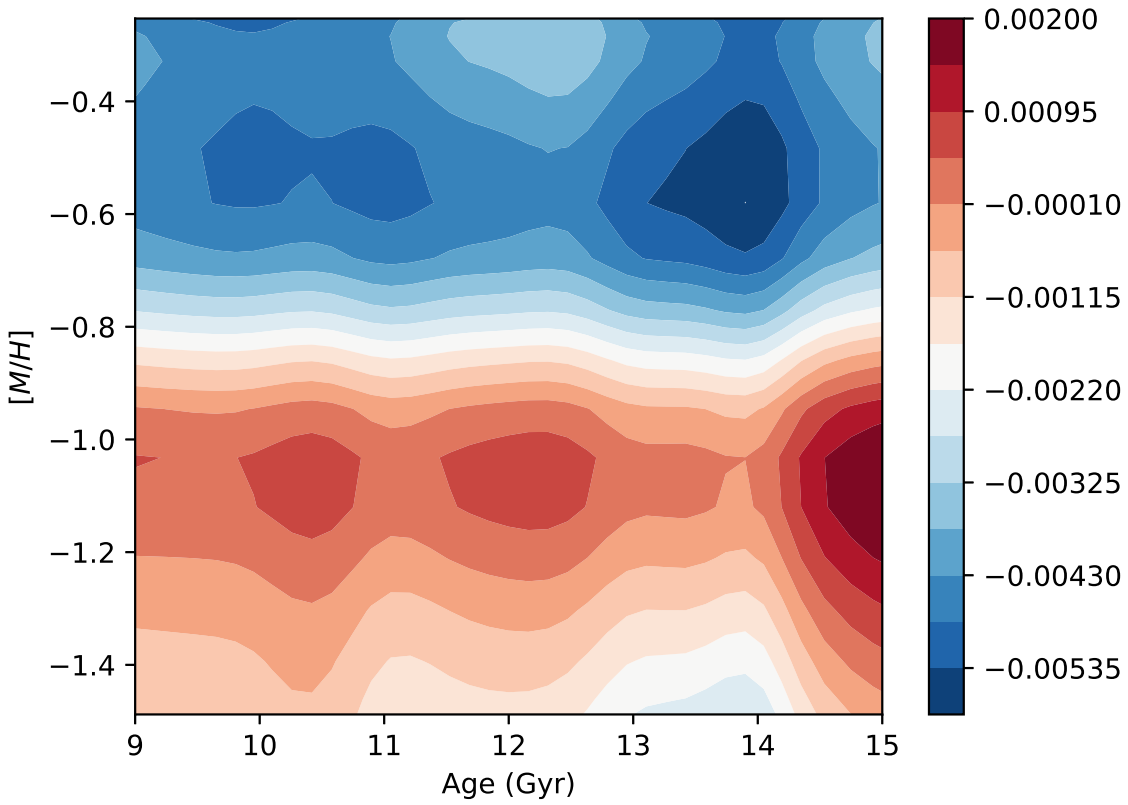

Figure A.65 Similar to A.1, but for the Ti I λ13932.3435 line in α-enhanced IL spectra.

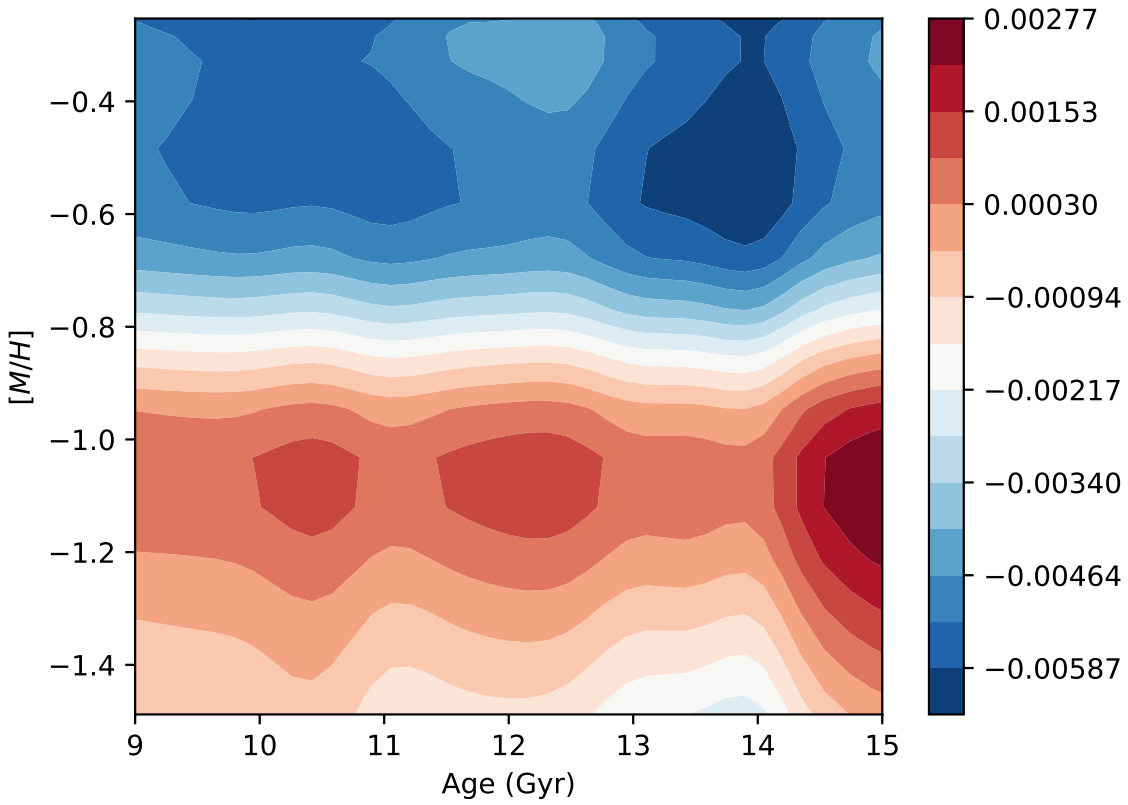

Figure A.66 Similar to A.1, but for the Ti I λ13976.8167 line in α-enhanced IL spectra.

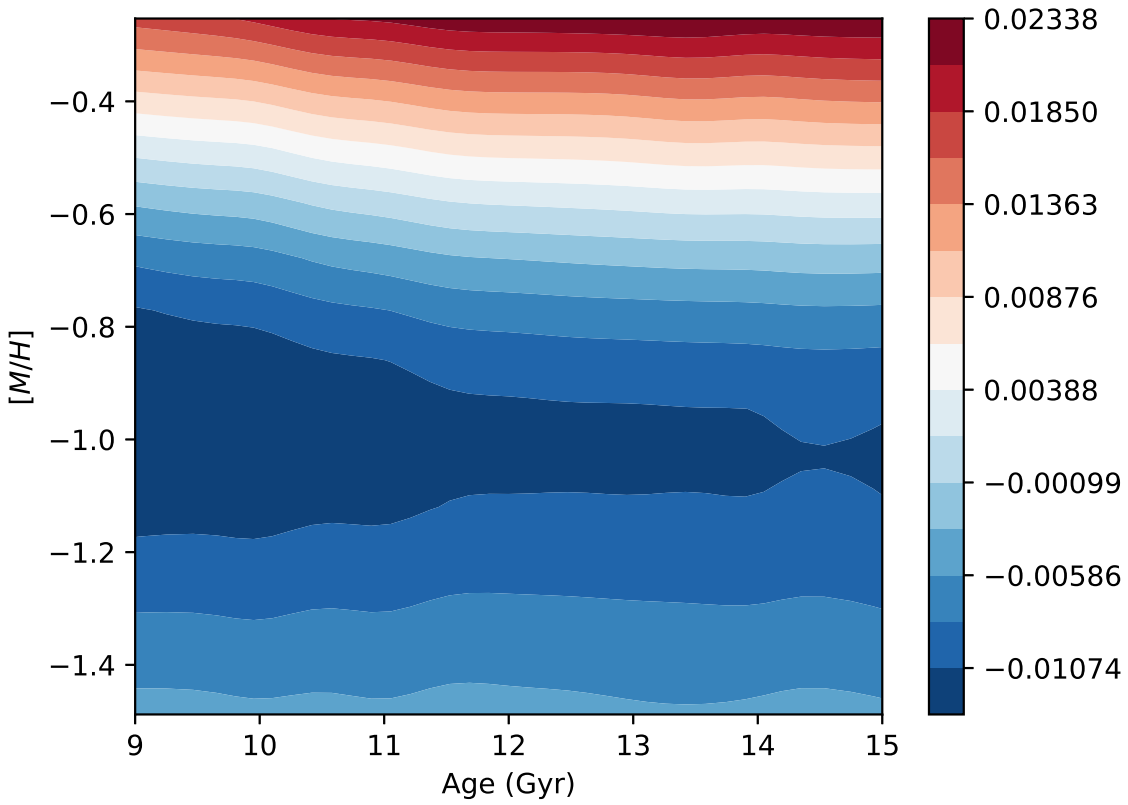

Figure A.67 Similar to A.1, but for the Ti I λ21903.3565 line in scaled-solar IL spectra.

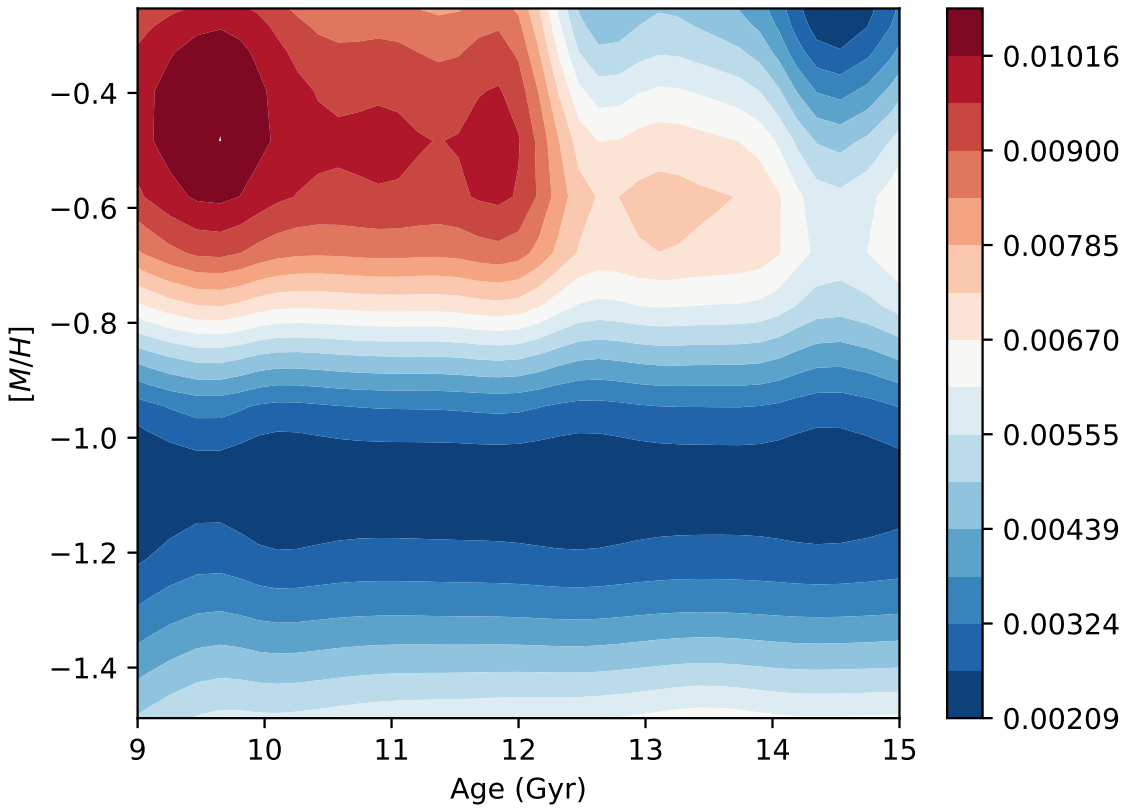

Figure A.68 Similar to A.1, but for the V I λ6298.2272 line in scaled-solar IL spectra.

B Representative Spectral Region Fits for Observed Clusters

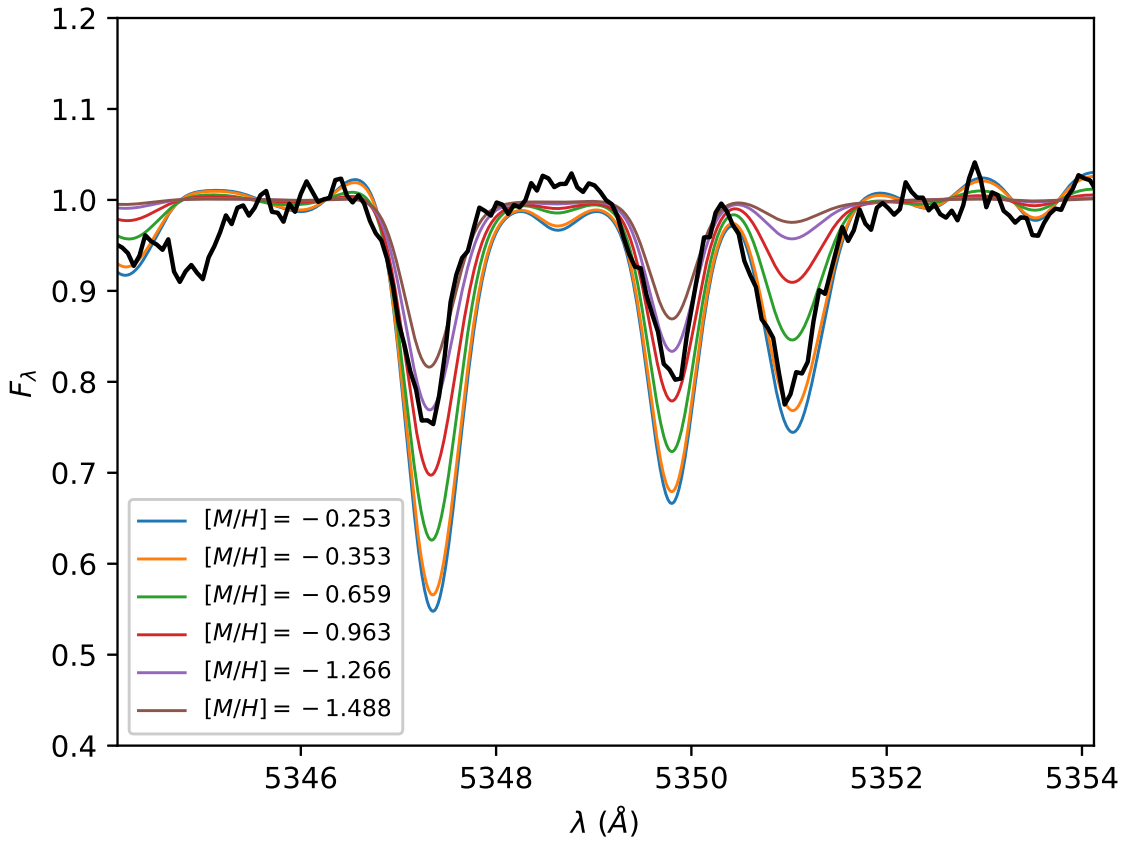

Figure B.1 Representative 10 $\mathring{A}$ window for NGC 104 in black with bracketing 13.0 Gyr NLTE α-enhanced IL spectra. The window contains the Cr I λ5347.2939 and λ5349.8276 lines, and the Ca I λ5350.9569 line.

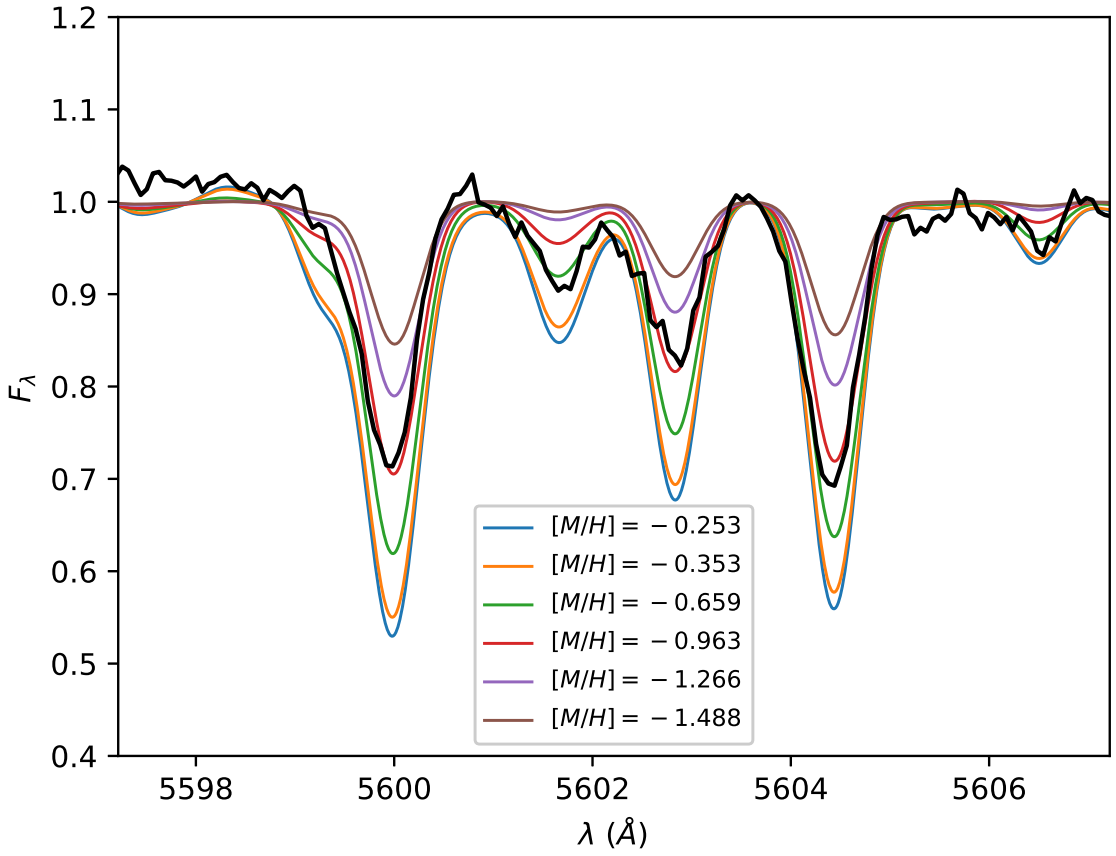

Figure B.2 Similar to Figure B.1, but containing the Ca I λ5600.0344, λ5602.8323 and λ5604.3985 lines.

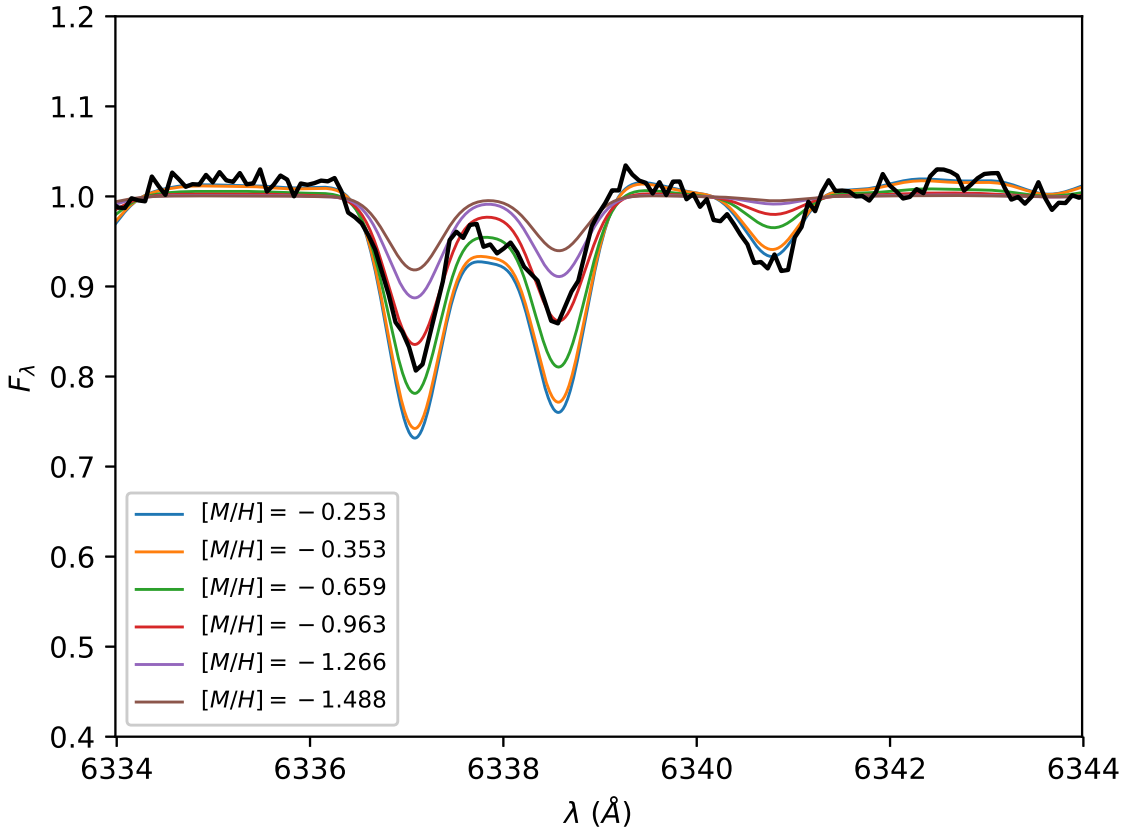

Figure B.3 Similar to Figure B.1, but containing the Fe I λ6337.0889 and λ6338.5823 lines, and the Ni I λ6340.8709 line.

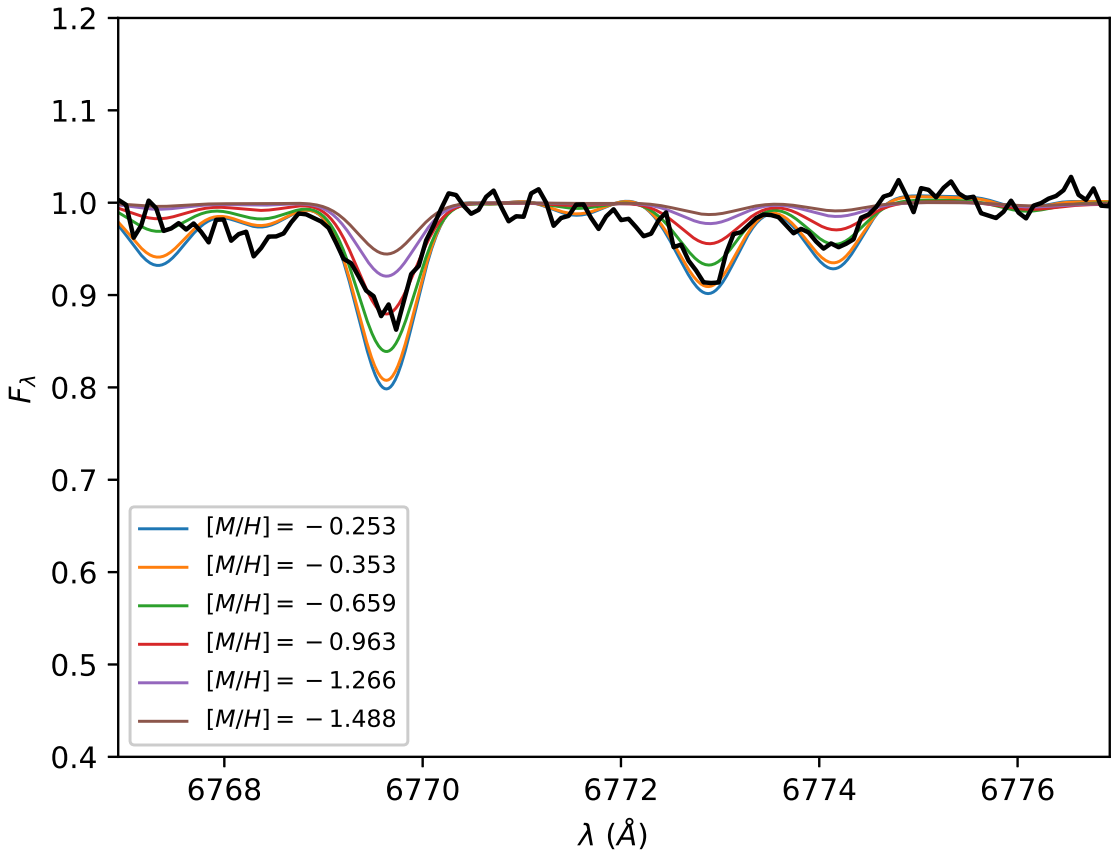

Figure B.4 Similar to Figure B.1, but containing the Ni I λ6769.6521 and λ6774.1903 lines, and the Co I λ6772.8390.

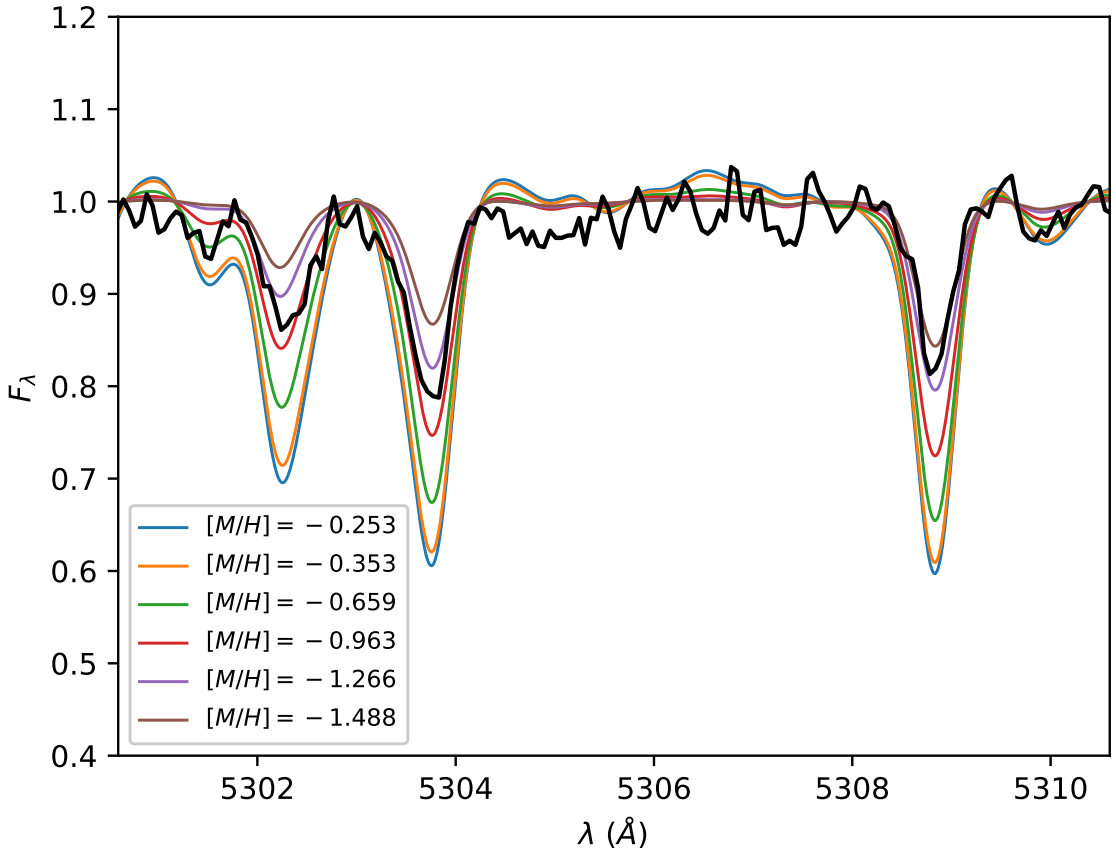

Figure B.5 Representative 10 $\AA$ window for NGC 362 (in black) with bracketing 12.5 Gyr NLTE α-enhanced IL spectra. The window contains the C I λ5302.3454 line, and the Fe I λ5303.7823 and λ5308.8457 lines.

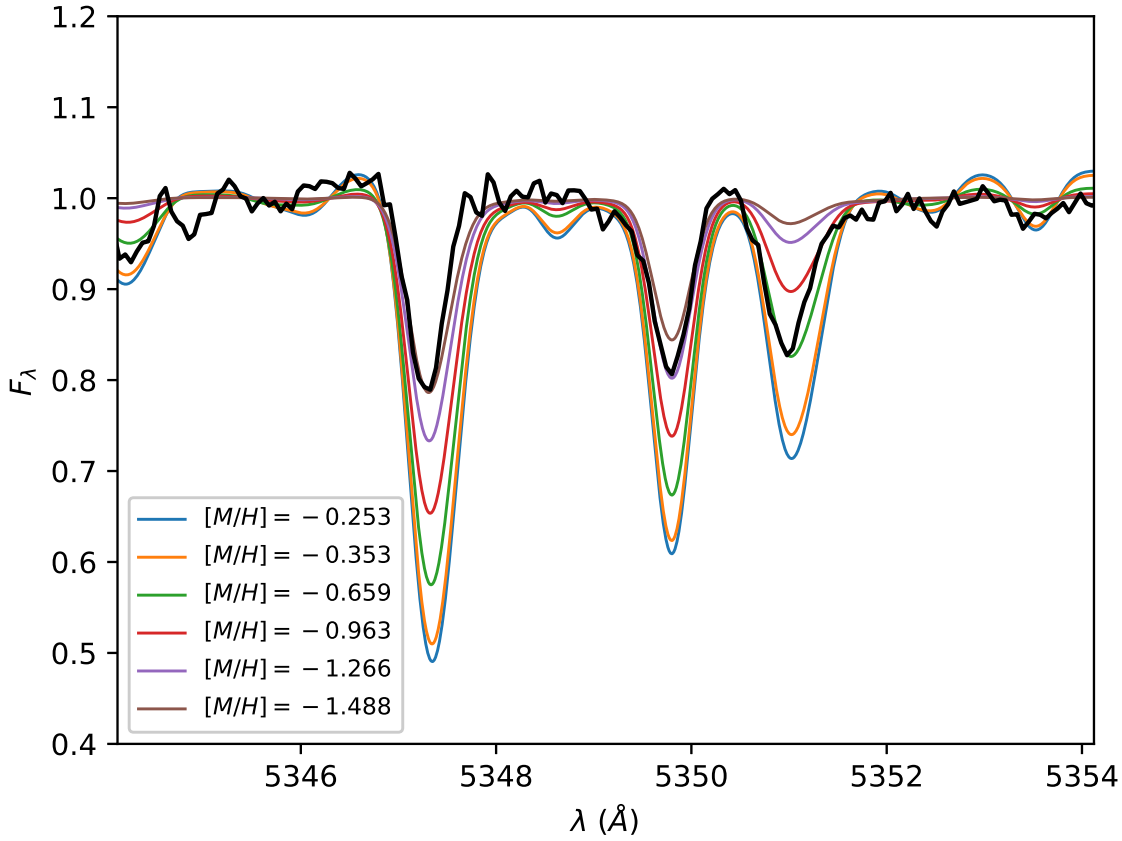

Figure B.6 Similar to Figure B.5, but containing the Cr I λ5347.2939 and λ5349.8276 lines, and the Ca I λ5350.9569 line.

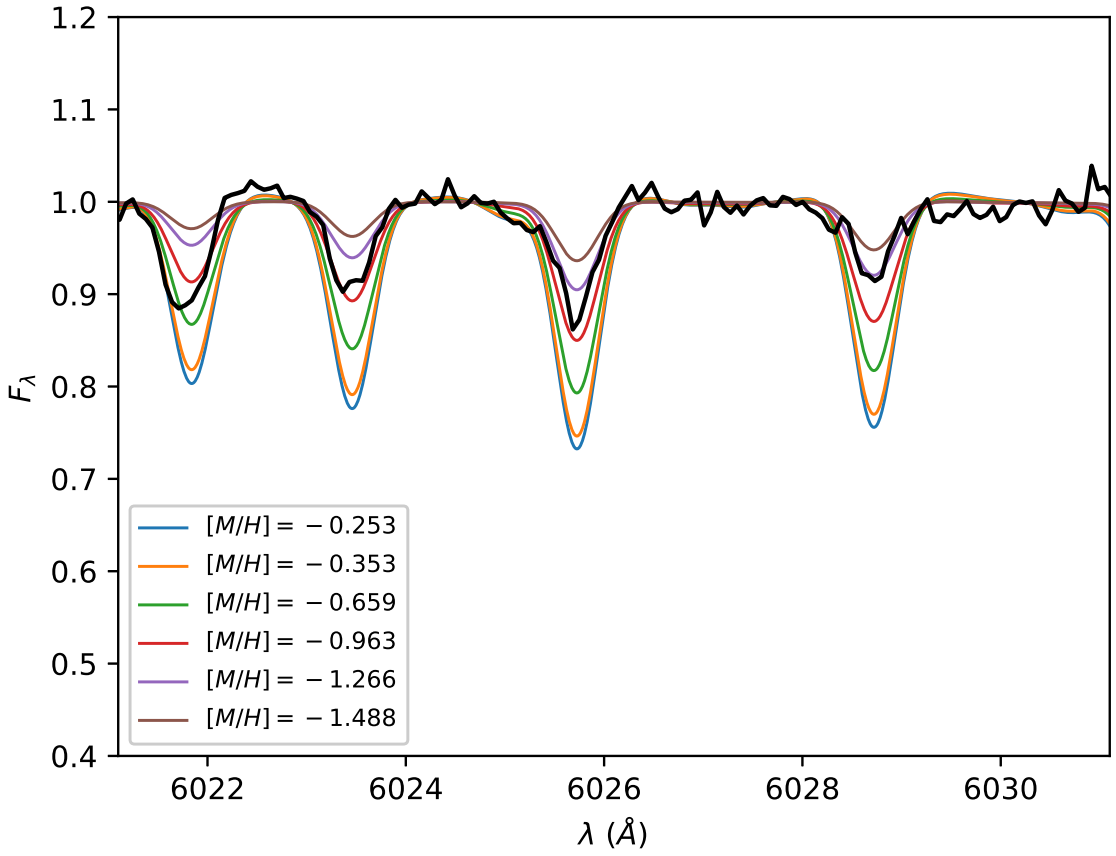

Figure B.7 Similar to Figure B.5, but containing the Mn I λ6023.4877 line, and the Fe I λ6025.7263 and λ6028.7201 lines.

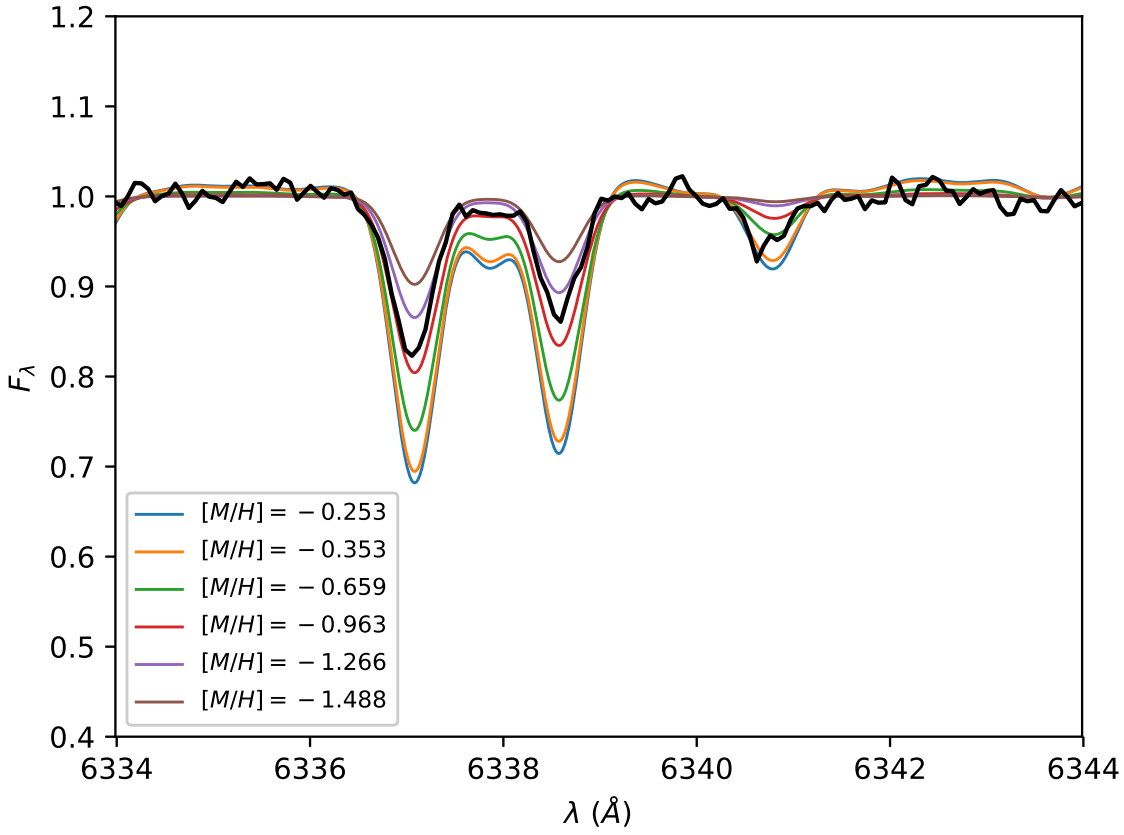

Figure B.8 Similar to Figure B.5, but containing the Fe I λ6337.0889 and λ6338.5823 lines, and the Ni I λ6340.8709 line.

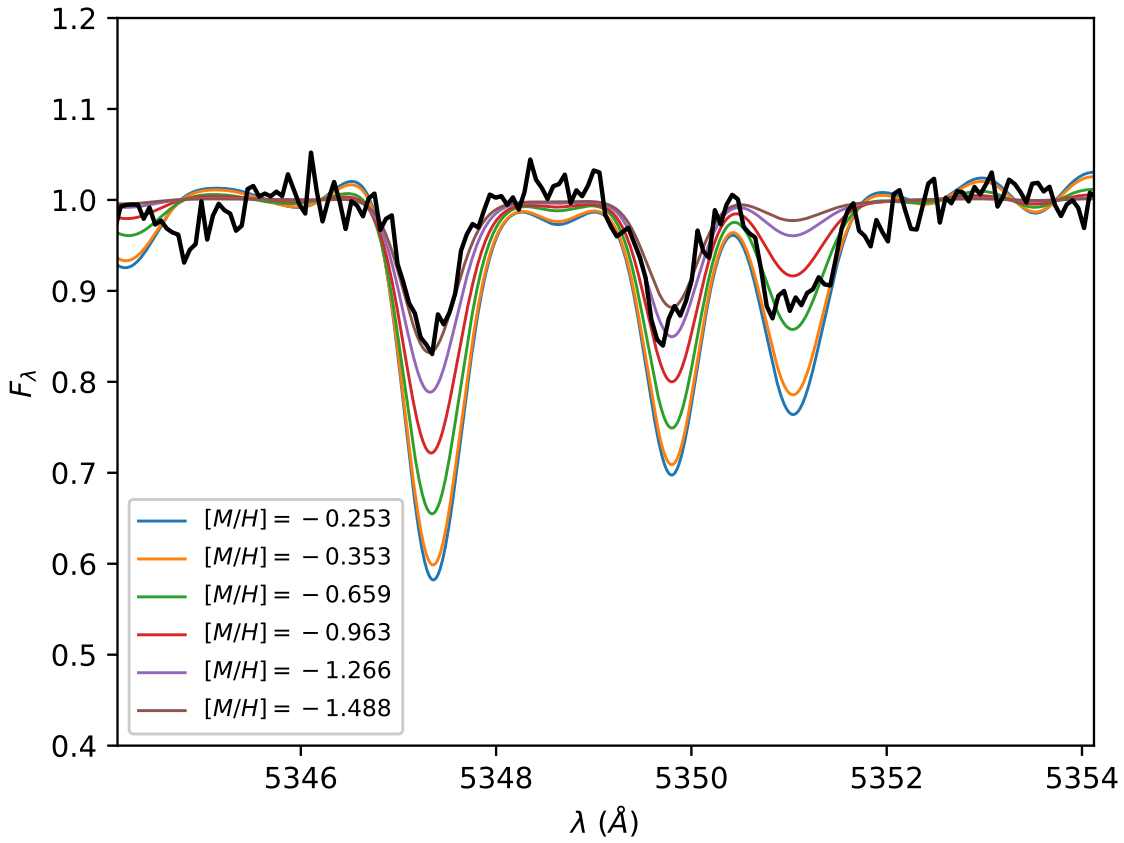

Figure B.9 Representative 10 $\mathring{A}$ window for NGC 2808 (in black) with bracketing 11.5 Gyr NLTE α-enhanced IL spectra. The window contains the Cr I λ5347.2939 and λ5349.8276 lines, and the Ca I λ5350.9569 line.

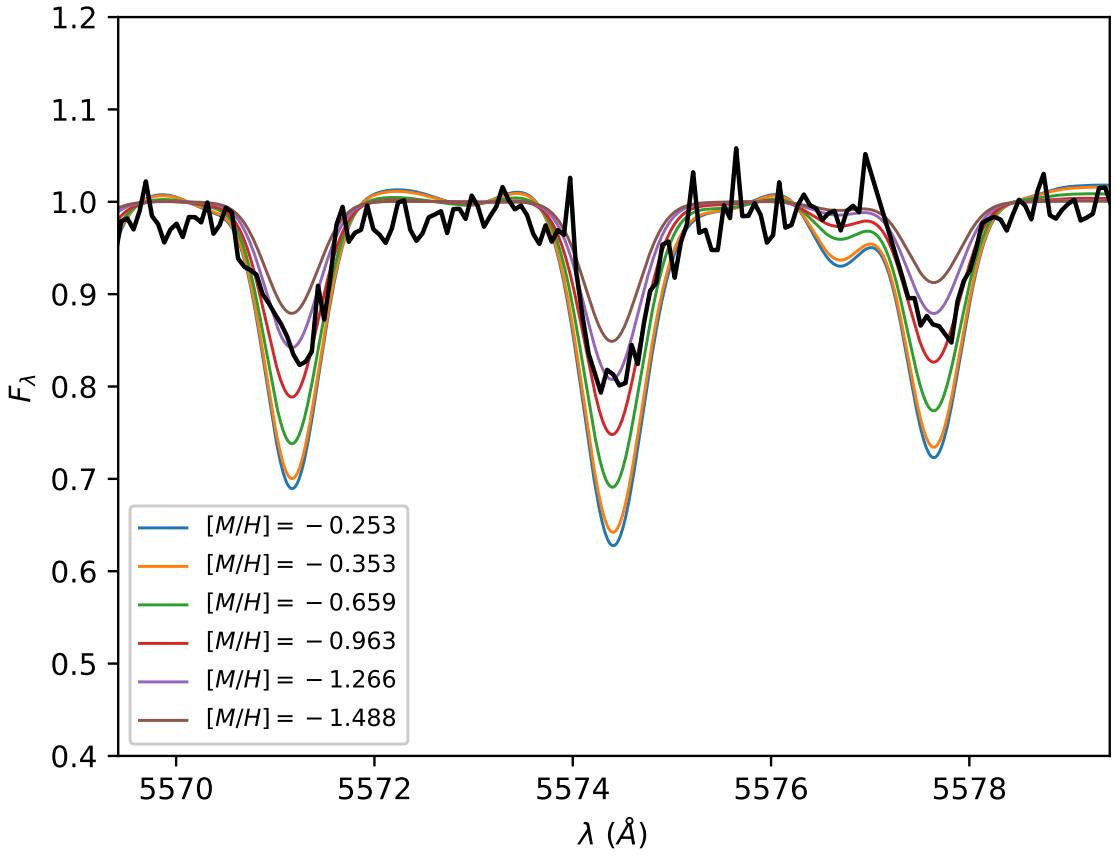

Figure B.10 Similar to Figure B.9, but containing the Fe I λ5571.1777, λ5574.3986 and λ5577.6474 lines.

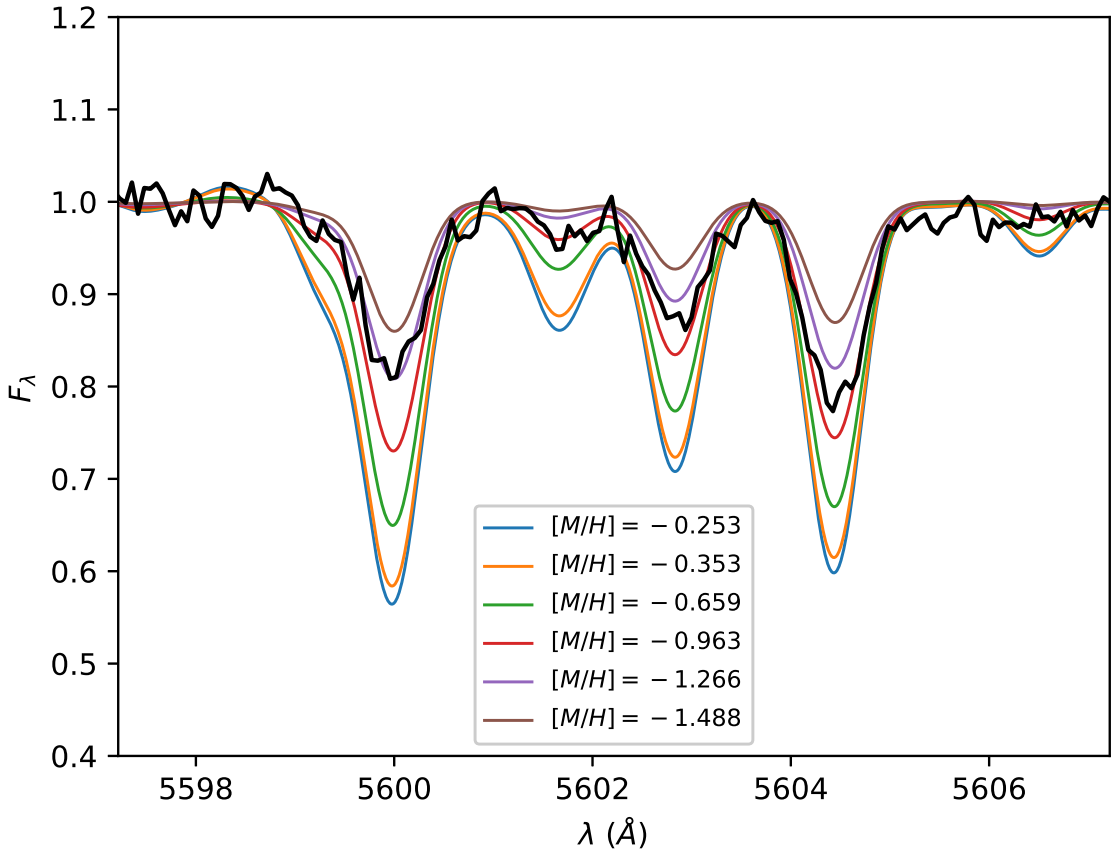

Figure B.11 Similar to Figure B.9, but containing the Ca I λ5600.0344, λ5602.8323 and λ5604.3985 lines.

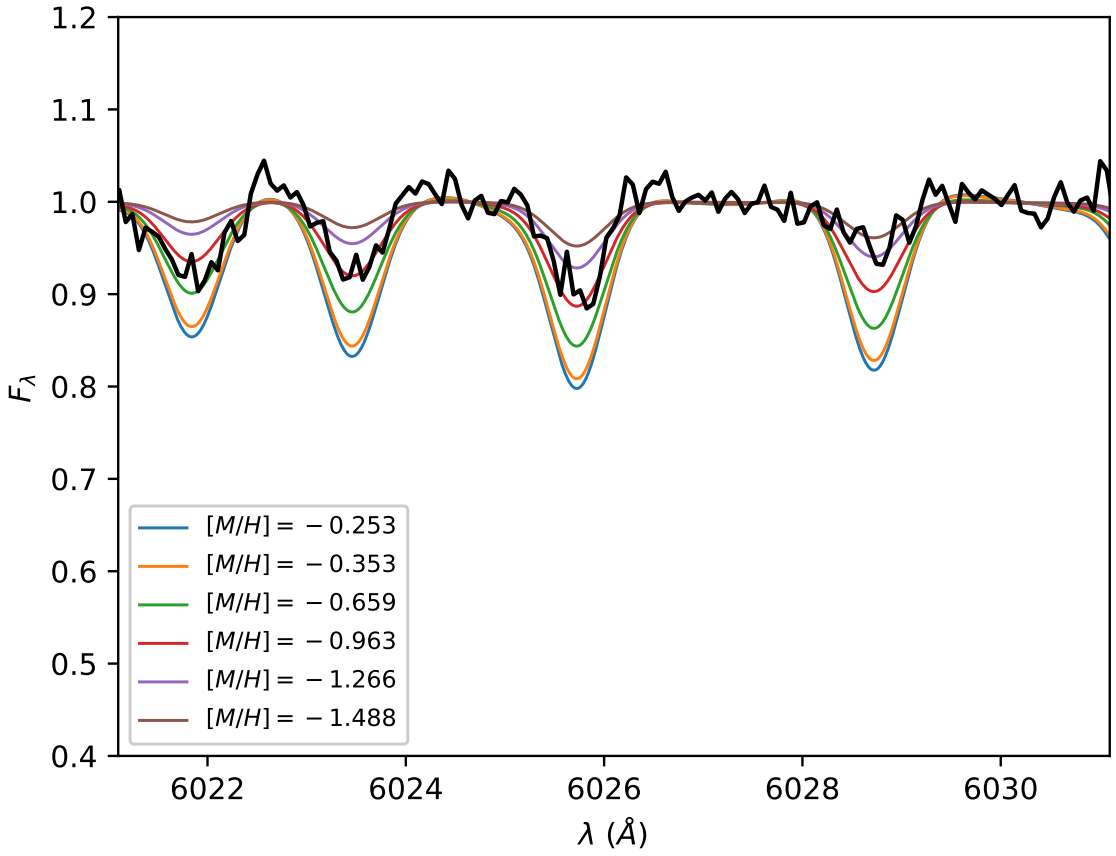

Figure B.12 Similar to Figure B.9, but containing the Mn I λ6023.4877 line, and the Fe I λ6025.7263 and λ6028.7201 lines.

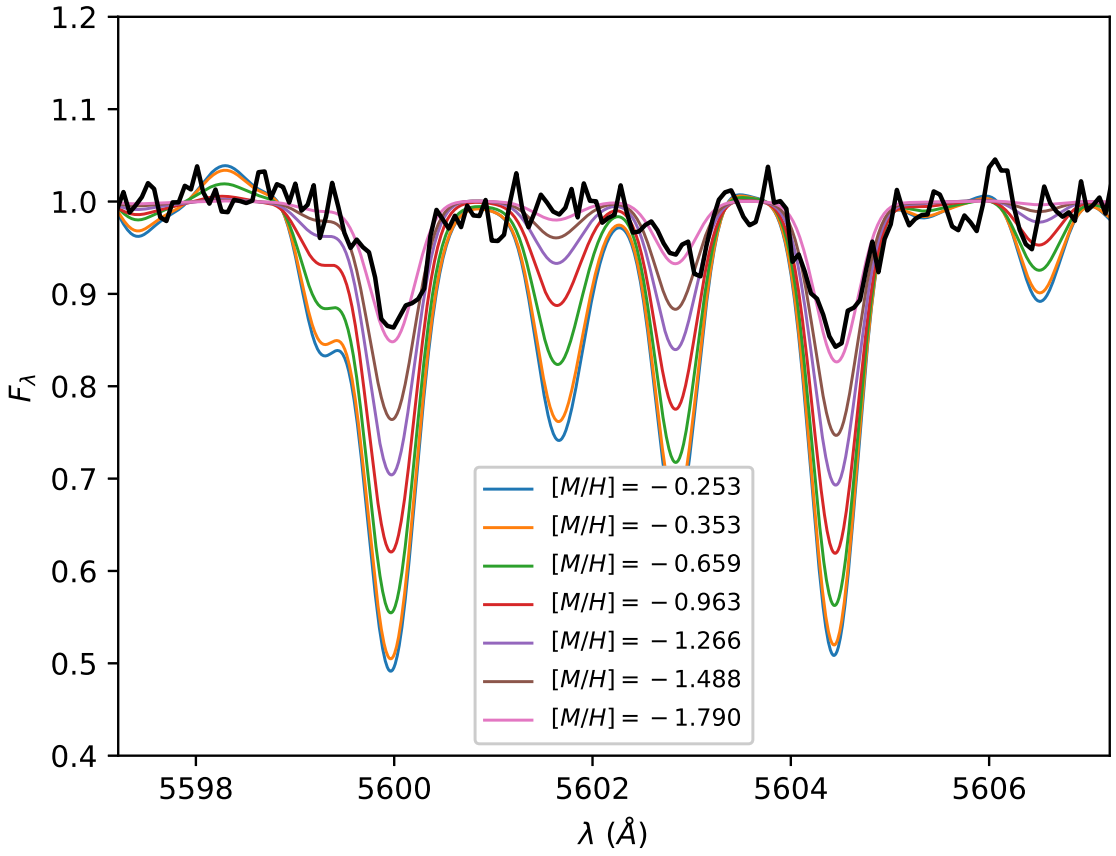

Figure B.13 Representative 10 $\mathring{A}$ window for NGC 6093 (in black) with bracketing 12.5 Gyr NLTE scaled-solar IL spectra. The window contains the Ca I λ5600.0344, λ5602.8323 and λ5604.3985 lines.

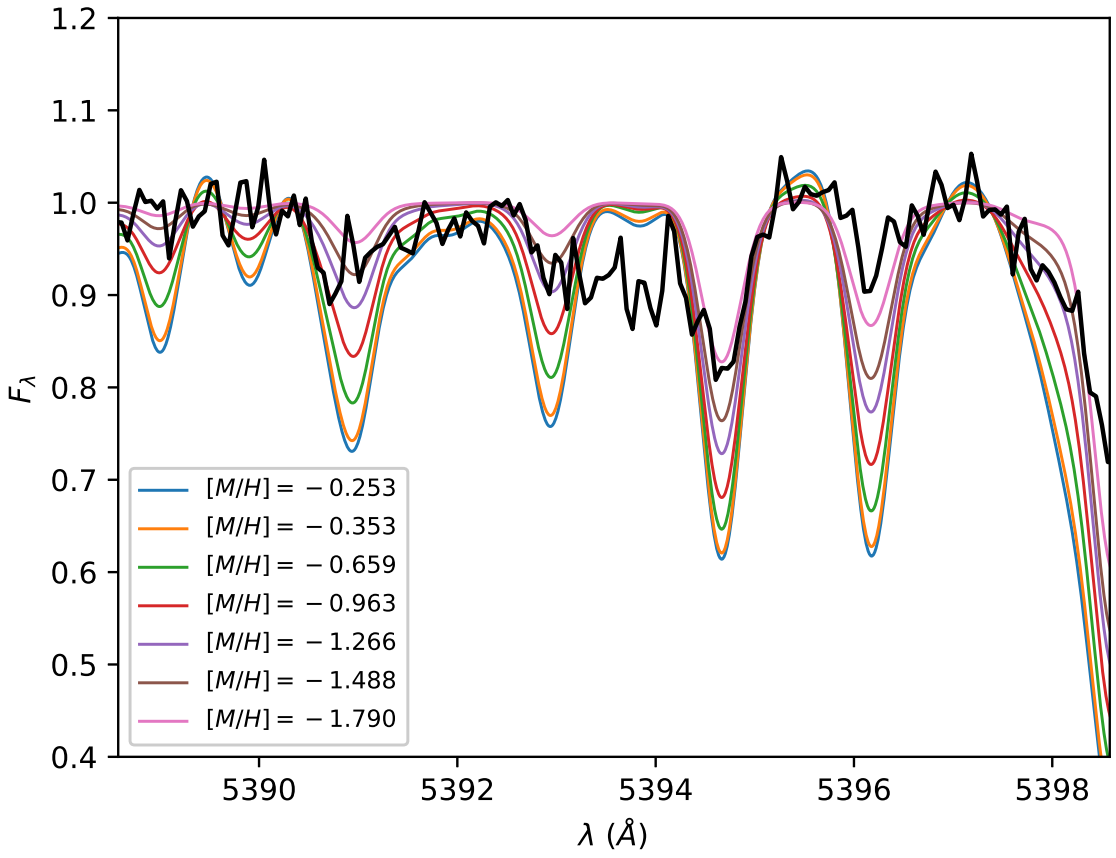

Figure B.14 Similar to Figure B.13, but containing the Fe I λ5390.9846 and λ5394.6756 lines, and the Mn I λ5396.1689 line.

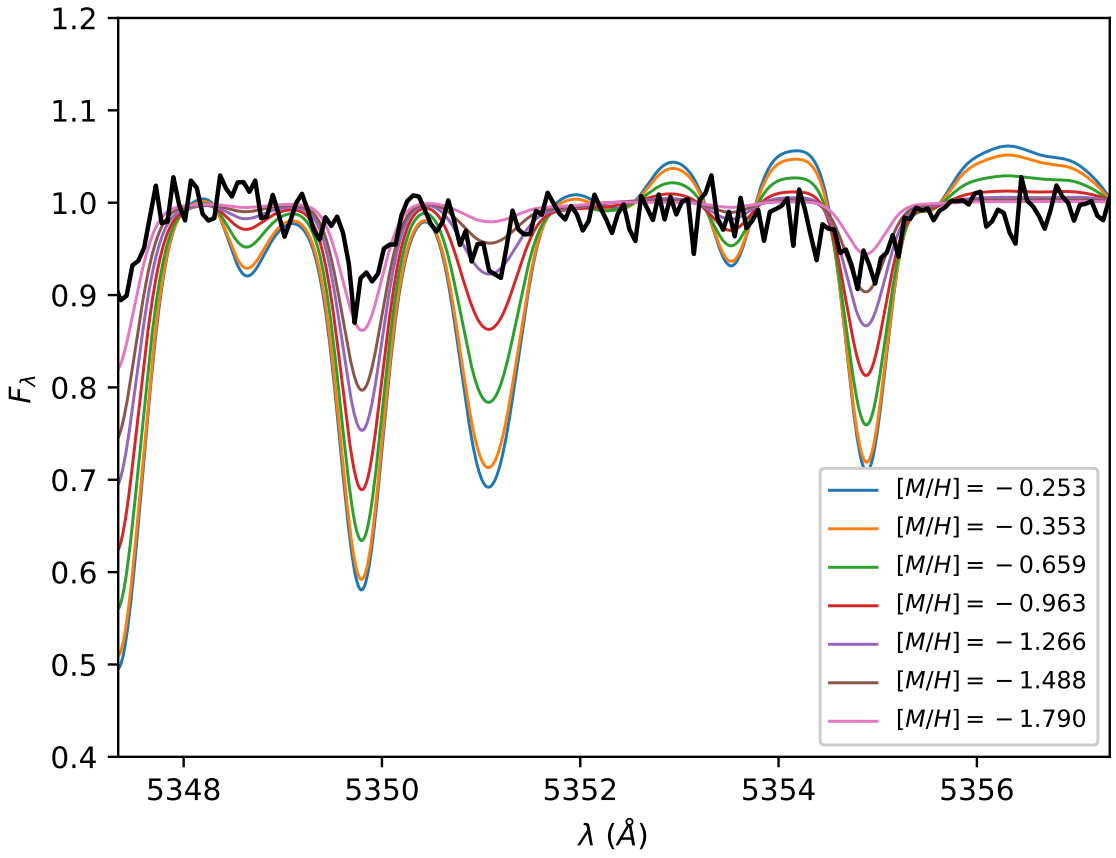

Figure B.15 Similar to Figure B.13, but containing the Cr I λ5349.8276 line, the Ca I λ5350.9569 line, and the Ni I λ5354.8797 line.

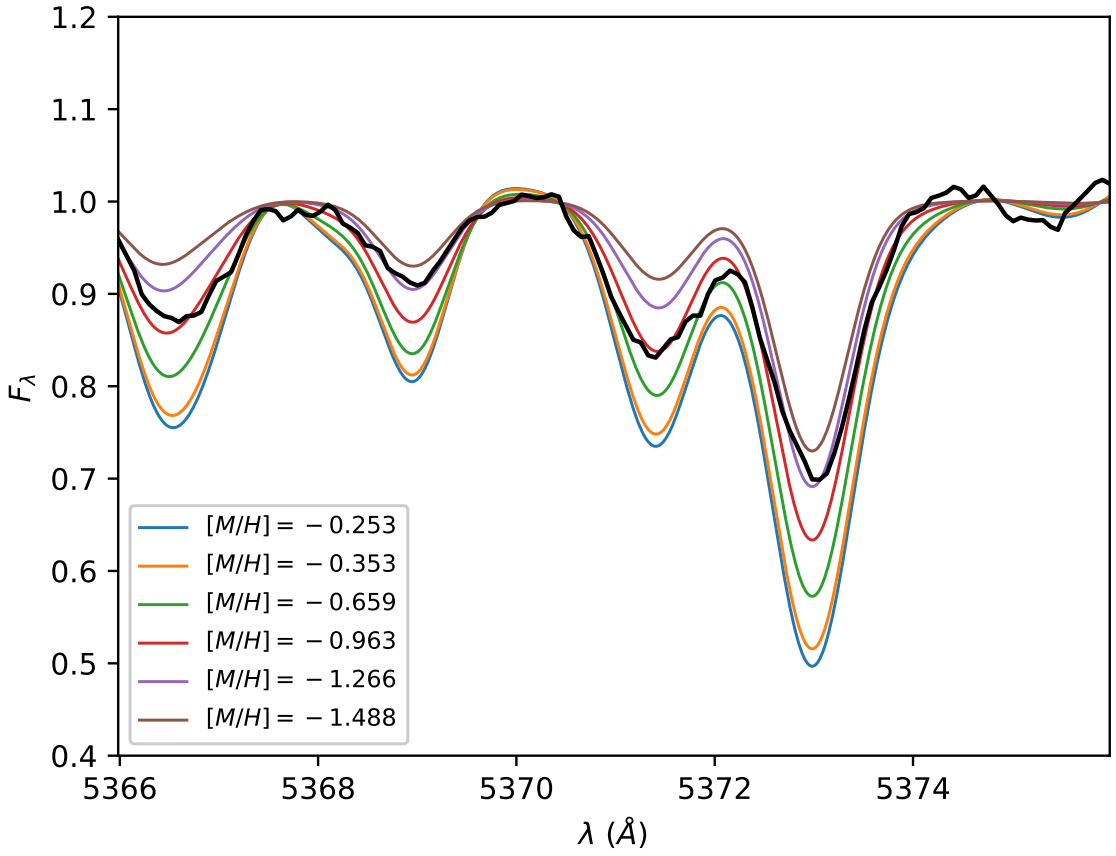

Figure B.16 Representative 10 $\mathring{A}$ window for NGC 6388 (in black) with bracketing 10.0 Gyr NLTE α-enhanced IL spectra. The window contains the Fe I λ5368.9687, λ5371.4674 and λ5372.9948 lines.

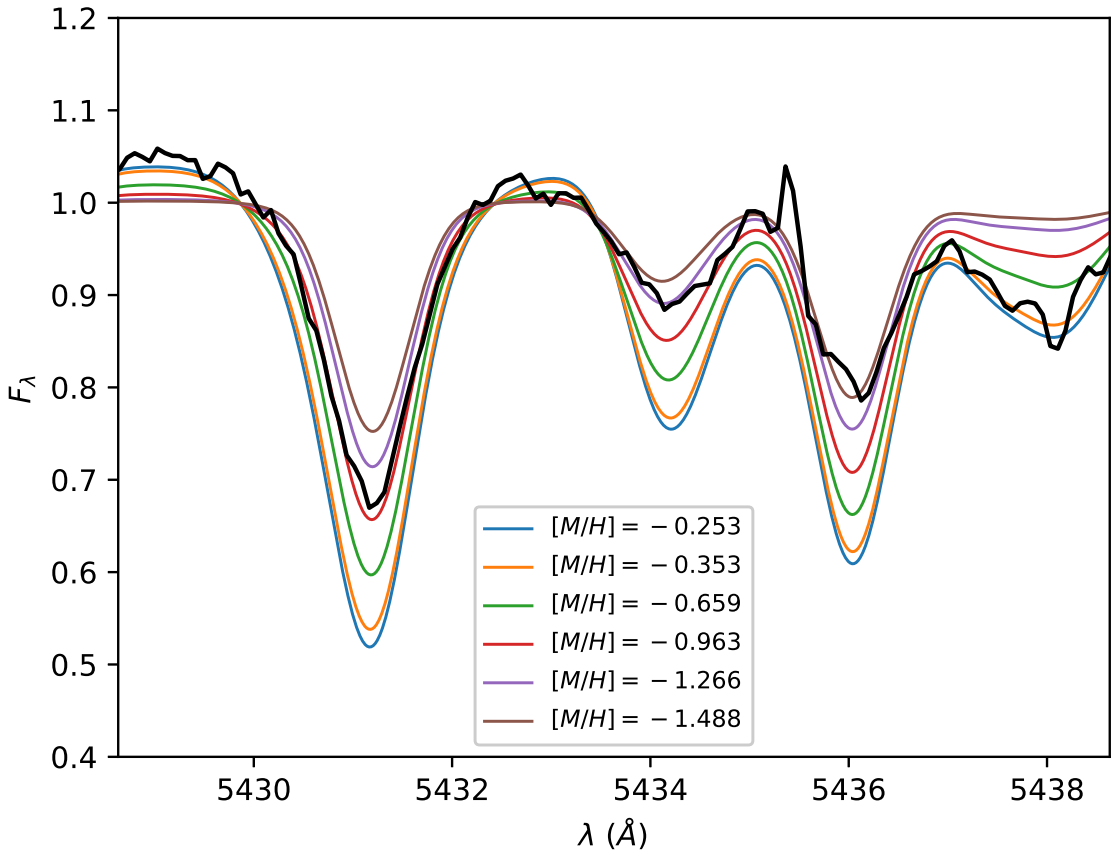

Figure B.17 Similar to Figure B.16, but containing the Fe I λ5431.2153 and λ5436.0446 lines, and the Mn I λ5434.0401 line.

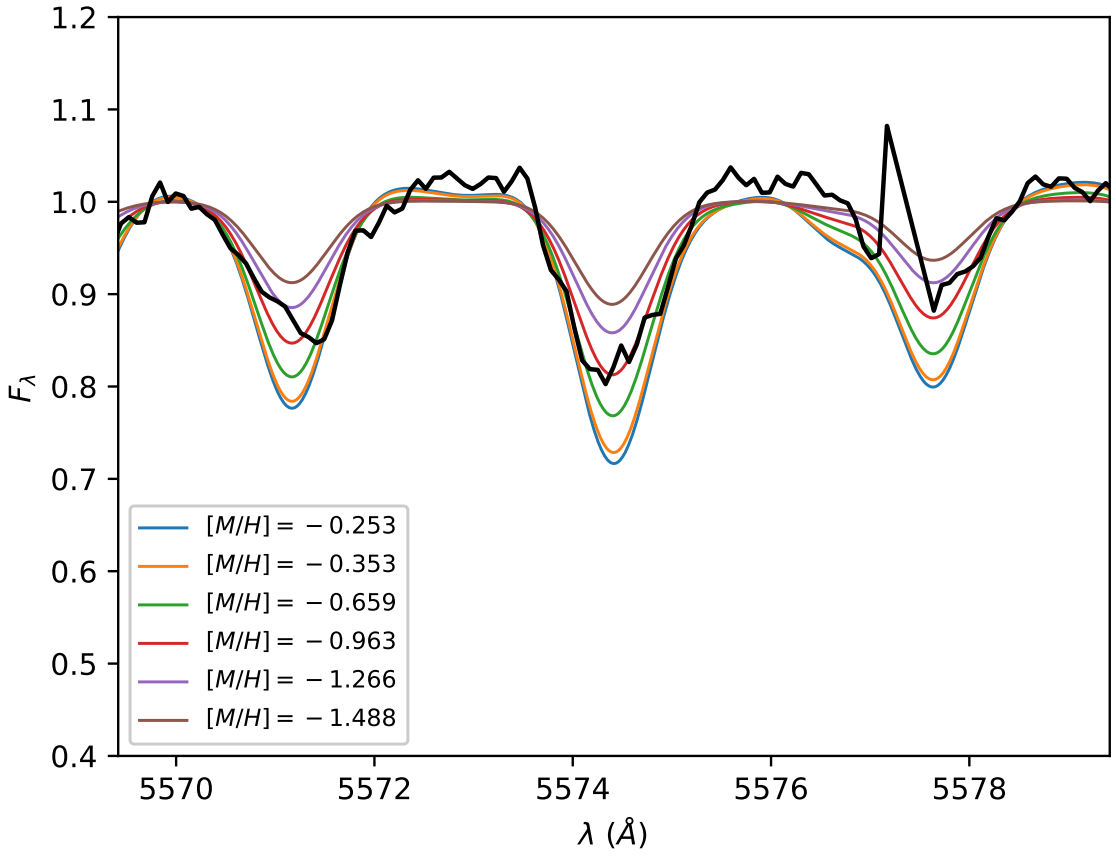

Figure B.18 Similar to Figure B.16, but containing the Fe I λ5571.1777, λ5574.3986 and λ5577.6474 lines.

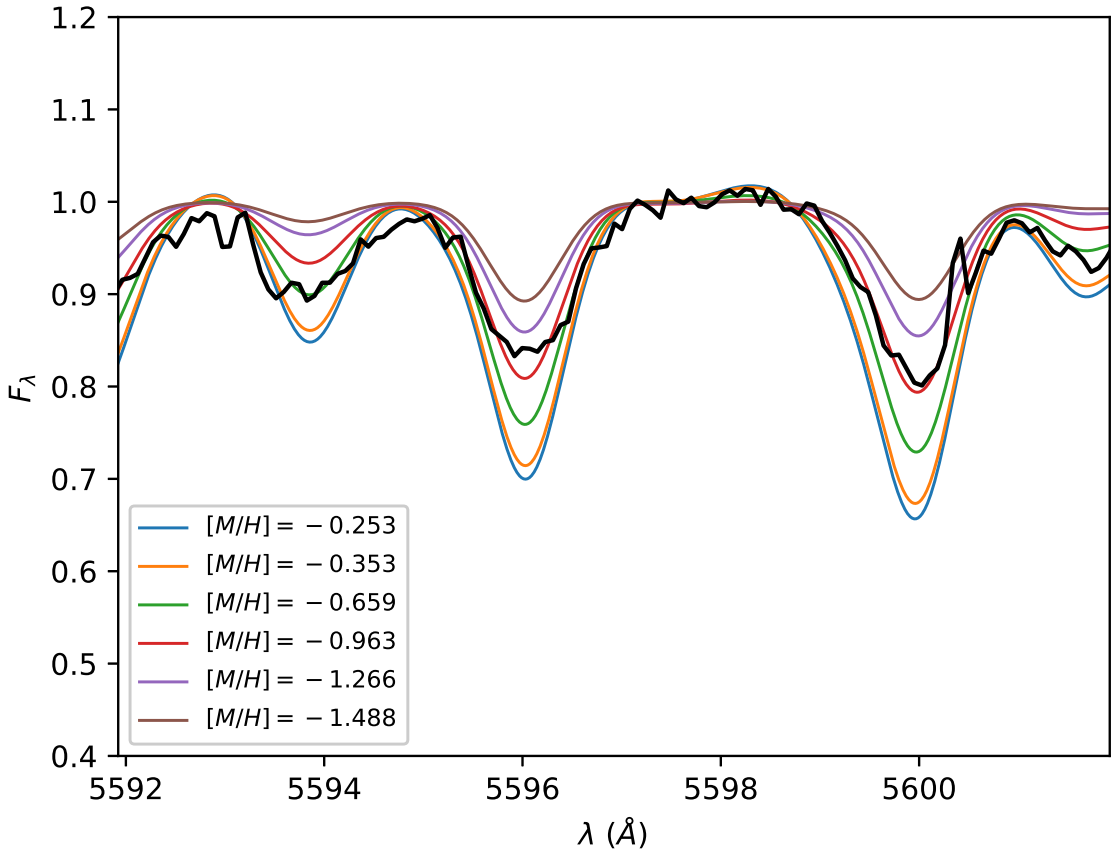

Figure B.19 Similar to Figure B.16, but containing the Ni I λ5593.8106 line, and the Ca I λ5596.015 and λ5600.0344 lines.

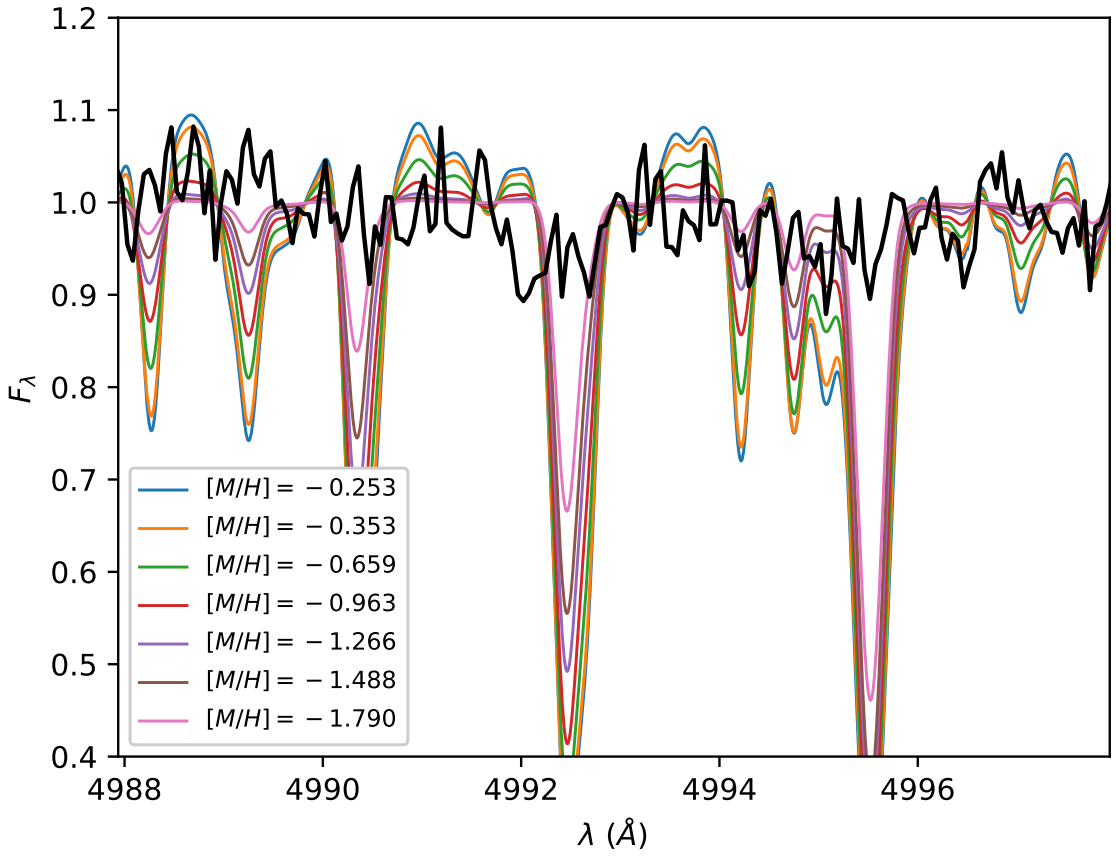

Figure B.20 Representative 10 $\mathring{A}$ window for NGC 6397 (in black) with bracketing 11.0 Gyr NLTE scaled-solar IL spectra. The window contains the Fe I λ4990.3411 and λ4995.5313 lines, and the Ti I λ4992.4574 line.

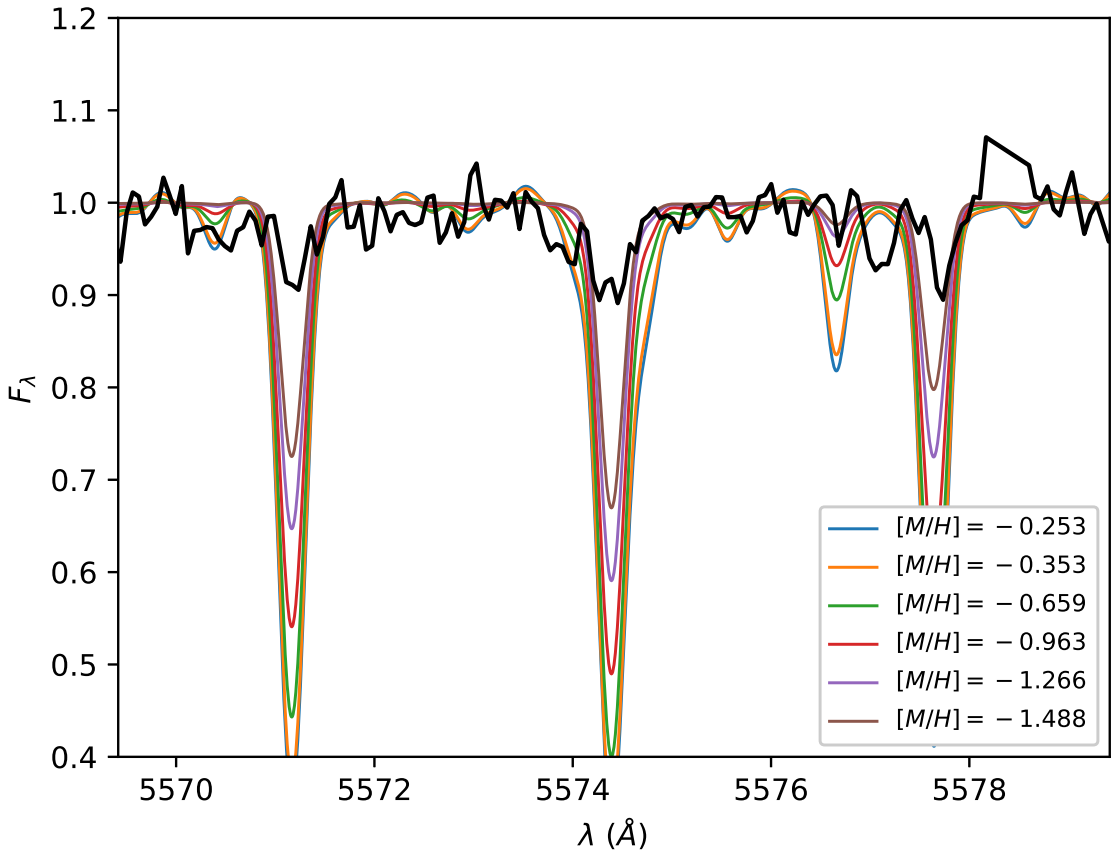

Figure B.21 Similar to Figure B.20, but with α-enhanced synthetic IL spectra and containing the Fe I λ5571.1777, λ5574.3986 and λ5577.6474 lines.

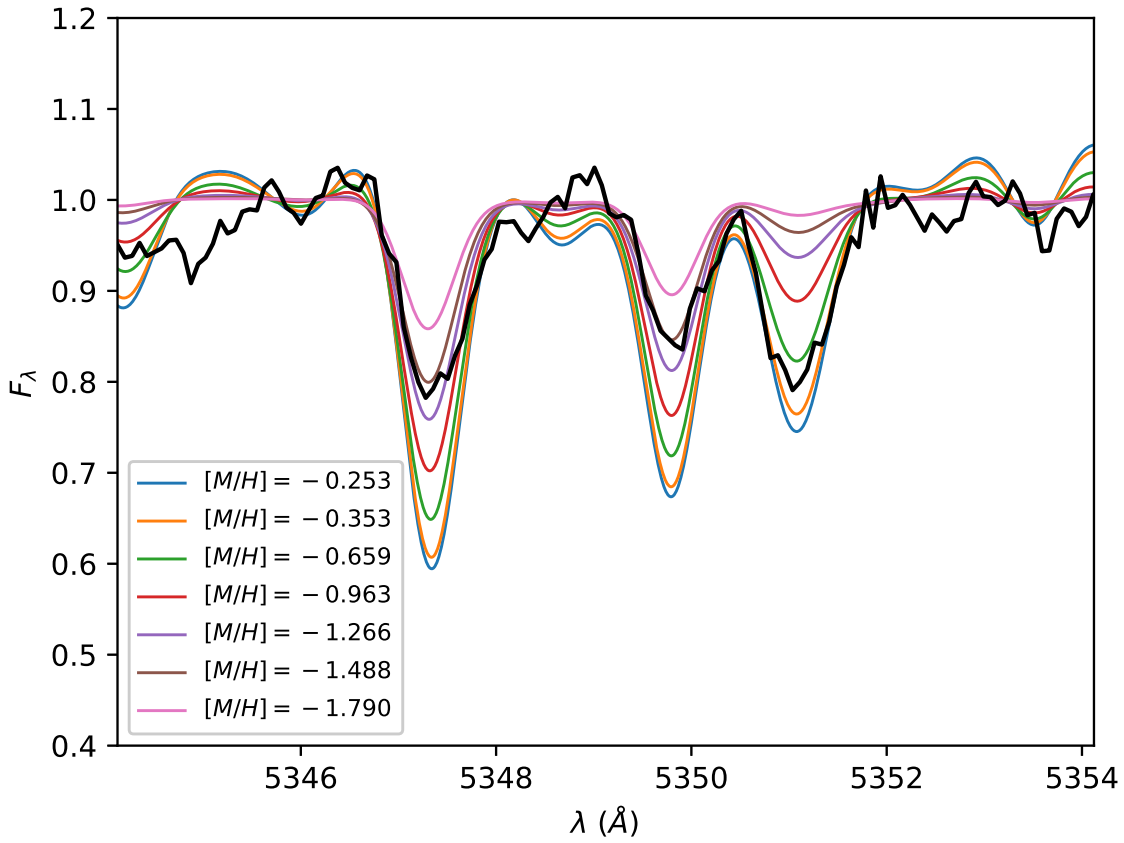

Figure B.22 Representative 10 $\mathring{A}$ window for NGC 6440 (in black) with bracketing 10.0 Gyr NLTE scaled-solar IL spectra. The window contains the Cr I λ5347.2939 and λ5349.8276 lines, and the Ca I λ5350.9569 line.

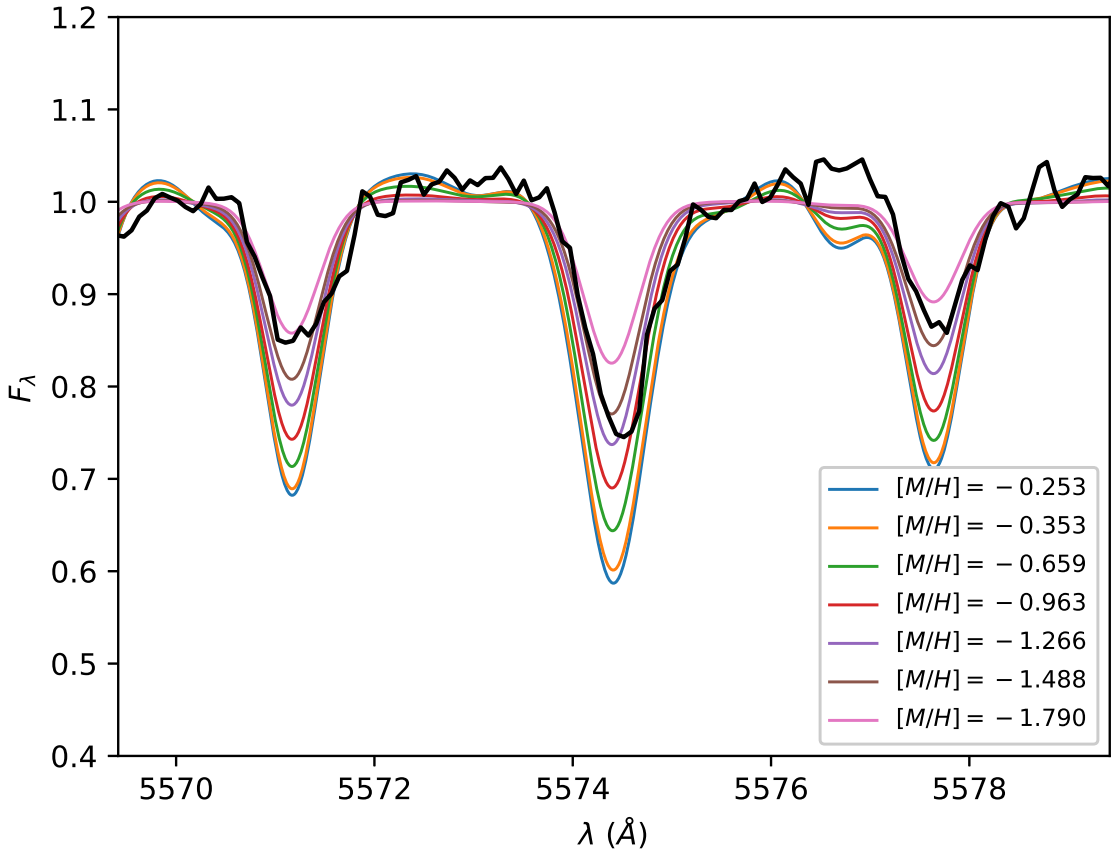

Figure B.23 Similar to Figure B.22, but containing the Fe I λ5571.1777, λ5574.3986 and λ5577.6474 lines.

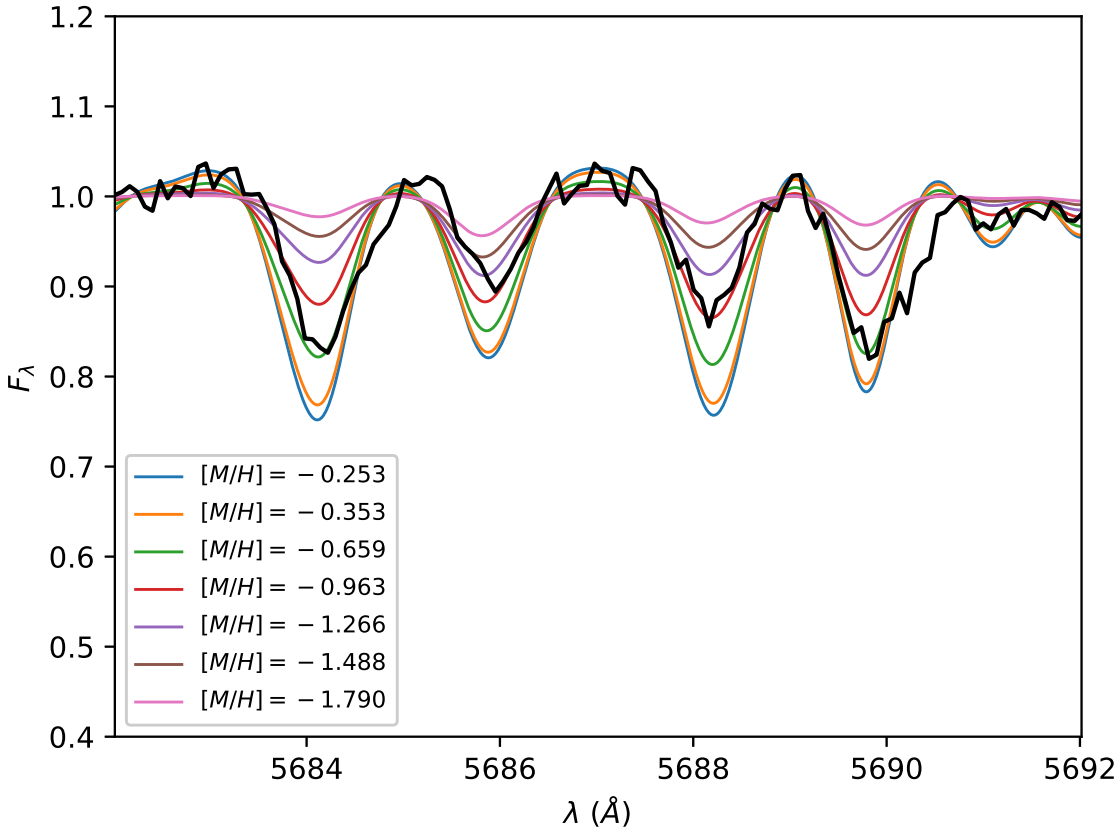

Figure B.24 Similar to Figure B.22, but containing the Na I λ5684.2269 and λ5689.7837 lines, and the Si I λ5686.0774 line.

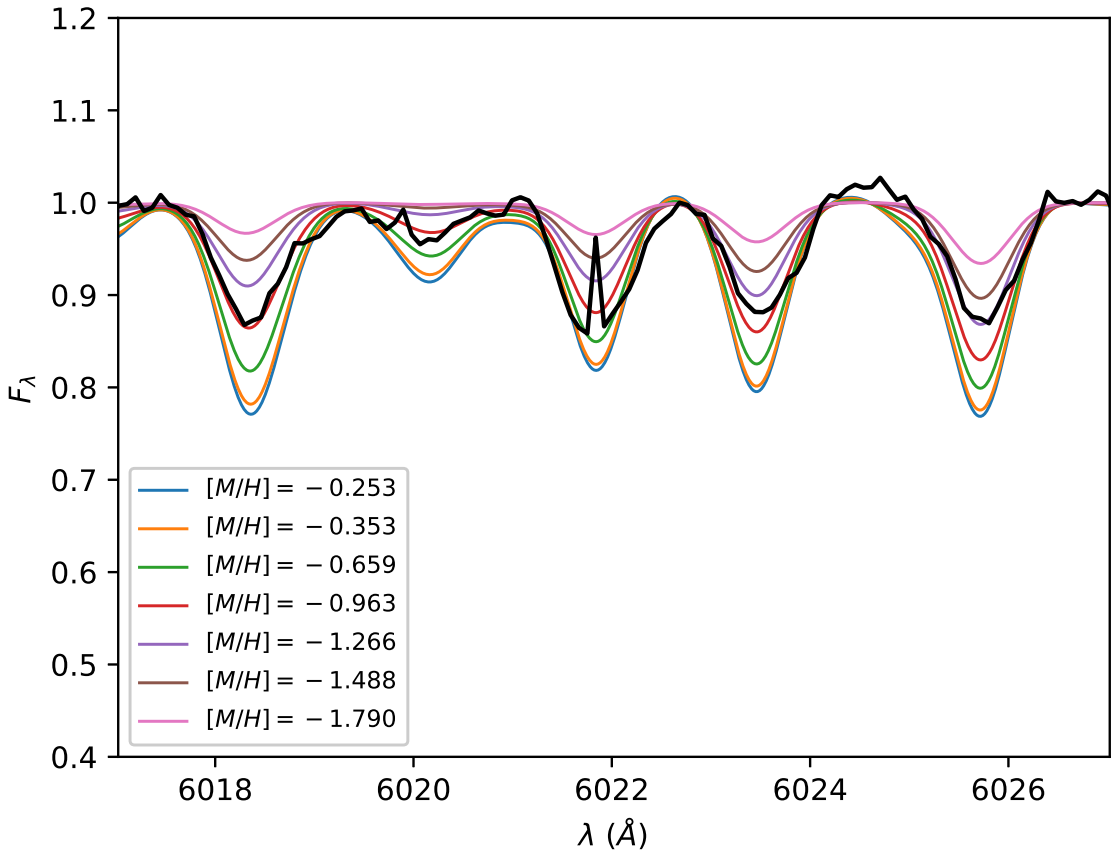

Figure B.25 Similar to Figure B.22, but containing the Mn I λ6018.3053 and λ6023.4877 line, and the Fe I λ6025.7263 line.

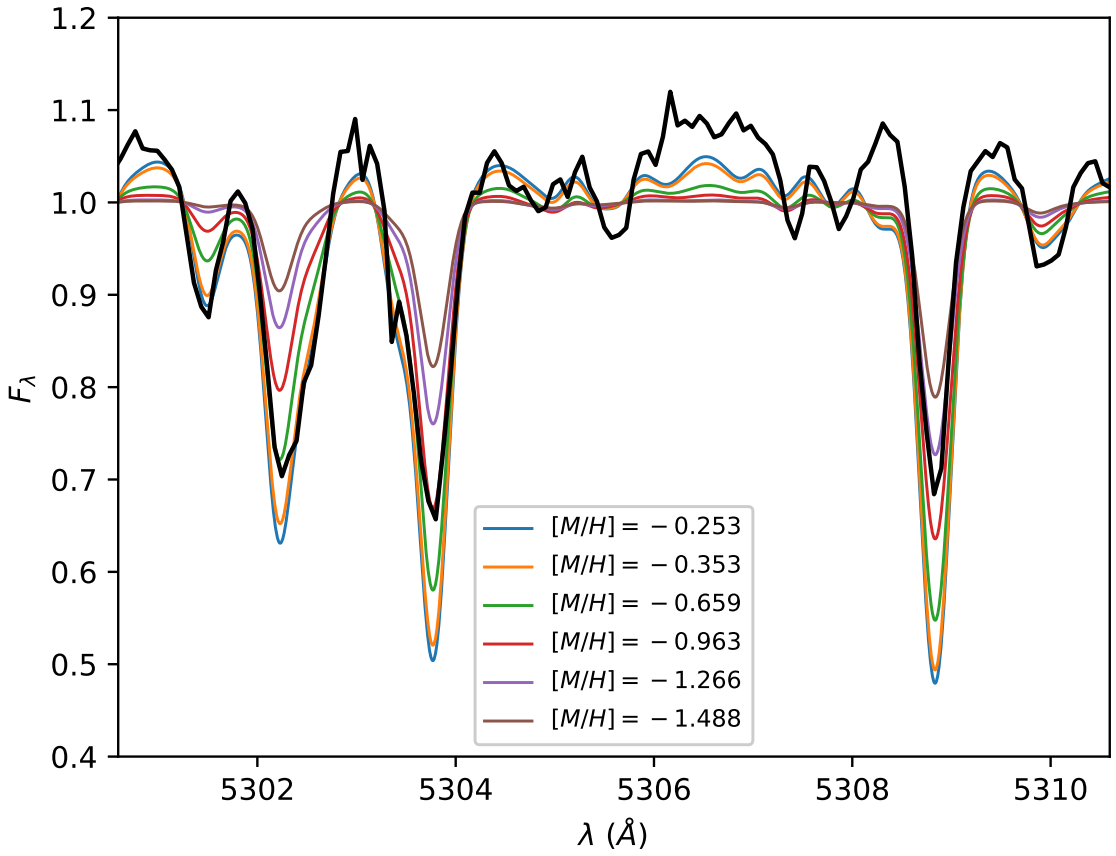

Figure B.26 Representative 10 $\mathring{A}$ window for NGC 6528 (in black) with bracketing 13.0 Gyr NLTE α-enhanced IL spectra. The window contains the Fe I λ5334.3831 and λ5341.4224 lines, and the Ti II λ5338.2645 line.

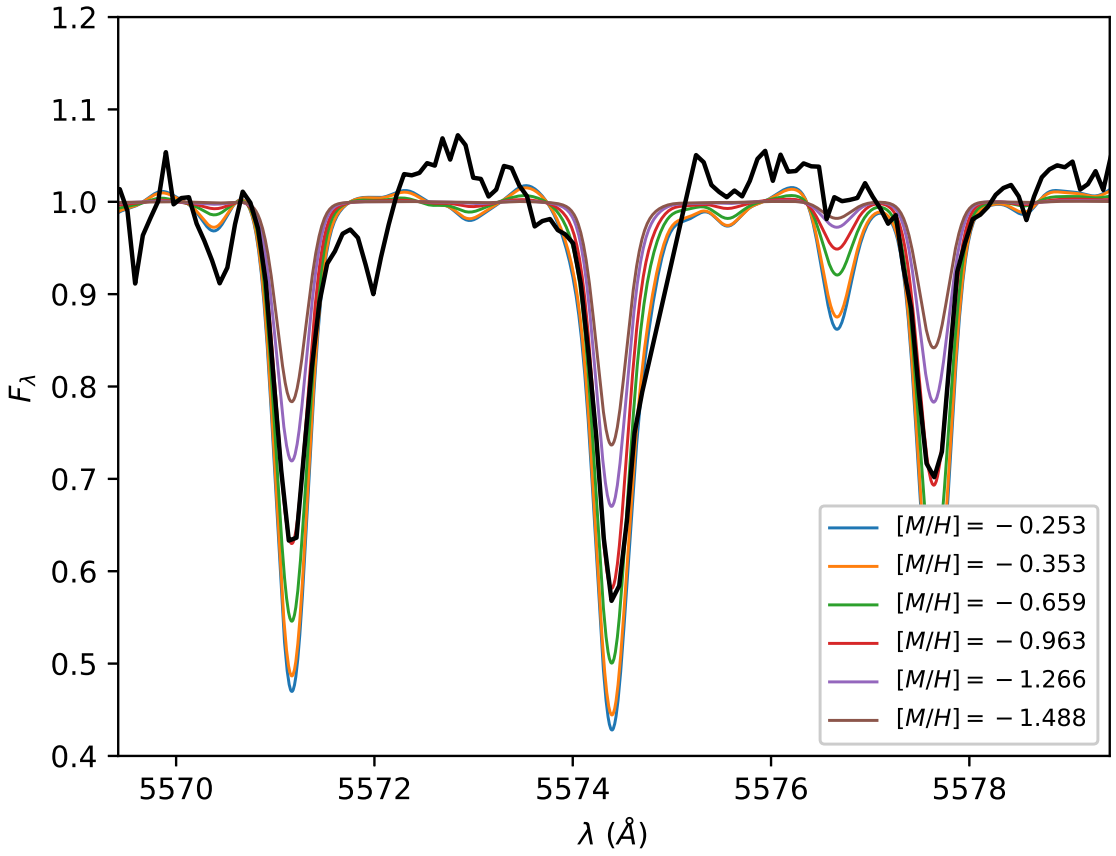

Figure B.27 Similar to Figure B.26, but containing the Fe I λ5571.1777, λ5574.3986 and λ5577.6474 lines.

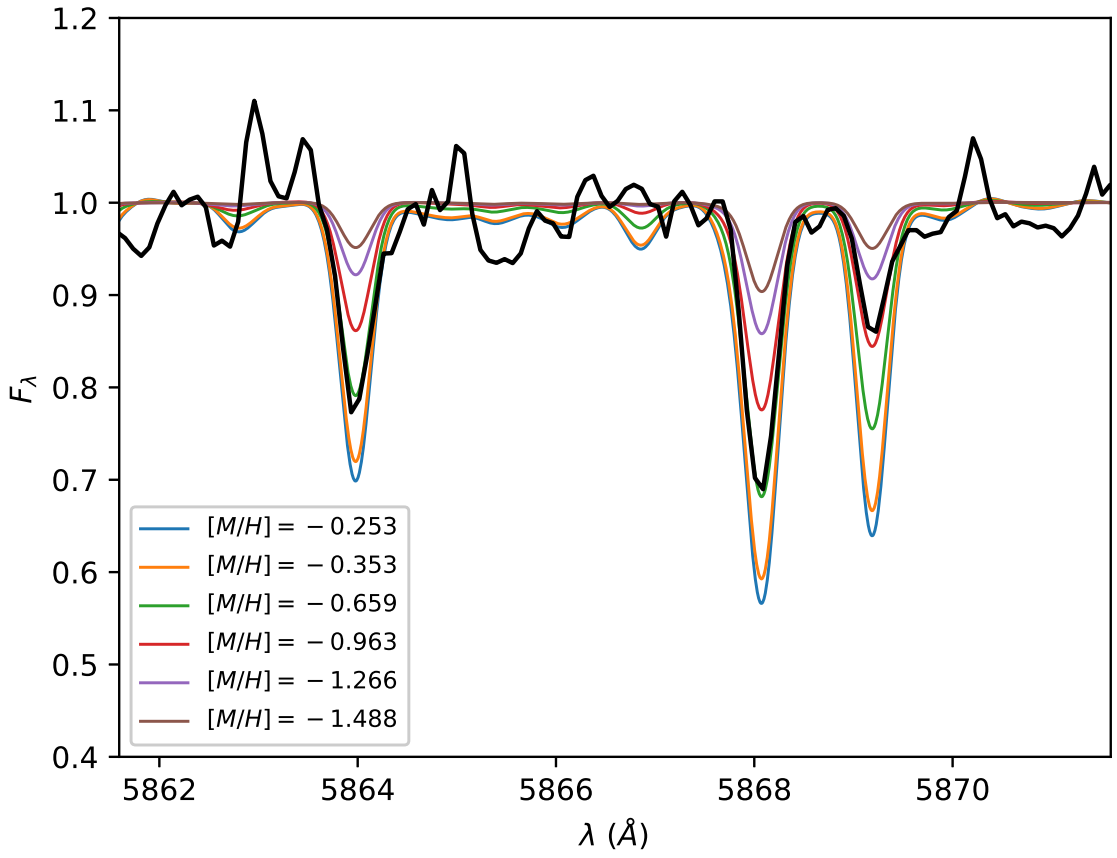

Figure B.28 Similar to Figure B.26, but containing the Fe I λ5863.9820 line, the Ti I λ5868.0784 line, and the Ca I λ5869.1984 line.

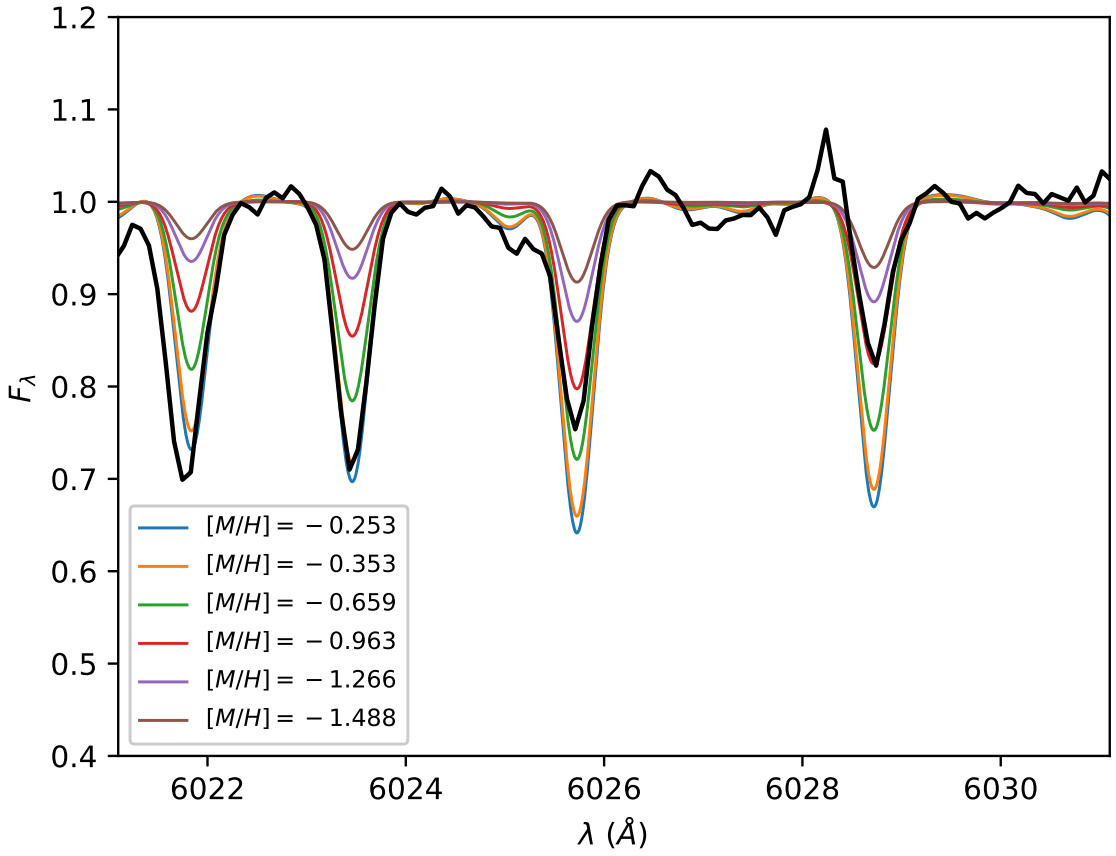

Figure B.29 Similar to Figure B.26, but containing the Mn I λ6023.4877 line, and the Fe I λ6025.7263 and λ6028.7201 lines.

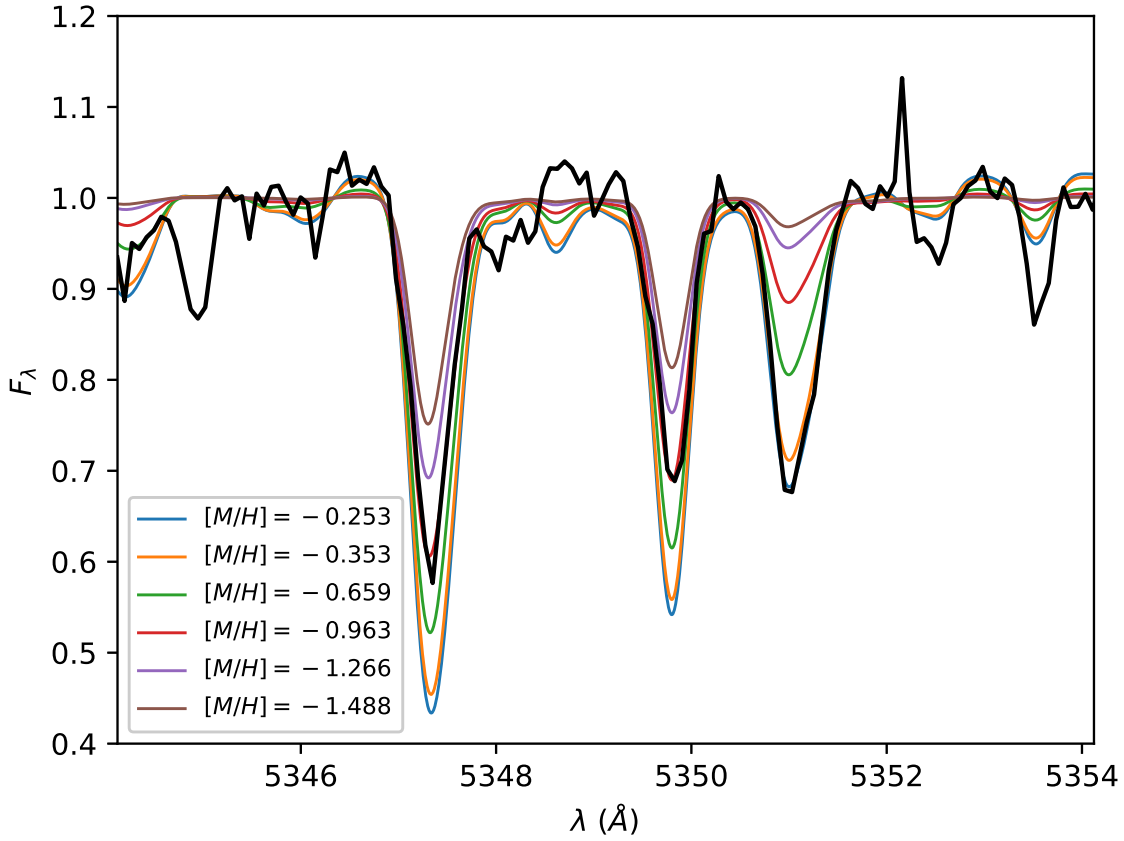

Figure B.30 Representative 10 $\mathring{A}$ window for NGC 6553 (in black) with bracketing 11.0 Gyr NLTE α-enhanced IL spectra. The window contains the Cr I λ5347.2939 and λ5349.8276 lines, and the Ca I λ5350.9569 line.

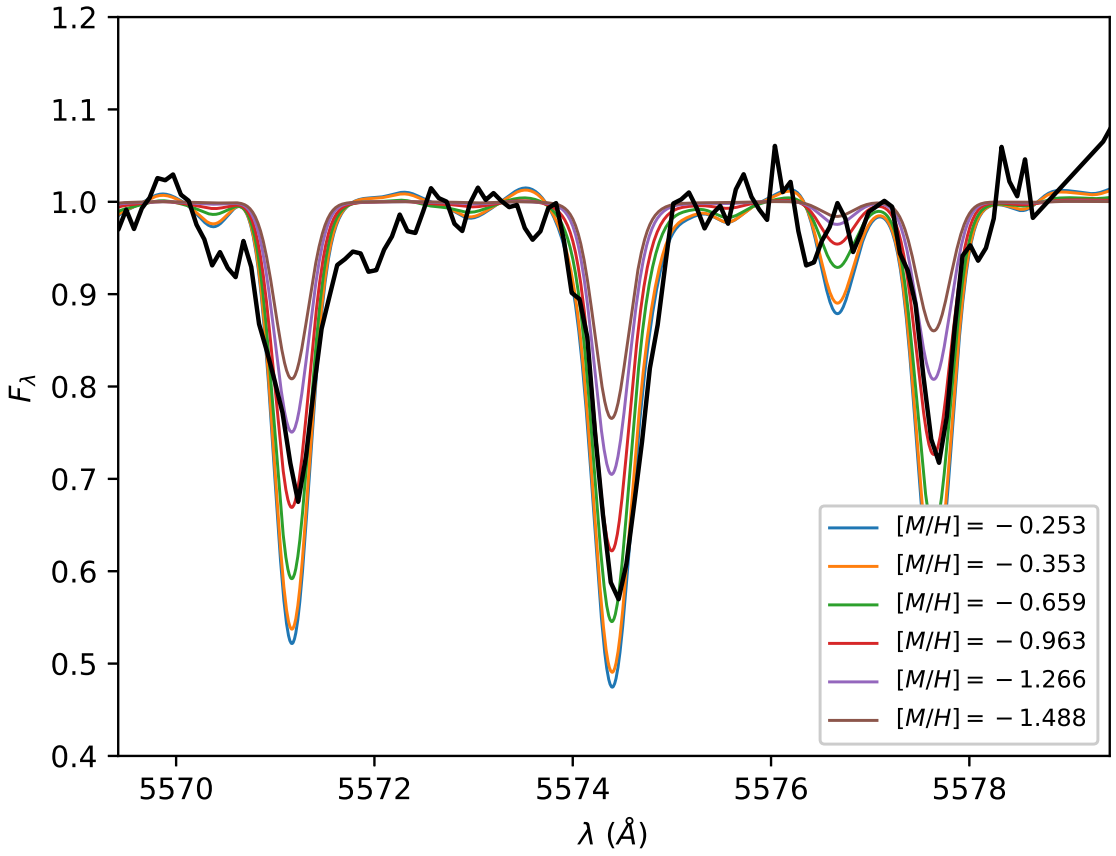

Figure B.31 Similar to Figure B.30, but containing the Fe I λ5571.1777, λ5574.3986 and λ5577.6474 lines.

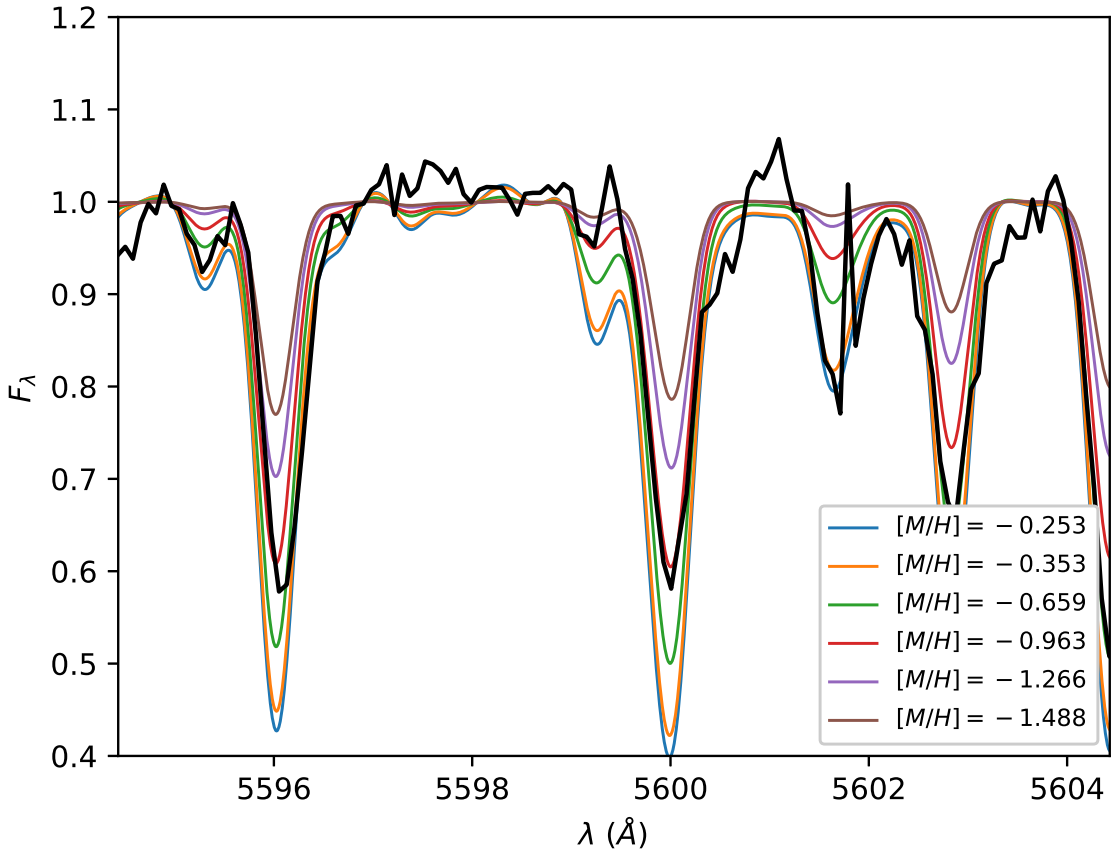

Figure B.32 Similar to Figure B.30, but containing the Ca I λ5600.0344, λ5602.8323 and λ5604.3985 lines.

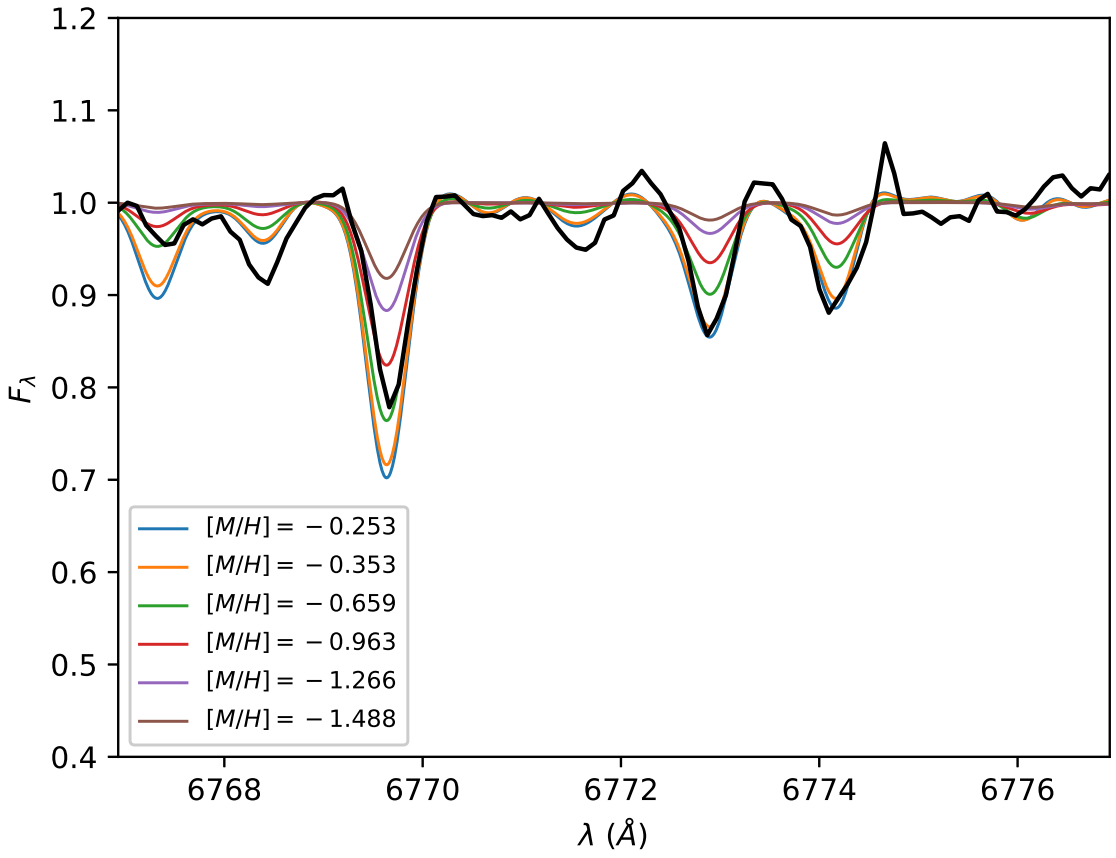

Figure B.33 Similar to Figure B.30, but containing the Ni I λ6769.6521 and λ6774.1903 lines, and the Co I λ6772.8390 line.

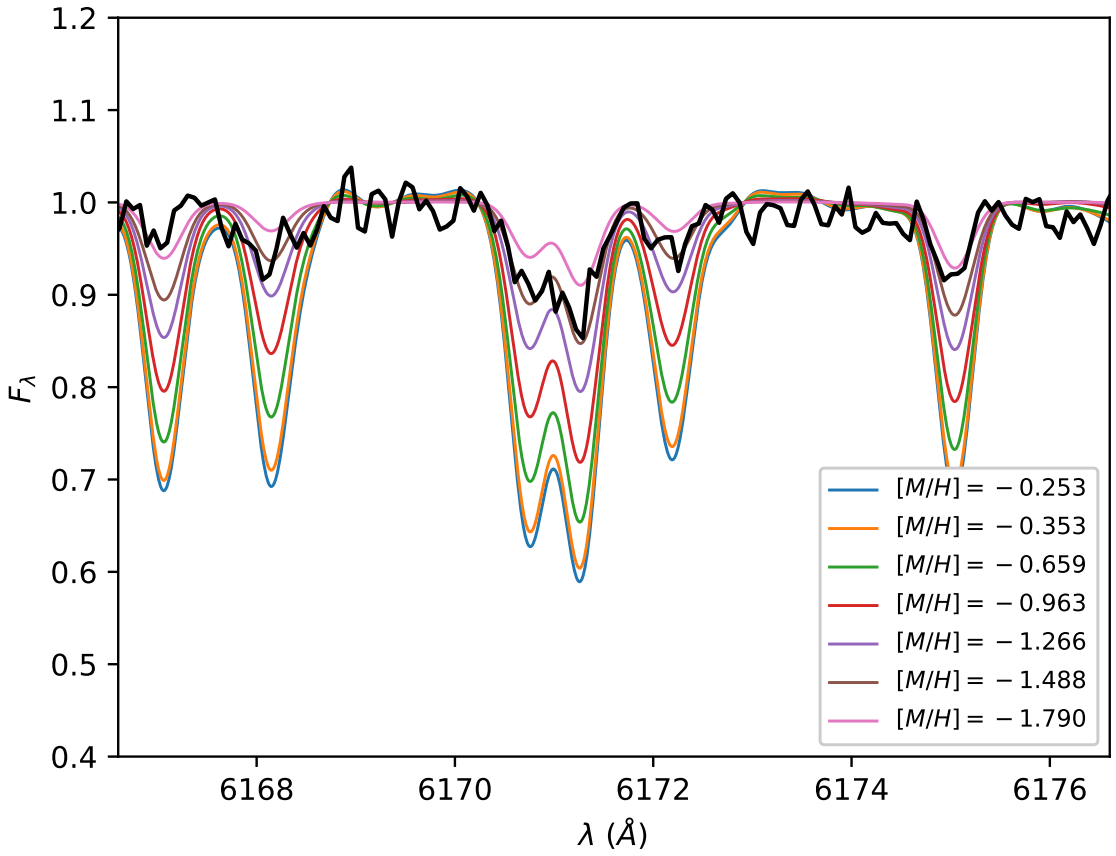

Figure B.34 Representative 10 $\mathring{A}$ window for NGC 6752 (in black) with bracketing 11.0 Gyr NLTE scaled-solar IL spectra. The window contains the Ca I λ6168.1465 and λ6171.2713 lines, and the Fe I λ6175.0484 line.

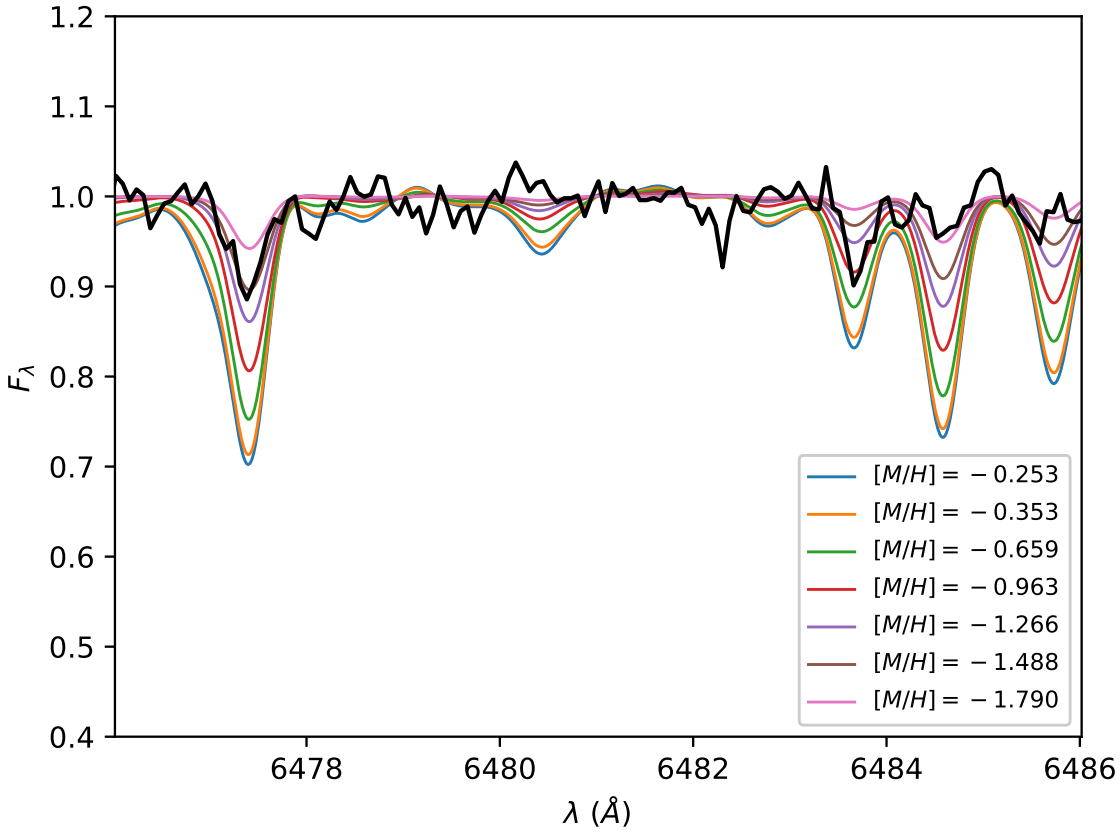

Figure B.35 Similar to Figure B.34, but containing the Fe I λ6477.4215 and λ6483.6692 lines, and the Ni I λ6484.6005 line.

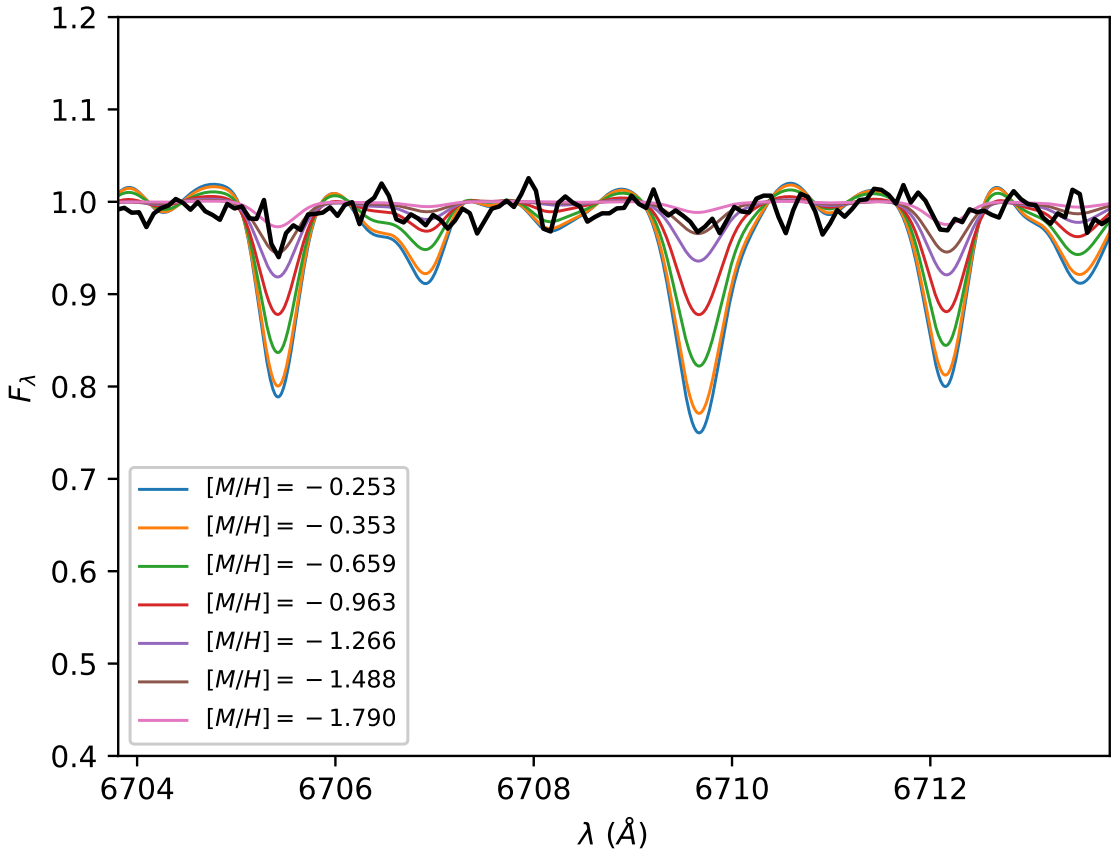

Figure B.36 Similar to Figure B.34, but containing the Fe I λ6705.4268, λ6706.9563 and λ6712.1757 lines.

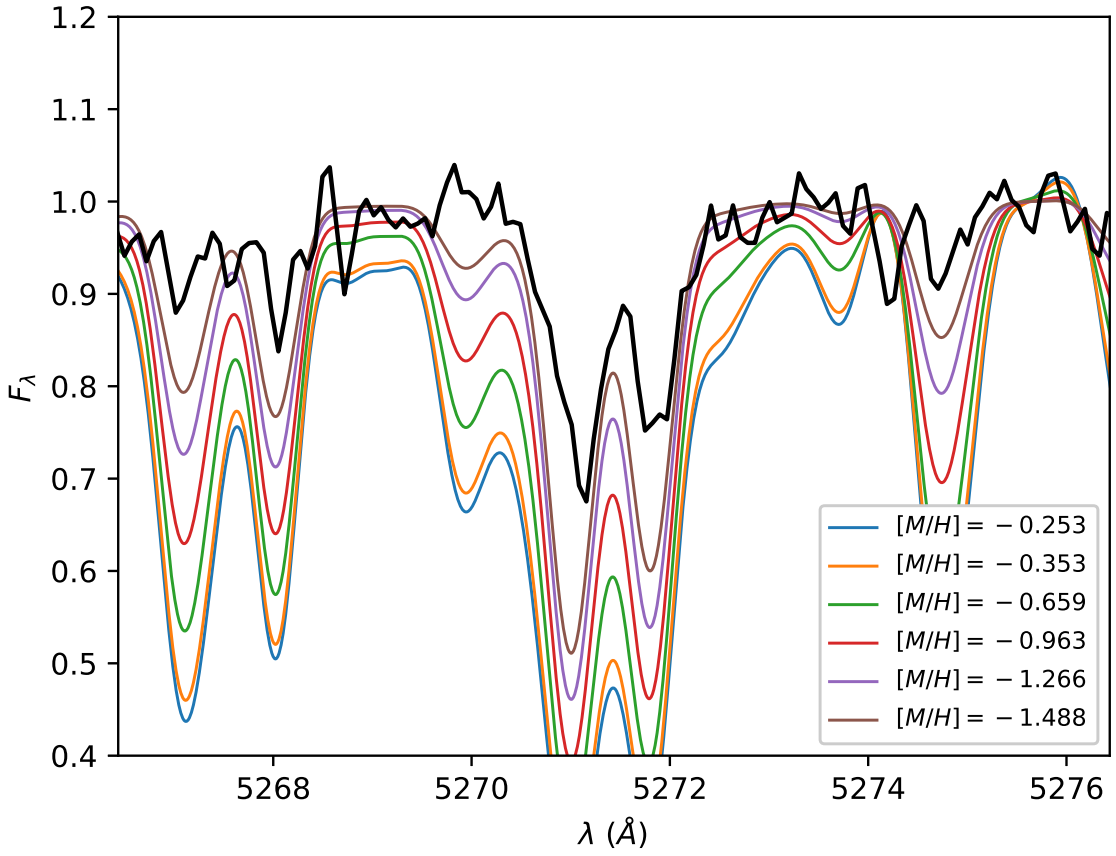

Figure B.37 Representative 10 $\AA$ window for Fornax 3 (in black) with bracketing 14.0 Gyr NLTE α-enhanced IL spectra. The window contains the Fe I λ5268.0288, λ5271.0166 and λ5274.8421 lines.

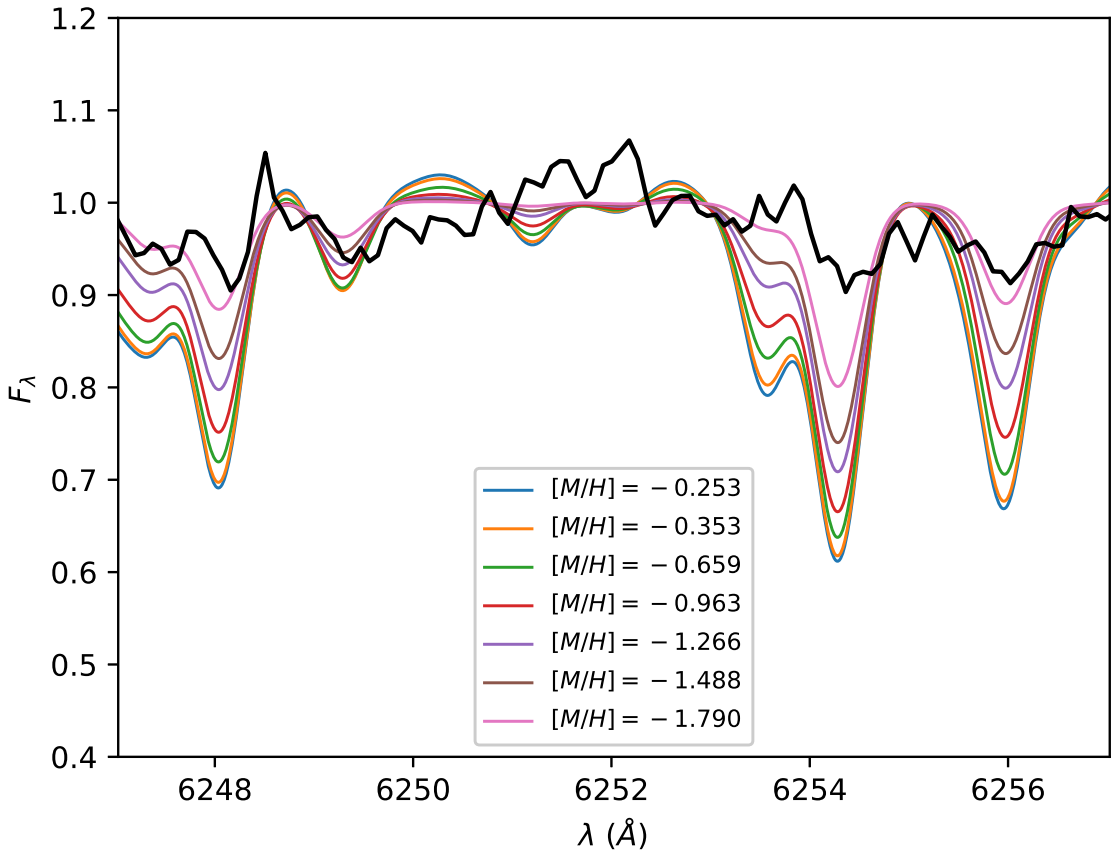

Figure B.38 Similar to Figure B.37, but with scaled-solar synthetic IL spectra and containing the Fe I λ6248.0550, λ6254.2946 and λ6255.9831 lines.